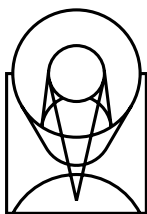

Version 3.0
June 1999

Near Infrared Camera and Multi-Object Spectrometer Instrument Handbook



For Use During Cycle 10 (NICMOS is not available in Cycle 9)



SPACE
TELESCOPE
SCIENCE
INSTITUTE

Science Support Division
3700 San Martin Drive
Baltimore, Maryland 21218
help@stsci.edu

User Support

For prompt answers to any question, please contact the Science Support Division Help Desk.

- **E-mail:** help@stsci.edu
- **Phone:** (410) 338-1082
(800) 544-8125 (U.S., toll free)

World Wide Web

Information and other resources are available on the NICMOS World Wide Web site:

- **URL:** <http://www.stsci.edu/instruments/nicmos>

NICMOS Instrument Team

Name	Title	Phone	e-mail
Antonella Nota	Group Lead	(410) 338-4520	nota@stsci.edu
Torsten Boeker	Instrument Scientist	(410) 338-4993	boeker@stsci.edu
Daniela Calzetti	Instrument Scientist	(410) 338-4518	calzetti@stsci.edu
Mark Dickinson	Instrument Scientist	(410) 338-4351	med@stsci.edu
Anand Sivaramakrishnan	Instrument Scientist	(410) 338-4480	anands@stsci.edu
Al Schultz	Instrument Scientist	(410) 338-5044	schultz@stsci.edu
Alex Storrs	Instrument Scientist	(410) 338-4903	storrs@stsci.edu
L. Eddie Bergeron	Data Analyst	(410) 338-1018	bergeron@stsci.edu
Sherie Holfeltz	Data Analyst	(410) 338-4418	holfeltz@stsci.edu
Lisa Mazzuca	Data Analyst	(410) 338-4811	mazzuca@stsci.edu
Brian Monroe	Data Analyst	(410) 338-4354	monroe@stsci.edu
Megan Sosey	Data Analyst	(410) 338-4365	sosey@stsci.edu

Revision History

Version	Date	Editors
1.0	June 1996	D.J. Axon, D. Calzetti, J.W. MacKenty, C. Skinner
2.0	July 1997	J.W. MacKenty, C. Skinner, D. Calzetti, and D.J. Axon
3.0	June 1999	D. Calzetti, L. Bergeron, T. Boeker, M. Dickinson, S. Holfeltz, L. Mazzuca, B. Monroe, A. Nota, A. Sivaramakrishnan, A. Schultz, M. Sosey, A. Storrs, A. Suchkov.

Citation

In publications, refer to this document as:

Calzetti, D. et al., 1999, "NICMOS Instrument Handbook", Version 3.0, (Baltimore: STScI).

Send comments or corrections to:
Science Support Division
Space Telescope Science Institute
3700 San Martin Drive
Baltimore, Maryland 21218
E-mail: help@stsci.edu



Acknowledgments

The technical and operational information contained in this Handbook is the summary of the experience gained both by members of the STScI NICMOS group and by the NICMOS IDT (P.I.: Rodger Thompson, U. of Arizona) during Cycle 7 and Cycle 7-N, and from subsequent analysis of the NICMOS data. Special thanks are due to Marcia Rieke, Glenn Schneider and Dean Hines (U. of Arizona), whose help has been instrumental in many sections of this Handbook.

We are also indebted with Wolfram Freudling (ST-ECF) for major contributions to the section on the NICMOS grisms.

Table of Contents

Acknowledgments	iii
------------------------------	-----

Part I: Introduction	1
-----------------------------------	---

Chapter 1: Introduction and General Considerations	3
---	---

<i>Purpose</i>	4
----------------------	---

Document Conventions	5
----------------------------	---

<i>Layout</i>	5
---------------------	---

<i>NICMOS Proposal Preparation</i>	9
--	---

<i>The Help Desk at STScI</i>	9
-------------------------------------	---

<i>The NICMOS Instrument Team at STScI</i>	10
--	----

<i>Supporting Information and the NICMOS Web Site</i>	10
---	----

<i>NICMOS History in Brief</i>	11
--------------------------------------	----

<i>Major Changes Relative to Cycles 7 and 7N</i>	12
--	----

<i>Recommendations for Proposers</i>	13
--	----

<i>Supported and Unsupported NICMOS Capabilities</i>	15
--	----

Chapter 2: Overview of NICMOS	17
--	----

<i>Instrument Capabilities</i>	17
--------------------------------------	----

<i>History of NICMOS</i>	19
--------------------------------	----

<i>NICMOS Instrument Design</i>	20
---------------------------------------	----

Physical Layout	20
-----------------------	----

Imaging Layout	22
----------------------	----

Camera NIC1	24
-------------------	----

Camera NIC2.....	24
Camera NIC3.....	24
Location and Orientation of Cameras	24
<i>The NICMOS Cooling System</i>	25
<i>Basic Operations</i>	28
Detectors' Characteristics and Operations	28
Comparison to CCDs.....	30
Target Acquisition Modes	31
Attached Parallels.....	31

Chapter 3: Designing NICMOS Observations..... 33

Part II: User's Guide..... 37

Chapter 4: Imaging..... 39

<i>Filters & Optical Elements</i>	39
Nomenclature	40
Out-of-Band Leaks in NICMOS Filters.....	47
<i>Photometry</i>	47
Solar Analog Absolute Standards.....	48
White Dwarf Absolute Standards.....	48
Photometric throughput and stability	49
Intrapixel sensitivity variations	49
Special Situations	49
Sources with Extreme Colors	49
Extended Sources with Extreme Spatial Color Variations	51
Creating Color-dependent Flat Fields	52
<i>Focus History</i>	52
<i>Image Quality</i>	55
Strehl Ratios	55
NIC1 and NIC2	55
Vignetting in NIC1 and NIC2	58
NIC3.....	60
Vignetting in NIC3	62
NICMOS Point Spread Function (PSF)	63
Optical aberrations: coma and astigmatism.....	63

Field Dependence of the PSF	64
Temporal Dependence of the PSF: HST Breathing and Cold Mask Shifts	64
<i>Cosmic Rays</i>	65
<i>Photon and Cosmic Ray Persistence</i>	65
<i>The Infrared Background</i>	67
Conversion Between Fluxes and Magnitudes	72

Chapter 5: Coronagraphy, Polarimetry and Grism Spectroscopy

<i>Coronagraphy</i>	75
Coronagraphic Acquisitions	78
Onboard Acquisition (Mode-2 Acquisition)	78
Reuse Target Offset (RTO) and Interactive Acquisitions	80
PSF Centering	81
Temporal Variations of the PSF	81
FGS Guiding	82
Cosmic Ray Persistence	83
Contemporary Flat Fields	83
Coronagraphic Decision Chart	84
<i>Polarimetry</i>	86
NIC 1 and NIC2 Polarimetric Characteristics and Sensitivity	86
Ghosting	88
Observing Strategy Considerations	89
Limiting Factors	90
Limiting Polarization	90
Position Angle of Incoming Polarization Relative to NICMOS Orientation	91
Polarimetry Decision Chart	91
<i>Grism Spectroscopy</i>	93
Multi-Object Spectroscopy	94
Grism Calibration	95
Relationship Between Wavelength and Pixel	95
Sensitivity	96
Grism A: G096	99
Grism B: G141	99
Grism C: G206	99

Intrapixel Sensitivity	99
Grism Decision Chart.....	100

Chapter 6: NICMOS Apertures and Orientation

.....	103
<i>NICMOS Aperture Definitions</i>	103
<i>NICMOS Coordinate System Conventions</i>	104
<i>Orients</i>	105

Chapter 7: NICMOS Detectors

<i>Detector basics</i>	107
<i>Detector Characteristics</i>	110
Overview	110
Dark current	111
Flat fields and the DQE.....	113
Read Noise	119
Linearity	120
<i>Detector Artifacts</i>	121
Shading.....	121
Amplifier Glow.....	123
Overexposure of NICMOS Detectors	124
Electronic bars	124
Bad Pixels.....	124
"Grot"	125

Chapter 8: Detector Readout

Modes	127
<i>Introduction</i>	127
Detector Resetting as a Shutter.....	129
Fast and Slow Readout Modes.....	129
<i>Accumulate Mode</i>	130
Multiple Initial and Final Sample Readout	131
<i>Multiple-Accumulate Mode</i>	133
<i>MULTIACCUM Predefined Sample Sequences (SAMP-SEQ)</i>	134
<i>Trade-offs Between ACCUM and MULTIACCUM</i>	137
<i>Read Times and Dark Current Calibration in</i>	

<i>ACCUM Mode</i>	138
<i>Acquisition Mode</i>	139

Part III: How to Plan an Observation..... 141

Chapter 9: Exposure Time

Calculations	143
<i>Overview</i>	143
Instrumental Factors	145
Detectors	145
Optics	146
Background Radiation	146
<i>Calculating NICMOS Imaging Sensitivities</i>	147
Signal to noise Calculation	147
Saturation and Detector Limitations.....	149
Exposure Time Calculation.....	149
<i>WWW Access to the Exposure Time Calculator</i>	152
Using the NICMOS Imaging Exposure Time Calculator ...	152

Chapter 10: Overheads and Orbit Time

Determination	155
<i>Overview</i>	155
<i>NICMOS Exposure Overheads</i>	156
<i>Orbit Use Determination</i>	159
Observations in the Thermal Regime Using a Chop Pattern and MULTIACCUM.....	159

Chapter 11: Techniques for Dithering, Background Measurement and Mosaicing..... 163

<i>Introduction</i>	164
<i>Strategies For Background Subtraction</i>	165
Compact Objects	165
Extended Objects	166
<i>Chopping and Dithering Patterns</i>	167
Note on Orientation:	169
Move the sky or the telescope?.....	169

Dither Patterns	170
Chop Patterns	171
Combined Patterns	172
Map Patterns	173
<i>Examples</i>	175
<i>Phase II Proposal Instructions for Patterns</i>	178
Types of Motions	178

Part IV: Calibration Overview 181

Chapter 12: Calibration Pipeline 183

<i>Overview</i>	183
Associations	184
Concept	184
Usage	185
Re-engineering	186
<i>NICMOS Pipeline</i>	187
Static Calibrations—calnica	187
Contemporaneous Observations—calnicb	190
<i>NICMOS Data Products</i>	191
Standard NICMOS Dataset Structure	191
Science Image (SCI)	192
Error Array (ERR)	192
Data Quality Flags Array (DQ)	192
Samples Array (SAMP)	192
Integration Time Array (TIME)	193
IRAF Access	193

Chapter 13: Calibration Goals and Plans 195

<i>Expected Calibration Accuracies</i>	195
Remarks	195
Areas of Significant Uncertainty	196
Provisional Cycle 10 Calibration Goals	197
<i>Calibration Plans</i>	197

Part V: Appendices 201

Appendix 1: Imaging Reference

Material	203
<i>Camera 1, Filter F090M</i>	205
<i>Camera 1, Filter F095N</i>	206
<i>Camera 1, Filter F097N</i>	207
<i>Camera 1, Filter F108N</i>	208
<i>Camera 1, Filter F110M</i>	209
<i>Camera 1, Filter F110W</i>	210
<i>Camera 1, Filter F113N</i>	211
<i>Camera 1, Filter F140W</i>	212
<i>Camera 1, Filter F145M</i>	213
<i>Camera 1, Filter F160W</i>	214
<i>Camera 1, Filter F164N</i>	215
<i>Camera 1, Filter F165M</i>	216
<i>Camera 1, Filter F166N</i>	217
<i>Camera 1, Filter F170M</i>	218
<i>Camera 1, Filter F187N</i>	219
<i>Camera 1, Filter F190N</i>	220
<i>Camera 1, Polarizer POL0S</i>	221
<i>Camera 2, Filter F110W</i>	222
<i>Camera 2, Filter F160W</i>	223
<i>Camera 2, Filter F165M</i>	224
<i>Camera 2, Filter F171M</i>	225
<i>Camera 2, Filter F180M</i>	226
<i>Camera 2, Filter F187N</i>	227
<i>Camera 2, Filter F187W</i>	228
<i>Camera 2, Filter F190N</i>	229
<i>Camera 2, Filter F204M</i>	230
<i>Camera 2, Filter F205W</i>	231
<i>Camera 2, Filter F207M</i>	232
<i>Camera 2, Filter F212N</i>	233
<i>Camera 2, Filter F215N</i>	234
<i>Camera 2, Filter F216N</i>	235

<i>Camera 2, Filter F222M</i>	236
<i>Camera 2, Filter F237M</i>	237
<i>Camera 2, Polarizer POL0L</i>	238
<i>Camera 3, Filter F108N</i>	239
<i>Camera 3, Filter F110W</i>	240
<i>Camera 3, Filter F113N</i>	241
<i>Camera 3, Filter F150W</i>	242
<i>Camera 3, Filter F160W</i>	243
<i>Camera 3, Filter F164N</i>	244
<i>Camera 3, Filter F166N</i>	245
<i>Camera 3, Filter F175W</i>	246
<i>Camera 3, Filter F187N</i>	247
<i>Camera 3, Filter F190N</i>	248
<i>Camera 3, Filter F196N</i>	249
<i>Camera 3, Filter F200N</i>	250
<i>Camera 3, Filter F212N</i>	251
<i>Camera 3, Filter F215N</i>	252
<i>Camera 3, Filter F222M</i>	253
<i>Camera 3, Filter F240M</i>	254
Appendix 2: Flux Units and Line Lists	255
<i>Infrared Flux Units</i>	255
Some History	256
Units for NICMOS and Available Software	257
<i>Formulae</i>	258
Converting Between F_n and F_l	258
Conversion Between Fluxes and Magnitudes	258
Conversion Between Surface Brightness Units	259
<i>Look-up Tables</i>	259
<i>Examples</i>	266
<i>Infrared Line Lists</i>	266
Appendix 3: Bright Object Mode	275
<i>Bright Object Mode</i>	275
Index	279

Introduction

The chapters in this part explain how to use this handbook, where to go for help, and describe special considerations for using NICMOS in Cycle 10.

Introduction and General Considerations

In This Chapter...

Purpose / 4
Layout / 5
NICMOS Proposal Preparation / 9
The Help Desk at STScI / 9
The NICMOS Instrument Team at STScI / 10
Supporting Information and the NICMOS Web Site / 10
NICMOS History in Brief / 11
Major Changes Relative to Cycles 7 and 7N / 12
Recommendations for Proposers / 13
Supported and Unsupported NICMOS Capabilities / 15

The Near Infrared Camera and Multi-Object Spectrometer, NICMOS, provides HST with infrared imaging and spectroscopic capabilities between 0.8 and 2.5 microns. From above the earth's atmosphere, NICMOS provides access to this complete spectral range without hindrance from atmospheric emission or absorption at a sensitivity and angular resolution not possible from the ground. NICMOS, which operated from February 1997 till November 1998 using passive cooling, is expected to be revived with the installation of the NICMOS Cooling System (NCS) during the Servicing Mission SM3B, currently scheduled for June, 2001. The NCS will provide active cooling through a series of closed circuit

loops containing cryogenic liquid. NICMOS is therefore offered to the community in Cycle 10 and beyond.

This Handbook provides the instrument specific information needed to propose HST observations (Phase I), design accepted proposals (Phase II, in conjunction with the Phase II Proposal Instructions), and understand NICMOS in detail. The Handbook has been revised from its original versions to include expected performance with the NCS.

This chapter explains the layout of the Handbook and how to get additional help and information through the Help Desk and STScI World Wide Web pages. It also lists the supported capabilities of NICMOS and includes basic recommendations on how to use the Instrument.

Purpose

The *NICMOS Instrument Handbook* is the basic reference manual for the Near Infrared Camera and Multi-Object Spectrometer and describes the instrument's properties, expected performance, operations, and calibration. The Handbook is maintained by the NICMOS Instrument Group at STScI.

We designed the document to serve three purposes:

- To provide instrument-specific information for preparing Cycle 10 observing proposals with NICMOS.
- To provide instrument-specific information to support the design of Phase II proposals for accepted NICMOS proposals (in conjunction with the Phase II Proposal Instructions).
- To provide technical information about the operation and performance of the instrument after the installation of the NCS, which can help in understanding problems and interpreting data acquired with NICMOS.

This Handbook is not meant to serve as a manual for the reduction and analysis of data taken with NICMOS. For this, please refer to the *HST Data Handbook*.



A significant change from the last version of the NICMOS Instrument Handbook is that the Cycle 10 NICMOS performance described here are those expected with operations with the NCS. The NCS is expected to cool NICMOS to about 72-75 K, a full 10-15 K higher than during Cycle 7 and Cycle 7-N operations. The higher operating temperature affects the expected performance of the Instrument.

Document Conventions

This document follows the usual STScI convention in which terms, words, and phrases which are to be entered by the user in a literal way on a proposal are shown in a typewriter font (e.g., BRIGHT=RETURN, FP-SPLIT). Names of software packages or commands (e.g., **synphot**) are given in bold type.

Wavelength units in this Handbook are in microns (μm) and fluxes are given in Janskys (Jy), unless otherwise noted.

Layout

NICMOS provides direct imaging in broad, medium, and narrow-band filters at a range of spatial resolutions in the near infrared from 0.8 to 2.5 microns, together with broad-band imaging polarimetry, coronagraphic imaging and slitless grism spectroscopy. To guide the proposer through NICMOS's capabilities and help optimize the scientific use of the instrument we have divided this Handbook into five parts: Part I: Introduction; Part II: User's Guide; Part III: How to Plan an Observation; Part IV: Calibration Overview; and Part V: Appendices. Figure 1.1 provides a roadmap to navigating the document.

The chapters of this Handbook are as follows:

Part I: Introduction

- Chapter 1: Introduction and General Considerations, describes the Handbook layout, where to find help and additional documentation, and important advice for preparing NICMOS proposals.
- Chapter 2: Overview of NICMOS, provides an introduction to the expected capabilities of NICMOS under NCS operations, the basic physical and imaging layout, a description of the NCS, and a summary of the detectors' operations.
- Chapter 3: Designing NICMOS Observations, shows in tabular form the required steps for designing a NICMOS observing proposal, guides through some of the technical details for choosing the optimal configuration for a given observation, and provides the reader with a "map" for the subsequent chapters.

Part II: User's Guide

- Chapter 4: Imaging, : provides a description of NICMOS's imaging capabilities including camera resolutions and throughputs, image quality and effects of cosmic rays. Described here is also the infrared background seen by NICMOS.

- Chapter 5: Coronagraphy, Polarimetry and Grism Spectroscopy, provides detailed information on coronagraphic imaging, grism spectroscopy, and polarimetry.
- Chapter 6: NICMOS Apertures and Orientation, describes the aperture definitions and the sky-projected orientation of the instrument.
- : Chapter 7: NICMOS Detectors, describes the basic properties of the detectors used in the three cameras including their physical characteristics, capabilities and limitations. Performance descriptions are based on expectations under NCS operations.
- Chapter 8: Detector Readout Modes, explains the data taking modes which take advantage of the non-destructive readout capabilities of the NICMOS arrays. While nearly all observers will choose to use MULTIACCUM mode, we give descriptions of other modes to help proposers/users choose the most appropriate for their observations.

Part III: How to Plan an Observation

- Chapter 9: Exposure Time Calculations, describes how to perform signal to noise calculations, either by using pencil and paper, or using software tools that are provided on the World Wide Web (WWW).
- Chapter 10: Overheads and Orbit Time Determination, : provides information to convert from a series of planned science exposures to an estimate of the number of orbits, including spacecraft and NICMOS overheads. This chapter applies principally to the planning of Phase I proposals.
- : Chapter 11: Techniques for Dithering, Background Measurement and Mosaicing, describes the implementation of a pre-defined set of patterns which accomplish dithering and chopping from the field of interest, and allow easy generation of large mosaic images.

Part IV: Calibration Overview

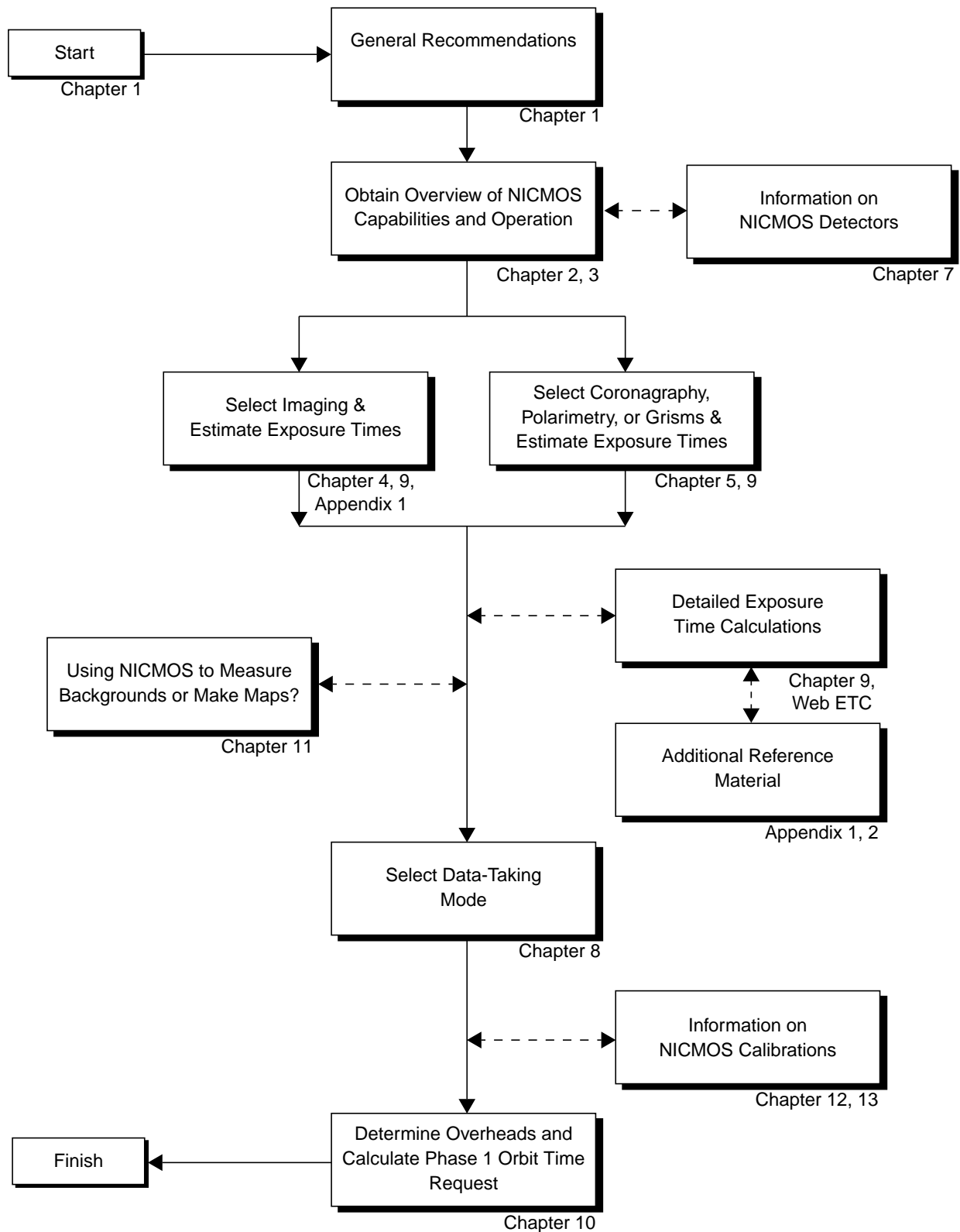
- Chapter 12: Calibration Pipeline : , briefly describes the processing of NICMOS data by the STScI pipeline and the data that will be sent to observers.
- Chapter 13: Calibration Goals and Plans, : summarizes the accuracies expected for NICMOS data calibrated by the STScI pipeline during Cycle 10, and gives an overview of the Cycle 10 calibration plan.

Part V: Appendices

- Appendix 1: Imaging Reference Material, : provides summary information, filter transmission curves, and sensitivity plots for each imaging filter, ordered by camera and increasing wavelength.

- Appendix 2: Flux Units and Line Lists, : provides formulae and tables for the conversion of flux units, and a list of common infrared spectral lines.
- Appendix 3: Bright Object Mode, : describes the BRIGHT OBJ and the RAMP read-out modes.

Figure 1.1: Roadmap for Using the NICMOS Instrument Handbook



NICMOS Proposal Preparation

The *NICMOS Instrument Handbook* and the *Cycle 10 Call for Proposals & Phase I Proposal Instructions* (CP) should be used when assembling NICMOS Phase I Proposals. The CP provides policy and instructions for proposing; the *NICMOS Instrument Handbook* contains technical information about NICMOS, describing its expected performance, and presenting suggestions for use.

If the Phase I proposal is accepted, the proposer will be asked to submit a Phase II proposal in which the exact configurations, exposure times and sequences of observations that NICMOS and the telescope should perform are specified. To assemble the Phase II proposal, the observer is referred to the *NICMOS Instrument Handbook* and to the *Phase II Proposal Instructions*. These instructions describe the rules and syntax that apply to the planning and scheduling of NICMOS observations and provide relevant observatory information.



At the time of this writing, the NCS has not been installed on HST yet. Given the uncertainties in the final NCS operating temperature, together with uncertainties in the NICMOS dark current (see Chapter 7), predictions of the performance of NICMOS should be treated as provisional, and users should adopt conservative expectations for proposing in Cycle 10.

The Help Desk at STScI

STScI maintains a Help Desk. The Help Desk staff at STScI quickly provide answers to any HST-related topic, including questions regarding NICMOS and the Cycle 10 proposal process. The Help Desk staff has access to all of the resources available at the Institute, and they maintain a database of answers so that frequently asked questions can be immediately answered. The Help Desk staff also provide STScI documentation, in either hardcopy or electronic form, including instrument science reports, instrument handbooks, and the like. Questions sent to the Help Desk during normal business hours are answered within one hour. Questions received outside normal business hours will be answered the next business day. Usually, the Help Desk staff will reply with the answer to a question, but occasionally they will need more time to investigate the answer. In these cases, they will reply with an estimate of the time needed to supply a full answer.

We ask proposers to please send all initial inquiries to the Help Desk. If a question requires a NICMOS Instrument Scientist to answer it, the Help Desk staff will put a NICMOS Instrument Scientist in contact with the proposer. By sending requests to the Help Desk, proposers are guaranteed that someone will provide them with a timely response.

To contact the Help Desk at STScI:

- **Send e-mail (preferred method):** help@stsci.edu
- **Phone:** (410) 338-1082

The Space Telescope European Coordinating Facility (ST-ECF) also maintains a help desk. European users should generally contact the ST-ECF for help: all other users should contact STScI. To contact the ST-ECF Help Desk:

- **Send e-mail:** stdesk@eso.org

The NICMOS Instrument Team at STScI

STScI provides a team of Instrument Scientists, Scientific Programmers, and Data Analysts who support the development, operation and calibration of NICMOS. The team is also responsible for supporting NICMOS users. The table inside the front cover of this Handbook lists the current members of the NICMOS Instrument Team at STScI.

Supporting Information and the NICMOS Web Site

The NICMOS Instrument Team at STScI maintains a World Wide Web page, as part of the STScI home page. The URL for the STScI NICMOS page is:

http://www.stsci.edu/ftp/instrument_news/NICMOS/topnicmos.html

Among the STScI NICMOS web pages, those relevant for proposal preparation are:

- **Advisories:** This is where we will post updates to instrument performance as these are produced through on-orbit verification.
- **Documentation:** An electronic version of this Handbook will be maintained on the WWW site. In addition, more detailed technical information (not needed to propose for Cycle 10) concerning the performance, operation and calibration of NICMOS itself during Cycle 7 and Cycle 7N, as well as the description of the Instrument's behavior during warm-up at the end of Cryogen, are found in a series of

NICMOS instrument science and calibration reports maintained on the web, while others can be obtained upon request from the Help Desk.

- **Frequently Asked Questions:** A list of frequently asked questions about NICMOS, and their answers, ranging from proposal preparation to data analysis.
- **NICMOS Image Data Anomalies:** The characteristics and ‘peculiarities’ of the NICMOS detectors, ranging from flat-field variations across each chip, to the effects of the ‘DC pedestal’, to image ghosts, vignetting, and to the effects of cosmic-ray persistence; plus more.
- **NICMOS Photometry:** A description of the NICMOS photometric performance and temporal stability during Cycle 7 and Cycle 7N.
- **Proposing:** Contains useful links to proposers’ documentation.
- **Software:** Useful software for proposal preparation, including the Exposure Time Calculator (ETC) and the Unit’s Conversion Tool.

NICMOS History in Brief

In order to understand the list of recommendations for proposal preparation given below, a brief history of the Instrument is presented here. A more detailed description of the NICMOS chronology, from installation on HST until its present status, is given in Chapter 2.

During its first operational period, which went from February 1997 (date of installation on HST) to January 1999, NICMOS was passively cooled by evaporating N₂. Science observations were obtained from the beginning of June 1997 till mid-November 1998, during which period the cryogen kept the detectors’ temperature around 60 K, with a slow upward trend, from 59.5 K to ~62 K, as the N₂ was evaporating. On January 3, 1999, the cryogen was completely exhausted, marking the official end of NICMOS operations under this cooling regime.

NICMOS offers infrared capabilities in three cameras, NIC1, NIC2, and NIC3 characterized by three magnification factors (see Chapter 2). The three cameras had been built to be parfocal and to operate simultaneously. A few months before launch, however, the NICMOS dewar underwent thermal stresses, which made the three cameras no longer parfocal (although they still retain the capability to operate simultaneously). Even worse, shortly after installation on HST, the NICMOS dewar developed a thermal short which had two consequences: 1. it pushed the NIC3 focus outside the range of the Pupil Alignment Mechanism (PAM); 2. created a “heat sink”, which caused the Nitrogen ice to evaporate at a quicker pace, thus shortening the lifetime of the instrument (from the expected 4.5 years

down to about 2 years). A couple of months after the start of the short, the instrument stabilized at the operating configuration which remained during the duration of its ‘cryogenic lifetime’ with NIC1 and NIC2 in focus and practically parfocal, NIC3 out of focus relative to the other two cameras and with its best focus slightly outside the PAM range. During Cycle 7 and Cycle 7N, two observing campaigns were organized to obtain in-focus NIC3 observations by moving the HST secondary mirror. See the next section and Chapter 4 for expected NIC3 operations in Cycle 10.

The dewar deformation provoked by the thermal short is most likely plastic. At the time of this writing we believe that when the NCS will be installed the NICMOS operating configuration will be the same as Cycle 7 and 7N: NIC1/NIC2 close to being parfocal and in focus, NIC3 non-parfocal with the other two cameras with the optimal focus slightly out of the PAM range but still perfectly usable with the best achievable focus.

Major Changes Relative to Cycles 7 and 7N

During Cycles 7 and 7N, the temperature of the three NICMOS detectors was kept within the range 59-62 K by passive N₂ cooling. During Cycles 10 and higher, the detectors' temperature is expected to be in the range 72-77 K, via the active cooling provided by the NCS. The different operating temperature implies a number of changes in the detector's performance. We summarize here what is expected to and not to change, referring the reader to Chapter 8 for a more detailed discussion.

- The dark current is expected to increase from <0.05 e-/s to 0.4 or 2.0 e-/s, for the best and worst case scenario, respectively (see Chapter 8). The longest exposures at wavelengths below ~ 1.7 microns will be slightly affected by the increased dark current (see Appendix 1).
- The DQE is expected to increase ~ 40 - 45% at $1\text{ }\mu\text{m}$, ~ 30 - 35% at $1.6\text{ }\mu\text{m}$, and ~ 20 - 25% at $2\text{ }\mu\text{m}$.
- The read-out noise is not expected to change and will still be ~ 30 e-.
- The filters, which are viewed by the entire wavelength response of the detectors, are expected to be cooled to less than 160 K. This is closer to their original design temperature than the ~ 100 K they were cooled at during Cycle 7 and 7N (because of the thermal short). Therefore, the filters will still be cold enough that their background will remain undetectable.
- Image quality is expected to be equivalent to that obtained during Cycle 7N.

As mentioned above, NIC3 is scientifically usable at the best achievable PAM focus (see, also, Chapter 4). Therefore:

- No NIC3 campaigns (involving moves of the HST secondary mirror) are expected to be planned in Cycle 10 and later Cycles.
- Because the NIC3 PAM focus position is different from that of the other two cameras, NIC3 observations will be ‘grouped’ together as much as possible. This is an effort to avoid wearing out the PAM mechanism with excessive usage. The ‘grouping’ of the NIC3 observations will be transparent to the vast majority of observers.

Recommendations for Proposers

We give here a summary of general recommendations for both Phase I and Phase II proposal preparation. Recommendations are based on the experience we gained with NICMOS performance during Cycles 7 and 7N. However, observers are strongly advised to read the technical sections that follow in order to develop an optimal observation strategy based on the demands of their individual scientific goals. Also the Advisories page maintained on the NICMOS WWW site should be consulted for updates.

Recommendations for Phase I proposals:

- NIC1 and NIC2 offer diffraction-limited capabilities at H and longer wavelengths, while NIC3 offers high sensitivity (due to the lower angular resolution) with the largest field-of-view among the three cameras. In particular, NIC3 reaches fainter magnitudes than the other two cameras (for the same exposure time) for observations which are *not* limited by photon noise from source + background, i.e. where read-out or dark noise are significant. This is true for most observations of faint targets. However, the poor sampling of NIC3 can limit its sensitivity for faint point sources.
- When choosing NIC3, proposers should be aware that this camera is slightly out-of-focus, with a typical loss of peak flux around 20% and a loss of encircled energy of about 10% - 15%. Chapter 4 should be consulted for the detailed performance of the out-of-focus NIC3.
- The highest sensitivity gain relative to ground-based observations is at wavelengths below 1.8 μm . The background at J and H seen by HST is a few hundred times smaller than at ground-based observatories. The background at K is only marginally better on HST, due to the telescope’s thermal emission. However, observations in the thermal regime (longward of 1.8 μm) may be more advantageous with NICMOS if high angular resolution is the requirement for the science goal.

- Observations of extended sources in the thermal regime (longward of $1.8\ \mu\text{m}$) may need to obtain background observations as well (chopping off the target). Given the stability of the thermal background, however, it will not be necessary to get background measurements more frequently than once per orbit. For point sources or extended sources which do not fill the camera field-of-view, images of the thermal background can be obtained with dithering (see recommendations below).
- For the purpose of removing cosmic rays, photon and cosmic-ray persistence, detector artifacts, and for averaging out flat-field sensitivity variations, observers are strongly advised to *dither* an observation as much as possible. This implies dividing single-orbit observations into at least three exposures and multi-orbit observations into two exposures per orbit. The general advice of dithering is generally not applicable to observations of faint sources around/near bright ones. If the bright source saturates the detector, the saturated pixels will be affected by persistence; in this case, the observers have two options: 1. not dithering, to avoid placing the faint target on the saturated pixels; 2. dithering by large amounts (by \sim quadrant) to move away from the persistency-affected region.
- The dithering requirement poses a practical upper limit of $\sim 1,500$ seconds to the longest integration time for a *single* exposure. This is roughly equivalent to having 2 exposures per orbit. Observers wishing to detect faint targets should work out their S/N requirements by determining (e.g., with the ETC) the S/N achieved in a single exposure and then co-adding n exposures according to \sqrt{n} , until the desired S/N is achieved. The latter is an essential step given the large read-out noise of the NICMOS detectors.
- Proposers who want to use the NIC3 GRISMs should be aware that the spectral resolution quoted in the Handbook ($R \sim 200$) is *per pixel*; the actual resolution, calculated over 2 pixels, is $R \sim 100$.
- Observers proposing to use the NICMOS coronagraphic hole should consider back-to-back visits of their targets with a roll of the spacecraft, for PSF subtraction.
- Observers proposing to use the NICMOS coronagraphic hole should consider adding contemporary flat-field observations.

Recommendations for Phase II proposals:

- For fields containing faint targets only, the linear MULTIACCUM sequences (SPARS...) should be preferred. They are best suited for removing instrumental effects from the astronomical data. However, for fields containing both bright and faint sources, logarithmic

sequences should be preferred (STEP...), as they offer the largest dynamical range and allow the calibration software to recover saturated targets.

- When designing their dithering patterns, observers should take into account that the sensitivity across each detector changes by as much as a factor 4 at short wavelengths and by a factor ~ 2 at long wavelengths. The sensitivities used in the ETC and in this Handbook are average values across each detector. The sensitivity variations will mostly affect observers interested in the full field-of-view.
- The NIC3 PSF is undersampled and intrapixel sensitivity variations are large in this camera. Photometry on point sources can vary by >0.2 mag in J and up to 0.2 mag in H depending on the placement within a pixel. Observers are encouraged to consider sub-pixel dithering in their NIC3 observations; 4-6 dithering positions minimum are recommended.
- The bottom 10-15 rows of the three cameras' field of views are vignetted and interesting targets should not be placed there.
- For coronagraphic observations: coronagraphic hole movements and HST focus changes (breathing) will result in residual noise during PSF subtraction. PSF stars should be observed close in time to the primary target.
- HST pointing is only good to about 1 arcsecond ($1\sigma = 0.33''$); dithering patterns should be designed to place science targets away from the edges of the cameras by at least this amount.

Supported and Unsupported NICMOS Capabilities

As was done for both NICMOS and STIS for past cycles, we have established a set of core scientific capabilities of NICMOS which will be supported for Cycle 10 science. These capabilities cover an enormous range of science applications.

Supported capabilities include:

- NIC1, NIC2, and NIC3 observations in any filter or polarizer/grism. NIC3 comes “as is”, namely slightly out-of-focus (see Chapter 4 for a detailed explanation of the NIC3 capabilities).
- MULTIACCUM and ACCUM detector readout modes (see Chapter 8 for a discussion of the problems that can be faced when using ACCUM mode).
 - The defined MULTIACCUM SAMP-SEQ exposure time sequences,
 - A subset of the ACCUM exposure times as defined in Chapter 8.

- ACCUM NREAD=1 or 9 values only.
- Coronagraphic observations, including on-board target acquisitions.

One additional capability is “available” (as *Engineering-only* capability), but not supported for Cycle 10. The use of this capability can be proposed upon consultation with a NICMOS Instrument Scientist, and is useful only for target acquisition of extremely bright sources for coronagraphic observations. The use of this capability requires approval from STScI and support for calibration is non-existent.

The unsupported (“available”) capability is:

- BRIGHTOBJ readout mode. The calibration and linearity of this mode is problematic.

The use of this capability is strongly discouraged if the acquisition of a target for coronagraphic observations can be obtained with any of the supported capabilities. Cycle 10 proposals which include use of the unsupported NICMOS capability must include a justification of why the target acquisition cannot be done with a supported configuration, and must justify the added risk of using an unsupported mode in terms of the science payback.

Overview of NICMOS

In This Chapter...

Instrument Capabilities / 17

History of NICMOS / 19

NICMOS Instrument Design / 20

Basic Operations / 28

The NICMOS Cooling System / 25

In this Chapter we provide an overview of the basic properties and capabilities of NICMOS under the NICMOS Cooling System (NCS). We first give an overview of the NICMOS capabilities, then a brief summary of the NICMOS history that led to the installment of the NCS. A description the optical and mechanical layout of the NICMOS instrument follows, before we proceed to the NCS design and its interface to NICMOS. Last, a summary of the NICMOS basic operations is given.

Instrument Capabilities

NICMOS, the Near Infrared Camera and Multi-Object Spectrometer, is an HST axial instrument, containing three cameras designed for simultaneous operation. The NICMOS optics offer three adjacent but not spatially contiguous fields-of-view of different image scales. The instrument covers the wavelength range from 0.8 to 2.5 microns, and contains a variety of filters, grisms, and polarizers. Each camera carries a complement of 19 optical elements, selected through independent filter wheel mechanisms, one per camera. In order to allow operation of the NICMOS detectors and to minimize the thermal background of the instrument, NICMOS needs to be cooled to cryogenic temperatures.

The basic capabilities of the instrument, and the chapters which discuss them are:

- **IR imaging:** NICMOS provides its highest sensitivity from 1.1 to ~2 microns, where it is superior to an 8m class telescope, and better sensitivity than the WFPC2 for all observations for wavelengths longward of 0.9 microns. Chapter 4 discusses the overall throughput of NICMOS and the optical elements available in each camera. The low background which HST offers between 0.8 and 2 microns will allow deep photometry. Our estimates of limiting sensitivities per pixel to give a 3σ detection in a 3,000 second integration are given in Table 2.1 for the worst dark current assumptions (see the last section of this Chapter and Chapter 8 for a discussion on the dark current).

Table 2.1: Limiting Sensitivities in Janskys for S/N = 3 detection of a point source in 3,000 seconds for worst dark current assumptions.

Camera	Filter	Bandwidth (microns)	Limiting Sensitivity	
			Jansky	Approx. Mag.
NIC1	F110W	0.8 - 1.35	5.9×10^{-7}	J \approx 23.7
NIC1	F140W	0.8 - 1.8	3.7×10^{-7}	J \approx 24.1
NIC1	F160W	1.4 - 1.8	6.8×10^{-7}	H \approx 22.9
NIC2	F110W	0.8 - 1.35	2.8×10^{-7}	J \approx 24.5
NIC2	F160W	1.4 - 1.8	3.4×10^{-7}	H \approx 23.7
NIC2	F237M	2.3 - 2.5	3.1×10^{-6}	K \approx 20.7
NIC3	F110W	0.8 - 1.35	2.8×10^{-7}	J \approx 24.5
NIC3	F160W	1.4 - 1.8	2.9×10^{-7}	H \approx 23.9
NIC3	F240M	2.3 - 2.5	6.1×10^{-6}	K \approx 19.9

- **Grism Spectroscopy:** Camera 3 has three gratings which provide a multi-object spectroscopic capability with a resolving power of R \sim 200 over the full field of view of the camera. Their wavelength ranges are 0.8 to 1.2 microns, 1.1 to 1.9 microns, and 1.4 to 2.5 microns. Because the gratings are slitless, the spectra of spatially resolved objects are confused and multiple objects can overlap.
- **Imaging Polarimetry:** Three polarizing filters with pass directions of 0, 120, and 240 degrees are provided for the wavebands 0.8–1.2 microns in Camera 1 and 1.9–2.1 microns in Camera 2.
- **Coronagraphy:** A 0.3 arcsec radius occulting spot and cold mask, in the intermediate resolution Camera 2, provides a coronagraphic imaging capability.

Chapter 5 discusses these three special capabilities in more detail.

History of NICMOS

NICMOS was installed onboard the HST during the second Servicing Mission (SM2) in February 1997. Prior to the SM2 launch, an extensive ground testing program was executed, during which the NICMOS dewar was filled with about 240 pounds of liquid nitrogen which was then solidified (in stages) by passing cold helium gas through a coil located at the aft end (see Figure 2.2). This reduced the temperature of the nitrogen to about 40K. During testing and storage, the block of solid nitrogen increased in temperature as expected (from passive heat inputs). To avoid reaching the triple point (at ~63K) the block was re-cooled approximately every 6-8 weeks, again using cold Helium gas circulating through the aft end cooling coil. During this process, nitrogen gas froze onto the cooling coil. This reduced the vapor pressure at the aft end, effectively pumping gas from the warmer fore end to the aft. As the dewar was allowed to warm up, the ice at the aft end expanded, pushing into the interior surfaces of the dewar and deforming it. By mid-1996 the three cameras in NICMOS were no-longer confocal although there were good reasons to expect that they would return to a nearly confocal state after a fraction of the nitrogen had evaporated on orbit. At that time a total deformation of ~4 mm had been observed and steps were taken to both assure that the dewar remained flightworthy and that subsequent re-cooling cycles did not stretch the dewar further. Also, the internal optical alignment and focus mechanism (the Pupil Alignment Mechanism—PAM) was replaced with a version providing twice the focus range and a demonstrated capability for frequent movement. The PAM, originally intended to align the input beam onto the corrective optic and to bring NICMOS into confocality with the WFPC2 (the only HST instrument without an internal focus mechanism), would be used to support a unique focus setting for each NICMOS camera and to switch between them routinely.

After NICMOS was installed in HST, the dewar was planned to warm up to about 57 K. This high a temperature was never allowed to be reached during ground testing. The ice expansion caused by this temperature raise resulted in an additional dewar deformation, to the extent that one of the (cold) optical baffles made mechanical contact with the vapor-cooled shield (VCS). The resulting heat flow caused the ice to warm up even more, to about 60 K, which in turn deformed the dewar more. The motion history of NICMOS and the resulting image quality are discussed in Chapter 4.

This unexpectedly large deformation had several undesirable effects, the most important of which are:

- The three cameras have significantly different foci, hence parallel observations are degraded. The difference between the NIC1 and NIC2 foci, however, is sufficiently small that an intermediate focus yields good quality images in both cameras.

- The NIC3 focus has moved outside of the range of the PAM. In order to enable execution of Cycle 7 programs that required the use of camera 3, two “NIC3 campaigns” were performed in spring and fall of 1998. These were periods of 2-3 weeks during which the HST secondary mirror was adjusted to bring the focus back into the NIC3 PAM range. During this time, HST performed exclusively NIC3 science, since no other HST instrument was in focus. While it was initially hoped that the NIC3 focus would eventually return to within the PAM range, we now do not expect this to happen. However, at the maximum PAM position, the degradation in terms of encircled energy is only 10-15%. This is considered sufficiently small, and NIC3 will be offered “as is” in Cycle 10 and future Cycles.
- The thermal short increased the heat flux into the inner shell (and therefore the solid nitrogen) by a factor of 2.5 and has thereby reduced the lifetime of NICMOS from 4.5 to ~ 2 years. The cryogen depleted in January 1999, and NICMOS has since been unavailable for science operation.

To enable completion of the NICMOS science program despite the shortened lifetime, NASA and STScI adjusted the HST scheduling in such a way that NICMOS observations were assigned 40-50% of the total observing time in Cycle 7. Moreover, a second Call for Proposals (CP) for additional NICMOS science was issued in summer 1997. The proposals were put through the normal peer review process, and the full science program was executed before the cryogen depletion.

To restore and conserve an infrared capability on HST, NASA has developed the concept of the NICMOS Cooling System (NCS), a mechanical cryocooler that will reenable NICMOS operation throughout the lifetime of HST. The NCS will cool the NICMOS dewar to temperatures around 72 - 77 K, significantly higher than during Cycle 7. Therefore, many NICMOS parameters will be different from Cycle 7, and users should pay close attention to the new NICMOS performance which is discussed in Chapter 4, Chapter 5, and Chapter 7.

NICMOS Instrument Design

Physical Layout

NICMOS is an axial bay instrument which replaced the Faint Object Spectrograph (FOS) in the HST aft shroud during the Second HST Servicing Mission in February 1997. Its enclosure contains four major elements: a graphite epoxy bench, the dewar, the fore-optics bench, and the electronics boxes. The large bench serves to establish the alignment and

dimensional stability between the HST optics (via the latches or fittings), the room temperature fore optics bench, and the cryogenic optics and detectors mounted inside the dewar. The NICMOS dewar was designed to use solid nitrogen as a cryogen for a design lifetime of approximately 4.5 ± 0.5 years. Cold gas vented from the dewar was used to cool the vapor cooled shield (VCS) which provides a cold environment for both the dewar and the transmissive optical elements (i.e., the filters, polarizers, and grisms). The VCS is itself enclosed within two layers of thermal electrically cooled shells (TECs).

Figure 2.1 is an overview of the NICMOS instrument; Figure 2.2 shows details of the dewar. The external plumbing at the dewar aft end, which was used for the periodical recooling of the solid nitrogen during ground testing, will now form the interface to the NCS. During SM3B, the NCS will be connected to the bayonet fittings of the interface plate, in order to allow cold Neon gas to circulate through the dewar, thus providing the cooling power to bring the instrument into the temperature range required for operation. The concept and working principle of the NCS is discussed in the next section.

Figure 2.1: Instrument Overview

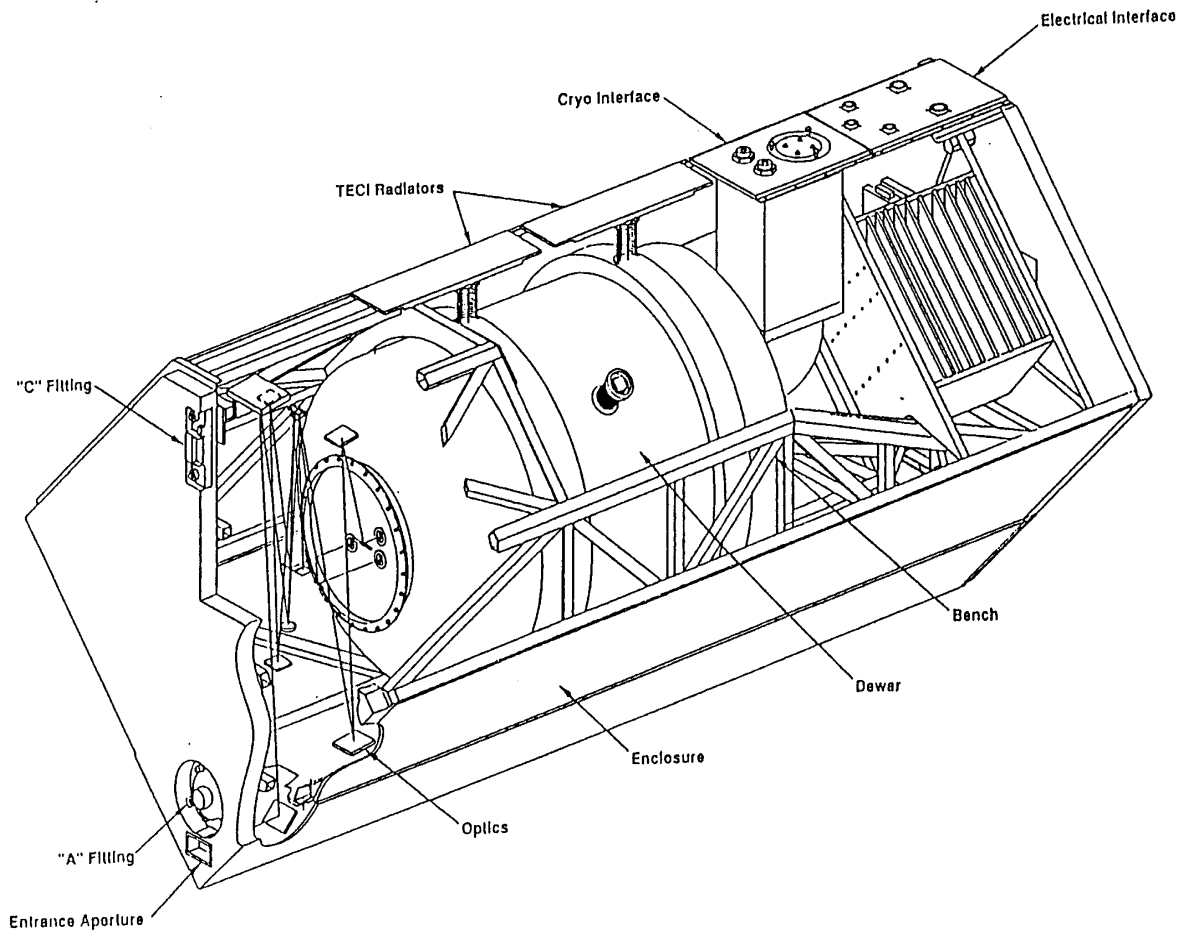
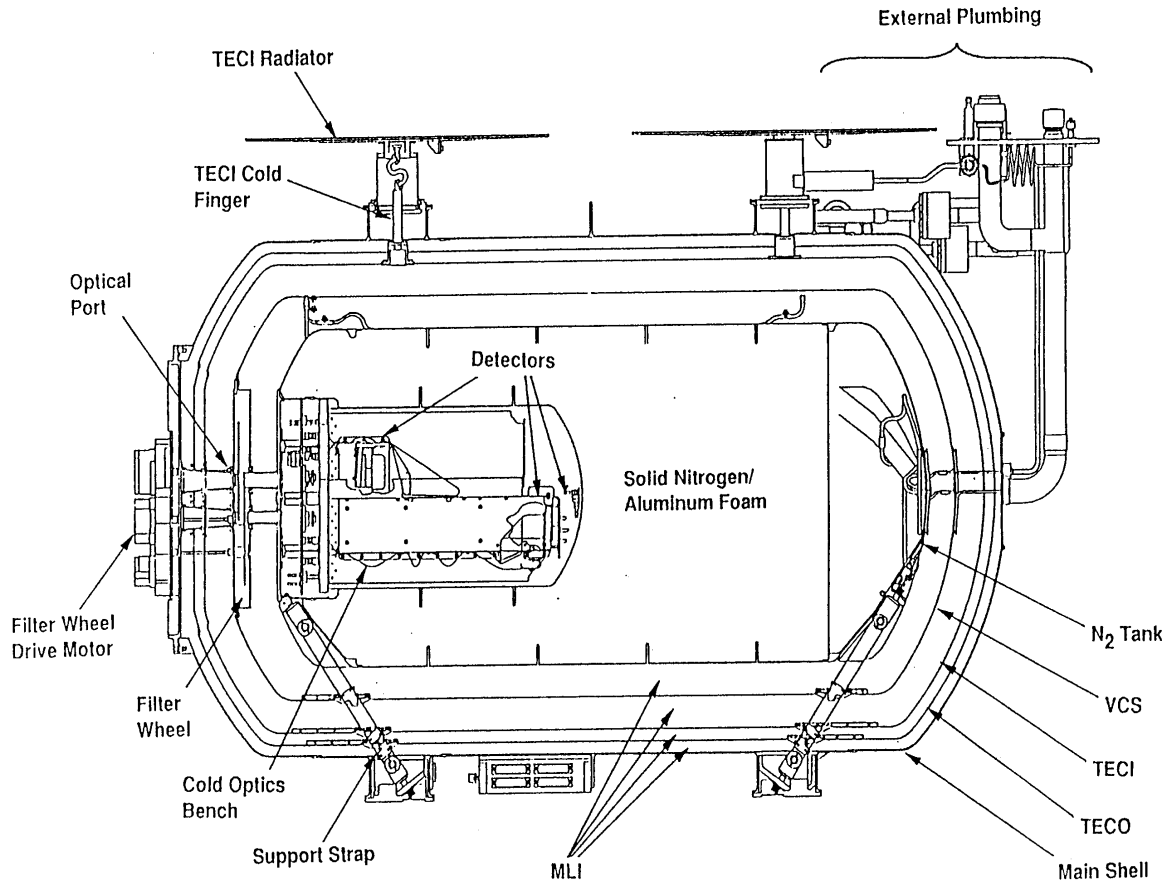


Figure 2.2: NICMOS Dewar



Imaging Layout

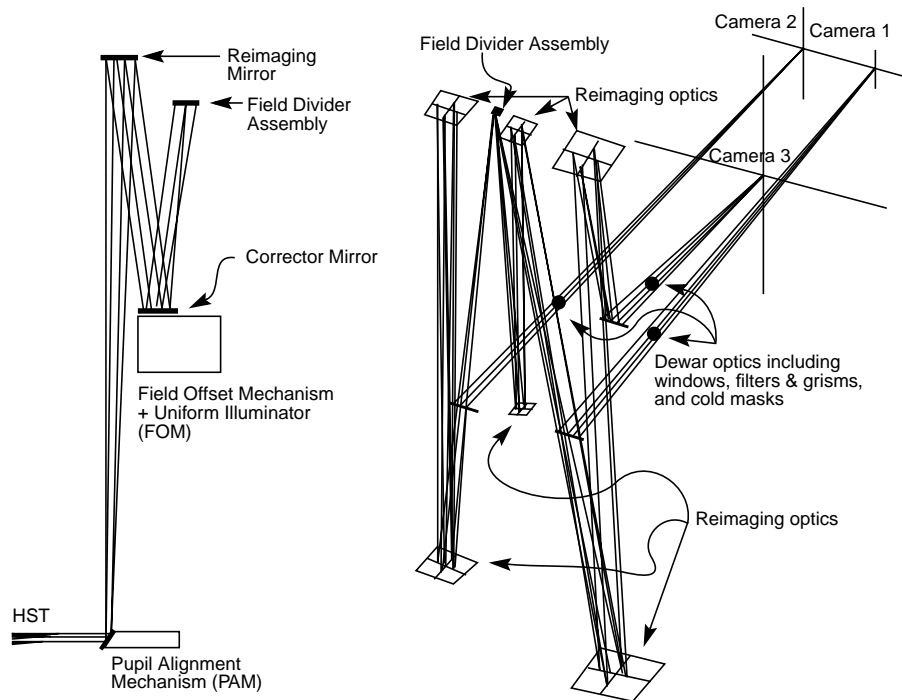
The NICMOS fore-optics assembly is designed to correct the spherically aberrated HST input beam. As shown in the left hand panel of Figure 2.3 it comprises a number of distinct elements. The Pupil Alignment Mechanism (PAM) directs light from the telescope onto a re-imaging mirror, which focuses an image of the Optical Telescope Assembly (OTA) pupil onto an internal Field-Offset Mechanism (FOM) with a pupil mirror that provides a small offset capability (26 arcsec). An internal flat field source is also included in the FOM assembly. In addition, the FOM provides correction for conic error in the OTA pupil.

After the FOM, the Field Divider Assembly (FDA) provides three separate but closely-spaced imaging fields, one for each camera (right hand panel of Figure 2.3). The dewar itself contains a series of cold masks to eliminate stray IR emission from peripheral warm surfaces.

A series of relay mirrors generate different focal lengths and magnifications for the three cameras, each of which contains a dedicated 256 x 256 pixel HgCdTe chip that is developed from the NICMOS 3

detector design. NICMOS achieves diffraction limited performance in the high resolution NIC1 longward of 1.0 microns, and in NIC2 longward of 1.75 microns.

Figure 2.3: Ray Diagrams of the NICMOS Optical Train. The left panel shows the fore-optics. The right panel shows the field divider and re-imaging optics for the three cameras.



The operation of each camera is separate from the others which means that filters, integration times, readout times and readout modes can be different in each, even when two or three are used simultaneously. The basic imaging properties of each of the cameras is summarized in Table 2.2.

Table 2.2: Basic Imaging Parameters

Parameter	Camera 1	Camera 2	Camera 3
Pixel Size (arcsec)	0.043	0.075	0.2
Field of View (arcsec x arcsec)	11 x 11	19.2 x 19.2	51.2 x 51.2
F ratio	F/80	F/45.7	F/17.2
Diffraction Limited Wavelength (μm)	1.0	1.75	...

Camera NIC1

NIC1 offers the highest available spatial resolution with an 11×11 arcsec field of view and 43 milliarcsec sized pixels (equivalent to the WFPC2 PC pixel scale). The filter complement includes broad and medium band filters covering the spectral range from 0.8 to 1.8 microns and narrow band filters for Paschen α , He I, [Fe II] λ 1.64 μ m, and [S III] λ 0.953 μ m, both on and off band. It is equipped with the short wavelength polarizers (0.8 to 1.3 microns).

Camera NIC2

NIC2 provides an intermediate spatial resolution with a 19.2×19.2 arcsec field of view and 75 mas pixels. The filters include broad and medium band filters covering the spectral range from 0.8 to 2.45 microns. The filter set also includes filters for CO, Brackett γ , H₂ S2 (1-0) λ 2.122 μ m, Paschen α , HCO₂ + C₂, and the long wavelength polarizers (1.9–2.1 microns). Camera 2 also provides a coronagraphic mask with a 300 milliarcsec radius.

Camera NIC3

NIC3 has the lowest spatial resolution with a large 51.2×51.2 arcsec field of view and 200 milliarcsec pixels. It includes broad filters covering the spectral range 0.8 to 2.3 microns, medium band filters for the CO band (and an adjacent shorter wavelength continuum region), and narrow band filters for H₂ S2 (1-0), [Si VI] λ 1.962 μ m, Paschen- α , [Fe II] λ 1.64 μ m, and He I λ 1.083 μ m. Camera 3 also contains the multi-object spectroscopic capability of NICMOS with grisms covering the wavelength ranges 0.8–1.2 microns, 1.1–1.9 microns, and 1.4–2.5 microns.

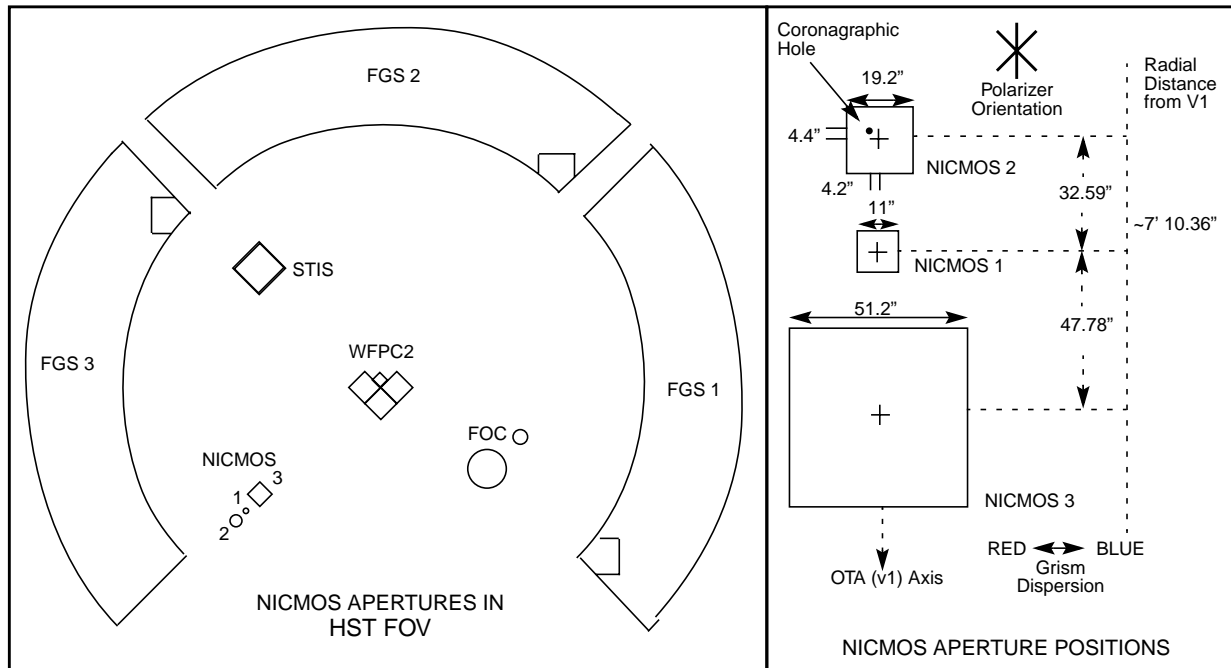
Location and Orientation of Cameras

The placement and orientation of the NICMOS cameras in the HST focal plane is shown in Figure 2.4. Notice that the cameras are in a straight line pointing radially outward from the center of the telescope focal plane. From the observer's point of view the layout of NICMOS is most relevant when trying to plan an observation of an extended source with all three cameras simultaneously. The user must then bear in mind the relative positions and orientations of the three cameras. The gaps between the cameras are large, and therefore getting good positioning for all cameras may be rather difficult.

The position of the NICMOS cameras relative to the HST focal plane (i.e., the FGS frame) depends strongly on the focus position of the PAM.

Since independent foci and their associated astrometric solutions are supported for each camera, this is transparent to the observer.

Figure 2.4: NICMOS Field Arrangement

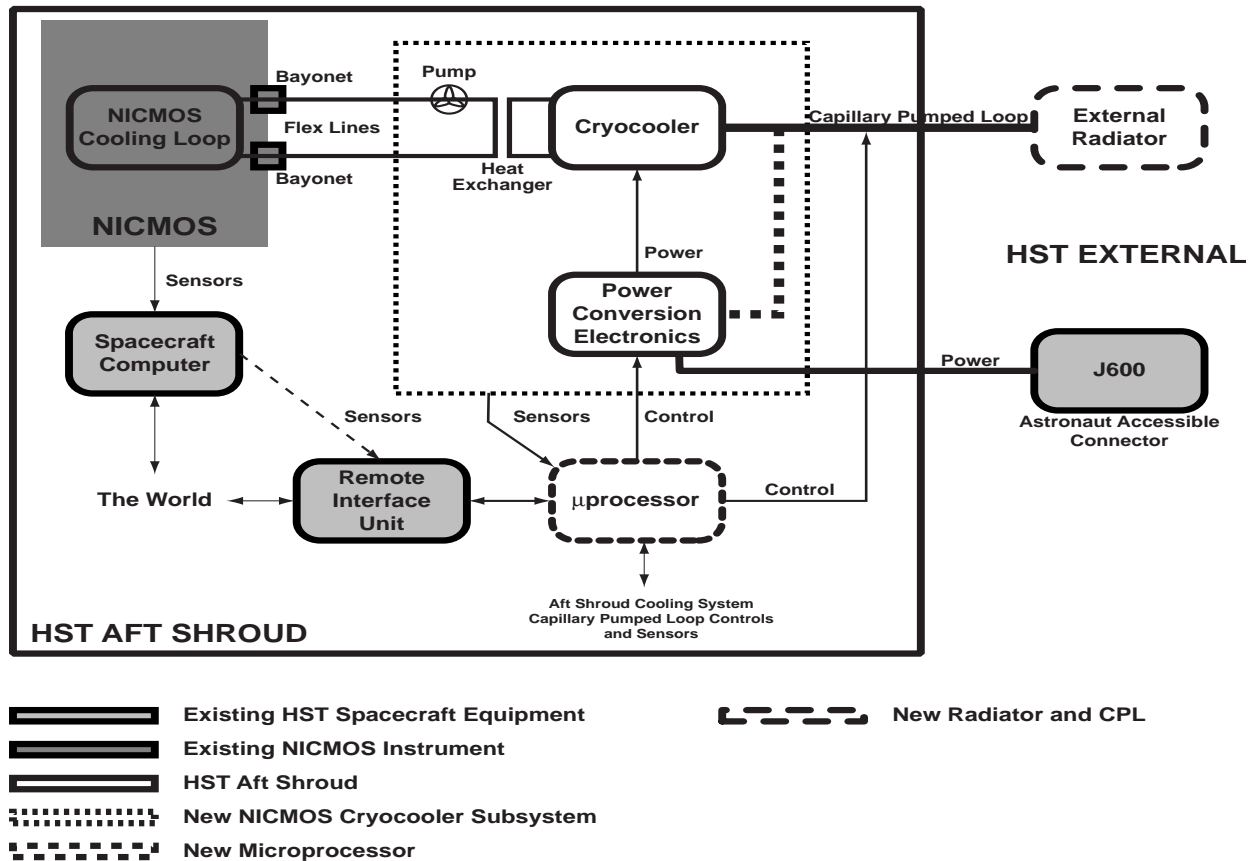


The NICMOS Cooling System

The purpose of the NICMOS Cooling System (NCS) is to enable continued operation of NICMOS by cooling the detectors and the entire instrument to temperatures around 75 K. This will be achieved by a closed-loop circuit which runs cryogenic liquid through a coil inside the NICMOS dewar.

The NCS consists of three major subsystems: 1) a cryocooler which provides the mechanical cooling, 2) a Capillary Pumped Loop (CPL) which transports the heat dissipated by the cryocooler to an external radiator, and 3) a circulator loop which transports heat from the inside of the NICMOS dewar to the cryocooler via a heat exchanger. Additional elements of the NCS are the Power Conversion Electronics (PCE) which provide the up to 400 W AC power needed by the cooler, and the Electronic Support Module (ESM) which contains a microprocessor (indicated as μ processor in Figure 2.5) to control the heat flow. Fig. 2.5 shows a schematic of the system.

Figure 2.5: Overview of the NCS



In what follows, we give a more detailed description of the NCS subsystems:

The cryocooler, manufactured by Creare, Inc., is a reverse-Brayton cycle turbine design. The compression and subsequent expansion of the Neon gas results in a net cooling which can be used to remove heat from the NICMOS dewar via the heat exchanger to the circulator loop (see below). The Creare design has several major advantages for application on HST. First, the closed loop system operates at very high speed -- about 7000 revolution per second -- which limits the probability of mechanical coupling to the HST structure, thus minimizing the risk of spacecraft jitter. Second, the system is capable of providing large cooling power. Since the parasitic losses due to the flex lines and bayonet couplings (see below) are rather large, delivering 400 mW of cooling power to NICMOS requires about 8 W from the cooler. Finally, the Creare design is compact enough to fit into the previously unused space between the NICMOS enclosure and the HST aft end bulkhead.

The cryocooler dissipates between 250 and 400 W of energy which needs to be removed from the aft shroud. This is achieved via a Capillary Pumped Loop (CPL) that thermally connects the housing of the compressor pump with an external radiator. The continuous heat flow through the (passive) CPL lines is maintained by a set of heaters that are

controlled by the ESM microcontroller. A separate set of CPL lines and a second radiator plate, combined into the Aft Shroud Cooling System (ASCS), provide cooling to the rest of the aft shroud environment, which benefits the other HST instruments. Since these CPL lines form a physically different system and are in no way connected to NICMOS, the ASCS is not further discussed here.

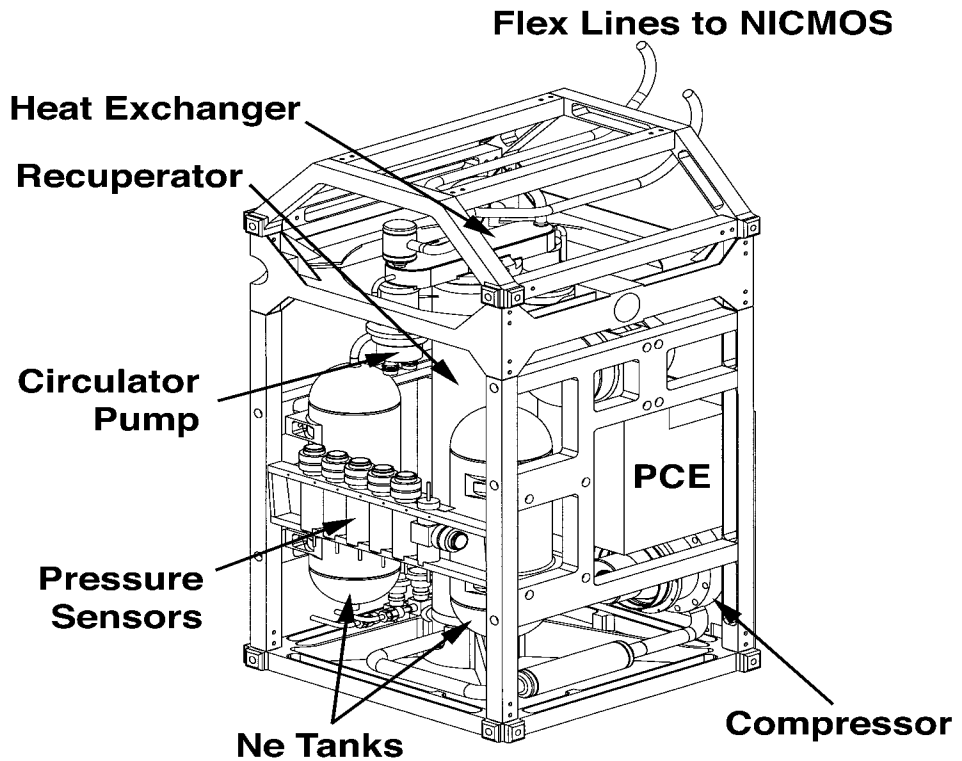
The heat from inside NICMOS is transported to the cryocooler via a set of flex lines. The flex lines connect to the inside of the dewar via bayonet fittings at an interface plate outside of the dewar which is accessible to the astronauts during SM3B. After installation, this loop -- the circulator loop -- will be filled with Neon gas from high pressure storage bottles. The bottles provide enough gas to purge, pressurize, and, if necessary, re-pressurize the circulator loop. The Neon gas, driven by a high speed circulator pump and cooled via the heat exchanger to the cryocooler loop, circulates through the cooling coil at the aft end of the NICMOS dewar (see Figure 2.2), thus cooling the entire instrument. The exact temperature of the Neon gas in the circulator loop - and thus the temperatures reached by the NICMOS detectors - will depend on the nature and amount of the parasitic heat loads to the flex lines and the NICMOS dewar. Current best estimates are 62 K at the heat exchanger, with about 400 mW of parasitic heat loads, this should result in detector temperatures between 72 and 77 K.

The ESM will use the telemetry readings of a number of temperature sensors inside the NICMOS dewar in an active control law in order to regulate the cooling power of the NCS, and thus provide stability of the operating temperature of the NICMOS detectors. Because of the sensitive dependence of a number of detector characteristics on temperature (see Chapter 7), the temperature stability is a crucial requirement on NCS performance. The stability specification of 0.1 K/orbit should allow a stable calibration of NICMOS data.

All components of the NCS are combined into a common enclosure, the NICMOS CryoCooler (NCC). Figure 2.6 shows a line drawing of the NCC, without all Multi-Layer Insulation (MLI). The system has been successfully tested in space during the HST Orbital Systems Test (HOST) shuttle mission in fall 1998.

Remaining uncertainties about the NCS performance stem from the natural lack of tests with the actual NICMOS dewar. In ground tests, as well as during HOST, a NICMOS simulator was used to mimic the expected parasitic heat loads from, and the mechanical connections to the actual NICMOS. How closely this simulator resembles the NICMOS dewar is somewhat uncertain, hence we expect a range of possible operating temperatures for the revived NICMOS detectors. How the actual operating temperature affects the NICMOS scientific performance is discussed in detail in Chapter 7.

Figure 2.6: Line drawing of the NCC structure



Basic Operations

In this section, we give a brief description of the basic operations of each NICMOS detector (see Chapter 7 for more details), giving also a comparison with CCDs; of the target acquisition modes for coronagraphy (see Chapter 5 for a more extensive description of coronagraphy); of the simultaneous use of the three Cameras.

Detectors' Characteristics and Operations

NICMOS employs three low-noise, high QE, 256x256 pixel HgCdTe arrays. Active cooling provided by the NCS keeps the detectors' temperature below 77 K; current expectations give the operating temperature between 72 K and 77 K. The detector design is based on the NICMOS 3 design; however, there are differences between the two (see Chapter 7). Here we summarize the basic properties of the NICMOS detectors most relevant to the planning of observations.

The NICMOS detectors have expected dark current values between 0.4 electrons per second (best case scenario) and 2.0 electrons per second (worst case scenario). See Chapter 7 for a detailed explanation of the best

and worst case scenarios. The effective readout noise for a single exposure is approximately 30 electrons.

The NICMOS detectors are capable of very high dynamic range observations and have no count-rate limitations. The dynamic range, for a single exposure, is limited by the depth of the full well, or more correctly by the onset of strong non-linearity, which limits the total number of electrons which can usefully be accumulated in any individual pixel during an exposure. Unlike CCDs, NICMOS detectors do not have a linear regime for the accumulated signal; the low- and intermediate-count regime can be described by a quadratic curve and deviations from this quadratic behavior is what we define as ‘strong non-linearity’. Current estimates under NCS operations give a value of ~145,000 electrons (NIC1 and NIC2) or 185,000 electrons (NIC3) for the 2% deviation from quadratic non-linearity.



There are no bright object limitations for the NICMOS detectors.

NICMOS has four detector read-out modes that may be used to take data (see Chapter 8) plus a target acquisition mode (ACCUM, MULTIACCUM, BRIGHTOBJ, RAMP, and ACQ).



For Cycle 10, only ACCUM, MULTIACCUM, and ACQ are supported and ACCUM mode observations are strongly discouraged.

The simplest read-out mode is ACCUM which provides a single integration on a source. A second mode, called MULTIACCUM, provides intermediate read-outs during an integration that subsequently can be analyzed on the ground. A third mode, BRIGHTOBJ, has been designed to observe very bright targets that would otherwise saturate the detector. BRIGHTOBJ mode reads-out a single pixel at a time. Due to the many resets and reads required to map the array there are substantial time penalties involved. BRIGHTOBJ mode may not be used in parallel with the other NICMOS detectors. BRIGHTOBJ mode appears to have significant linearity problems and has not been tested, characterized, or calibrated on-orbit. RAMP mode implements a subset of the MULTIACCUM mode with onboard processing to avoid the transfer of large volumes of data. With the successful installation of the Solid State Recorder during the Second Servicing Mission, this mode is not necessary, has not been tested, and is not supported.

Users who require time-resolved images will have to use either ACCUM where the minimum exposure time is about 0.6 seconds, and the minimum time between successive exposures is ~ 8 - 12 seconds, or MULTIACCUM

where the shortest spacing between non-destructive exposures can be reduced to 0.203 seconds.

It is expected that MULTIACCUM mode will be used for most observations. It provides the best dynamic range and correction for cosmic rays, since post-observation processing of the data can make full use of the multiple readouts of the accumulating image on the detector. In some cases, a sequence of ACCUM mode observations may offer a significant advantage for read noise limited observations using the NREADS option to decrease the effective read noise by up to a factor of ~ 2 (see Chapter 8). However, exposures longer than about 10 minutes should always opt for the MULTIACCUM read-out mode, because of the potentially large impact of cosmic rays. To enhance the utility of MULTIACCUM mode and to simplify the implementation, execution, and calibration of MULTIACCUM observations, a set of predefined MULTIACCUM sequences has been defined. The observer, when filling up the Phase II proposal, needs only to specify the name of the sequence and the number of samples which should be obtained (which defines the total duration of the exposure).

Comparison to CCDs

These arrays, while they share some of the same properties as CCDs, are not CCDs and offer their own set of advantages and difficulties. Users unfamiliar with IR arrays should therefore not fall into the trap of treating them like CCDs. For convenience we summarize the main points of comparison:

- As with CCDs, there is noise (read-noise) and time (read-time) associated with the reading out. The dark current associated with NICMOS arrays is quite substantial compared to that produced by the current generation of CCDs. In addition, there is an effect called *shading* which is an extraneous bias generated by the readout amplifiers.
- Unlike a CCD, the individual pixels of the NICMOS arrays are strictly independent and can be read-out non-destructively. Read-out modes have been designed which take advantage of the non-destructive read capabilities of the detectors to yield the optimum signal to noise for science observations (see Chapter 7, 8). Because the array elements are independently addressed, the NICMOS arrays do not suffer from some of the artifacts which afflict CCDs, such as charge transfer smearing and *bleeding* due to filling the wells. If, however, they are illuminated to saturation for sustained periods they retain a *memory (persistence)* of the object in the saturated pixels. This is only a concern for the photometric integrity of back to back exposures of very bright targets, as the ghost images take many minutes, up to one hour, to be flushed from the detectors.

Target Acquisition Modes

Most target acquisitions can be accomplished by direct pointing of the telescope. The user should use target coordinates which have been measured with the **Guide Star Astrometric Support Package (GASP)** to ensure the best accuracy with respect to the HST Guide Star Catalog. Particular care must be exercised with targets in NIC1 due to its small field of view.

However, direct pointing will not be sufficient for coronagraphic observations since the achieved precision (~ 1 arcsec rms) is much larger than the 0.3 arcsec radius coronagraphic spot. *Note that this is a function of the total HST pointing error and not only the result of uncertainties in the target's coordinates.*

There are three target acquisition options for coronagraphic observations, which are extensively discussed in Chapter 5:

- On-board acquisition (Mode-2 Acquisition). This commands NICMOS to obtain an image of the target and rapidly position the brightest source in a restricted field of view behind the coronagraphic spot. This is one of the pre-defined acquisition modes in the Phase II proposals (ACQ mode).
- The RE-USE TARGET OFFSET special requirement can be used to accomplish a positioning relative to an early acquisition image.
- A real time acquisition (INT-ACQ) can be obtained although this is costly in spacecraft time and is a limited resource.

While ACQ mode is restricted to coronagraphic observations in Camera 2, the last two target acquisition modes may be useful for positioning targets where higher than normal (1–2 arcsec) accuracy is required (e.g., crowded field grism exposures).

Attached Parallels

While the three NICMOS cameras are no longer at a common focus, under many circumstances it is desirable to obtain data simultaneously in multiple cameras.



The foci of Cameras 1 and 2 are still close enough that the two cameras can be used simultaneously, while Camera 3 will be generally used by itself.

The rest of this section applies only to Phase II proposals— there is no need to worry about this for Phase I proposals.

Although some programs by their nature do not require more than one camera (e.g., studies of isolated compact objects), observers are still

encouraged to add exposures from the other camera(s) to their proposals in order to obtain the maximum amount of NICMOS data consistent with efficiently accomplishing their primary science program. Detailed instructions for obtaining parallel exposures with the unused Cameras will be included in the Phase II proposal instructions. Internal NICMOS parallel observations obtained under this policy will be known as *attached parallels* and will be delivered to the prime program's observer and will have the usual proprietary period.

The recommendations attached below are intended for General Observers (GOs) who do not establish a scientific rationale for observations with the non-prime NICMOS camera(s) in their Phase I submission to the TAC. They are subject to revision.

Table 2.3: Attached Parallel Recommendations

Pointing	Camera 1	Camera 2
Extragalactic	F160W	F110W, F160W
Galactic Clouds	F164N, F166N	F110W, F160W, F205W
(if \leq orbits)	F164N, F166N	F212N, F215N
Galactic Plane	F160W	F110W, F160W
(add if > 1 orbit)	F110W	F205W

Pointings are defined as:

- Extragalactic: > 5 degrees above the galactic plane.
- Galactic Clouds: Dark/molecular cloud regions (e.g., OMC, rho Oph, etc.)
- Galactic Plane: all pointings not Extragalactic or Galactic Clouds.

Designing NICMOS Observations

In This Chapter...

Designing NICMOS Observations / 33

In the preceding Chapters, we provided an overview of the scientific capabilities of NICMOS and the basic layout and operation of the instrument. Subsequent Chapters will provide detailed information about the performance and operation of the instrument. In this Chapter, we briefly describe the conceptual steps which need to be taken when designing a NICMOS observing proposal. The scope of this description is to refer proposers to the relevant Chapters across the Handbook. The basic sequence of steps in defining a NICMOS observation are shown in flow diagram form in Figure 3.1, and are:

- Identify the science requirements and select the basic NICMOS configuration to support those requirements (e.g., imaging, polarimetry, coronagraphy). Refer to the detailed accounts given in Chapter 4 and Chapter 5.
- Select the wavelength region of interest and hence determine if the observations will be Background or Read-Noise limited using the Exposure Time Calculator available on the STScI NICMOS WWW page (see also Chapter 9 and Appendix 1).
- Establish which MULTIACCUM sequence to use. Detailed descriptions of these are provided in Chapter 8. This does not need to be specified in a Phase I proposal. However, if a readout mode other than MULTIACCUM is required, this should be justified in the Phase I proposal.

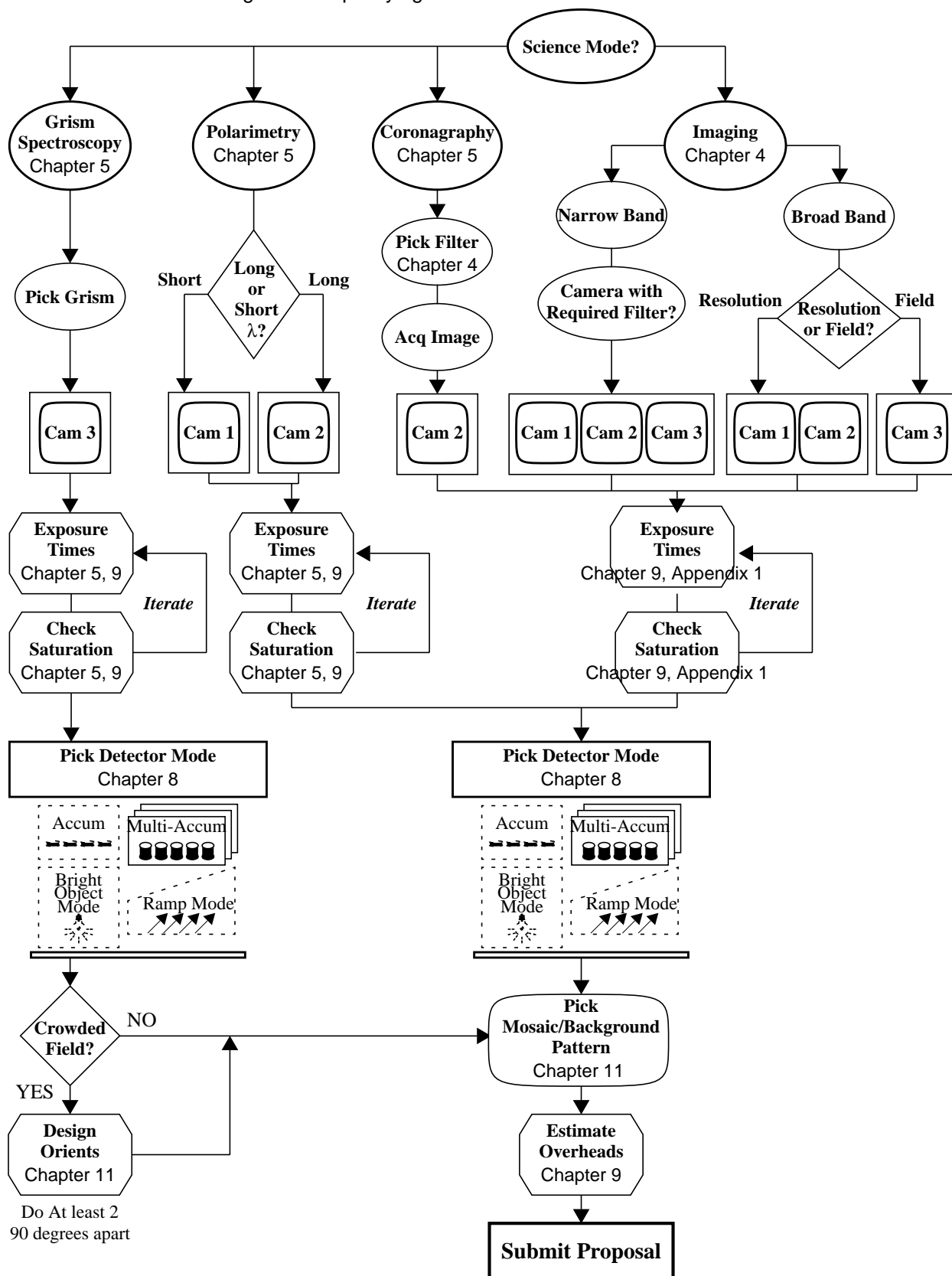
- Estimate the exposure time to achieve the required signal to noise ratio and check feasibility (i.e., saturation limits). To determine exposure time requirements and assess whether the exposure is close to the brightness and dynamic range limitations of the detectors, the Exposure Time Calculator on the WWW or the sensitivity plots in Appendix 1 should be used.



Proposers should always assume the worst case scenario for the NICMOS dark current to calculate exposure times (see Chapter 8 for an explanation of the best and worst dark current scenarios). This corresponds to adopting a dark current of ~ 2 e-/s/pixel in the exposure time estimation.

- If necessary a chop and dithering pattern should be chosen either to measure the background or to enable mapping. See Chapter 11.
- If coronagraphic observations are proposed, additional target acquisition exposures will be required to center the target in the aperture to the accuracy required for the scientific goal (e.g., the proposer may wish to center the nucleus of a galaxy in a crowded field behind the coronagraphic spot). The target acquisition overheads must be included in the accounting of orbits.
- Calculate the total number of orbits required, taking into account the overheads. In this, the final step, all the exposures (science and non-science, alike) are combined into orbits, using tabulated overheads, and the total number of orbits required are computed. Chapter 10 should be used for performing this step.

Figure 3.1: Specifying a NICMOS Observation



User's Guide

The chapters in this part describe the capabilities and performance of NICMOS. It provides a description of the imaging, polarimetric, coronagraphic, and spectroscopic capabilities of the instrument; the performance, readout modes, and limitations of its detectors.

Imaging

In This Chapter...

Filters & Optical Elements /	39
Photometry /	47
Focus History /	52
Image Quality /	55
Cosmic Rays /	65
Photon and Cosmic Ray Persistence /	65
The Infrared Background /	67

This chapter contains the description of the NICMOS filters and optical elements. The NICMOS focus history, image quality, encircled energy, Point Spread Functions, and the NIC3 performance are also presented. The photometric performance of the instrument, together with issues regarding both photon and cosmic ray persistence, are discussed. Finally, the background seen by NICMOS is described. Additional considerations regarding the special modes: coronagraphy, polarimetry and grism capabilities, are reported in Chapter 5.

Filters & Optical Elements

Each camera has 20 filter positions on a single filter wheel: 19 filters and one blank. As a result, not all filters are available in all cameras. Moreover, the specialized optical elements, such as the polarizers and grisms, cannot be crossed with other filters, and can only be used in fixed bands. In general the filters have been located in a way which best utilizes the characteristics of NICMOS, thus at shorter wavelengths the most important narrow band filters are located in NIC1 so that the diffraction limited performance can be maintained wherever possible, while those in NIC2 have been selected

to work primarily in the longer wavelength range where it will also deliver diffraction limited imaging.

Table 4.1 through Table 4.3 list the available filters and provide an initial general description of each, starting with NIC1 and working down in spatial resolution to NIC3. Figure 4.1 through Figure 4.3 show the effective throughput curves of all of the NICMOS filters for Cameras NIC1, NIC2, and NIC3, respectively, which includes the filter transmission convolved with the OTA, NICMOS foreoptics, and detector response. Appendix 1 provides further details and the individual filter throughput curves.

Nomenclature

The name of each optical element starts with a letter or group of letters identifying what kind of element it is: filters start with an “F”, grisms with a “G”, and polarizers with “POL”. Following the initial letter(s) is a number which in the case of filters identifies its approximate central wavelength in microns, e.g., F095N implies a central wavelength of 0.95 microns. A trailing letter identifies the filter width, with “W” for wide, “M” for medium and “N” for narrow. In the case of grisms, the initial “G” is followed by a number which gives the center of the free-spectral range of the element, e.g., G206. For the polarizers, a somewhat different notation is used, with the initial “POL” being followed by a number which gives the PA of the principal axis of the polarizer in degrees, and a trailing letter identifying the wavelength range it can be used in, which is either “S” for short (0.8-1.3 microns) or “L” for long (1.9-2.1 microns).

In Figure 4.1, Figure 4.2, and Figure 4.3, the wide, medium, and narrow bandwidth filters are plotted separately for each camera.

Table 4.1: NIC 1 Filters

Name	Central Wavelength (μm)	Bandwidth (μm)	Comment
Blank	N/A	N/A	blank
F110W	1.025	0.8–1.35	Broad Band
F140W	1.3	0.8–1.8	
F160W	1.55	1.35–1.75	
F090M	0.9	0.8–1.0	Water
F110M	1.1	1.0–1.2	
F145M	1.45	1.35–1.55	
F165M	1.6	1.55–1.75	
F170M	1.7	1.6–1.8	
F095N	0.953	1%	[S III]
F097N	0.97	1%	[S III] continuum
F108N	1.083	1%	He I
F113N	1.13	1%	He I continuum
F164N	1.644	1%	[Fe II]
F166N	1.66	1%	[Fe II] continuum
F187N	1.87	1%	Paschen α
F190N	1.90	1%	Paschen α continuum
POL0S	1.1	0.8–1.3	Short λ Polarizer
POL120S	1.1	0.8–1.3	Short λ Polarizer
POL240S	1.1	0.8–1.3	Short λ Polarizer

Figure 4.1: Filters for NIC 1

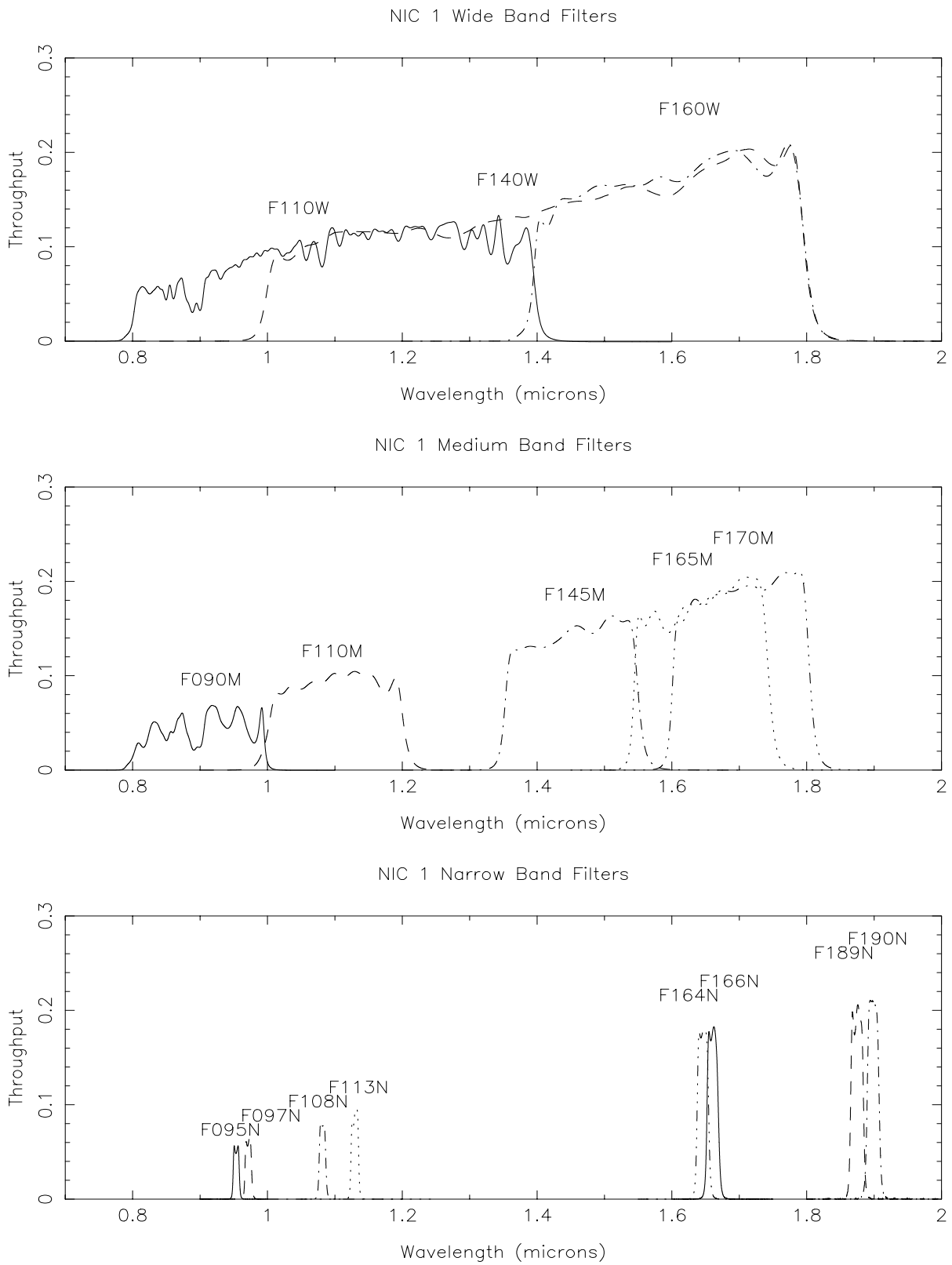


Table 4.2: NIC 2 Filters

Name	Central Wavelength (μm)	Bandwidth (μm)	Comment
Blank	N/A	N/A	blank
F110W	1.1	0.8–1.4	
F160W	1.6	1.4–1.8	Minimum background
F187W	1.875	1.75–2.0	Broad
F205W	1.9	1.75–2.35	Broad Band
F165M	1.7	1.55–1.75	Planetary continuum
F171M	1.715	1.68–1.75	HCO ₂ and C ₂ continuum
F180M	1.80	1.765–1.835	HCO ₂ and C ₂ bands
F204M	2.04	1.9–2.09	Methane imaging
F207M	2.1	2.0–2.15	
F222M	2.3	2.15–2.30	CO continuum
F237M	2.375	2.3–2.45	CO
F187N	1.87	1%	Paschen α
F190N	1.9	1%	Paschen α continuum
F212N	2.121	1%	H ₂
F215N	2.15	1%	H ₂ and Br γ continuum
F216N	2.165	1%	Brackett γ
POL0L	2.05	1.9–2.1	Long λ polarizer
POL120L	2.05	1.9–2.1	Long λ polarizer
POL240L	2.05	1.9–2.1	Long λ polarizer

Figure 4.2: Filters for NIC 2

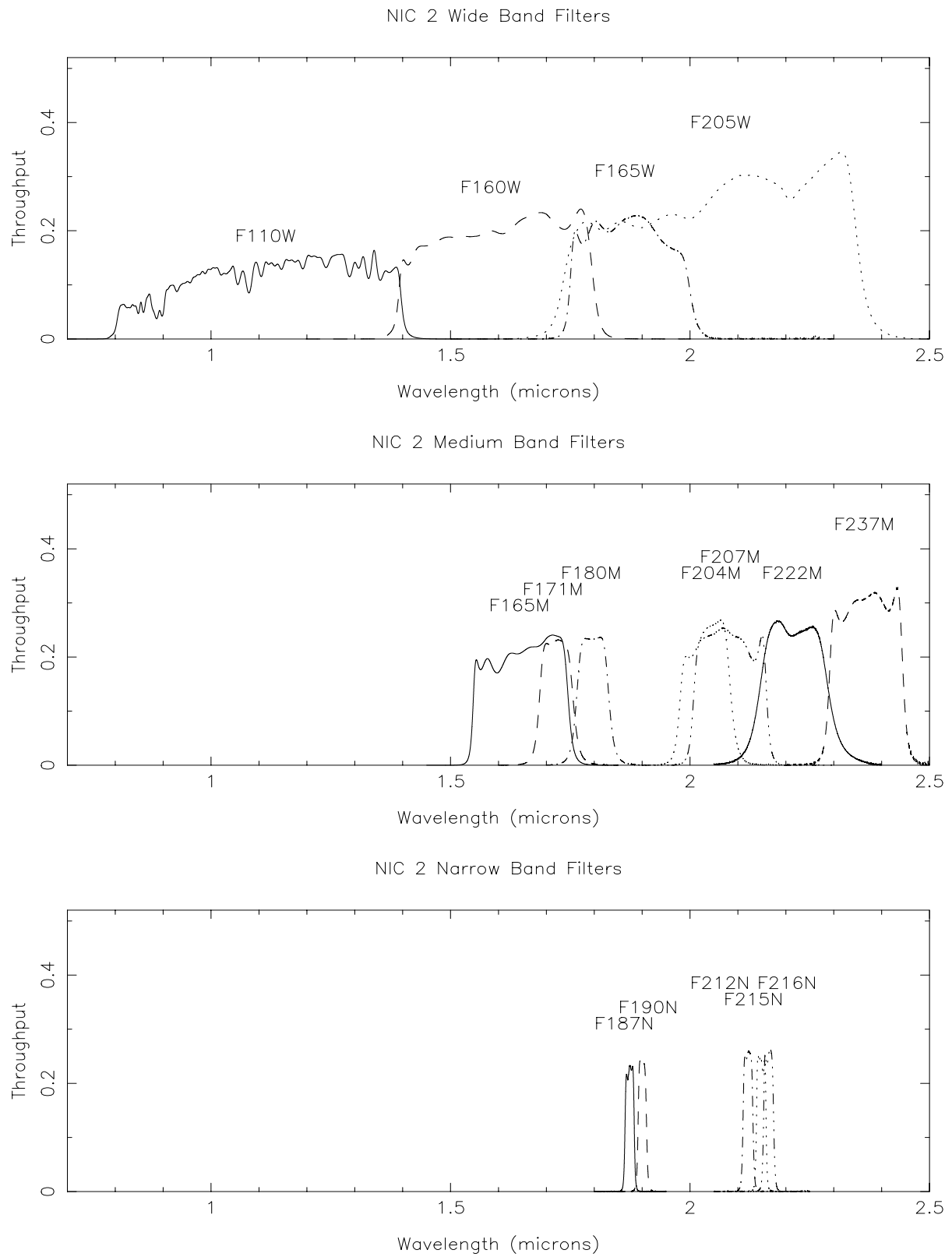
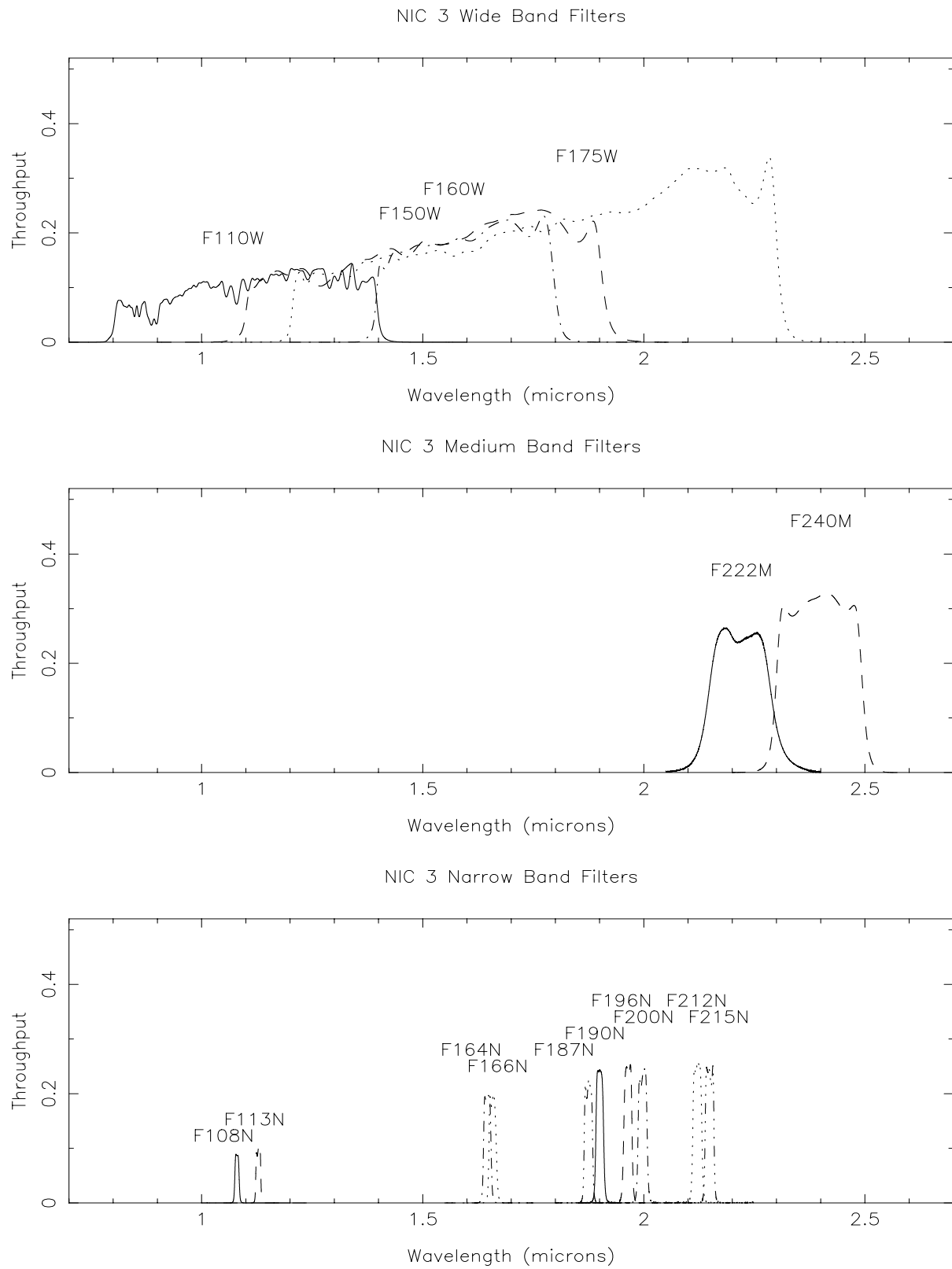


Table 4.3: NIC 3 Filters

Name	Central Wavelength (μm)	Bandwidth (μm)	Comment
Blank	N/A	N/A	blank
F110W	1.1	0.8–1.4	
F150W	1.5	1.1–1.9	Grism B continuum
F160W	1.6	1.4–1.8	Minimum background
F175W	1.75	1.2–2.3	
F222M	2.3	2.15–2.3	CO continuum
F240M	2.4	2.3–2.5	CO band
F108N	1.0830	1%	He I
F113N	1.13	1%	He I continuum
F164N	1.644	1%	[Fe II]
F166N	1.66	1%	[Fe II] continuum
F187N	1.875	1%	Paschen α
F190N	1.9	1%	Paschen α continuum
F196N	1.962	1%	[Si VI]
F200N	2.0	1%	[Si VI] continuum
F212N	2.121	1%	H ₂
F215N	2.15	1%	H ₂ continuum
G096	0.9673	0.8–1.2	GRISM A
G141	1.414	1.1–1.9	GRISM B
G206	2.067	1.4–2.5	GRISM C

Figure 4.3: Filters for NIC 3



Out-of-Band Leaks in NICMOS Filters

In order to make use of the high spatial resolution of HST, many observers will wish to use NICMOS to observe very red objects (e.g., protostars) at relatively short wavelengths. By their very nature, these very red objects have very low effective color temperatures. Thus if we observe such an object at a wavelength of 1.0 microns, we can expect that its flux at 2.5 microns will be orders of magnitude larger than its flux at the desired wavelength. In such a case, exceptionally good out-of-band blocking is required from the filter. We have therefore investigated whether the measured filter transmissions would allow any sources with extreme colors to yield erroneous photometry due to out-of-band leaks.

For observations of objects with extreme colors (such as highly reddened sources, protostars, etc.), out-of-band filter leaks could potentially have a detrimental impact on photometry. Early estimates based on pre-flight filter transmission measurements suggested that there might be red leaks for several filters, and the original edition of the Instrument Handbook recommended caution for the filters F090M, F095M, F097N, F108N, F110M, F110W, F113N, F187N, and F190M. A limited set of in-flight tests for red leaks was made, and although the results have not been fully analyzed, preliminary indications are that actual red leaks were *insignificant or non-existent*.

Photometry

Ground-based near-infrared observations are limited to a set of transparent atmospheric windows, while NICMOS suffers no such restrictions. For this reason, there are no suitable faint flux standards with continuous, empirical spectrophotometry throughout the $0.8 \mu\text{m} < \lambda < 2.5 \mu\text{m}$ range. The absolute flux calibration of NICMOS, therefore, has been calculated using observations of stars for which reliable spectral models, normalized by ground-based photometry, are available. Two types of flux standards have been observed: pure hydrogen white dwarfs, and solar analog stars. Grism sensitivity is determined directly from flat-field corrected spectra of these stars using their known spectral energy distributions. Filter sensitivities are calculated from imaging measurements according to the synthetic photometry procedure detailed in Koorneef *et al.* (1986). Since the pipeline calibration cannot utilize color information, the headers of reduced data contain the calibration constant that specifies the equivalent count rate for a spectral energy distribution that is constant with wavelength. For convenience, this calibration constant appears twice, once in Jansky units and once in $\text{erg/s/cm}^2/\text{\AA}$ units. Color transformations could be defined for post-pipeline analysis.

Solar Analog Absolute Standards

For calibration using solar analogs, a reference spectrum of the Sun is normalized to the flux levels of the NICMOS standards using ground-based photometry of the standard stars in the J, H and K bands. This continuous spectral model is then integrated through the total system throughput function for a given bandpass (including filter, detector, instrument and telescope optics), and the integral flux is compared to the measured count rate from the star in observations through that filter to derive the flux calibration constants. The absolute flux accuracy achieved by this method relies on two assumptions:

1. that the absolutely calibrated reference spectrum of the sun is known with an uncertainty of a few percent (Colina, Bohlin and Castelli, 1996), and
2. that the near-infrared spectra of the solar analogs are nearly identical to that of the sun.

In the past, this method has been used to determine the absolute calibration of near-infrared photometry at ground-based observatories. In these cases, the absolute calibration accuracy was estimated to be at least 5%, and for some bands 2% to 3% (Campins, Rieke and Lebofsky, 1985).

Ground-based photometry by Persson *et al.* (1998, AJ, 116, 2475) of several solar analog stars used in the NICMOS calibration program has shown that the stars P330E and P177D (see Colina & Bohlin 1997, AJ, 113, 1138; Colina, Bohlin & Castelli 1996, AJ, 112, 307) are most closely matched to the colors of the Sun, and are thus most suitable for NICMOS photometric calibration. P330E is the primary NICMOS solar analog standard for photometric calibration.

White Dwarf Absolute Standards

Pure hydrogen white dwarfs are useful calibration standards because their spectral energy distributions can be accurately modeled from the UV through the near-IR (Bohlin, Colina & Finley 1995, AJ, 110, 1316; Bohlin 1996, AJ, 111, 1743). The star G191B2B has therefore served as a primary calibration standard for several HST instruments, and was selected for NICMOS observation along with another star, GD153. At present, only G191B2B has ground-based JHK photometry of suitable quality (Persson, private communication) to verify absolute photometry in the near-infrared. It was found to be necessary to renormalize the G191B2B spectral model by a few percent relative to its optical calibration in order to get good agreement with the ground-based JHK photometry. It is believed that this reflects uncertainties in the white dwarf spectral model at the Paschen limit. Once this renormalization is made, the white dwarf and solar analog flux calibrations for NICMOS agree with one another at the 1% to 3% level.

The largest remaining discrepancies are in the K-band, and are presently being investigated.

Photometric throughput and stability

Overall, NICMOS throughput (i.e. photoelectrons per second detected from a source with given flux) is generally within 20% of pre-launch expectations in all observing modes. The photometric stability of NIC1 and NIC2 was monitored once a month since August 1997, and more frequently near the end of the NICMOS Cryogen lifetime. Observations of the solar analog P330E were taken through a subset of filters (5 for NIC1, 6 for NIC2) covering the entire wavelength range of the NICMOS cameras, and dithered through three or four pointings. NIC3 has also been monitored in a similar fashion, although only two filters were used for part of the instrument's lifetime. For most filters and cameras the zeropoints have been stable to within 3% throughout the lifetime of the instrument, although there may be some evidence for a slow secular drift.

Intrapixel sensitivity variations

The response of a pixel in the NICMOS detectors to light from an unresolved source varies with the positioning of the source within the pixel due to low sensitivity at the pixel's edges and dead zones between pixels. This effect has no impact on observations of resolved sources, and little effect on well-sampled point sources (e.g. observations with NIC1 and NIC2 through most filters). However in NIC3, point sources are badly under-sampled, especially at short wavelengths where the telescope diffraction limit is much smaller than the NIC3 pixel size. Object counts may vary by more or about 0.2 mag at J and by ~ 0.2 mag at H (Todd Lauer, 1999, private communication) depending on the positioning of a star within a pixel. Well dithered exposures will average out this effect, but NIC3 observations of stars with few dither positions can have significant uncertainties which set a fundamental limit to the achievable quality of point source photometry.

Special Situations

Sources with Extreme Colors

We have carried out tests to establish the likely impact on photometric observations of sources of extreme colors induced by the wavelength-dependent flat field. For each filter, we used two sources with different colors assuming spectral energy distributions were black-body functions. The first case had a color temperature of 10,000K, and thus is

typical of stellar photospheres and the resultant color is representative of the bluer of the sources that will be seen with NICMOS. (It is worth noting that for reflection nebulae illuminated by hot stars, a significantly bluer spectrum is often seen.) The second source had a color temperature of 700K which in ground-based terms corresponds to $[J - K] = 5$, a typical color encountered for embedded sources, such as Young Stellar Objects (YSOs). (Again, there are sources which are known to be redder. The Becklin-Neugebauer object, for example, has no published photometry at J, but has $[H - K] = 4.1$, and the massive YSO AFGL2591 has $[J - K] = 6.0$. YSOs with $[J - K] = 7$ are known, although not in large numbers.)

An example of a pair of the simulated spectra is shown Figure 4.4, for the F110W filter. In this filter an image of a very red source will be dominated by the flat field response in the 1.2 to 1.4 micron interval, while for a blue source the most important contribution will come from the 0.8 to 1.0 micron interval. The results of our study for the worst affected filters are shown in Table 4.4.

- Even for the broadest NICMOS filters the wavelength dependence of the flat field response generates only small photometric errors, typically less than 3% for sources of unknown color. Not surprisingly, the largest errors arise in the 3 broadband filters whose bandpasses include some part of the regions where the flat field response changes most rapidly.
- The same results hold true even for filters at the most extreme wavelengths (e.g., F090M, F222M and F240M) because of their small bandwidth.
- It will probably be difficult to obtain photometry to better than the limits shown in Table 2.1 for the F090M, F110W, F140W, F205W and F240M filters, and observers requiring higher accuracy should contact the Help Desk at STScI for guidance.
- These errors can probably be corrected if more accurate photometry is needed, by taking multi-wavelength observations and using an iterative correction technique.
- For observers requiring high precision photometry, these represent non-trivial limits beyond which it will not be possible to venture without obtaining multi-wavelength images. In order to obtain 1% precision using the F110W filter, for instance, observers should observe at a minimum of one other wavelength. The color information derived from the pair (or group) of images could then be used to construct a more appropriate flat field image, which could then be applied to improve the color information, and so on.

Figure 4.4: Detected Source Spectrum. These are for sources with color temperatures of 700K (solid line) and 10,000K (dashed line). It is easy to see that the detected image will be dominated by the flat field response in the 1.2-1.4mm region for a 700K source, while for a 10,000K source the detected image will be affected by the flat field response throughout the filter bandpass.

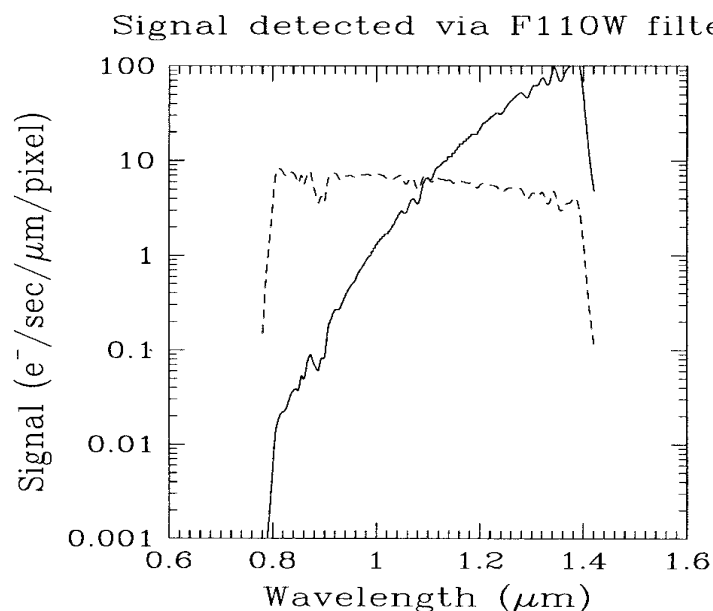


Table 4.4: Filters with Largest Photometric Errors for Sources of Extreme Color

Filter	10,000K model. Error (percent)	700K model. Error (percent)
F090M	<0.1	1.9
F110W	1.1	2.9
F140W	0.7	3.1
F160W	<0.1	0.3
F187W	<0.1	0.3
F205W	0.4	2.1
F222W	<0.1	0.1
F240M	1	0.9

Extended Sources with Extreme Spatial Color Variations

Our analysis has been limited to point sources, but some mention should be made of the situation for extended objects. A good example is the YSO AFGL2591. This has an extremely red core, whose $[J - K] = 6$ and which is entirely undetected optically. However, it also has a large IR nebula which is quite prominent at J and K, and in the red visual region, but much fainter

at L, and which is probably a reflection nebulosity. Spatially, the nebula has highly variable color, some parts of it having fairly neutral or even slightly blue colors in the NICMOS waveband, while other parts are extremely red. Obtaining very accurate measurements of the color of such a source would again require the use of images at more than one wavelength and an iterative tool of the kind described earlier. A further example of this kind of complicated object is the prototypical post-AGB object CRL2688, the Cygnus Egg Nebula, which has an extremely blue bipolar reflection nebula surrounding an extremely red core. Techniques which require very accurate measurements of the surface brightness of extended objects, such as the brightness fluctuation technique for distant galaxies, will need to be applied with care given to the photometric uncertainties such as those discussed here.

Creating Color-dependent Flat Fields

NICMOS ISR 99-002 describes two methods for creating color-dependent flat fields, and programs and calibration files for making them are available in the software part of the website. One way of approaching the problem is to make monochromatic flats, by doing a linear least squares fit to several narrowband (and, if necessary for increase wavelength coverage) medium band flats, for each pixel. The slope and intercept images that result from such a fit can be used to determine what the detector response would be to a monochromatic source. Note that this method works best if the desired wavelength is within the range covered by the observed flats-- extrapolation with this method gives questionable results.

If the source spectrum is known, a composite flat made from the weighted sum of the narrowband flats in the passband of the observed image can be made. A program to do this, given an input spectrum and the calibration database in **STSDAS**, is available. If you have a variety of sources in your image you may want to make several flatfields and apply them to regions defined by some criterion, say color as defined by a couple of narrowband images on either side of the broadband image.

Focus History

The PAM consists of an adjustable mirror in the NICMOS optical train that can be moved to make small corrections to the NICMOS focus and serves to properly position the pupil image of the telescope primary mirror onto the corrective optic. The motion of the PAM is limited to ± 10 mm in focus travel from its zero position. The NICMOS cameras were designed to share a common focus with the PAM close to its zero position. In the current state of the dewar, NIC1 and NIC2 can each be focussed within the

range of the PAM. NIC3, however, cannot be entirely focussed by motions of the PAM alone and remains slightly out of focus although still scientifically usable (see next section).

The focus positions of all three NICMOS cameras have changed since launch with motion in the dewar. The positions are measured by observations of stars over a range of focus settings on a frequent basis. The focus history since shortly after launch is shown in Figure 4.5. The focus position is given for the detector center, the focus variation across camera's field of view is ~ 1.5 mm in PAM space in NIC2, and about half of that in NIC1. The two largest focus excursions, on January 12 and June 4, 1998, are due to the secondary mirror reset used to place NIC3 in focus during NIC3 campaigns. A noticeable improvement in NIC3 focus occurred after December 17, 1997, when the FOM had been tilted by 16 arcsec to reduce vignetting in that camera (see also the appropriate section on the vignetting of NIC3, below).

Figure 4.5: NICMOS Focus History through January 4, 1999.

NICMOS Focus history through January 4, 1999

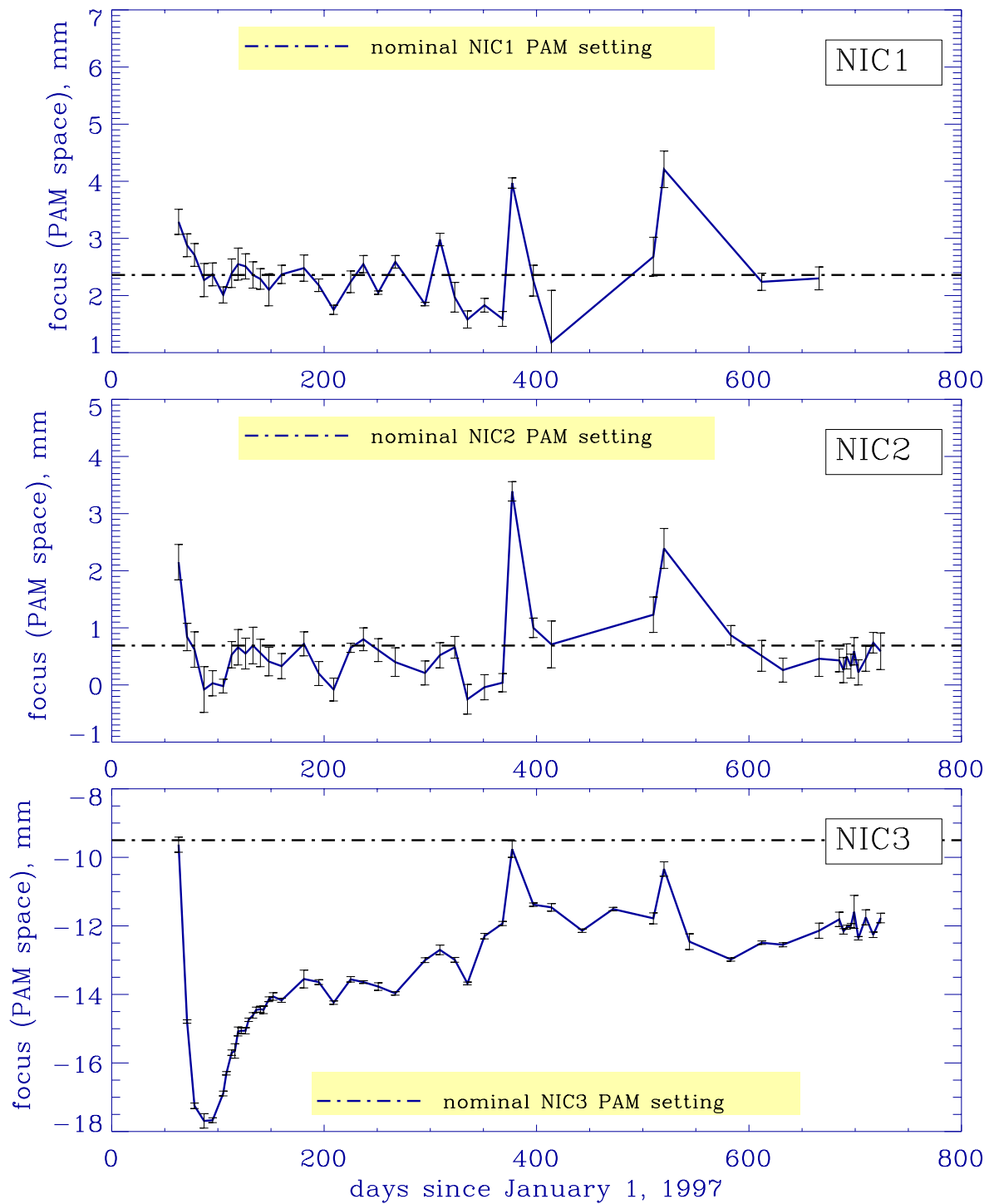


Image Quality

Strehl Ratios

The high image quality of NICMOS is summarized by the Strehl ratio of the PSF, namely by the ratio of the observed-to-perfect PSF peak fluxes. Here, by peak of the “perfect PSF” we mean the one derived from **TinyTim** PSFs for the selected camera/filter/focus configuration. Table 4.5 lists the Strehl ratios for representative filters in all three NICMOS cameras (courtesy of John Krist, STScI). The ratio is very high, between 0.8 and 0.9 for NICMOS images, at all wavelengths and in all Cameras.

Table 4.5: NICMOS Strehl Ratios

Filter	NIC1	NIC2	NIC3
F110W	0.91	0.89	0.81
F160W	---	0.90	0.86
F222M	---	0.90	0.92

NIC1 and NIC2

The changes in dewar geometry leading to the degraded focus in NIC3 have also affected NIC1 and NIC2. By measuring the PSFs of stars at a series of PAM positions it was determined that the optimal focus for NIC1 occurred for a PAM position of $\sim +2.4$ mm and the optimal focus for NIC2 at ~ 0.7 mm during 1998. This difference is significant enough that NIC1 and NIC2 are no longer considered to be parfocal. However, the NIC1 and NIC2 foci are still sufficiently close that the intermediate focus position between the two cameras, NIC1-2, has been defined for simultaneous observations. The image degradation induced by this “compromise” focus is smaller than a few percent in each camera, and negligible for most purposes. The “compromise” focus position has been chosen to share the wavefront error equally between NIC1 and NIC2. Additionally, a separate PAM position at the optimal focus is defined and maintained for each camera. Most users will find the compromise focus sufficient to reach their scientific goals.

The encircled energy profiles for NIC1 and NIC2 at representative wavelengths are shown in Figure 4.6 through Figure 4.9.

Figure 4.6: Encircled Energy for NIC1, F110W.

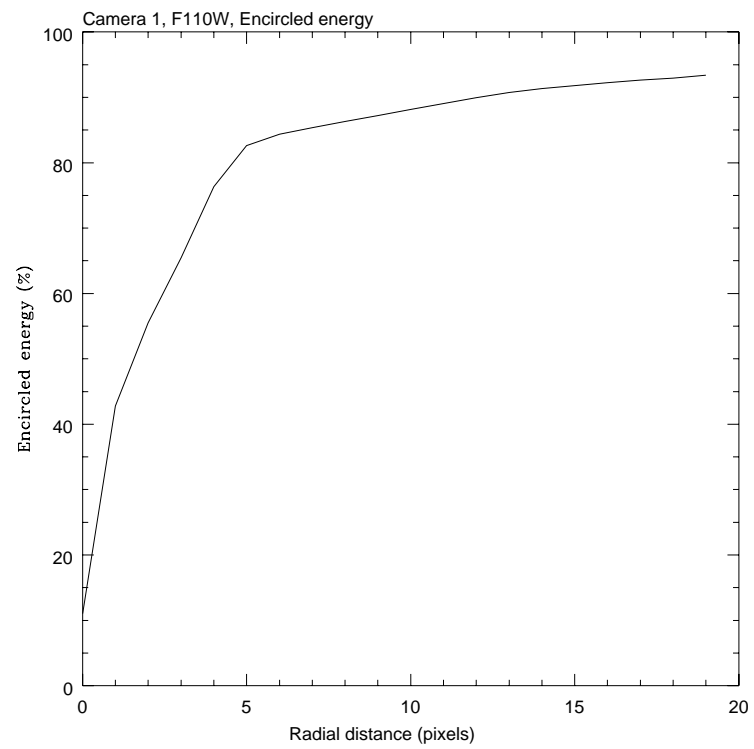


Figure 4.7: Encircled Energy for NIC1, F160W.

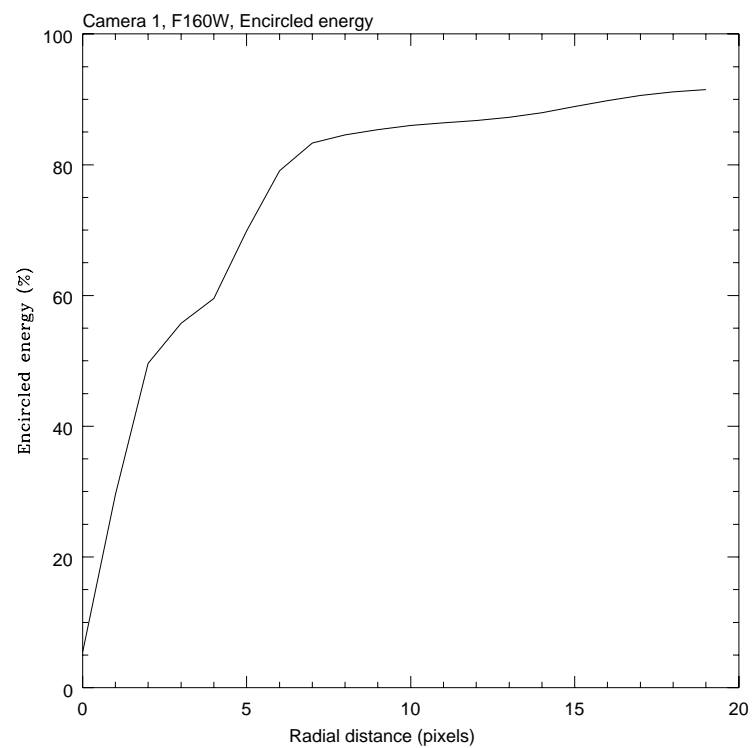


Figure 4.8: Encircled Energy for NIC2, F110W.

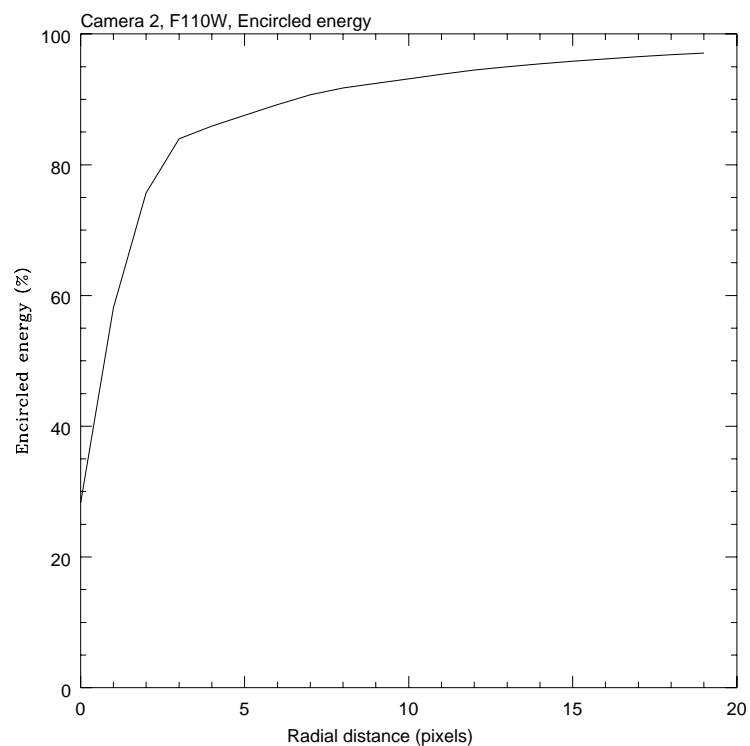


Figure 4.9: Encircled Energy for NIC2, F160W.

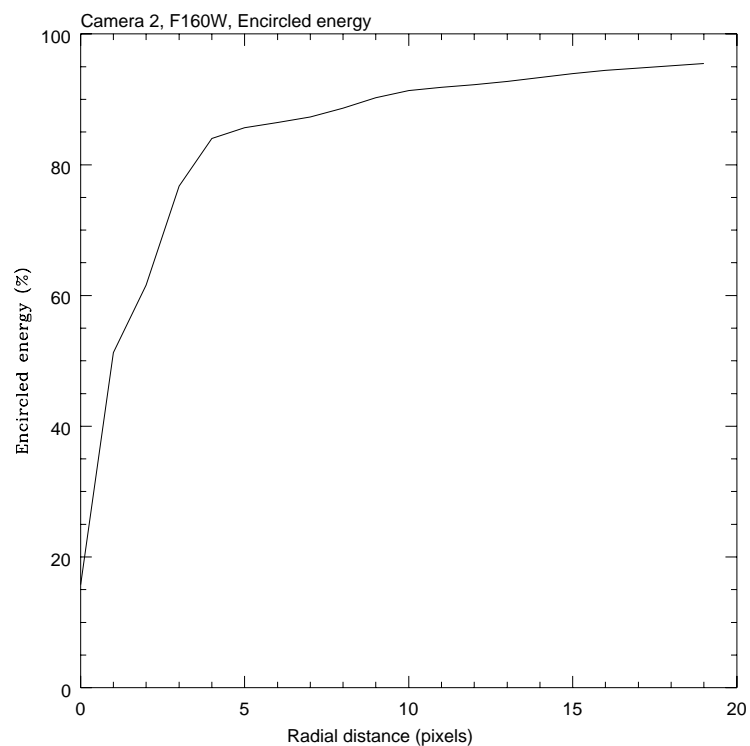
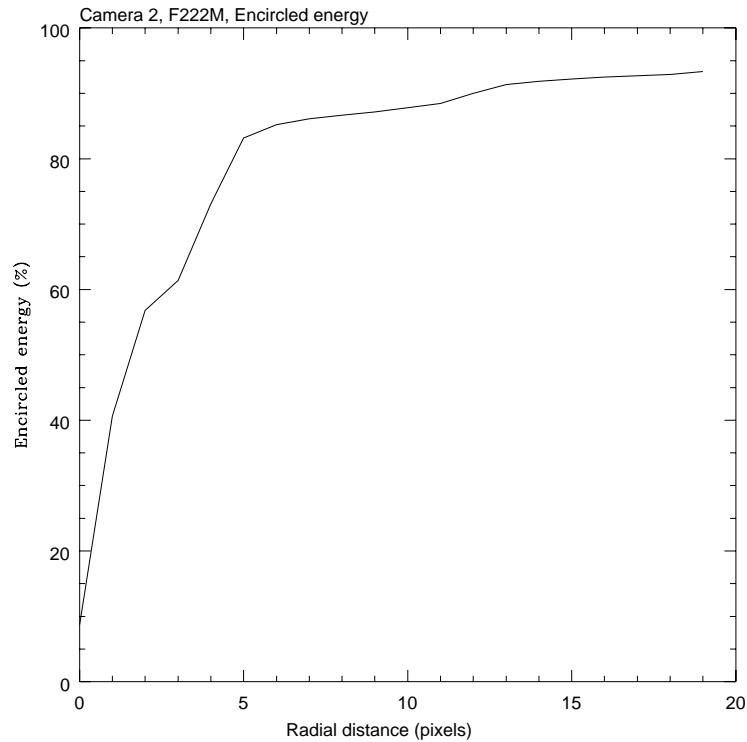


Figure 4.10: Encircled Energy for NIC2, F222M.



Vignetting in NIC1 and NIC2

The lateral shifts of the NICMOS dewar have resulted in vignetting in NIC1 and NIC2 in addition to NIC3. In the case of NIC1 and NIC2, the source of the vignetting is a slight misalignment of the FDA mask. Relatively small losses in throughput are observed at the bottom ~ 15 rows of both NIC1 and NIC2 as shown in Figure 4.11 and Figure 4.12.

In Figure 4.10, the column plot of the ratio of an in-flight flat field to a pre-launch flat field is shown for NIC1 and the F110W filter, in order to highlight the effect of the FDA vignetting. The overall normalization of the y-axis ratio scale is arbitrary. The approximately 6% decrease seen in rows near the bottom of the detector (left region in the Figure) shows the region of the NIC1 detector where vignetting has affected the throughput.

Figure 4.11 shows a similar plot for NIC2. Here, the decrease in throughput due to vignetting is approximately 10% for the bottom 10-15 rows.

Figure 4.11: One column of the ratio between a recent NIC1 flat field and a pre-launch flat field taken before launch, at $1.1\text{ }\mu\text{m}$, plotted as a function of row number (indicated as Line).

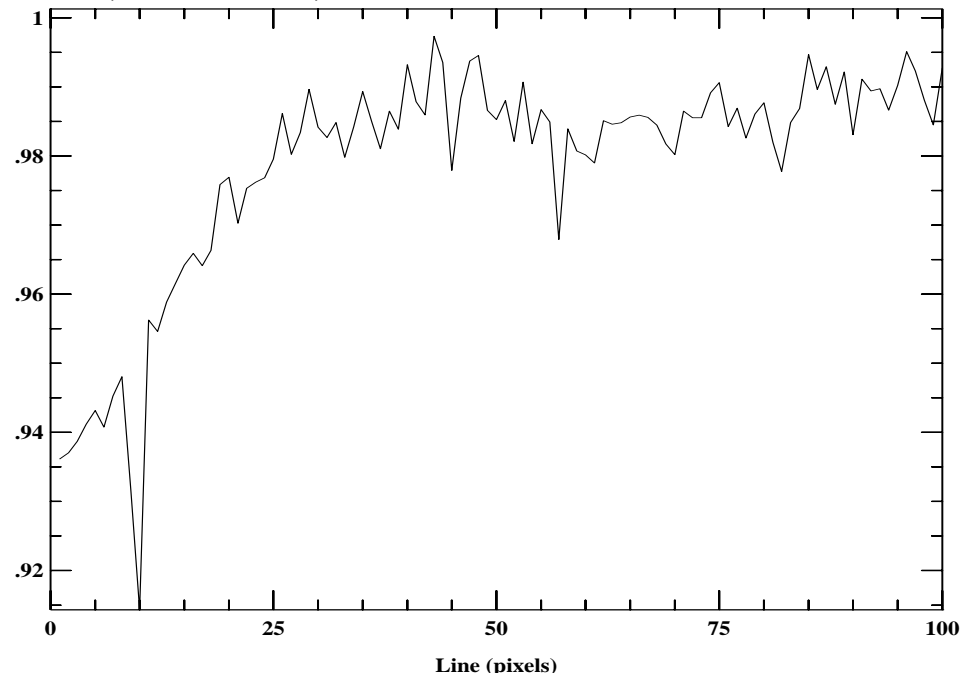
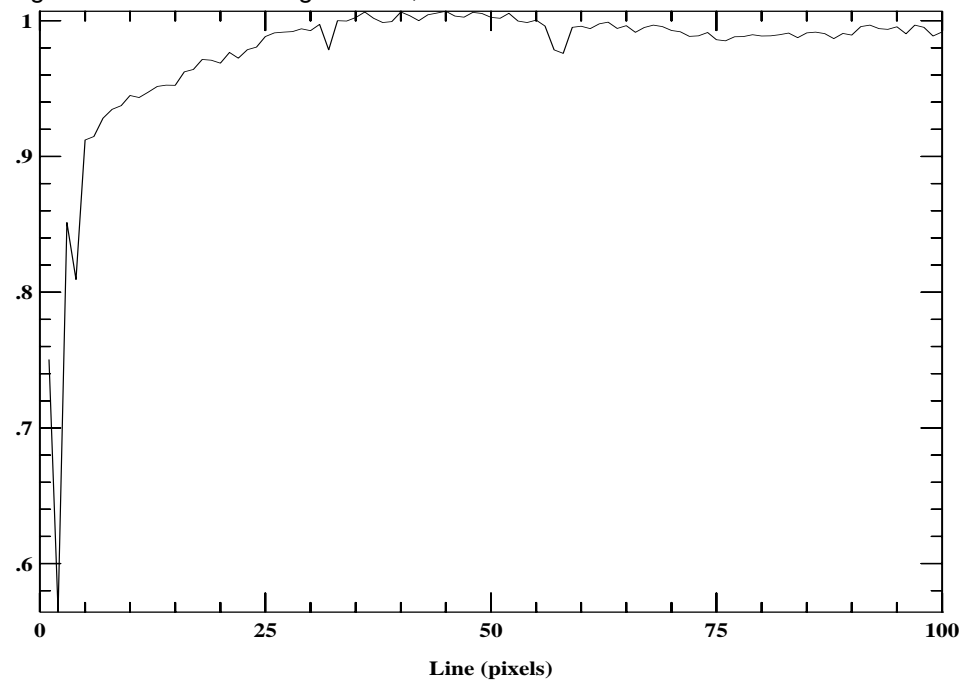


Figure 4.12: Similar to Figure 4.11, for NIC2.



NIC3

NIC 3 has suffered the largest shift in focus, which was estimated to be around -12 mm in PAM space when the last valid measurement was performed, i.e. during the final stages of cryogen exhaustion (January 4, 1999). This value of the optimum focus is outside the range which can be reached with the PAM (maximum negative value is -9.5 mm).

During Cycle 7 and 7N, NIC3 was operated in optimal focus during two special observing campaigns of 2-3 weeks each, in January and June 1998, when the HST secondary mirror was moved to recover optimal focus. Outside those two periods, NIC3 was operated at best focus, namely with the PAM at -9.5 mm.

The typical FWHM of NIC3 images (both at optimal and best focus) is ~1.3 pixels, with small variations between different wavelengths (NICMOS ISR-98-006); the fractional flux within the first Airy ring goes from 43% in J to 49% in H to 58% in K with NIC3 in focus. The size of the Airy ring for NIC3 PSF has been calculated for oversampled **TinyTim** PSFs.

Because NIC3 undersamples the PSF, the degradation of image quality with the PAM mirror at -9.5 mm was found to be relatively small compared to the optimal-focus image quality. Figure 4.13 shows the encircled energy for NIC3 at 1.6 microns for both the optimal focus (PAM=-13 mm at the time of the measurement) and the best focus (PAM=-9.5 mm). Figure 4.14 shows the PSF in the same conditions. Both figures report simulations obtained with **TinyTim** PSFs convolved with the NIC3 pixel response, but the results are very similar to the actual observations. The loss in the peak flux is around 20% and the loss in encircled energy beyond one pixel radius (0.2") is no more than 10% - 15%.

If thermal and mechanical model predictions are correct, we expect that the revived NICMOS will have similar focus characteristics. Given the little loss of performance with the slight out-of-focus operations, NIC3 will be operated without moving the HST secondary mirror and offered "as is"

Some observers may consider to obtain NIC3 parallel observations, while NIC1 and NIC2 are used for the primary science observations. At the NIC1-2 best focus, the image quality of NIC3 is obviously degraded, with a PSF FWHM over 3 times larger than the NIC3 best focus PSF FWHM.

Figure 4.13: NIC3 encircled energy at 1.6 microns at optimum focus (PAM=-13 mm, solid line) and at the best achievable focus (PAM=-9.5 mm, dashed line) with the HST secondary mirror at nominal position.

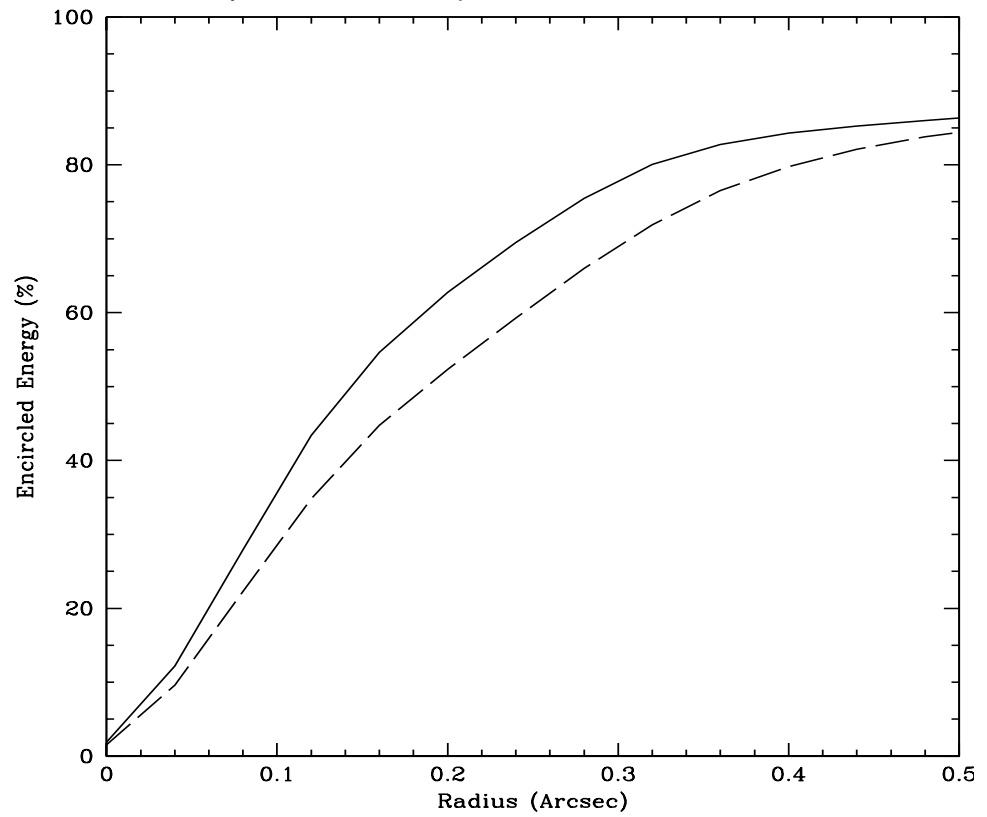
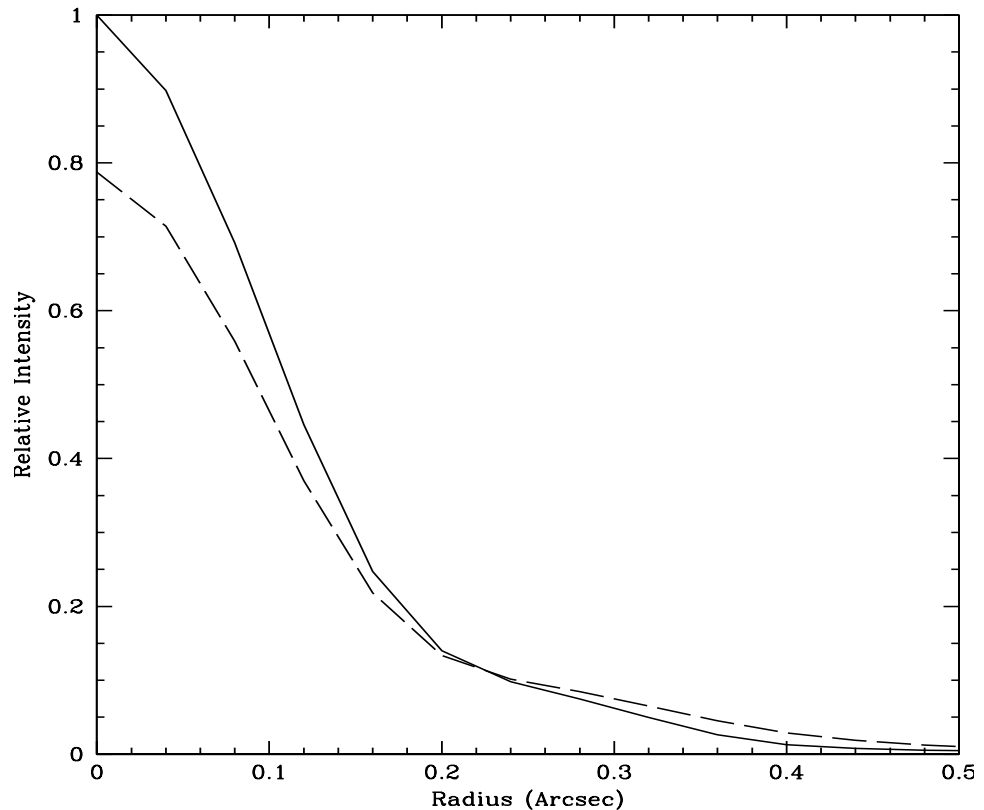


Figure 4.14: NIC3 PSF at 1.6 microns at optimum focus (PAM=-13 mm, solid line) and at the best achievable focus (PAM=-9.5 mm, dashed line) with the HST secondary mirror at nominal position.



Vignetting in NIC3

In addition to be affected by focus loss, NIC3 is also affected by vignetting from two sources. The first is a cold vignetting, due to the lateral shift of the FDA mask, similar to the vignetting affecting NIC1 and NIC2. The second is due to a warm bulkhead edge, which produces elevated thermal background and degraded image quality over the bottom 25% of the detector (bottom ~60 rows).

The warm vignetting was successfully removed during early 1998 by moving the FOM to a position $X=+16$ arcsec, producing a corresponding translation in the NIC3 field-of-view. This translation removed the warm vignetting and slightly improved focus. The price was the introduction of a mild astigmatism, which is however below the $\lambda/14$ criterion for image quality (except at J, where the wavefront error is $\lambda/10$).

The only vignetting left in NIC3 with the FOM at $X=+16$ arcsec is the one produced by the FDA and affects the bottom 10-15 rows of the detector, in the same manner as NIC1 and NIC2. We expect to operate NIC3 in Cycle 10 with the FOM at the +16 arcsec default position, which will be totally transparent to users.

NICMOS Point Spread Function (PSF)

NICMOS provides full Nyquist sampling down to 1 μm and $\sim 1.7 \mu\text{m}$ in NIC1 and NIC2, respectively. In addition to all the properties of diffraction-limited imaging, the NICMOS PSF has a few ‘off-nominal’ characteristics. These are mostly an effect induced on the optics by the thermal stress suffered by the dewar early in the instrument’s life.

Each NICMOS camera has a cold mask located at the entrance to the dewar that is designed to block thermal emission from the OTA pupil obstructions. The NIC2 cold mask also serves as the Lyot stop for the coronagraph. Due to the thermal stress suffered by the NICMOS dewar, the cold masks are misaligned relative to the OTA.

Because of the cold mask misalignment, NICMOS images of point sources show slightly elliptical diffraction rings and the diffraction spikes show alternating light and dark bands and asymmetries. The diffraction pattern is not symmetric. The elliptical shaped diffraction rings and the asymmetric banding patterns along the diffraction spikes are caused by unequal offsets between the corresponding pairs of spider diagonals.

Optical aberrations: coma and astigmatism

Coma and astigmatism in the NICMOS cameras are generally small, with the wavefront error typically less than 0.05 μm , that is, less than 5% of the wavelength at 1 μm . The mean values of coma and astigmatism measured during Cycles 7 and 7N along the detector’s x - and y -coordinates, are given in Table 4.5, expressed as wavefront errors. In NIC3, the astigmatism along the detector’s x -axis increased to $\sim 5\%$ and became more unstable after the nominal FOM y -tilt had been changed from 0 to 16 arcsec in December of 1997 in order to reduce the significant vignetting in this camera. With regard to the temporal behavior of NICMOS aberrations, the y -coma in all three cameras had been gradually increasing by ~ 2 -5% during NICMOS operations throughout the 1997-1998 lifetime period.

Table 4.6: Mean and standard deviation of NICMOS aberrations

	NIC1	NIC2	NIC3	
	FOM=0"	FOM=0"	FOM=0"	FOM=16"
x -coma, μm	0.017 ± 0.008	0.018 ± 0.012	0.026 ± 0.006	0.030 ± 0.013
y -coma, μm	-0.034 ± 0.011	-0.028 ± 0.016	-0.040 ± 0.011	-0.058 ± 0.015
x -astigmatism, μm	0.002 ± 0.007	0.000 ± 0.009	0.003 ± 0.016	0.053 ± 0.023
y -astigmatism, μm	0.016 ± 0.012		0.027 ± 0.013	0.022 ± 0.014

Field Dependence of the PSF

The PSF is at least to some extent a function of position in the OTA field of view. Preliminary data indicate that this effect is extremely small (less than ~6% on the PSF FWHM) and that only a small degradation will be observed. Movement of the FOM, on the other hand, has been shown to have a greater effect on the PSF quality.

Temporal Dependence of the PSF: HST Breathing and Cold Mask Shifts

The NICMOS PSF suffers from small temporal variations induced by the HST breathing and by variable shifts of the instrument's cold masks.

The HST focus (the focal length) is known to oscillate with a period of one HST orbit. Changes in the focus are attributed to thermal contraction/expansion of the OTA resulting from the telescope warm up and cool down during an orbital period.¹ These short term focus variations are usually referred to as “OTA breathing”, “HST breathing”, “focus breathing”, or simply “breathing”. Breathing affects all data obtained with all instruments onboard HST.

Thermally induced HST focus variations are also large after the telescope undergoes a large slew across the sky. After a telescope slew, the telescope temperature variation exhibits the regular orbital component plus a component associated with the change in telescope attitude. The focus changes due to telescope attitude are complicated functions of Sun angle and telescope roll. More information and models can be found on the “Observatory focus monitoring” web site at URL

http://www.stsci.edu/ftp/instrument_news/Observatory/focus/focus2.html.

The telescope attitude also appears to affect the temperature of the NICMOS fore-optics, which are outside the dewar. A noticeable oscillatory pattern about the NICMOS focus trend lines was found to correlate with temperature variations of the fore-optics. It has not been fully investigated whether or not the correlation of the fore-optics temperature with NICMOS focus changes is an additional focus change, or only reflects the OTA focus change.

Another source of temporal variation for the PSF is the “wiggling” of the cold masks on orbital timescales. This causes asymmetries in the PSFs and residuals in PSF subtracted images.

The HST breathing and the cold mask “wiggling” produce variations of 5% to 10% on the FWHM of the NIC2 PSFs on the typical timescale of one orbit.²

1. NICMOS Instrument Science Report, NICMOS ISR-98-015

2. NICMOS Instrument Science Report, NICMOS ISR-98-018

Cosmic Rays

As with CCDs, cosmic ray hits will produce unwanted signal in the output images, but hot pixels are not expected to develop from such hits. The NICMOS arrays have been subjected to radiation doses much higher than expected in their entire lifetime in accelerator tests without sustaining any long-term damage or measurable depreciation in DQE. Hence, cosmic rays should have little impact on the long-term array performance in orbit.

On-orbit measurement of the distribution of cosmic rays shows 1.2 to 1.6 events/second/Camera for 5σ events. With a typical hit generating a 5σ event in ~ 2 pixels, this corresponds to 2 to 3 pixels/second/Camera. For a 2000 second integration, about 10% of the pixels in the detector will show cosmic ray events.

Therefore, the frequency of cosmic ray hits is large enough that we recommend the use of MULTIACCUM for all exposures longer than ~ 10 minutes, in order to filter out cosmic rays. MULTIACCUM provides a series of intermediate non-destructive reads as well as the final image (see Chapter 9). These intermediate reads can be used to identify cosmic ray hits, analogous to the use of CRSPLITS in WFPC2 or STIS observations. The calibration pipeline, described in Chapter 12, can identify and remove cosmic ray hits from MULTIACCUM observations.

See below for a more detailed discussion of persistence from massive cosmic ray hits during, e.g., passages in the South Atlantic Anomaly.

Photon and Cosmic Ray Persistence

HgCdTe detector arrays like those in NICMOS are subject to image persistence. When pixels collect a large amount of charge, they will tend to “glow” for some time after the end of the exposure.



Overexposure of the NICMOS detectors will not cause permanent harm and therefore NICMOS does not have bright object limitations.

The persistent signal is an excess dark current and decays exponentially with a time scale of about 160 ± 60 seconds (different pixels show different decay rates), but there is also a long, roughly linear tail to the decay such that persistence from very bright sources remains detectable as much as 30 to 40 minutes after the initial exposure. Subsequent exposures can therefore show residual images. With NICMOS, this can happen under a number of circumstances. Exposures of bright astronomical targets can

leave afterimages which appear in subsequent images taken within the same orbit. If you are observing bright objects you should be aware of this potential problem: dithered exposures may contain “ghosts” of bright stars from previous images. It appears that all sources of illumination probably leave persistent afterimages, but under typical conditions they are most noticeable for sources which have collected 20000 or more ADU during the previous exposure. There is little that can be done to avoid this. If observations are well dithered, then the persistent afterimages can usually be recognized and masked during data processing when combining the images to form a mosaic. This, however, is not done by the standard calibration pipeline.

More insidiously, during regular passages of HST through the South Atlantic Anomaly, the arrays are bombarded with cosmic rays, which deposit a large signal in nearly every pixel on the array. The persistent signal from these cosmic rays may then be present as a residual pattern during exposures taken after the SAA passage. This appears as a “mottled,” “blotchy” or “streaky” pattern of “noise” (really signal) across the images, something like a large number of faint, unremoved cosmic rays. These persistent features cannot be removed by the MULTIACCUM cosmic ray processing done by the standard pipeline because they are not transient. Rather, they are a kind of signal, like a slowly decaying, highly structured dark current.

Cosmic ray persistence adds non-Gaussian, spatially correlated noise to images, and can significantly degrade the quality of NICMOS data, especially for exposures taken less than 30 minutes after an SAA passage. Count rates from moderately bad cosmic ray persistence can be of order 0.05 ADU/second, with large pixel-to-pixel variations reflecting the spatial structure of the signal. The effective background noise level of an image can be increased by as much as a factor of three in the worst cases, although 10% to 100% are more typical. This “noise” is primarily due to the spatially mottled structure in the persistence, not the added Poisson noise of the persistence signal itself. Because HST passes through the SAA many times a day, a large fraction of NICMOS images are affected by cosmic ray persistence to one degree or another. Observations of bright objects are hardly affected, since the persistent signal is usually quite faint. Similarly, short exposures are not likely to be badly affected because the count rate from persistence is low and may not exceed the detector readout noise. But deep imaging observations of faint targets can be seriously degraded. The NICMOS ISR-98-001 (Najita *et al.* 1998) presents a detailed discussion of this phenomenon and its effects on imaging observations.

There is no true cure for cosmic ray persistence, but STScI is presently exploring options to minimize the impact of cosmic ray persistence in future observing cycles with NICMOS. Short dark exposures taken immediately after an SAA passage, when the persistent signal is strongest,

can, in principle, be used to create a map of the persistence which can be scaled and subtracted from subsequent science images taken later in the orbit. This method, while not perfect, can greatly reduce the impact of cosmic ray persistence. In addition, observers can plan observations to further minimize the impact of cosmic ray persistence, should it occur. Taking images with as many independent dither positions as possible is one good strategy (which can help in many ways with NICMOS imaging). Without dithers, the persistent pattern will stay fixed relative to the astronomical targets (although its intensity will decay), and co-adding successive exposures will just reinforce the contamination. Dithered images will move the targets relative to the persistence so that it adds incoherently when the data are summed. With well dithered data (at least three positions), one can also take advantage of the “drizzling” procedure and associated software in the STSDAS “dither” package to identify and mask the worst effects of persistence (as described, e.g., in the “Drizzling Cookbook,” Gonzaga *et al.* 1998, STScI ISR WFPC2 98-04). The HST Data Handbook reports more details on how to best handle images affected by cosmic ray persistence.

The Infrared Background

From the ground, the infrared background is affected by telluric absorption and emission which limits the depth of astronomical imaging. As is well known, between 1 and 2.5 μm there are a number of deep molecular absorption bands in the atmosphere (top panel of Figure 4.14), and the bandpasses of the conventional near-IR bands of JHK were designed to sit in the gaps between these opaque regions (middle panel of Figure 4.14). Unfortunately, outside the absorption features there is also considerable background emission in both lines and continuum. Most of the background between 1 and 2 μm comes from OH and O₂ emission produced in a layer of the atmosphere at an altitude ~ 87 km (bottom panel of Figure 4.14).

The location of HST above the atmosphere removes these terrestrial effects from the background. Now, the dominant sources of background radiation will be the zodiacal light at short wavelengths and the thermal background emission from the telescope at long wavelengths. The sum of these two components will be a minimum at 1.6 microns (roughly the H band). All three NICMOS cameras carry broad-band filters which are centered on this wavelength.

At wavelengths shorter than 1.6 μm , NICMOS reaches the natural background provided by the scattering of sunlight from zodiacal dust, which is, of course, strongly dependent on the ecliptic latitude and longitude (see Table 4.5).

Observations by the COBE satellite have implied that at positions 45° out of the ecliptic the zodiacal background can be approximated as:

$$5.0 \times 10^8 / \lambda^{1.69} + 6 \times 10^{-8} B_\lambda(\lambda, T) \text{ photons cm}^{-2} \mu\text{m}^{-1} \text{ steradian}^{-1}$$

Where λ is the wavelength in μm and B_λ is the blackbody function for the zodiacal dust temperature T (roughly 265 K).

Figure 4.15: Atmospheric Absorption and Emission Line Spectrum in NICMOS Operational Range.

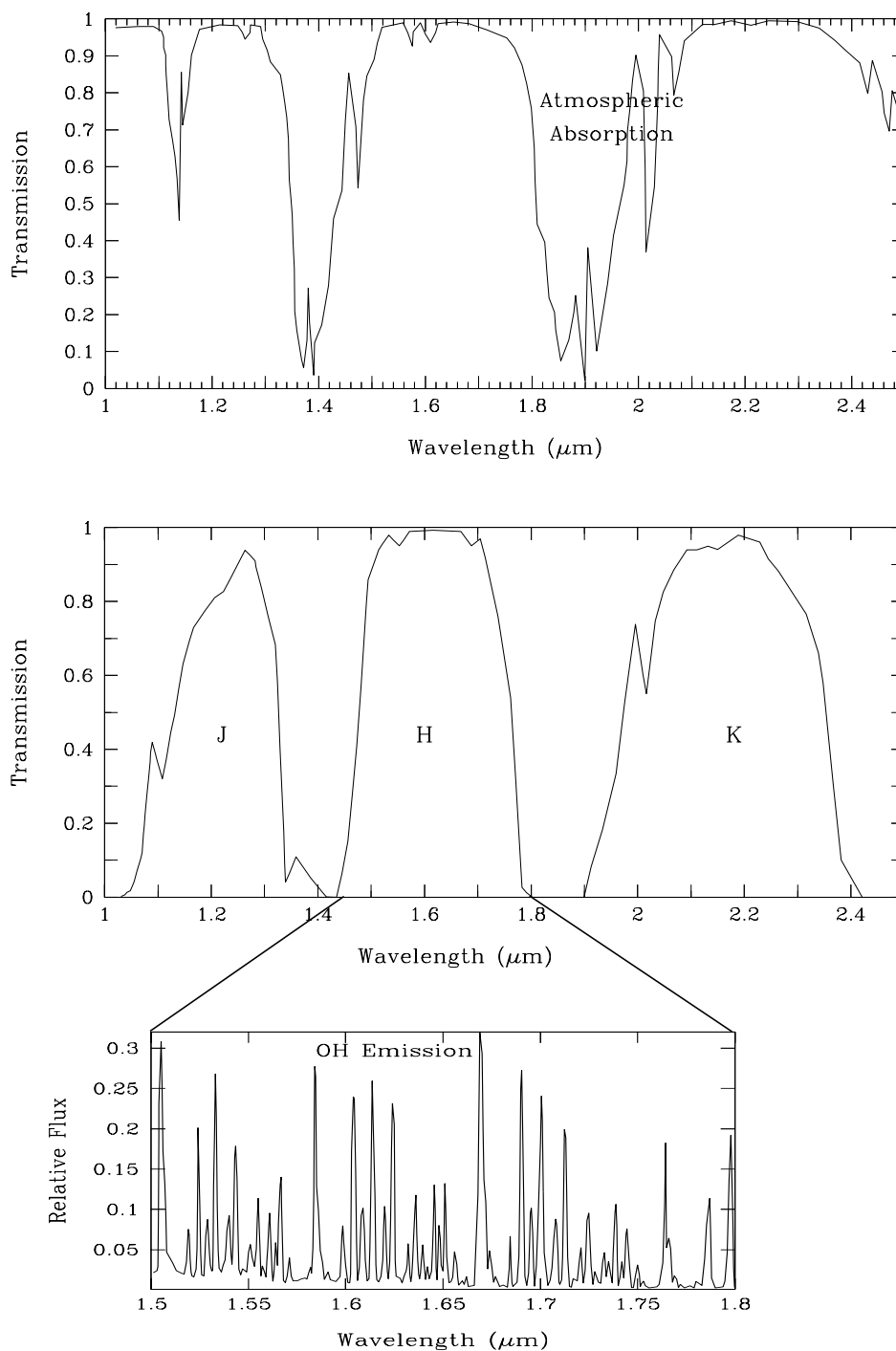


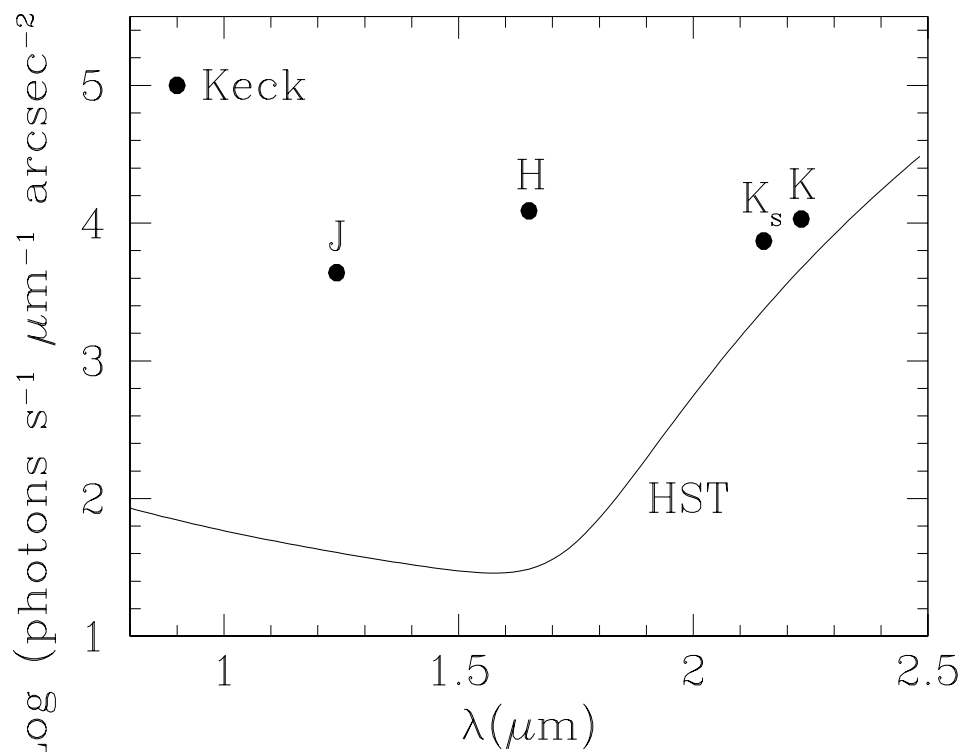
Table 4.7: Sky Brightness (V mag arcsec⁻²) as a Function of Heliocentric Ecliptic Latitude and Longitude. “SA” denotes that the target is unobservable due to solar avoidance.

Heliocentric Ecliptic Longitude	Ecliptic Latitude						
	0°	15°	30°	45°	60°	75°	90°
180°	22.1	22.4	22.7	23.0	23.2	23.4	23.3
165°	22.3	22.5	22.8	23.0	23.2	23.4	23.3
150°	22.4	22.6	22.9	23.1	23.3	23.4	23.3
135°	22.4	22.6	22.9	23.2	23.3	23.4	23.3
120°	22.4	22.6	22.9	23.2	23.3	23.3	23.3
105°	22.2	22.5	22.9	23.1	23.3	23.3	23.3
90°	22.0	22.3	22.7	23.0	23.2	23.3	23.3
75°	21.7	22.2	22.6	22.9	23.1	23.2	23.3
60°	21.3	21.9	22.4	22.7	23.0	23.2	23.3
45°	SA	SA	22.1	22.5	22.9	23.1	23.3
30°	SA	SA	SA	22.3	22.7	23.1	23.3
15°	SA	SA	SA	SA	22.6	23.0	23.3
0°	SA	SA	SA	SA	22.6	23.0	23.3

At wavelengths longer than 1.6 microns the HST thermal emission dominates the background seen by NICMOS. The thermal emission from the HST is composed of the contributions of the telescope’s primary and secondary mirrors and of the NICMOS fore-optics. The emission of the HST primary and secondary mirrors can be approximated as a blackbody with effective temperature of ~290 K. The emissivity of each mirror is about 5%. The NICMOS fore-optics are approximated by a blackbody with temperature ~270 K.

Figure 4.15 shows the cumulative HST background as a function of wavelength. This background has been calculated assuming a zodiacal light contribution consistent with the mean observed by COBE for an ecliptic latitude of 45°, and also includes thermal emission by the HST primary and secondary mirrors, the NICMOS optics, and the transmission of all the NICMOS fore-optics. It does not include the transmission of any filter, nor the response of the detectors. For comparison, we report in the same figure the J, H, K_s and K band background as observed from the Keck telescope, averaged over one year.

Figure 4.16: HST Background as seen by NICMOS. For comparison, the broad-band infrared background seen by the Keck telescope is shown.



Monitoring of the changes in the thermal background as a function of time, telescope's attitude and slews across the sky has shown that the background is stable to better than 5% on orbital timescales and to about 8% (peak-to-peak) over timescales of several months. In addition, the thermal background is uniform across each detector. The lack of significant variations within orbits removes the necessity for rapid dithering or chopping when observing in wavebands affected by thermal background (i.e., longward of $\sim 1.7 \mu\text{m}$).



When using NICMOS filters with central wavelengths longer than $\sim 1.7 \mu\text{m}$, observers should obtain background measurements as well (through either dithering or chopping). However, given the stability of the HST thermal background, no more than one such measurement per orbit is required.

Table 4.6 lists the measured background for a representative set of NIC2 filters. The Exposure Time Calculator tool on the STScI NICMOS WWW page also produces background count rates for any filter/camera combination.

Table 4.8: Background count rates for selected filters in NIC2

Filter	Background (e-/s/pix)
F110W	0.15
F160W	0.12
F180M	0.051
F187W	0.40
F190N	0.034
F207M	2.5
F215N	0.60
F222M	9.3
F237M	36

For pointings very close to the Earth, the zodiacal background may be exceeded by the earthshine. The brightness of the earthshine falls very rapidly with increasing angle from the Earth's limb, and for most observations only a few minutes at the beginning and end of the target visibility period will be significantly affected. The major exception to this behavior is a target in the continuous viewing zone (CVZ). Such a target will always be rather close to the Earth's limb, and so will always see an elevated background (at the shorter wavelengths where zodiacal emission would ordinarily dominate). For targets faint enough that the background level is expected to be much brighter than the target, the observer is recommended to specify the `LOW-SKY` option. This will increase the minimum allowed Earth avoidance angle, requiring scheduling during a time for which the zodiacal background is no greater than 30% above the minimum achievable level, at the cost of a slight decrease of the available observing (visibility) time during each orbit. Note that this restriction is only helpful when observations are background limited.

Conversion Between Fluxes and Magnitudes

Throughout the NICMOS documentation we will mostly use flux units of Janskys (Jy). A detailed discussion of the conversion between various units and Janskys is given in Appendix 2. Here we summarize the central wavelengths and zero-point fluxes for the more commonly encountered

photometric bands in Table 4.7, using the most commonly encountered photometric systems, the CIT and the UKIRT systems.

Table 4.9: Effective Wavelengths and Zero-points for Photometric Bands

Band	$\lambda[\mu\text{m}]$	$F_o[\text{Jy}](\text{CIT})$	$F_o[\text{Jy}](\text{UKIRT})$
V	0.56	3540	3540
R	0.70	2870	-
I	0.90	2250	-
J	1.25	1670	1600
H	1.65	980	1020
K	2.2	620	657
L	3.4	280	290
L'	3.74	-	252
M	4.8	150	163
N	10.1	37	39.8
Q	20.0	10	10.4

Coronagraphy, Polarimetry and Grism Spectroscopy

In This Chapter...

Coronagraphy / 75

Polarimetry / 86

Grism Spectroscopy / 93

This chapter provides information on three specialized uses of NICMOS, namely, coronagraphy, polarimetry, and grism spectroscopy.

Coronagraphy

NICMOS Camera 2 (NIC2) has a coronagraphic observing mode. A hole was bored through the Camera 2 FDA mirror. This hole, combined with a cold mask at the pupil (Lyot stop), provides coronagraphic imaging capability. Internal cold baffling was designed to screen out residual thermal radiation from the edges of the HST primary and secondary mirrors and the secondary mirror support structures (pads, spider, and mounts).

An image of a star is formed on the FDA mirror and is re-imaged on the detector. The image of a star in the hole will have diffraction spikes. The hole traps the light from the core of the PSF, reducing the diffracted energy

outside of the hole by reducing the high frequency components in the PSF. The light scattering downstream of the FDA is greatly reduced. The hole edge acts as a new diffraction aperture, and the residual roughness about the hole from the drilling process (Figure 5.1) creates a complex image of the star in the hole. At a radius of 0.3 arcsec, in an idealized PSF, a natural break occurs in the encircled energy profile at $1.6\ \mu\text{m}$ with 93% of the energy in the PSF enclosed. Beyond this radius, the encircled energy profile flattens out toward larger radii.

Figure 5.1: Image of the coronagraphic hole in NIC2. The rough edges created by the final drilling process are evident in this figure.

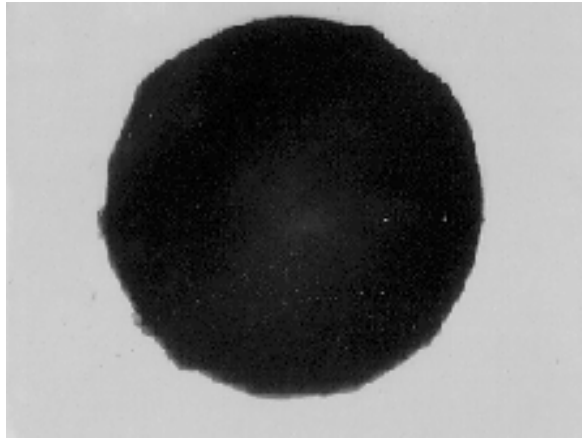
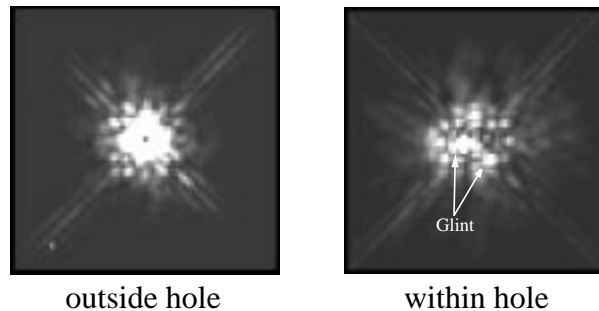


Figure 5.2: Star images. Star imaged outside the hole (left) and within the coronagraphic hole (right). Images were obtained with the F160W filter. Two of the three bright glint regions are marked with arrows. The other is on top of the hole.



The light pattern about the coronagraphic hole is not symmetric due in part to the coronagraphic optics and to the Optical Telescope Assembly (OTA) input PSF. The spectral reflections from the roughness about the hole, and imaged in Camera 2, will vary depending upon the location of the target in the hole. There is one azimuth region where the residual light pattern, historically called *glint*, is brightest. Figure 5.2 presents enlarged images of the same target outside and positioned within the coronagraphic hole displayed to the same stretch. The structure of the scattered light

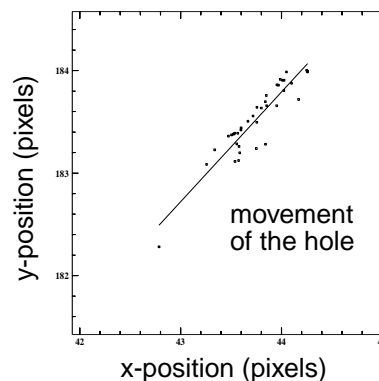
pattern about the hole is different from the NICMOS stellar PSF pattern. The presence of *glint* brings the useful coronagraphic radius at the detector to ~ 0.4 arcsec.

The FDA mirror and the Camera 2 f/45 optics image planes are not exactly confocal. For nominal Camera 2 imaging, the PAM is positioned to achieve optimal image quality at the detector. For coronagraphic imaging, the PAM is adjusted slightly for optimal coronagraphic performance. The PAM is moved to produce a focused star image at the position of the coronagraphic hole. This results in a very slight degradation of the image quality at the detector. The PAM movement is automatic whenever `OPMODE=ACQ` or `APERTURE=NIC2-CORON` are specified on the Phase II exposure line. If a series of exposures need the CORON focus position, only one move is performed.

The tilt of the PAM is changed to compensate for translation from the nominal to coronagraphic setting, and to remove off-axis aberrations.

The NICMOS dewar anomaly caused the coronagraphic hole to migrate to different locations on the detector, during Cycle 7 and 7N. The position of the hole on the detector has been observed to move as much as ~ 0.25 pixel in three orbits. During the interval April-December 1998, the hole moved about 1 pixel. The movement of the hole is not linear. Rather, the hole “jitters” back and forth along an X-Y diagonal by as much as ± 0.5 pixel. The movement of the hole is presented in Figure 5.3.

Figure 5.3: Coronagraphic hole location (detector coordinates). The movement in the position of the hole over time is represented by the solid line.



The movement of the hole may cause a problem for coronagraphic observations. Repeat positioning of targets in the coronagraphic hole to a fraction of a pixel is necessary for PSF subtraction. For this reason, the acquisition software is set up to locate the hole position for every acquisition of an astronomical target.

Coronagraphic Acquisitions

Coronagraphic imaging requires an acquisition sequence at the beginning of the observation to center the target in the coronagraphic hole. The size of the coronagraphic hole is smaller than typical HST blind-pointing errors. The procedure for a coronagraphic acquisition is to first image the target in Camera 2 using blind-pointing and then use either an onboard (using the NIC2-ACQ aperture), reuse target offset, or interactive acquisition to acquire the target. A telescope slew is calculated and commanded to move the image of the target over the position of the hole.

The target is positioned on the NIC2-CORON aperture, which has the aperture fiducial point at the image position of the coronagraphic hole on the detector. The science exposures are then specified using any of the NICMOS observing modes and any of the NIC2 filters. The science observations following the ACQ will specify the `APERTURE = NIC2-CORON`.

Onboard Acquisition (Mode-2 Acquisition)

The Mode-2 Acquisition for coronagraphy includes two steps: first, the position of the coronagraphic hole is located; second, the target is acquired and placed under the hole.

The location of the coronagraphic hole is determined from pointed flat field observations. Two short F160W filter exposures (7.514 seconds each) with calibration Lamp 1 on (flat field) and two identical exposures with the lamp off (background) are obtained before the acquisition images. The background images are needed because NICMOS does not have a shutter and the flat field images are also imaging the sky. The flight software (FSW) combines the two background and two flat field images by performing a pixel-by-pixel minimum to eliminate cosmic rays (using the lower valued pixel of the two frames). The processed background is subtracted from the processed lamp flat. A small 32 x 32 pixel subarray containing the hole is extracted and a small checkbox (7x7 pixels) is used to find the location with the minimum total counts. Once the minimum checkbox sum is located, a weighted moment algorithm is applied to determine the flux-weighted centroid within the checkbox. The location of the hole is temporarily stored onboard, but it is not saved in the images sent to the ground.

The target is positioned within a square area on the detector, a 128 x 128 pixel aperture (center at 157,128) of size 9.6 x 9.6 arcseconds. Two images of equal exposure are obtained. (The Phase II exposure time is not split.) The two images are pixel-by-pixel minimized to eliminate cosmic ray hits and a constant value (data negative limit) is added to the processed image. The brightest point source in the acquisition aperture is determined by summing the counts in a checkbox of size 3x3 detector pixels. The algorithm passes the checkbox over the entire acquisition aperture. The

brightest checkbox is selected and the location of the target is determined by centroiding the X,Y center of the 3x3 checkbox.

The observer needs only to specify a NICMOS onboard Acquisition (ACQ) to acquire the target. The software schedules the background and flat field observations first, followed by the observations of the target. The exposure times for the pointed background and flat field observations are 7.514 seconds.

Note that the telescope is not slewed to position the target out of the FOV for the background and flat field observations. If the target saturates the NIC2 detector in 7.514 seconds with the F160W filter, a residual image will be created that will contaminate the onboard target ACQ observation. This persistence image may introduce some error into the centroiding algorithm.

Very bright targets will cause saturation, leading to poor results in the centroid solution, and in the subsequent placement behind the occulting spot. To avoid this, a narrow band filter may have to be used to reduce the target flux. Targets brighter than $H \sim 3.6$ will saturate the central pixel of the PSF when observed with the F187N filter (narrowest Camera 2 filter) using the shortest ACQ integration time of 0.228 seconds. Since the NICMOS filters are essentially at a pupil plane, there will not be an image shift introduced by using a different filter for the acquisition than for the science observations. Shading will be a problem for centroiding when the target lands near the shading break.

The location of the target and the slew are saved, and sent to the ground together with the science observation.

The NICMOS ACQ exposure times, T_{ACQ} , are quantized and with a minimum exposure time of 0.228 seconds. For an ACQ exposure with $T_{ACQ} = 0.356$ SEC, the overhead to complete the hole finding and location of the target is about 3 minutes which includes the telescope slew to move the hole over the target. A full description of the overheads for Mode-2 Acquisitions is given in Chapter 10.



For T_{ACQ} exposures longer than ~5 minutes the probability of cosmic ray hits occurring in the same pixel in each of the two acquisition images is sufficiently high that observers must instead use an early acquisition to avoid their observations failing due to a false center determination. Early acquisitions are described in the next section. In practice, this should not be a severe restriction as in the F160W filter one will reach a signal-to-noise of 50 at $H=17$ in only 2-3 minutes.

The flight software processed images are not saved, but the two background, two flat field, and two acquisition ACCUM images are sent to the ground. These images, which are executed in a single target acquisition observation, have been packaged into one data set with the same rootname

but with different extensions. A full description of the extensions is given in the HST Data Handbook.

Reuse Target Offset (RTO) and Interactive Acquisitions

Bright targets will saturate the NICMOS Camera 2 detector resulting in possible failure of the onboard software (Mode-2 Acquisition) to successfully acquire and position the target into the coronagraphic hole. Any target that will saturate the detector in the shortest possible Mode-2 ACQ exposure time, 0.228 seconds, should be considered a bright target. A variation of the Reuse Target Offset (RTO) capability can be used to acquire and position a bright target into the coronagraphic hole. However, the onboard acquisition software may not successfully acquire the desired target in a crowded field. For this case, an interactive acquisition (INT-ACQ) maybe required to successfully acquire the target.

The following discussion describes the necessary steps for a Reuse Target Offset (RTO) acquisition to acquire a bright target and position the target into the coronagraphic hole. These steps can also be used for an interactive acquisition of a target in a crowded field. It is recommended for RTO acquisition that two orbits be used when observing a bright target except possibly for an INT-ACQ. The first orbit is used for the acquisition and the second orbit for the coronagraphic observations.

Images of the target and coronagraphic hole are obtained a few orbits in advance of the coronagraphic observations, and sent to the ground for analysis (RT ANALYSIS). The target exposures should be offset from the NIC2-CORON aperture fiducial point to avoid having the target fall in the hole.

The observer needs to specify at least two background, two flat field, and two on-target exposures in the Phase II template. The background and flat field observations should be offset by 18-25 arcseconds from the target position to avoid the diffraction spike from the image of an overexposed target crossing the coronagraphic hole and introducing errors in the measured position of the coronagraphic hole. The recommended pairs of images are needed to remove cosmic ray hits.¹

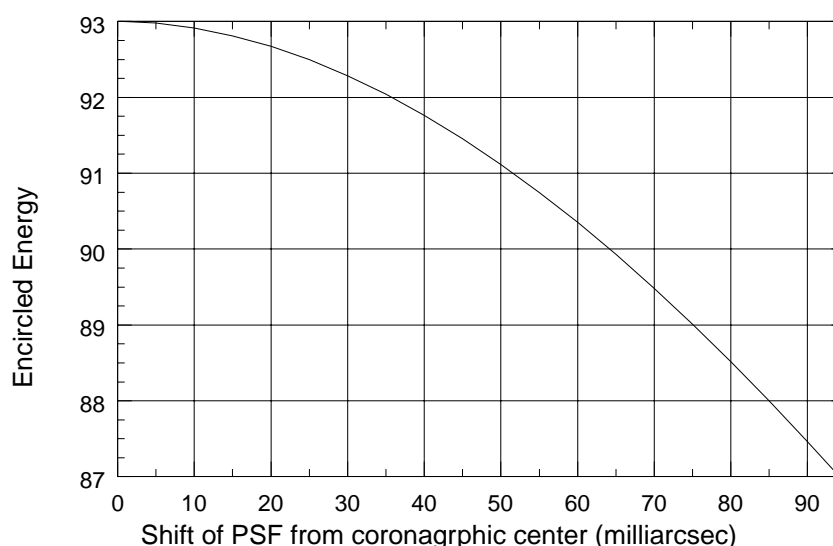
OPUS staff will assist the PI in identifying the target, centroiding, and determining offsets. OPUS staff will then provide the offsets to the Mission Operations and Systems Engineering Support (MOSES) office personnel, Goddard Space Flight Center (GSFC) for uplink to the spacecraft in advance of the coronagraphic observations. The ultimate responsibility for determining the offsets will be the PI (or the PI's representative), who must be present at STScI at the time of the target/hole location observations.

1. NICMOS Instrument Science Report, NICMOS-ISR-031.

PSF Centering

Both the total encircled energy rejection (from the occulted core of the PSF) and the local contrast ratio obtainable in a coronagraphic image depend on the accuracy of the target centering on the occulting spot. The goal is to center the PSF of the occulted source to a precision of a 1/6 pixel at a position $x=-0.75$, $y=-0.25$ pixels from the center of the hole, “the Sweet Spot”. The decrease in the fractional encircled energy due to imprecise centering of the core of an idealized PSF in the occulting spot is 0.3 percent for a 1/4 pixel offset, and 4.4 percent for a 1 pixel (75 milliarcseconds) offset at 1.6 microns. The predicted fractional decrease in the encircled energy relative to that for a perfectly centered PSF is plotted against the shift of the center of the PSF from the center of the hole in Figure 5.4. In the figure, each Camera 2 pixel = 75 milliarcseconds.

Figure 5.4: Contrast Decrease Due to PSF De-centering



In addition, a small error in target centering will create an asymmetric displacement of the PSF zonal structures both in and out of the occulting spot, leading to position dependent changes in the local image contrast ratios.

Temporal Variations of the PSF

Temporal variations of the NICMOS PSF due to HST breathing and “wiggling” of the misaligned cold mask in NIC2 are discussed in Chapter 4. Of relevance to coronagraphic observers is that the effects of temporal variations for PSF subtraction can be minimized by obtaining observations of the same PSF in back-to-back orbits or twice in the same orbit, with a

roll of the spacecraft between the two observations. The success of this technique is due to the orbital timescale of the PSF temporal variations.



During Cycles 7 and 7N, the NICMOS IDT reported exceptional results for PSF subtraction when the same target was observed twice in the same orbit with a roll of the spacecraft between observations. It has yet to be demonstrated that this result can be achieved by observing in back-to-back orbits (NICMOS ISR-98-009). It is not known at this time if future coronagraphic observers will be allowed to observe this way.

FGS Guiding

Two guide star (GS) guiding is strongly recommended when performing coronagraphic observations. For best coronagraphic results, the target should be centered to better than 1/6 pixel.

Coronagraphic observations executed in back-to-back orbits should be scheduled with the same guide star pair, except possibly if a roll of the HST is performed between orbits. This is also critical for Reuse Target Offset (RTO) Acquisitions, which require the same guide stars be used for all observations. Switching guide stars between the acquisition and science observations will force the respective target to either be positioned away from the coronagraphic hole or on the edge of the hole.

The use of a single guide star is discouraged for coronagraphic observations. The drift about a single guide star is small, but will yield intense residuals for PSF subtraction. If we represent the linear motion due to gyro drift around a star as $X = D \sin(at)$, where X equals the linear motion, D the distance from the guide star to the aperture, a the angular gyro drift rate, and t the time since the last FHST update, then for $D = 20$ arcmin (worst case) = 1200 arcsec and $a = 0.001$ arcsec/sec, for one visibility period $t = 50$ min = 3000 sec we get $X = 0.0175$ arcsec or less than 1/4 pixel in Camera 2. For two orbits $t = 146$ min = 8760 sec, $X = 0.051$ arcsec or a little over 2/3 pixel in Camera 2.



HST SNAP observations are normally scheduled with single guide star guiding. It is not known at this time whether or not NICMOS coronagraphic SNAP observations will become the exception to the rule and be scheduled with two guide star guiding.

For RTO acquisitions, the maximum default slew is 10 arcseconds. This is set by the coordinate uncertainties as specified in the Phase II template. If a slew larger than the default 10 arcseconds is scheduled, it has to be

approved by the STScI Commanding Group and GSFC notified that a slew of this size or larger will not force the guide stars out of the FGS field of view (a.k.a. pickle). Increasing the target coordinate uncertainties will increase the slew limit. STScI Commanding will use the coordinate uncertainties to determine the size of the slew request timing. Guide star selection is also affected. If the requested amount of guide star movement will force the guide star out of the pickle, the guide star selection software will not select that star. This may result in single star guiding. One solution to this problem is to decrease the distance between the star and the hole and correspondingly decrease the target uncertainties.

Cosmic Ray Persistence

Coronagraphic observations scheduled over more than one visibility period will most probably be impacted by an SAA passage and possibly be affected by charged particle induced persistence (see Chapter 4 for a discussion on the cosmic ray persistence). To avoid breaking exposures across visibility periods, coronagraphic observations should be scheduled using the exposure level Special Requirement “SEQ <EXP. LIST> NON-INT”, which forces all observations to be within the same visibility window. That is, without interruptions such as Earth occultations or SAA passages.

Contemporary Flat Fields

One of the coronagraphic calibration problems is “proper” calibration of images near the edge of the hole due to motion of the hole itself. The problem arises from the fact that the OPUS flat field reference files are not contemporary with the coronagraphic images. During Cycle 7 and 7N, the coronagraphic hole moved about 0.1 to 0.2 pixels per month. In addition, there is a 2nd short term component to the movement along a pixel diagonal (back-and-forth) and imposed upon this motion a random jitter 3rd component of a few tenths of a pixel.

The light pattern about the coronagraphic hole is not symmetric due to *glint* (see Figure 5.2), and will vary depending upon the location of the target in the hole. Calibrating with a contemporary flat, which has the coronagraphic hole pattern at the correct location, restores the flux level and re-establishes the light pattern about the hole at the time of the observation. For distances greater than ~ 0.7 arcseconds from the hole (diameter ~ 17 pixels), the standard, high S/N flat is the best reference file to use for calibration.

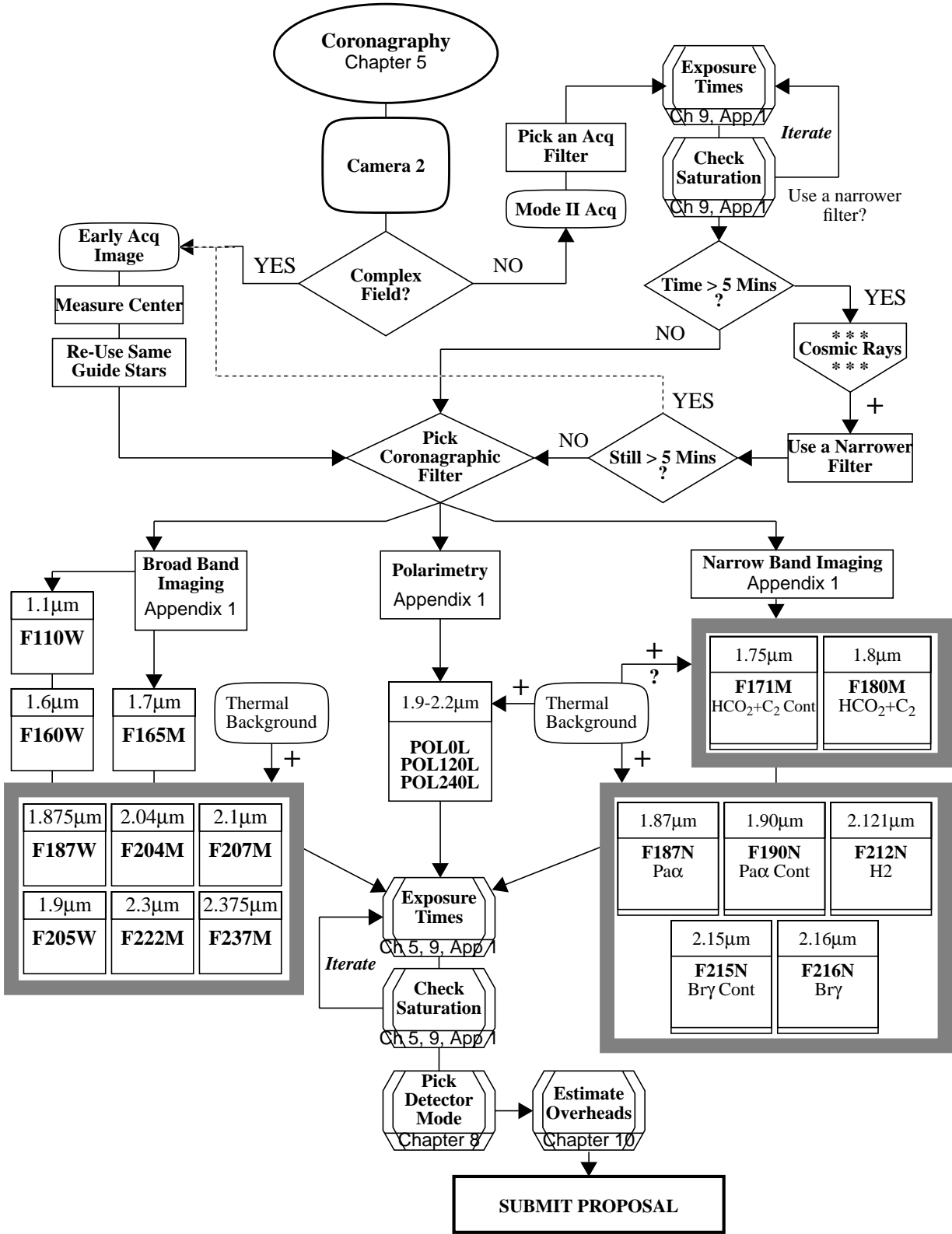
“Proper” calibration of coronagraphic images is a problem that can be resolved with lamp and background observations obtained close in time to the coronagraphic observations. These contemporary calibration

observations could be scheduled within the time allowed and would increase the scientific return of the science data. Calibration observations are normally obtained as part of the STScI calibration program and GOs are not usually allowed to request calibration data. However, the coronagraphic programs are allowed to obtain lamp and background observations to be used to locate the coronagraphic hole. It should be possible to include calibrations for specific filters to support the data reductions. For RTO Acquisitions, if there are no pressing scientific reasons to fill the remaining acquisition orbit with science observations, then it is recommended that lamp and background observations be obtained to support the coronagraphic science observations.

Coronagraphic Decision Chart

The decision chart presented in Figure 5.5 helps through the selection process to construct coronagraphic observations when using an onboard acquisition or an early acquisition image. The process for specifying RTO acquisitions of bright target is presented in NICMOS-ISR-031. The observer is advised to contact the STScI help desk, help@stsci.edu, for additional information.

Figure 5.5: Coronagraphic Decision Chart



Polarimetry

NICMOS contains optics which enable polarimetric imaging with high spatial resolution and high sensitivity to linearly polarized light from 0.8 to 2.1 microns. The filter wheels of NIC1 and NIC2 each contain three polarizing filters (sandwiched with band-pass filters) with unique polarizing efficiencies and position angle offsets. The design specified that the position angle of the primary axis of each polarizer (as projected onto the detector) be offset by 120° from its neighbor, and that the polarizers have identical efficiencies. While this clean concept was not strictly achieved in NICMOS, the reduction techniques described in the HST Data Handbook permit accurate polarimetry using both cameras over their full fields of view.

The spectral coverage is fixed for each camera, and the polarizers cannot be crossed with other optical elements. For NIC1 the polarizers cover the wavelength range 0.8 to 1.3 microns (short wavelength), and for NIC2 the coverage is 1.9 to 2.1 microns (long wavelength). Observations in all three polarizers will provide the mechanism for calculating the degree of polarization and position angle at each pixel. To properly reduce polarimetry data obtained with NICMOS, a new algorithm different from that needed for ideal polarizers has been developed². Combined with calibration measurements of polarized and unpolarized stars, this algorithm enables accurate imaging polarimetry to about $< \sim 1\%$ (in percentage polarization) over the entire field of view in both cameras.



In principle, polarimetry can be performed with the coronagraph, but scattered light emanating from the hole and decentering makes this extremely difficult.

NIC 1 and NIC2 Polarimetric Characteristics and Sensitivity

The three polarizers in NIC1 are called POL0S, POL120S and POL240S, and in NIC2 are called POL0L, POL120L, and POL240L, where the suffix 0, 120 and 240 indicates the design specifications for the position angle of the polarizer's primary axis (in degrees). A summary of

2. Hines, D.C., Schmidt, G.D., & Lytle, D., The Polarimetric Capabilities of NICMOS, in The 1997 HST Calibration Workshop with a New Generation of Instruments, ed. Casertano et al, 1997

the characteristics of the NIC 1 and NIC2 polarizers are given in Table 5.1 below.

Table 5.1: Polarizer Characteristics

Camera	Central (μm)	Mean (μm)	Peak (μm)	FWHM (μm)	Range (μm)	Pixel fraction
NIC 1	1.0450	1.0384	1.0245	0.4750	0.8–1.3	0.048
NIC 2	1.9943	1.9946	1.9100	0.2025	1.9—2.1	0.33



Observations must be obtained at all three primary axis' angles (POL0, POL120*, and POL240*) to measure the three linear Stokes parameters I, Q and U, from which derive the polarization intensity, the degree of polarization and the position angle at each pixel.*

In each Camera the three polarizers were designed to be identical and to have the position angle of the primary axis of each polarizer offset by 120° from its neighbor. In practice, this was not completely achieved and:

1. Each polarizer in each camera has a unique polarizing efficiency.
2. The offsets between the position angles of the polarizers within each filter wheel differ from their nominal values of 120° .

Table 5.2 below lists for each polarizer the position angle of the primary axis and the filter efficiency (throughput of the filter only).

Table 5.2: Characteristics of the NIC1 and NIC2 polarizers

Filter	Position Angle	Throughput
POL0S	1.42	0.9717
POL120S	116.30	0.4771
POL240S	258.72	0.7682
POL0L	8.84	0.7313
POL120L	131.42	0.6288
POL240L	248.18	0.8738



In NIC1 the POL120S filter only has 48% transmission while the POL0S filter has 98%. Observers may wish to consider using POL0S at multiple spacecraft roll angles rather than POL120S.

The instrumental polarization caused by reflections off the mirrors in the NICMOS optical train is small (approximately less than 1%).

As with the imaging filters, sensitivity plots for the two sets of polarizers for both extended and point sources are shown in Appendix 1, which also contains throughput curves (convolved with the HST and NICMOS optics and the detector's response) for the polarizers. To work out how many integrations are needed to get the desired S/N, the observer can use the Exposure Time Calculator available on the WWW (see Chapter 1) or Chapter 9. To get the total exposure time required for a polarimetric observation the final answer must be multiplied by three to account for the fact that all three polarizers must be used to get a measurement.



The proposer should be aware that the Exposure Time Calculator computes the intensity based on the highest transmission of all the polarizers for each camera and an unpolarized signal. Therefore, any computations with less efficient transmissions must be taken into account.

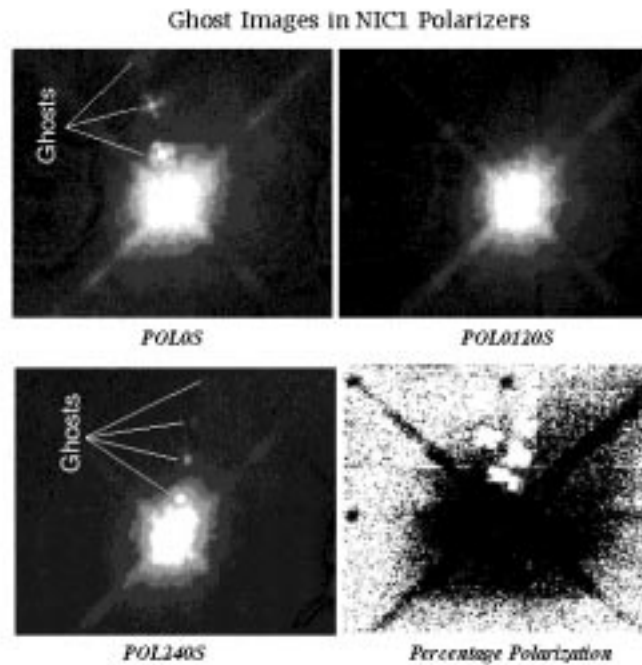
For the long wavelength polarizers in NIC 2, thermal background must be considered (see Chapter 4 for a description of the thermal background seen by NICMOS and Chapter 11 for related observing strategies).

For a polarized source, the intensity measured by the detector depends on the orientation of the spacecraft relative to the source in the sky. The range of intensities is given by the Exposure Time Calculator value multiplied by $(1 \pm p\epsilon_k)$, where p is the fractional polarization of the source and ϵ_k is the polarizer efficiency.

Ghosting

Multiple ghost images are present in data obtained through POL0S and POL240S in NIC1 in exposures of very bright targets. No such ghosting is apparent through POL120S or in any of the NIC2 polarizers. The location of ghosts in each polarizer appears constant on the detector relative to the position of the target (i.e. independent of telescope or object orientation). The ghosts are offset between POL0S and POL240s, which produces a very highly polarized signal (100%) in percentage polarization. This allows them to be easily distinguished from real polarized signal. While all emission in the POL0S and POL240S frames will produce ghosts, experience with real data shows that the effect is most important for strong point sources.

Figure 5.5 shows an example of the ghosts in POL0S, POL240S, and the percentage of polarization. These ghosts will typically be seen as regions of 100% polarization (seen as white blobs)

Figure 5.6: Ghost Images in NIC1 Polarizers³

For NIC1, observers may want to consider an additional visit specifying a different ORIENT to recover information lost due to ghosts so that important structures in the object are not near the image ghosts in POL0S and POL240S.

Observing Strategy Considerations

Observers should always use a dither pattern to help alleviate residual image artifacts, cosmic rays, and image persistence, as well as to improve sampling. The best choice for the number and size of the dithers depends on the amount of time available and the goals of the project, but a minimum of four positions will allow optimal sampling and median filtering.

One strong recommendation is to execute a four position pattern in each polarizing filter with $N+1/2$ pixel offsets, where N 10-50 depending on the structure of the object and the field of view that the observer wants to maintain. $N=10$ alleviates most persistence problems from point sources, and the additional $1/2$ pixel ensures good sampling. The same observing

3. Refer to <http://ecf.hq.eso.org/nicmos/sardinia/node14.html#2206>, “Imaging Polarimetry with NICMOS” for more details

process should be applied to each polarizer observation (e.g. POL120L and POL240L). This strategy will result in a minimum of 12 images with which to construct the linear Stokes parameters (I , Q , U).⁴

Exposure times should be set such that the source does not drive the arrays into saturation, and only one exposure should be attempted per dither position because the long decay time for persistence. If more integration time is needed to achieve the desired S/N, the entire dither pattern for each polarizer should be repeated. For the best results, the observing sequence should be POL0*, POL120*, POL240*, then repeat POL0*, POL120*, POL240*, etc.



Observers are reminded that for polarimetry observations in NIC2 the thermal background must be considered. In this case, background images need to be obtained in all three polarizers

The raw polarimetric images obtained through each polarizer are routinely processed by the first stage of the pipeline like any other exposure, but may require recalibration using updated flats and darks.



For NICMOS polarimetry, MULTIACCUM mode (see Chapter 8) is the only exposure read-out mode recommended.

Limiting Factors

Limiting Polarization

Because the errors for percentage polarization follow a Rice distribution⁵, precise polarimetry requires measurements such that $p/\sigma_{p, meas} > 4$, where p is the percentage polarization and σ_p its standard deviation. Therefore, uncertainties 0.5-3% (per pixel) imply that objects should have minimum polarizations of at least 2-12% per pixel.

Binning the Stokes parameters before forming the percentage polarization p and the position angles reduces the uncertainties by $\sim 1/\sqrt{N}$, where N is the number of pixels in the bin. Uncertainties as low as 0.2% in NIC2 should be achievable with bright objects.

4. For more information on dithering, see Chapter 11

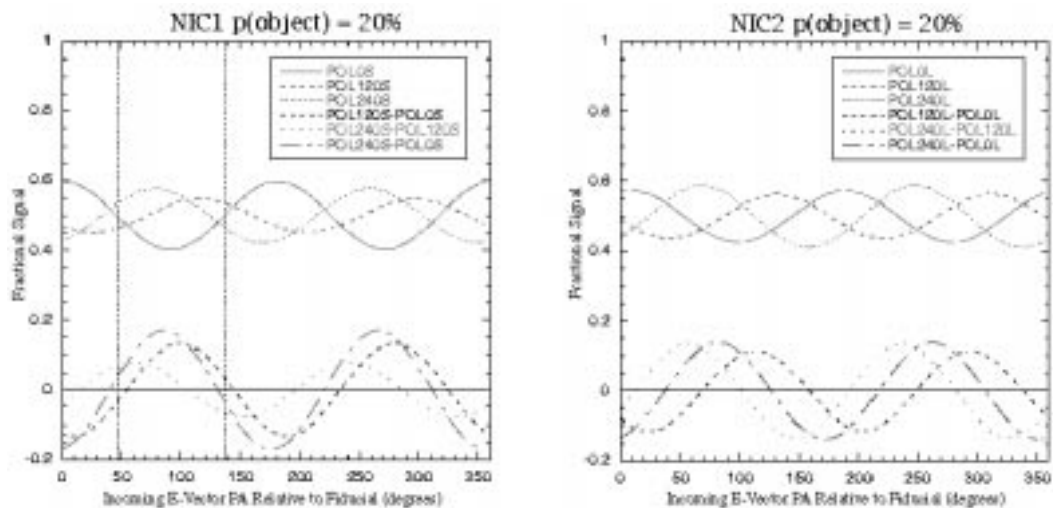
5. Refer to Simmons, Stewart, "Point and Interval Estimation of the True Unbiased Degree of Linear Polarization in the Presence of Low Signal-to-noise Ratios", A&A142, pp100-106, 1985

Position Angle of Incoming Polarization Relative to NICMOS Orientation

The non-optimum polarizer orientations and efficiencies cause the uncertainty in polarization to be a function of the position angle of the electric vector of the incoming light. For observations with low signal-to-noise ratios (per polarizer image), and targets with lower polarizations, the difference between the signals in the images from the three polarizers becomes dominated by (photon) noise rather than analyzed polarization signal. Therefore, observations that place important incoming electric vectors at approximately 45° and 135° in the NICMOS aperture reference frame should be avoided in NIC1. No such restriction is necessary for NIC2.

Figure 5.6 shows the fractional signal measured in each NICMOS polarizer as a function of incident electric position angle (PA) for 20% polarized light. The lower curves are the differences in fractional signal between images taken with successive polarizers. The vertical dashed lines in the left panel (NIC1) represent the position angles of the incoming electric vector where these differences are all small, and thus produce the largest uncertainties in the measured polarization.

Figure 5.7: Fractional signal measured in each NICMOS polarizer as a function of incident electric position angle.⁶

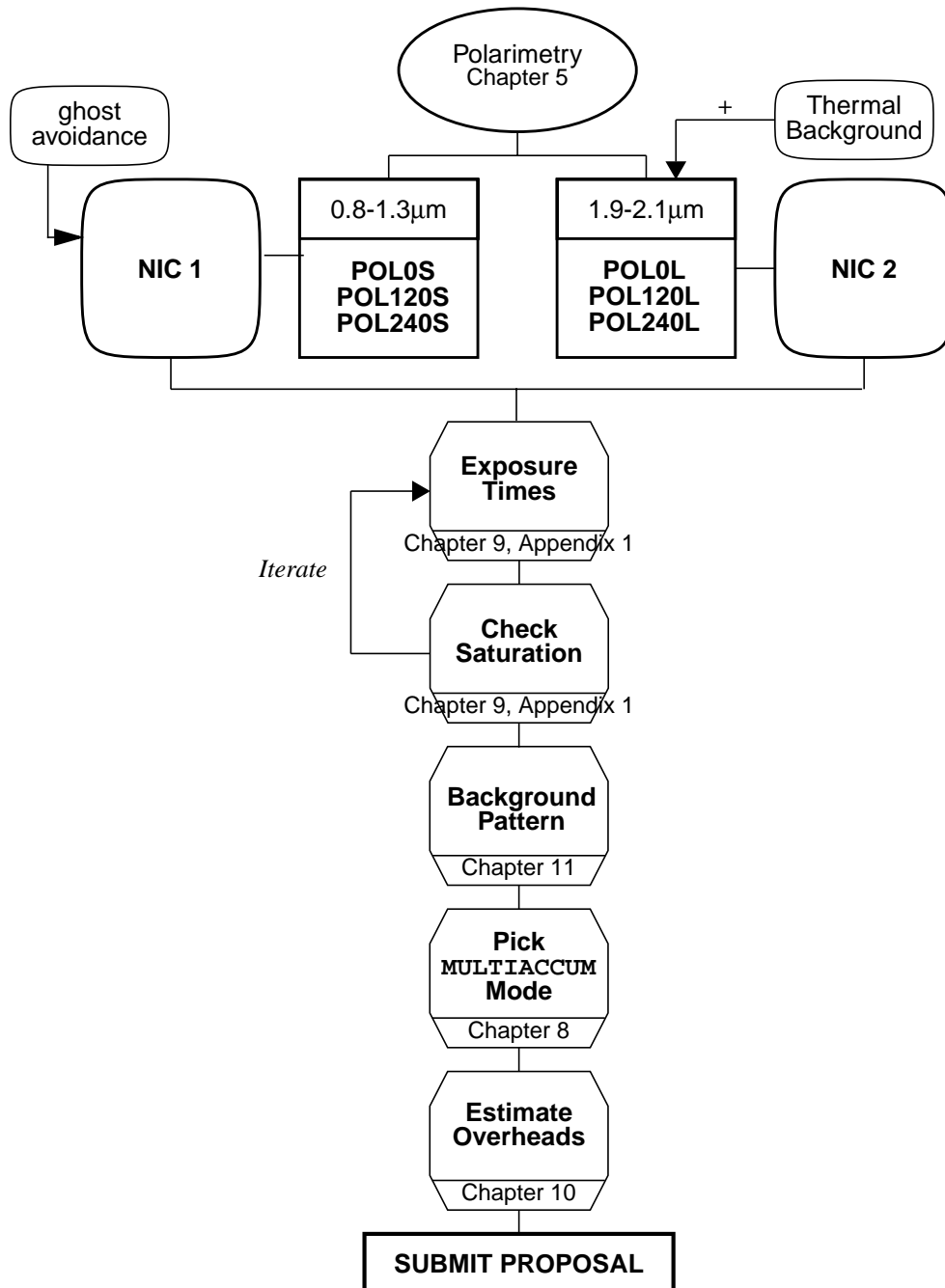


Polarimetry Decision Chart

The decision chart given in Figure 5.7 below helps through the selection process to construct a polarimetry observation.

6. Refer to <http://ecf.hq.eso.org/nicmos/sardinia/node14.html#2206>, "Imaging Polarimetry with NICMOS" for more details

Figure 5.8: Polarimetry Decision Chart



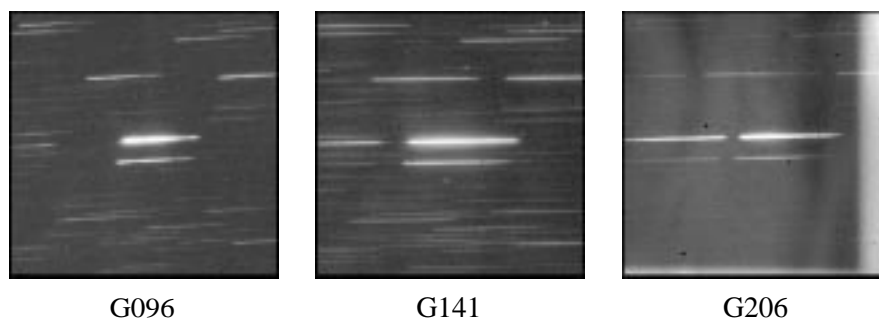
Grism Spectroscopy

NICMOS provides grism imaging spectroscopy in the spectral range between 0.8 and 2.5 μm with Camera 3.⁷ NICMOS is used in this mode of operation without any slit or aperture at the input focus, so all objects in the field of view display their spectra for true multi-object spectroscopy. The gratings reside in the NIC3 filter wheel, therefore the spatial resolution of the spectroscopy is that of this Camera. The filter wheel contains three gratings (G096, G141, G206), of infrared grade fused silica, which cover the entire NICMOS wavelength range with a spectral resolving power of ~ 200 per pixel.

A grism is a combination of a prism and grating arranged to keep light at a chosen central wavelength undeviated as it passes through the grism. Grisms are normally used to create spectra in a camera by inserting the grism into the normal camera beam. The grism then creates a dispersed spectrum centered on the location of the object in the camera field of view. Figure 5.8 shows an example of grism spectra of a point source using G096, G141, and G206. The target is the brightest source in the FOV, although many other sources yield useful spectra as well. The band along the bottom of the images, about ~ 15 -20 rows high, is due to shading by the FDA mask. The observed vignetting results from this mask. The resolution of a grism is proportional to the tangent of the wedge angle of the prism in much the same way as the resolution of gratings are proportional to the angle between the input and the normal to the grating.

The two shorter wavelength gratings exploit the low natural background of HST while the longest wavelength grism is subject to the thermal background emission from HST.

Figure 5.9: Grism slitless spectroscopy of a point source, using G096 (left), G141 (middle), and G206 (right).



7. NICMOS Instrument Science Report, NICMOS ISR-97-027

The basic parameters of the NICMOS grisms are given in Table 5.3.

Table 5.3: Grism Characteristics

Grism	Resolution per Pixel	Central Wavelength	Wedge Angle	Bandpass	Lines per mm
G096	200	0.964	5.219	0.8 - 1.2	45.0
G141	200	1.401	5.5889	1.1 - 1.9	30.769
G206	200	2.058	5.6944	1.4 - 2.5	21.05

Multi-Object Spectroscopy

Grism observations are carried out in a similar manner as other NICMOS imaging. A target is selected and imaged with one of the grisms. We encourage all grism observers to dither their observations in the direction perpendicular to the dispersion direction. Dithering parallel to the dispersion may result in loss of data off the edge of the detector. Dither spacing should be a non-integer number of pixels, e.g 2.1 arcsec (10 and a half pixels) and several positions should be observed. Dithering the target on the detector will minimize image anomalies such as grot affected pixels, cosmic ray hits, pixel sensitivities, and residual persistence images due to over exposures.

Although multi-object spectroscopic observations can stand alone with no supporting observations, we recommend pairing them with a direct image in NIC3, through an appropriate filter, at the same pointing. This provides the location of each object in the field and aids in the identification of their individual spectra. Because of this natural pairing it is anticipated that most spectroscopy observations will be at least a two image pattern, that is, direct and grism images at the first dither point, move to next dither position, direct and grism images at the second point, etc. The new pattern syntax (see Chapter 11) makes this possible.

The direction of dispersion is perpendicular to the radial direction in Camera 3 where the radial direction is defined by a vector originating at the center of the field of view for Camera 3 and pointing toward the center of the HST OTA axis. In complex fields, such as extended objects and crowded fields, individual spectra of targets may overlap and cause confused images. In such cases, it may be possible to alleviate the superposition of spectra by requesting a specific orientation of the telescope during the Phase II Proposal submission. For complex fields or extended targets, observations of the same field at 3 or more different spacecraft orientations (roll-angles) are advisable, to deconvolve overlapping spectra. It is essential that matching direct images be obtained in this case. It should be recognized that specifying an orientation for a grism observation creates constraints on the number of visibility windows

available for scheduling. If different orientations are needed over a short period of time to unscramble the source spectra, telescope scheduling will be difficult.

Grism Calibration

The NICMOS spectroscopic grism mode calibrations were determined from on-orbit observations (Cycle 7 and 7N calibration program IDs: 7695, 7696, 7806, 7903, 7959). Observations were obtained with each grism in and out of Camera 3 campaign mode. Wavelength calibration was carried out by observing planetary nebulae, VY 2-2 (before January 1998) and HB12 (after this date). The inverse sensitivity curves were derived from observations of the white dwarf G191-B2B and G-dwarf P330E. Grism calibration data reductions were performed at the Space Telescope European Coordinating Facility (ST-ECF). The ST-ECF NICMOS web page is <http://ecf.hq.eso.org/nicmos/nicmos.html>.

Relationship Between Wavelength and Pixel

Table 5.4 gives the dispersion relationship in the form:

$$\text{wavelength} = m * \text{pixel} + b,$$

where wavelength is in microns and the 0 pixel is at the central wavelength defined by the position of the object in the direct image. The relationship is plotted in Figure 5.9. The actual location of the positive and negative pixels will be dependent on the grism orientation and the location of the source in the image. The grisms were aligned as accurately as possible along a row or column of the array. We do not expect any distortion or curvature in the spectrum.



During Cycle 7 and 7N, there was a measured change in the angle between the NIC3 chip axes and the GRISM dispersion. A half a degree of rotation was determined between the January 1998 and June 1998 NIC3 campaigns, with the rotation with respect to the detector X axis increasing with time.

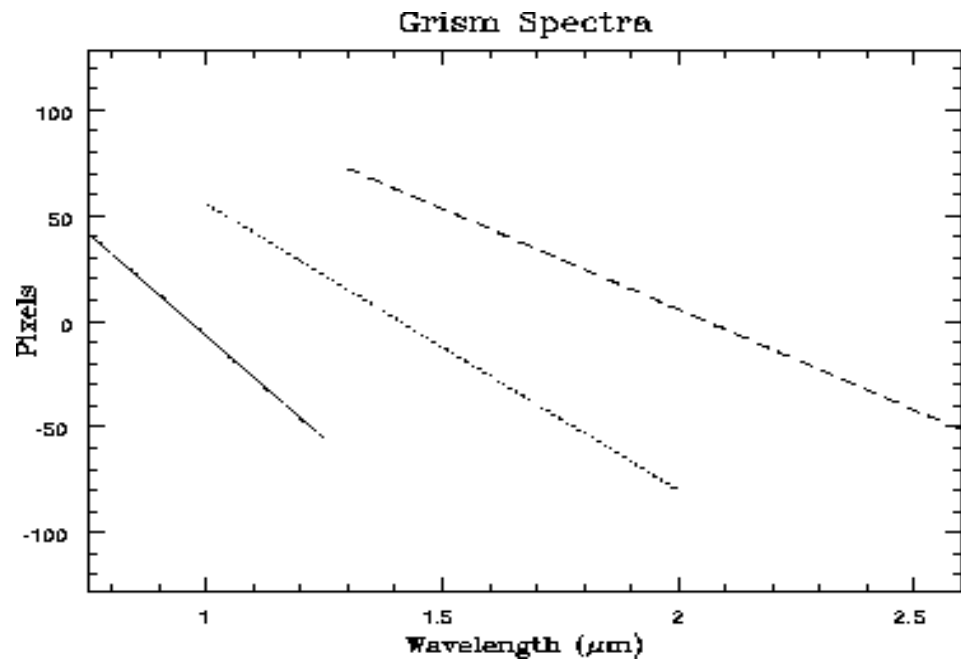
The orientation and position of the spectra relative to the direct object has been measured in orbit and has been found to be similar to the Thermal Vacuum measurements. The dispersion parameters have remained fairly constant during the in-orbit observations. They are significantly different

from the pre-flight measurements, and the current best estimates of the dispersion relations are those determined from on-orbit observations.

Table 5.4: Grism wavelength to pixels relationship

Grism	m	b
G096	-0.00536	0.9487
G141	-0.007992	1.401
G206	-0.01152	2.045

Figure 5.10: Wavelength Versus Pixel Number for each Grism. Note that the actual location of the central wavelength on the detector depends on the position of the source.



Sensitivity

Background radiation will be a greater concern for grisms than for imaging observations. Every pixel on the array will receive background radiation over the spectral bandpass of the particular grism, while the source spectrum will be dispersed over many pixels. Therefore, the ratio of the source to background flux will be much lower for the grisms than for the regular imaging mode filters. The background rate per pixel expected with NCS operations is presented in Table 5.5 below for the three grisms. The increase in the background flux for the G206 grism is dramatic. Grisms G096 and G141 should therefore be used when possible. Despite its broad wavelength coverage, the G206 grism should be used for the longest

wavelengths only. Dithered observations, especially when the field is uncrowded, can often be used to remove the background quite well. Thus breaking observations into several spectra, taken on different parts of the detector, is strongly recommended.

Table 5.5: Grism Background Radiation

Grism	Wavelength range microns	Background (e ⁻ /sec/pixel)	Background (Jansky/pix)
G096	0.8-1.2	0.61	4.4×10^{-7}
G141	1.1-1.9	2.2	6.3×10^{-7}
G206	1.4-2.5	440	7.3×10^{-5}

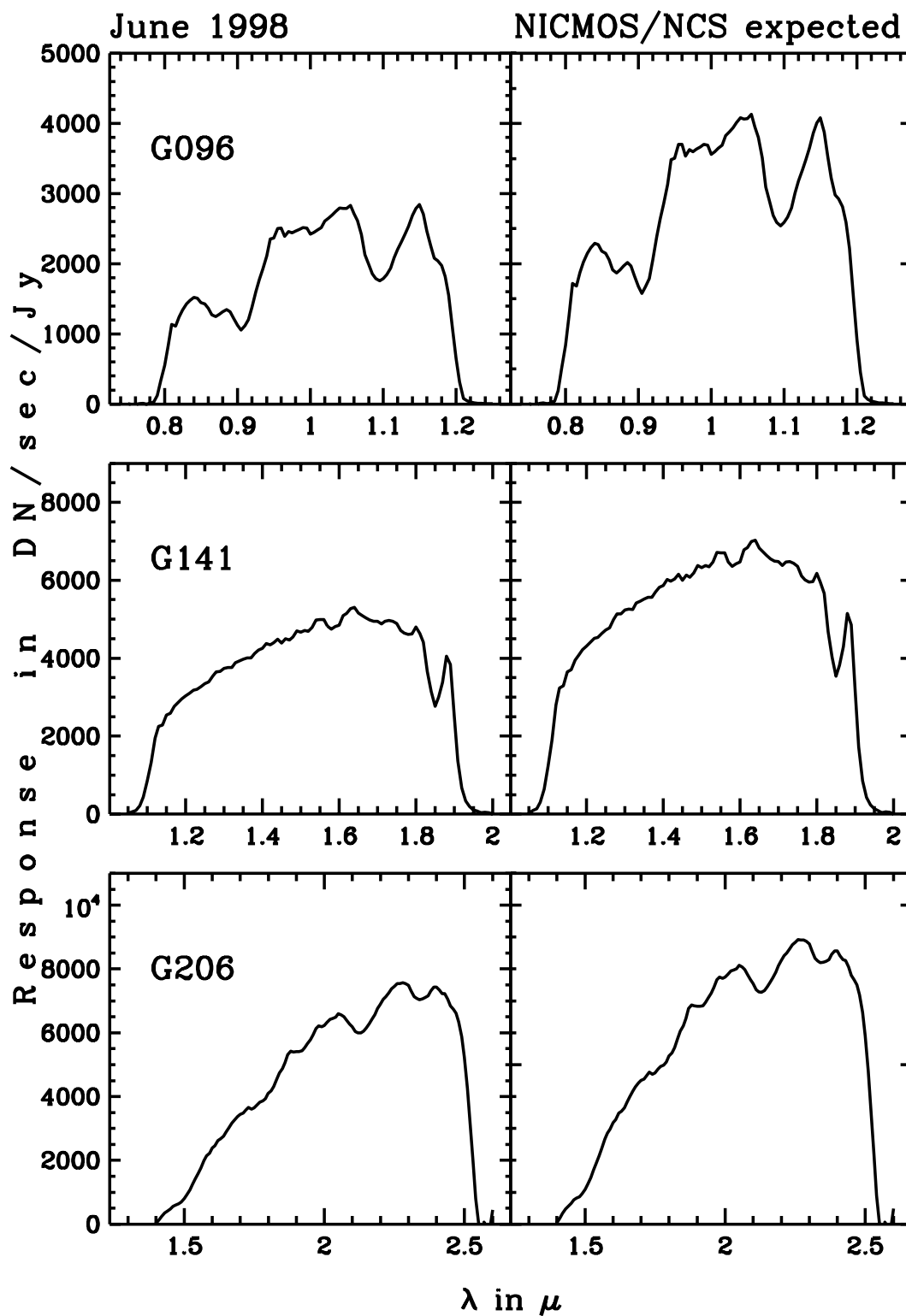
Figure 5.10 gives the sensitivity of each grism as a function of wavelength, as measured for the standard star P330E in June 1998 (left panels) and renormalized to the DQE expected in Cycle 10 onward, after installation of the NCS (right panels). The signal was measured in an aperture of 10 pixels (2 arcsec) in the spatial direction. Table 5.6, 5.7, and 5.8 present the basic information for the three NICMOS grisms. In the same tables, the best direct imaging filter to associate with each grism is given with the list of its characteristics.



Note that for the G206 grism, the large thermal background means that exposures can never be longer than about five minutes, even for faint sources, because the detector will be saturated by the background. See Chapter 4 for more details on the thermal background seen by NICMOS. The dithering/chopping strategies described in Chapter 11 for background removal should be used with this grism.

As with other modes, the Exposure Time Calculator for grism observations will be available in Cycle 10 on the WWW to estimate the signal-to-noise and exposure times.

Figure 5.11: Grism Inverse Sensitivity Curves, G096 (top), G141 (middle), and G206 (bottom), both measured (June 1998 observations, left) and predicted with the expected Cycle 10 DQEs (right).



Grism A: G096

Table 5.6: Grism A: G096

Central (microns)	Mean (microns)	Peak (microns)	FWHM (microns)	Range	Max Trans. (percent)
0.9673	0.9911	1.0010	0.4029	0.8–1.2	69.8
Direct Imaging Filter F110W					
1.0998	1.1035	1.2035	0.5915	0.8–1.4	94.9

Grism B: G141

Thermal background is important.

Table 5.7: Grism B: G141

Central (microns)	Mean (microns)	Peak (microns)	FWHM (microns)	Range (microns)	Max Trans. (percent)
1.414	1.5100	1.4020	0.7914	1.1–1.9	74.7
Direct Imaging Filter F150W					
1.5035	1.5069	1.6355	0.8020	1.1–1.9	97.7

Grism C: G206

High thermal background. Use only for bright sources, at longest wavelengths.

Table 5.8: Grism C: G206

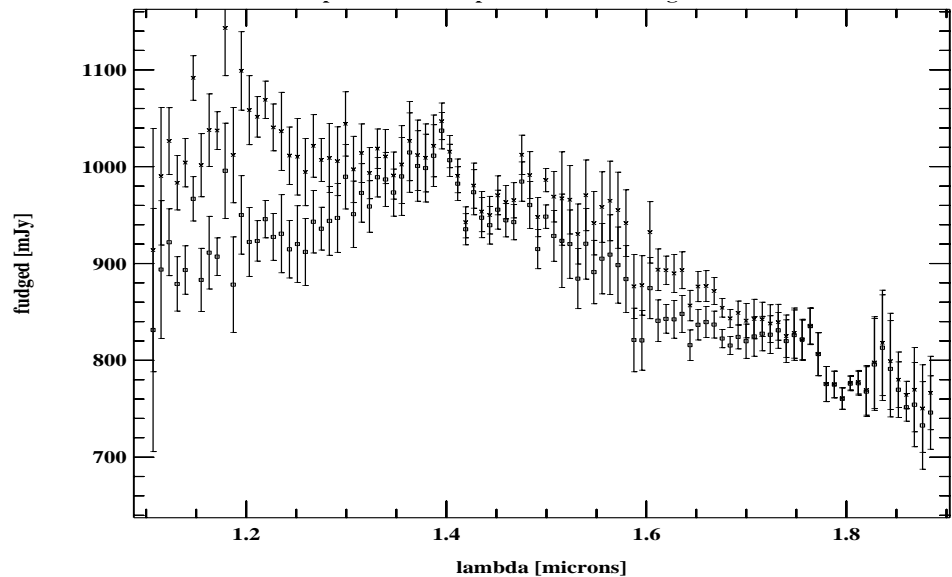
Central (microns)	Mean (microns)	Peak (microns)	FWHM (microns)	Range (microns)	Max Trans. (percent)
2.067	1.9523	2.0880	1.1575	1.4 - 2.5	73.4
Direct Imaging Filters F175W, F240M					
1.7530	1.7508	1.9070	1.0940	1.2–2.3	96.6
2.3978	2.3977	2.3155	0.1975	2.3–2.5	92.4

Intrapixel Sensitivity

The same intrapixel sensitivity problem which affects NIC3 images (see Chapter 4) will affect the grism spectra since the dispersion direction is not exactly aligned with the detector rows: as the heart of the spectrum crosses from one row to the next, the flux will dip by 20 percent or so. This effect is not obvious in emission line spectra but can be very clear in continuous

spectra. The frequency of the dip and the placement of the sensitivity minima within the spectrum will depend on exactly where the spectrum falls on the detector, and the angle between the dispersion direction and the detector X axis. Note that the former changes with the dithering position, and the latter is temporally variable. As noted earlier, the grisms and the detector appear to have rotated with respect to each other by a half a degree between the two NIC3 observing campaigns. STScI will characterize this problem in an upcoming ISR and will make a program to correct for the problem to the extent possible. The results of a preliminary procedure are shown in Figure 5.11 below using the spectrum of the standard star P330E. Note the maximum deviation near $1.2\ \mu\text{m}$ and $1.6\ \mu\text{m}$ wavelength, where the spectrum crosses from one row to the next. The NICMOS WWW site should be checked periodically for updates on this developing issue.

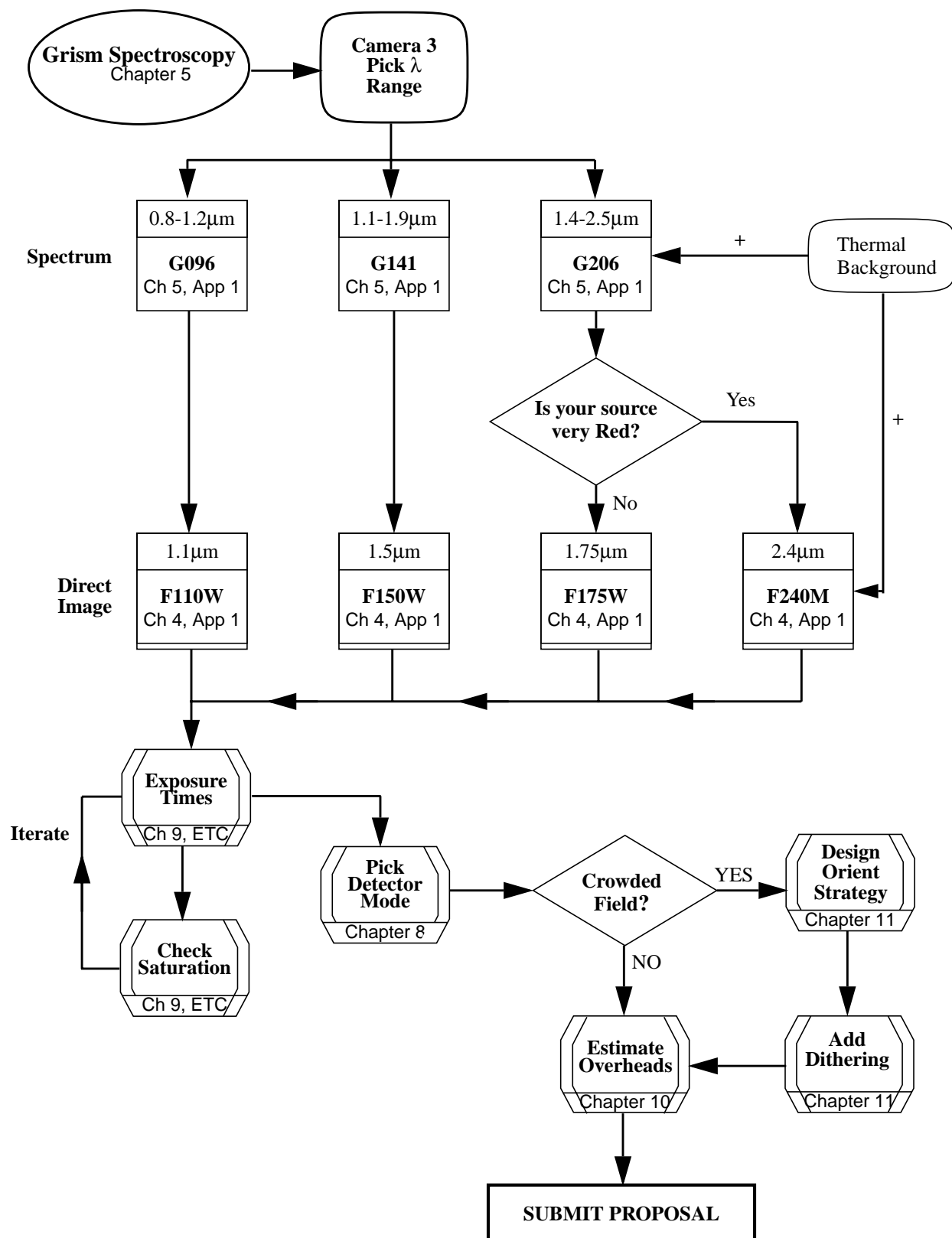
Figure 5.12: G141 spectrum of solar type standard P330E. The uncorrected spectrum is shown by boxes, the corrected spectrum by crosses.



Grism Decision Chart

The decision chart given in Figure 5.13 helps through the construction of a grism observation.

Figure 5.13: Grism Decision Chart



NICMOS Apertures and Orientation

In This Chapter...

NICMOS Aperture Definitions / 103
NICMOS Coordinate System Conventions / 104
Orients / 105

In this Chapter we give the aperture definitions, the instrument orientation on the sky and the coordinates' convention.

NICMOS Aperture Definitions

Each HST Science Instrument requires its own local coordinate system and apertures to support both target acquisition and small angle maneuvers (SAMs). Apertures are calibrated locations in the HST focal plane relative to the FGS frame. All acquisitions and SAMs are relative to apertures. Any location within the field of view of a NICMOS camera can be specified by the POSTARG special requirement (described in the HST Phase II Proposal Instructions).

The basic philosophy of the NICMOS aperture definitions follows that used by WF/PC-1 and WFPC2. Each NICMOS camera has two primary apertures. One is positioned at the geometric center of the detector and the other at an *optimal* position close to the center. The first of these apertures is anchored to that fixed location, while the second may be moved in the future. In this way the optimal aperture may be shifted to avoid array

defects, even if these are time dependent. Observers with large targets which fill the field of view of a particular camera are generally advised to use the first type of aperture, while for observers with smaller targets the second type is recommended.

Additional apertures are defined in Camera 2 for use in the Mode 2 coronagraphic acquisition.

The names of the defined apertures are listed in Table 6.1 along with a description of their function and their initial location

Observers should note that while apertures are defined by their pixel position in each detector, displacements relative to the default aperture position given with POSTARG are expressed in arcseconds (see the Phase II Proposal Instructions).

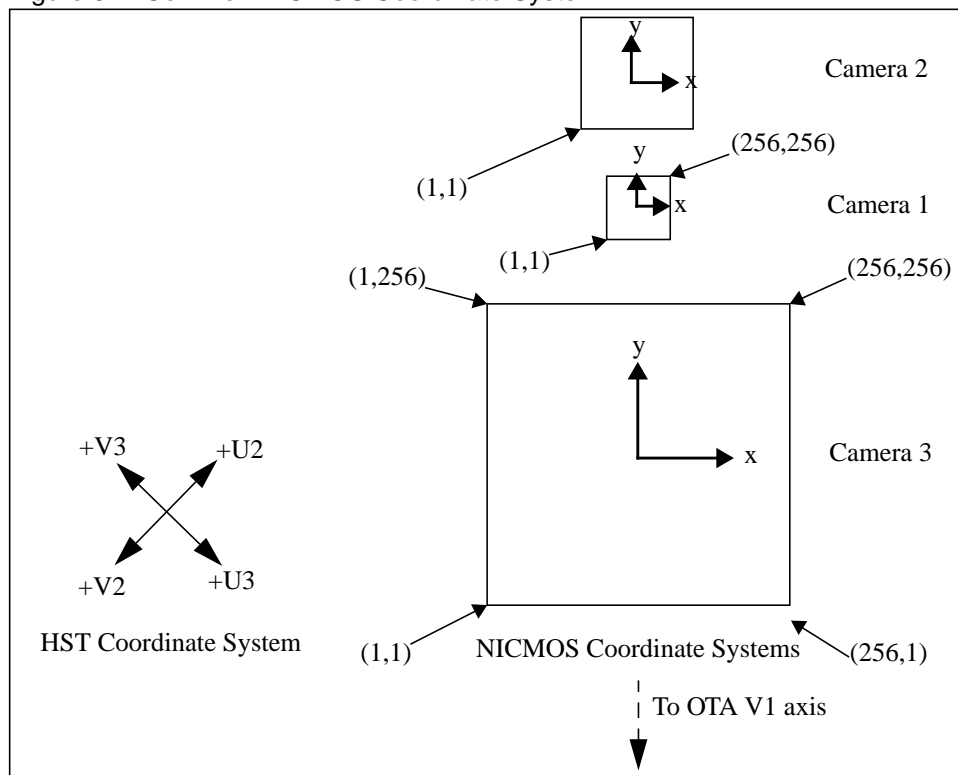
Table 6.1: NICMOS Aperture Definition

Aperture Name	Description	Position (detector pixels)
NIC1	Optimal center of Camera 1	162,100
NIC1-FIX	Geometric center of Camera 1	128,128
NIC2	Optimal center of Camera 2	149,160
NIC2-FIX	Geometric center of Camera 2	128,128
NIC2-CORON	Center of coronagraphic Mask	
NIC2-ACQ	Center of Mode 2 ACQ region	157,128
NIC3	Optimal center of Camera 3	140,135
NIC3-FIX	Geometric center of Camera 3	128,128

NICMOS Coordinate System Conventions

Figure 6.1 shows how the NICMOS cameras are arranged in the HST field of view. The alignment of each camera is not exact, and the internal coordinate systems attached to each of them will differ by small rotations (< 1 degree). The FITS format data files generated for NICMOS observers will have a World Coordinate System specified appropriately for each camera. The adopted coordinate system for the 3 cameras is summarized in Figure 6.1.

Figure 6.1: Common NICMOS Coordinate System



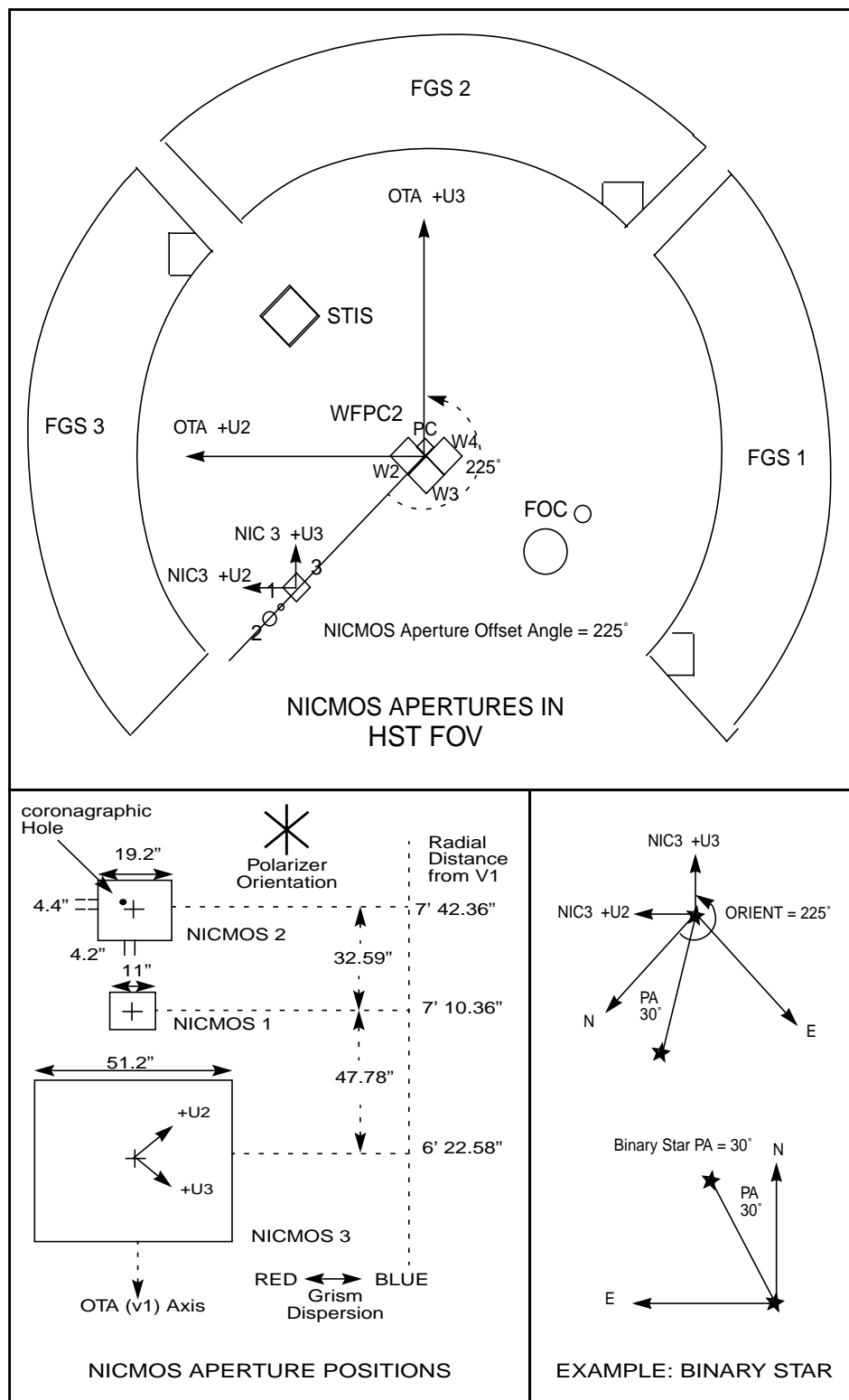
Orients

NICMOS orientations are specified relative to the +y axis shown in Figure 6.1. Eastward rotations are counterclockwise (in the usual astronomical convention). Spacecraft orientations are specified relative to the U2-U3 telescope axis (Figure 6.2). The NICMOS coordinate system is rotated by 225 degrees from U3 axis.

Due to the linear arrangement of the 3 NICMOS cameras on the sky, it will often be advantageous to consider the specification of a unique telescope orientation. Observers should be aware that such constraints may decrease the duration and number of scheduling opportunities for their observations and, under some circumstances, may make the identification of suitable guide stars impossible.

While the Phase II proposal instructions contain the definitive instructions and examples for specifying the desired orientation for HST, we provide a simple example in Figure 6.2. A binary star with a position angle (PA) 30° measured east from north is to be positioned with the southern star in Camera 3 and the northern star in Camera 2. That is, we want the line connecting the two stars to lie along the NICMOS +y axis. The resulting HST orientation is $225^\circ + 30^\circ = 255^\circ$. (HST ORIENT = PA + 225° for NICMOS).

Figure 6.2: Definition of Orient for NICMOS



NICMOS Detectors

In This Chapter...

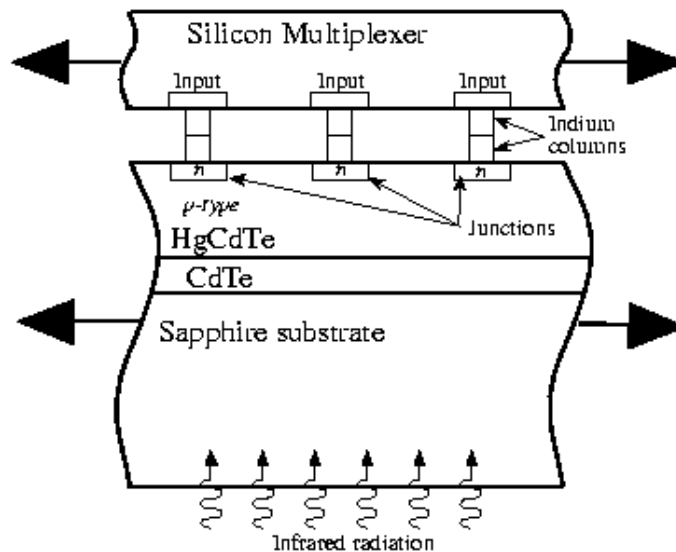
Detector basics / 107
Detector Characteristics / 110
Detector Artifacts / 121

In this chapter, we first briefly explain the physical principles of the NICMOS detectors. We then report on a number of properties that have significance for the scientific performance of NICMOS. Many of these properties are temperature dependent, which is important since the operating temperature for NICMOS under NCS is not yet well known. Expectations for performance in Cycle10 come from a set of monitoring programs executed at the end of Cycle 7N, during the period November 1998 - January 1999. These programs monitored darks, flat-field and focus position while NICMOS was warming up, due to cryogen exhaustion. During warm-up, NICMOS went from ~ 62 K to environment temperature, crossing the region around 72 - 77 K, which is the target temperature range under NCS operations. We will discuss how the various aspects like e.g. quantum efficiency, read-noise, or dark current depend on temperature, and how this will affect the NICMOS sensitivity. Also, we discuss a number of detector artifacts like shading, amplifier glow, and others, all of which can be corrected, either in pipeline processing or at the analysis level.

Detector basics

In this section we briefly describe the operational principle of the NICMOS3 detectors. Figure 7.1 (adapted from McLean 1997) shows the basic physical principle of a photovoltaic detector.

Figure 7.1: Top: band structure of intrinsic HgCdTe. Bottom: band structure across a p-n junction.

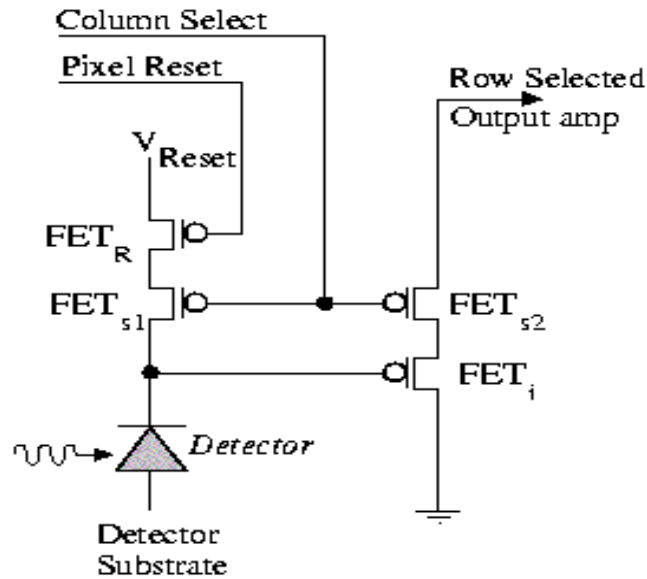


Cross section NICMOS3 detector

Not to scale

An infrared detector is basically a photodiode, the core of which is a p-n-junction created during the wafer processing. The Fermi-levels of the p- and n-type materials, i.e. the highest occupied energy state of the electron gas within the semiconductor material, must match, which effectively creates an electric field across the junction. The incident infrared photons free electron-hole pairs into the conductance band at or near the junction which are immediately separated by the electric field. This reduces the recombination noise, an important advantage over photoconductive detectors. The accumulated charge carriers cause a voltage change across the junction which can be detected and used as a measure of the incident light. One can think of the detector as a capacitor that is discharged by the infrared photons. In practice, the voltage change is monitored by a Si field effect transistor (FET), used as a source follower amplifier. Figure 7.2 shows the equivalent circuit diagram for the NICMOS3 “unit cell”

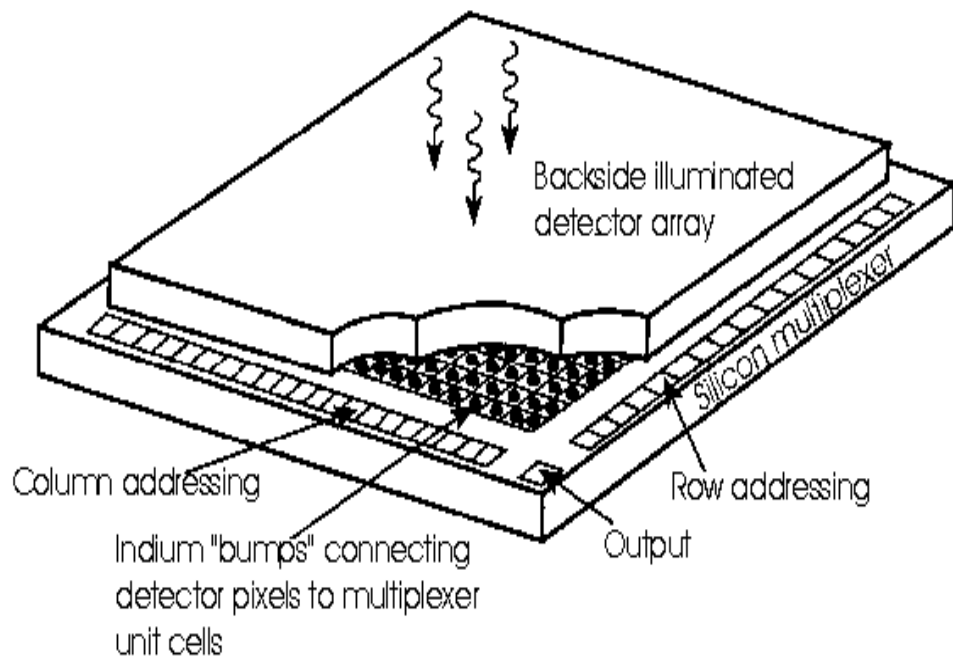
Figure 7.2: Equivalent circuit diagram of the NICMOS3 unit cell.



NICMOS Unit Cell

In order to produce an “imaging” detector, a large number of such unit cells, or pixels, are combined into an array. The photon-sensitive layer (HgCdTe in the case of NICMOS3 detectors) and the Si-multiplexer (which contains the array of FETs) are combined in a “sandwich” structure, connected via tiny indium bumps (Figure 7.3). For better mechanical stability, the “sandwich” array structure is put on an infrared-transparent Sapphire substrate. Since each pixel contains its own FET, there is no “bleeding” along columns, as in CCD chips, and bad pixels do not block the rest of the column.

Figure 7.3: Basic “hybrid” structure of infrared array detectors. Top: schematic of the detector array. Bottom: enlarged cross-section of a few unit cells, or pixels.



Detector Characteristics

Overview

Each NICMOS3 detector comprises 256×256 square pixels, divided into 4 quadrants of 128×128 pixels, each of which is read out independently. The basic performance of the nominal flight detectors is summarized in Table 7.1. Typically, the read-noise is $\sim 30e^-/\text{pixel}$. Only a few tens of bad pixels (i.e., with very low response) were expected, but particulates—possibly paint flakes—have increased this number to >100 per detector. The gain, $\sim 5\text{--}6 e^-/\text{ADU}$, has been set so as to map the full useful dynamic range of the detectors into the 16-bit precision used for the output science images.

Table 7.1: Flight Array Characteristics

Characteristics	Camera 1	Camera 2	Camera 3
Dark Current (e^- /second) ^a	0.4-2.0	0.4-2.0	0.4-2.0
Read Noise (e^-) ^b	~30-35	~30-35	~30-35
Bad Pixels (including particles)	213 (.33%)	160(0.24%)	139(0.21%)
Conversion Gain (e^- / ADU)	5.4	5.4	6.5
SATURATION (e^-) ^c (98% Linearity)	145,000	145,000	185,000
50% DQE Cutoff Wavelength (microns)	2.55	2.53	2.52

a. The dark current strongly depends on whether the “bump” anomaly will be observed or not (see next section) when NICMOS will be cooled down to operating temperatures with the NCS.

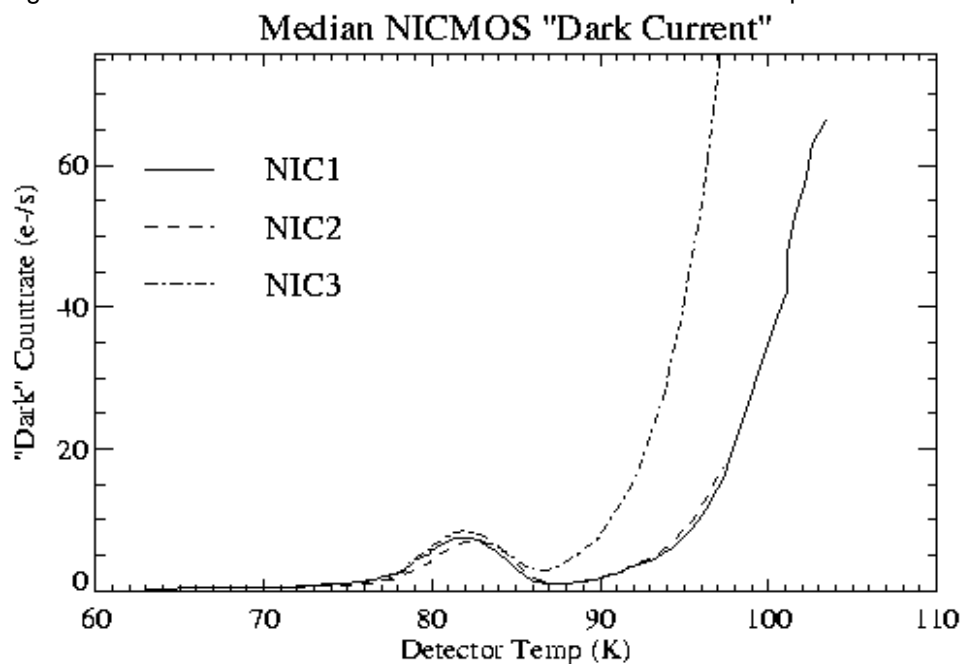
b. The quoted readout noise is the realized noise from a pair of readouts (i.e., the quadrature sum of a single initial and final readout). The following sections will give more information for each of the quantities of this table.

c. Saturation is defined as 2% deviation from quadratic non-linearity.

Dark current

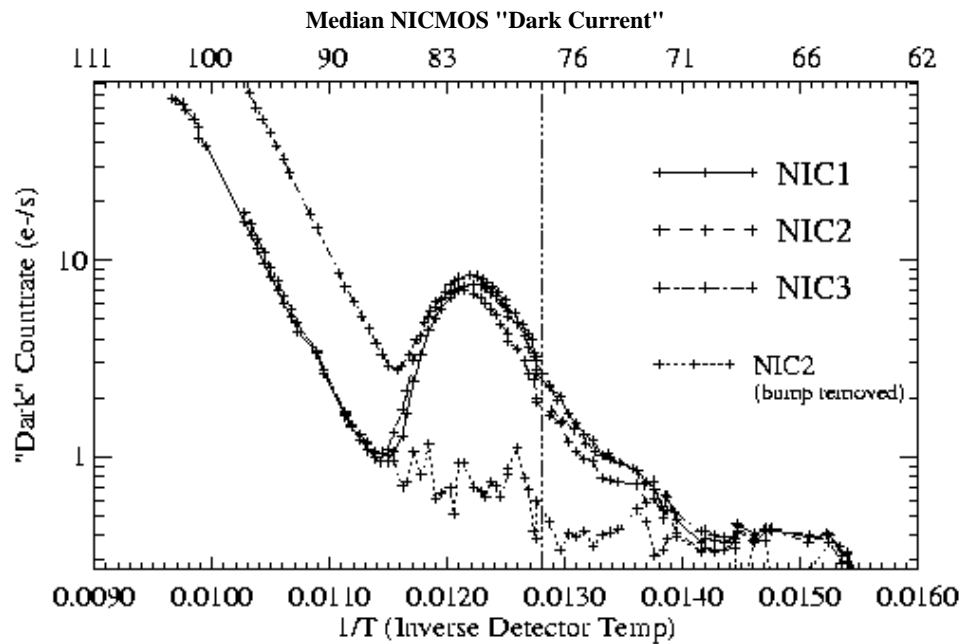
A NICMOS exposure taken with the blank filter in place should give a measure of the detector dark current. However, the signal in such an exposure consists of three different components: amplifier glow, shading, and linear dark current. The linear dark current is the current produced by the minority carriers inside the detector material, it increases linearly with exposure time, hence the name. It can be measured after subtraction of amplifier glow and correction for shading, both of which we will describe in the next section. The linear dark current was carefully monitored throughout the NICMOS warm-up at the end of Cycle 7N in order to estimate its value for operation under the NCS. Special care was taken to minimize the impact of those measurements that were affected by cosmic ray persistence after passage through the South-Atlantic Anomaly (see Chapter 4). The mean signal of all three NICMOS chips for the whole temperature range of the warm-up is plotted in Figure 7.4. The characteristic increase and subsequent decline of the dark current between 80 and 95 K is an unexpected feature which is commonly referred to as the “bump”.

Figure 7.4: NICMOS linear dark current as function of detector temperature.



The theoretical expectation for the dark current at temperatures above ~ 140 K is to follow the charge carrier concentration, which rises with temperature according to the Boltzmann factor $e^{-E/kT}$. At temperatures between 90 and 140 K, generation-recombination models provide the best agreement with laboratory measurements. The two regimes both produce a basically linear relation of $\log(\text{dark current})$ vs. $1/T$, but with different slopes. At temperatures below 90 K, poorly understood tunneling effects are known to cause a deviation from the generation-recombination model. These result in a flattening of the dark current decrease towards colder temperatures, until a basically constant dark current is reached. Except for the bump, the NICMOS dark current follows these general trends, as demonstrated in Figure 7.5.

Figure 7.5: Same as Figure 7.4, but plotted on a logarithmic scale vs. inverse temperature. The lowest, dotted line shows the expected dark current in the case of a non-recurring bump.



Since the signal responsible for the bump shows the flatfield structure (see NICMOS ISR 99-001 for more details), there is reason to believe that the bump is not due to an increased “true” dark current, but rather to a radiant signal falling onto the photosensitive layer of the detectors. Moreover, the fact that the small specks of black paint known as “grot” are not visible in these images suggests that the radiation is coming from behind or within the detectors. The idea of an additional radiant component to the dark current signal is supported by the fact that subtracting a scaled flatfield exposure - constructed from the set of calibration flats and weighted by the DQE curve appropriate for the respective temperature - effectively flattens the dark current image, and smoothly interpolates the dark measurements before and after the bump (lowest line in Figure 7.5). This suggests that the bump is indeed due to an additional signal component whose nature is as yet unexplained. A possible explanation for the radiant signal, which is currently being discussed, is the release of energy stored in the detector material by cosmic ray hits, by mechanisms comparable to the annealing process known from CCD chips. Additional laboratory tests are under way to further investigate this theory.

Flat fields and the DQE

Uniformly illuminated frames taken with the NICMOS arrays show response variations both on large and small scales. These fluctuations are corrected in the normal way by flat fielding, which is an essential part of

the calibration pipeline. In order to monitor the flat field structure of the NICMOS detectors, a large program of sky and earth flats has been executed during Cycle 7 and throughout the warm-up. At the NICMOS temperatures achieved during Cycle 7, the flat field exposures showed considerable spatial structure, i.e. the relative responsivity of individual pixels varied by a large amount. Peak-to-peak variations between the most and least sensitive areas on the array were as much as a factor of 5 at 0.8 microns. The amplitude of the variations declines with wavelength, it is a factor of ~ 3 at 2.2 microns, and at 2.5 microns, the array is almost flat.

The flat field structure is due to variations in the detective quantum efficiency (DQE) of the individual pixels which is a function of temperature. The DQE monitoring program during the warm-up of the instrument was designed to determine what exactly the response function of the NICMOS detectors at the NCS operating temperatures will be. Expectations were that low sensitivity pixels would experience a significant increase in DQE, especially at shorter wavelengths. Figure 7.6 shows the pixel response of all camera/filter combinations that were used during the monitoring (details of the data reduction are found in NICMOS ISR 99-001).

For all regions, the DQE increases roughly linearly between 63 K and 78 K, with a usually small curvature term. In all cameras, the linear slope is higher than average for low-sensitivity regions, and lower than average for high sensitivity regions. This behavior effectively flattens out the DQE variations across the array, relative to Cycle 7 and 7N. The average responsivity at 75 K increased by about 45% at J, 33% at H-, and 17% at K. The resulting wavelength dependence of the expected DQE for NICMOS operations at 75 K is shown in Figure 7.7. Here, we have scaled the pre-launch DQE curve, which was derived from ground testing of the detectors, to reflect the changes measured at the wavelengths used in the monitoring program.

Figure 7.6: DQE variations with temperature for all camera/filter combinations of the monitoring program. The coefficients of a second order polynomial fit are listed on the top left of each plot. For each dataset, the three curves depict a low sensitivity region on the chip (highest curve), the median DQE over the full chip (middle curve), and a high sensitivity region (bottom curve). Note that the DQE increase is highest at the shortest wavelengths

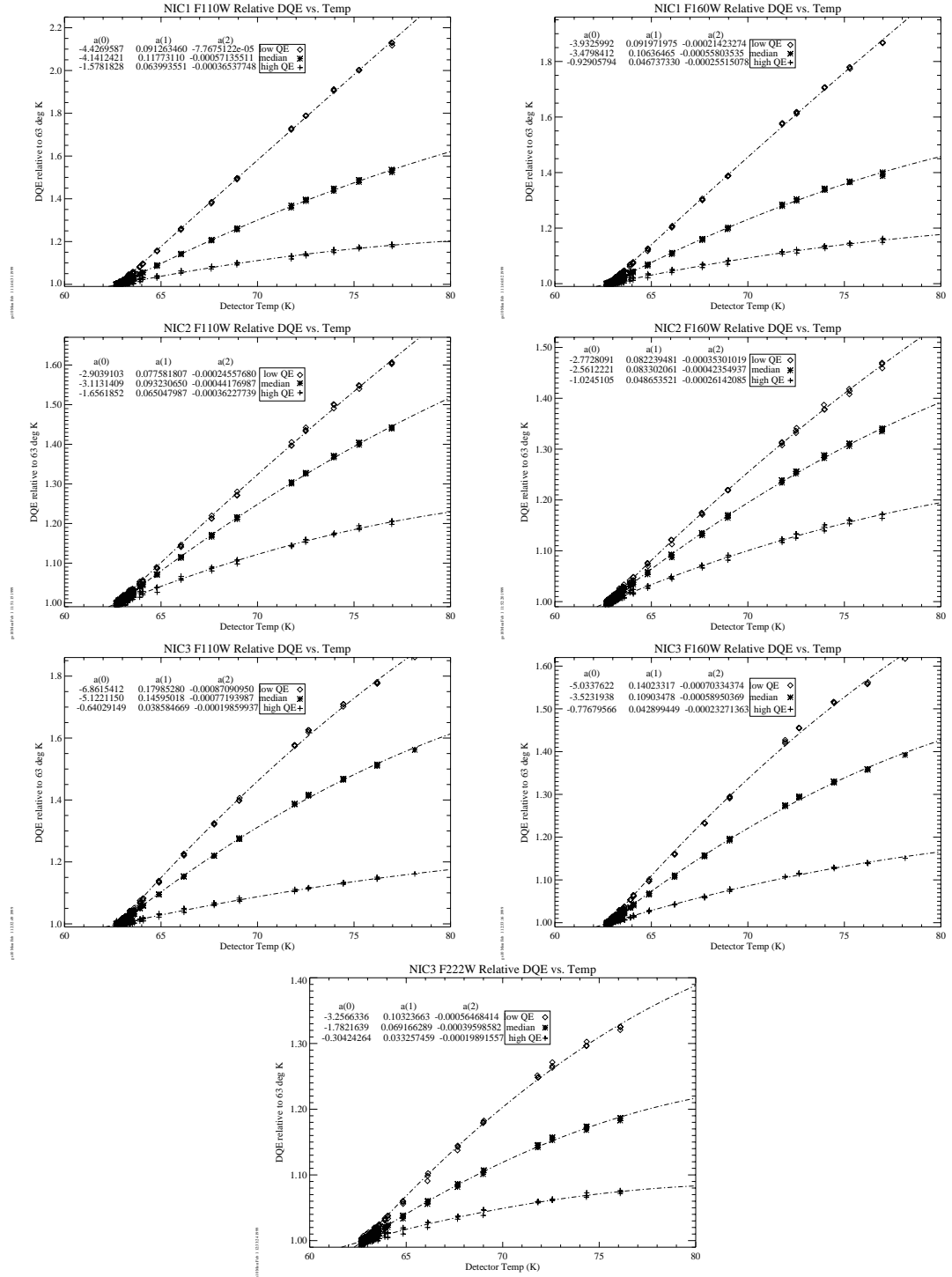


Figure 7.7: Expected NICMOS DQE as a function of wavelength for operations at 75 K (crosses), compared to pre-launch measurements.

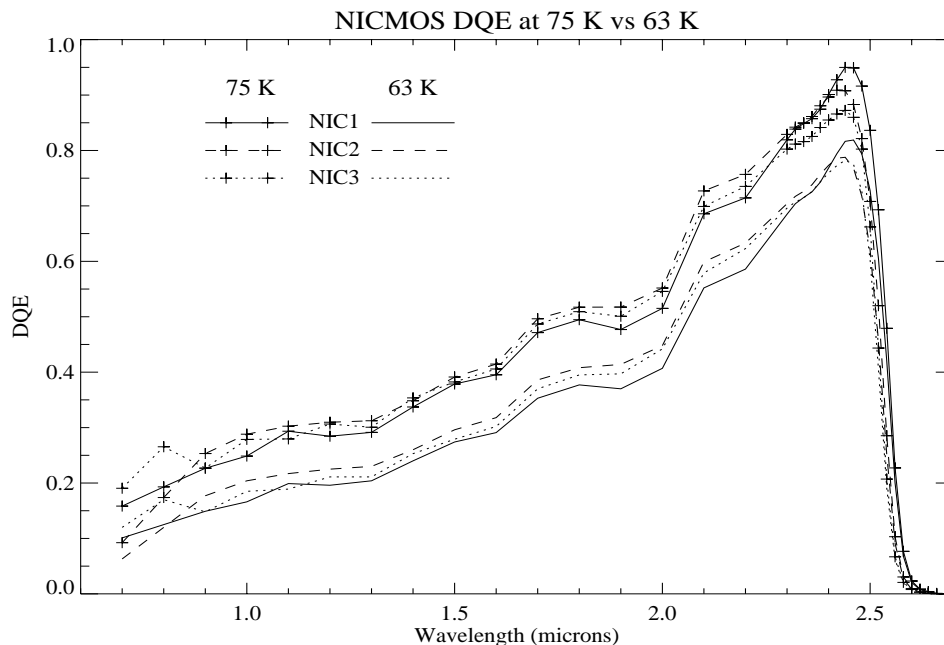
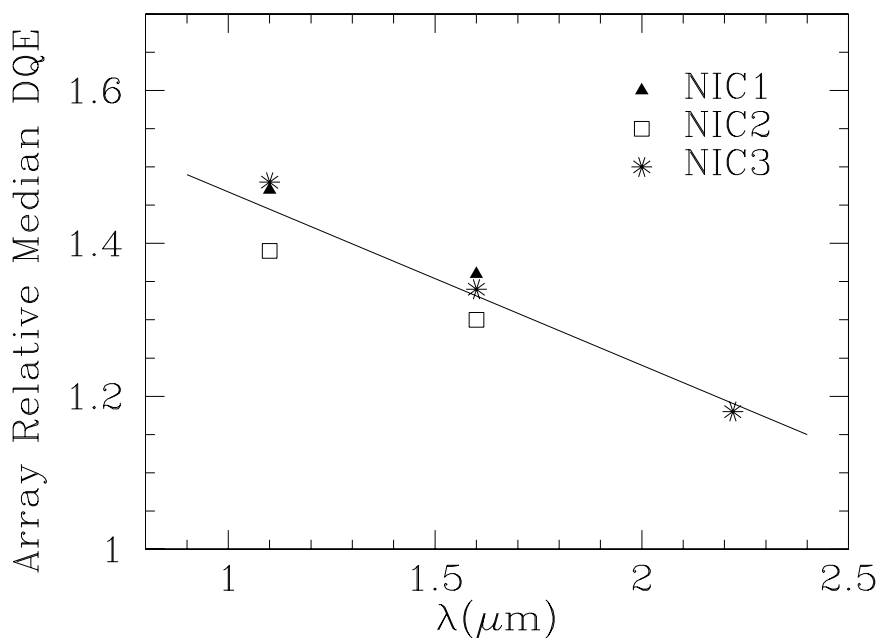


Figure 7.8: The ratio of the expected DQE at 75 K to the DQE at 63 K for the three NICMOS cameras. The symbols are measurements. The continuous line is a linear extrapolation.

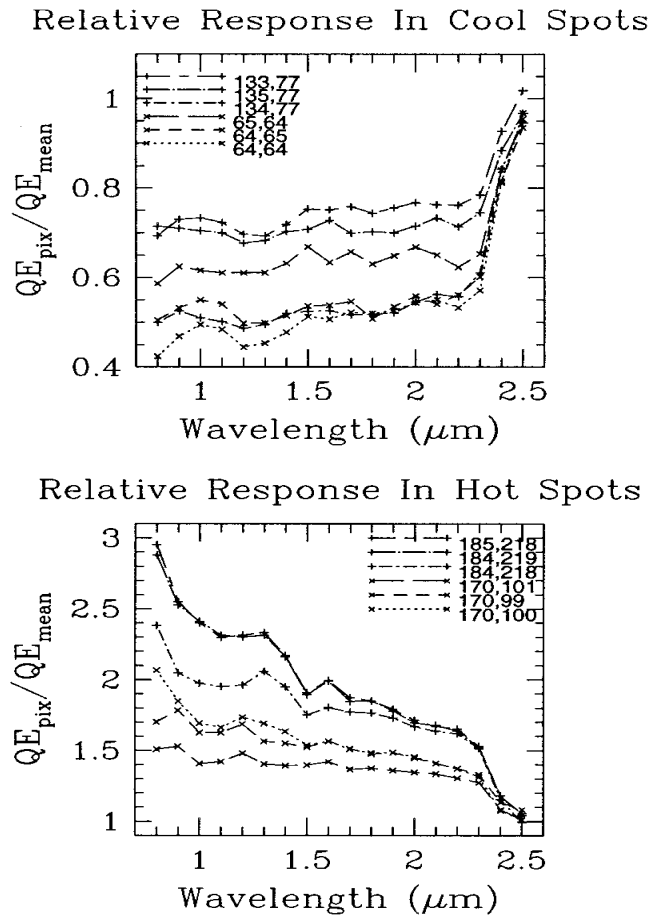


The fine details in these DQE curves should not be interpreted as detector features, as they may be artifacts introduced by the test set-up. At the blue end, near 0.9 microns, the DQE at 75 K is ~20%; it rises

quasi-linearly up to a peak DQE of ~90% at 2.4 microns. At longer wavelengths, it rapidly decreases to zero at 2.6 microns. The NICMOS arrays are blind to longer wavelength emission. Figure 7.8 shows the ratio of the DQE at 75 K to the DQE at 63 K, as a function of wavelength. The continuous line is extrapolated from the average measured in the three cameras during the warm-up monitoring for a subset of wavelengths (filters). When looking at these DQE curves, the reader should bear in mind that this is not the only criterion to be used in determining sensitivity in the near-IR. For example, thermal emission from the telescope starts to be an issue beyond $\sim 1.7 \mu\text{m}$. The shot-noise on this bright background may degrade the signal to noise obtained at long wavelengths, negating the advantage offered by the increased DQE.

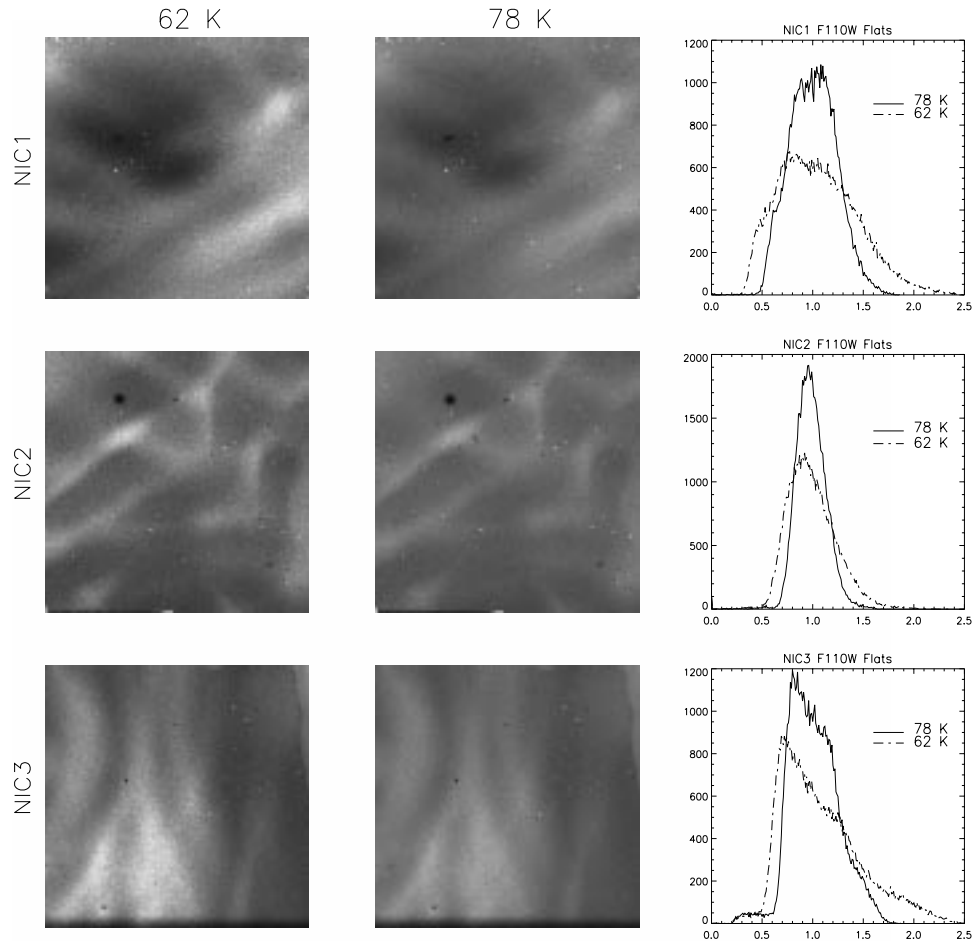
It is important, especially for observations of very faint targets for which the expected signal to noise is low, to note that the DQE presented here is only the average for the entire array. The flat field response is rather non-uniform, and thus the DQE curves for individual pixels may differ substantially. To demonstrate this, we plot the relative response of four selected detector areas in Figure 7.9. Each region consists of three adjacent pixels, either in a line or in an “L” shape. Two of them have relatively high sensitivity, and the other two show a lower than average sensitivity. The pixel sensitivity relative to the average over the entire array is plotted versus wavelength, using a number of 10% bandwidth measurements. For many pixels, the response variation is fairly slow between 1.0 and 2.2 microns. However, at about 2.25 microns, there is a pronounced turnover, beyond which the change with wavelength is significantly larger. Note, however, that these data were taken at temperatures around 60 K.

Figure 7.9: Relative Response as a function of wavelength of three-pixel groups. The curves show the DQE of individual pixels relative to the mean DQE for the entire array, for low- (top panel) and high sensitivity pixels (bottom panel).



The steeper gradient in the flat field response longward of 2.25 microns is likely to somewhat degrade the photometric accuracy of observations in the longest wavelength NICMOS filters. However, In Cycle 10, the NICMOS detector arrays are expected to be much flatter compared to Cycle 7 because of the stronger DQE increase with temperature of the low-sensitivity pixels described above. Figure 7.10 demonstrates this effect. As can be seen from the histograms on the right, the overall spread in pixel response values is much smaller at the temperatures expected for Cycle 10. Therefore, the photometric accuracy at the long wavelength end should be improved. Nevertheless, special care should be taken when observing sources with extreme colors (see Chapter 4).

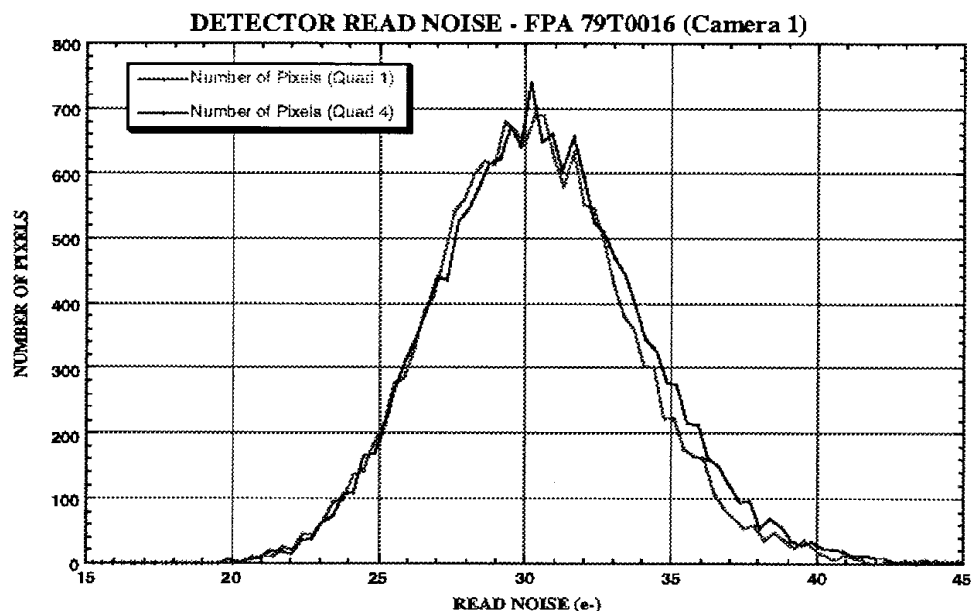
Figure 7.10: Normalized flat field exposures of all NICMOS detectors, taken through the F110W filter at temperatures of 62 K (left) and 78 K (right). The color stretch is the same for both temperatures in each camera. The histograms on the right show the “flattening” of the arrays at the higher temperature which can also be seen by comparing the images.



Read Noise

Each detector has four independent readout amplifiers, each of which reads a 128 x 128 quadrant. The four amplifiers generate very similar amounts of read noise. This is illustrated in Figure 7.11 which compares the pixel read noise distributions for the 1st and 4th quadrants of Camera 1. The distributions for all quadrants is relatively narrow, with a FWHM of 8 electrons. This means that there are only few very noisy pixels.

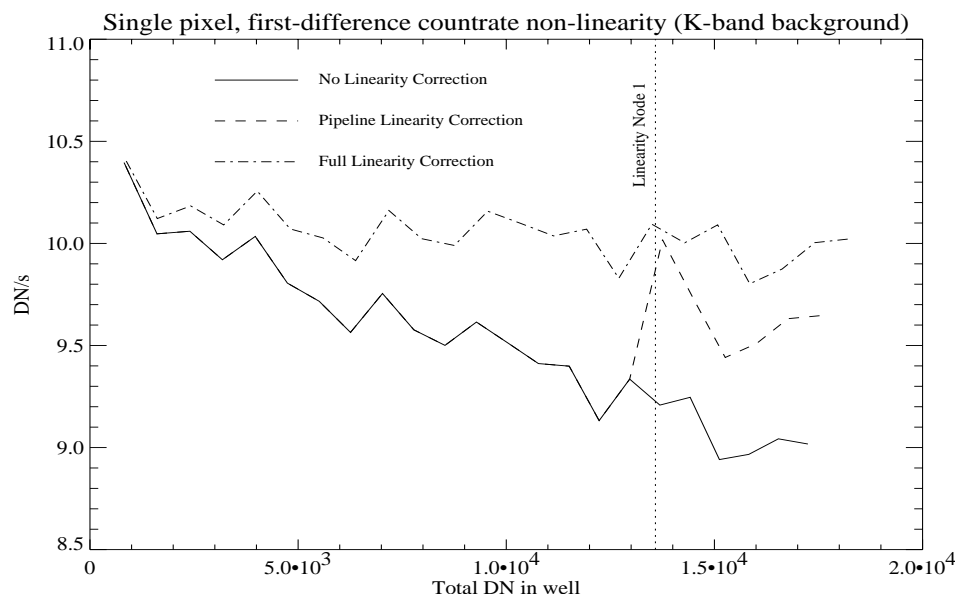
Figure 7.11: Read Noise Characteristics for Two Quadrants on Camera 1 Detector



Linearity

Until after Cycle 7, the linearity correction of the calibration pipeline had been based on the assumption that the NICMOS detector response was perfectly linear until count numbers reached a certain value, usually referred to as Node 1. No linearity correction was performed until this point was reached. The pixel was flagged as saturated when the deviation from the linear response reached 2%. This point, the so-called Node 2, occurs at about 90% of the well. However, an extensive Cycle 7 calibration program indicated that the detector response is in fact non-linear over the full dynamic range. For Cycle 10, a revised linearity correction will be implemented into the calibration pipeline which will correct all non-destructive readouts of an exposure in a non-linear fashion; in other words, Node 1 will be set to zero. Figure 7.12 compares the new procedure to the one previously used. Here, we plot the response of a (arbitrary) NIC3 pixel, as derived from differencing subsequent readouts (“first differences”).

Figure 7.12: Comparison between previous(dashed) and new (dash-dotted) linearity correction. The true pixel response is shown by the solid line.



Detector Artifacts

Shading

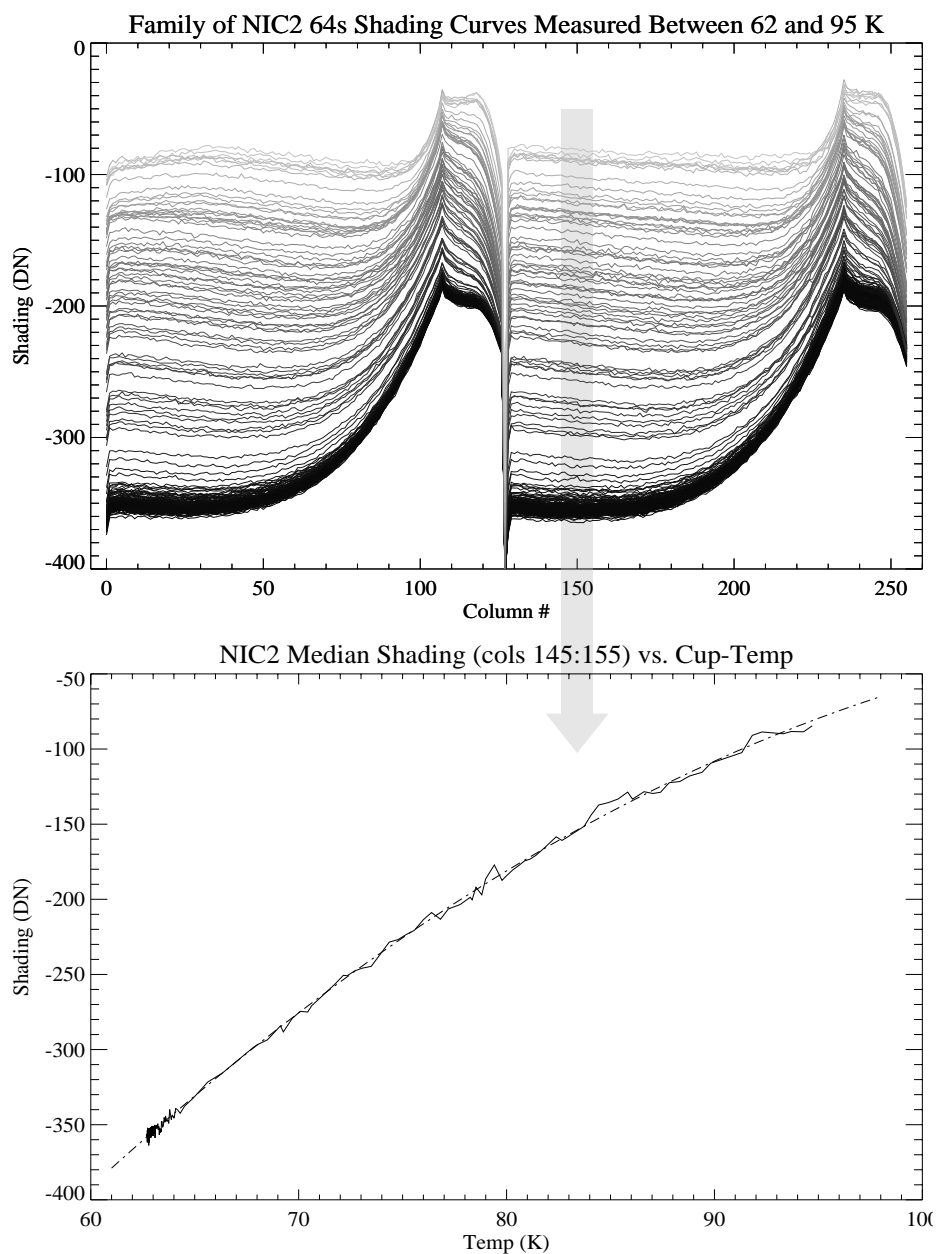
The NICMOS arrays exhibit a noiseless signal gradient orthogonal to the direction of primary clocking, which is commonly referred to as *shading*. It is caused by changes of the pixel bias levels as a function of temperature and time since the last readout (“delta-time”). The amplitude of the shading can be as large as several hundred electrons for some pixels under some circumstances. The first pixels to be read show the largest bias changes, with the overall shading pattern decreasing roughly exponentially with row number. The shading is a noiseless contribution to the overall signal, therefore it can be completely removed during pipeline processing once it has been calibrated with delta-time and temperature.

For a given delta-time, the bias level introduced by the shading remains constant. For MULTIACCUM readout sequences (see Chapter 9) where the time between readouts is increasing logarithmically, the bias level changes with each successive read, and thus the overall shading pattern evolves along the MULTIACCUM sequence. We have calibrated the dependence of shading as a function of delta-time for each of the three NICMOS detectors using Cycle 7 darks, and are now able to use this information to construct “synthetic” dark current calibration reference files for NICMOS

observations. The accuracy of this calibration is good (a few percent for most readout times).

The warm-up monitoring program provided an opportunity to measure the temperature dependence of the shading signal. Figure 7.13 shows how the shading profile of NIC2 varied with increasing detector temperature, and how this change can be effectively modeled for calibration.

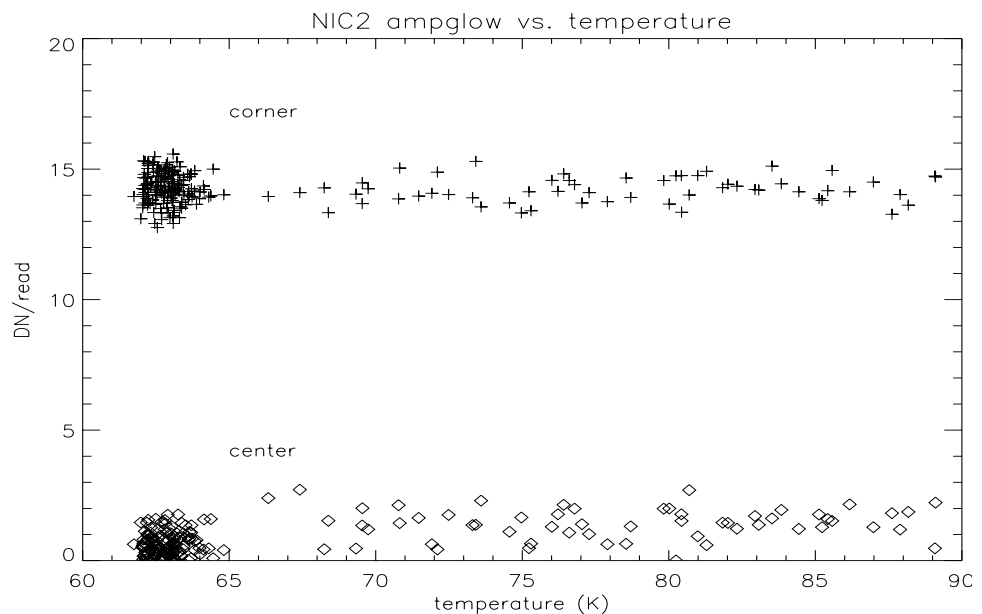
Figure 7.13: Top: temperature dependence of the shading profile in camera 2. Shown are cuts along the line direction for all dark exposures throughout the warm-up, with the lowest curves corresponding to the lowest temperatures. Bottom: mean shading signal over columns 145 to 155 (indicated by the grey arrow) as a function of detector temperature.:



Amplifier Glow

Each quadrant of a NICMOS detector has its own readout amplifier situated close to the corners of the detector. Each time the detector is read out, the amplifier warms up and emits infrared radiation that is detected by the chip. This signal, known as amplifier glow, is largest in the array corners with ~ 80 e^- /read, and falls rapidly towards the center of the detector where it is about 10 e^- /read. The signal is cumulative with each non-destructive readout of an exposure. It is highly repeatable, and almost exactly linearly dependent on number of reads (however, there is some minor evidence that there may be a small non-linearity for reads made very close together in time; the amplitude of this non-linearity typically amounts to only a few electrons accumulated over an entire set of 25 non-destructive readouts in the brightest parts of the amplifier glow signal, so that our detection of this non-linearity is marginal). It also is constant with temperature, as shown in Figure 7.14.

Figure 7.14: Amplifier glow signal as a function of detector temperature



In contrast to the shading, the amplifier glow is a photon signal, and thus is subject to Poisson statistics. It therefore contributes to the total noise in NICMOS exposures. For the case of an ACCUM exposure with multiple and initial and final reads (see Chapter 9), the photon noise produced by amplifier glow can outweigh the read noise reduction from the multiple reads, especially close to the array corners producing a total noise reduction never larger than $\sim 40 - 50\%$. Similarly, the trade-off between improved cosmic ray rejection, reduced read noise, and increased photon noise in a MULTIACCUM sequence is complicated.

Overexposure of NICMOS Detectors

Effects of photon and cosmic-ray persistence are described in Chapter 4.

Electronic bars

The "bars" are narrow stripes that cross the quadrants of an array, and occur identically in all 4 quadrants at the same rows/columns in each. It is thought that these bars are caused by pick-up of an amplifier signal on one of the row/column address lines, causing a momentary change in the bias for that pixel.

They typically run the length of a quadrant (128 pixels), and are 3 pixels wide - the first pixel is lower than the mean, the second is at the mean level and the third is higher than the mean, giving the impression of an undersampled sinusoidal spike with an amplitude of up to ~10 DN peak-to-peak. If a bar appears in the 0th readout, it will be subtracted from all the other readouts as part of the normal calibration process, and will appear to be the negative of the above description. The bars are almost always broken in at least one place, with a shift of 2-10 pixels in the narrow direction. These sometimes correspond loosely with the breaks in the "bias jump" bands in the last readout of a MULTIACCUM sequence, indicating they may be related to the same electronic phenomenon.

The bars run parallel to the slow readout direction, which is vertical in NIC1, and horizontal in NIC2 and NIC3. Normally there is only one bar per quadrant, but occasionally there are more, always reflected in all 4 quadrants. Sometimes the bars will be "in synch" and appear at the same place in successive or every other readout, or may appear to march across the frame over the course of a MULTIACCUM sequence. A more detailed description of the electronic bars is given in the NICMOS WWW site:

http://www.stsci.edu/ftp/instruments/nicmos/nicmos_anomalies.html

We are currently working on an observing procedure to reduce/eliminate the electronic bars for observations in Cycle 10 and beyond. This procedure will be completely transparent to users.

Bad Pixels

Hot pixels are pixels with excessive charge compared to the surrounding pixels, while cold pixels are less sensitive than the surrounding pixels or have no sensitivity. Many of these pixels were identified during the Thermal Vacuum testing performed on the ground in August 1996. A statistics of the hot/cold pixels in the three NICMOS cameras is given in Table 7.2. The best way to minimize the effect of hot or cold pixels is to dither the observations

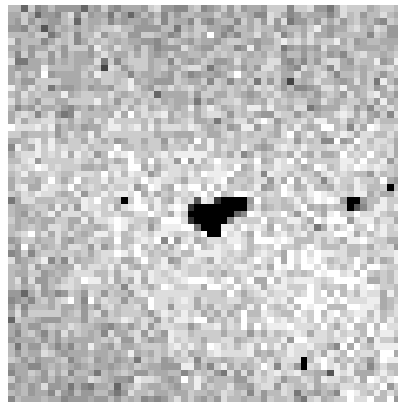
Table 7.2: Hot and Cold Pixels in NICMOS

Pixel Characteristics	NIC1	NIC2	NIC3
Cold	68	94	17
Hot	10	11	3

"Grot"

Flat fields taken on orbit show a population of pixels with very low count rates. It is believed that the bad pixels are caused by debris lying on top of the detectors. Paint flakes from the optical baffles are one possible source of this debris. The largest of these areas of bad pixels occurs in NIC1 and is shown in Figure 7.15 below. Approximately 100 - 200 pixels in each of NIC1, NIC2 and NIC3 are affected by this debris. Dithering is recommended for observers who believe that these and other pixel defects could adversely affect their science goals. We expect the "grot" to be present in cycle 10 as it was in Cycle 7 and 7N.

Figure 7.15: A portion of a NIC1 flat field image shows the largest of the groups of pixels affected by debris ("grot"). This bit of "grot" is roughly 5 by 9 pixels and is located in the upper left quadrant of NIC1.



Detector Readout Modes

In This Chapter...

Introduction / 127
Accumulate Mode / 130
Multiple-Accumulate Mode / 133
MULTIACCUM Predefined Sample Sequences (SAMP-SEQ) / 134
Trade-offs Between ACCUM and MULTIACCUM / 137
Read Times and Dark Current Calibration in ACCUM Mode / 138
Acquisition Mode / 139

The NICMOS flight software supports several detector readout modes which take advantage of the non-destructive read capabilities of the detectors to yield the optimum signal to noise for science observations. These are described in detail in this chapter. In describing these we introduce the nomenclature used to command each of the modes in the Phase II proposal instructions.



Nearly all observers should use the MULTIACCUM mode.

Introduction

NICMOS has four detector readout modes that may be used to take data. After observing time has been approved, the choices of readout mode can be selected by the observer when completing the Phase II proposal entry.

However, a potential observer must understand the advantages and limitations of each of the readout modes in order to properly design their Phase I proposal. Since BRIGHTOBJ is an available mode (i.e., not supported by STScI), the necessity for its use should be spelled out in the Phase I proposal. Efficiency is not a reason to use an available mode. In addition the RAMP readout mode is obsolete and no longer offered.

There are three supported readout options within this general framework:

1. Multiple-accumulate Mode.
2. Accumulate Mode.
3. Acquisition Mode.

The basic scientific rationale behind each of these modes, and a summary of their capabilities is outlined in Table 8.1, along with a recommendation regarding their use. The Phase II proposal instructions needed to identify the readout modes are given in brackets under the mode name.

Table 8.1: Readout Modes and their Functions

Mode	Use	Functionality	Recommendation
Accumulate (ACCUM)	Simplest observing mode Produces a single image May help ease data volume constraints	Can reduce noise by performing and averaging multiple initial and final readouts $t > 0.57$ seconds Limited to 173 tabular integration times, 32 of which may have matched dark current calibrations.	MULTIACCUM mode is preferred.
Multiple-Accumulate (MULTIACCUM)	Faint targets Large dynamic range Optimal image construction. Ground processing of cosmic rays and saturation. Long wavelength integrations	Multiple readouts at specific times during an integration $8590 > t > 0.215$ seconds Number of readouts ≤ 25	Suitable for most programs. Use whenever high dynamic range need e.g., source with bright core and faint extended emission or long integrations times.
Onboard Acquisition (ACQ)	Locate brightest source in a subarray and reposition telescope to place source behind coronagraphic spot	ACCUM exposures are obtained, combined with cosmic ray rejection, hole located, sources located and centered.	Reasonably bright sources on uncrowded fields. See Chapter 5 for more details.
Bright Object (BRIGHTOBJ)	For coronagraphic acquisition of bright targets which would saturate the arrays in the other modes with the shortest integration time allowed	reset/read/wait/read each pixel sequentially in a quadrant $t < 0.2$ seconds	When possible use a narrow filter with ACCUM or MULTI-ACCUM instead

Table 8.1: Readout Modes and their Functions

Mode	Use	Functionality	Recommendation
Ramp (RAMP)	Faint targets Large dynamic range Uncertain target flux On-board cosmic ray removal On-board saturation detection	Slope computation Reduces Data Volume Provides Variance and valid samples array $t > 50$ seconds number of readouts ≤ 50	MULTIACCUM superior. This mode is not offered in Cycle 10 and beyond.



The BRIGHTOBJ mode is not supported for Cycle 10; it is, however, an available mode for the special case of acquisition of very bright targets under the coronagraphic spot. See Appendix 3 for a more detailed description of this mode.



The RAMP mode is obsolete and MULTIACCUM is far superior in performance. Therefore, the RAMP mode is not offered for science observations and has not been calibrated or characterized. It is not described further.

Detector Resetting as a Shutter

It is important to remember that NICMOS *does not have a physical shutter mechanism*. Instead, the following sequence of operations are performed to obtain an exposure:

- **Array reset:** All pixels are set to zero—the bias level.
- **Array read:** The charge in each pixel is measured and stored in the on-board computer's memory. This happens as soon as practical after the array reset. In effect, a very short exposure image is stored in memory.
- **Integration:** NICMOS exposes for the period specified for the integration.
- **Array read:** The charge in each pixel is measured and stored in the on-board computer's memory.

Fast and Slow Readout Modes

The NICMOS detectors have two readout speeds: FAST and SLOW. The use of SLOW mode imposes a 3 second readout overhead which increases the minimum possible integration time (to slightly more than 3 seconds).

When multiple readouts are obtained in ACCUM mode, the readout overhead becomes rather large (e.g., 30 seconds at the beginning and end of an exposure for NREAD=10 making 60 seconds the minimum exposure time).



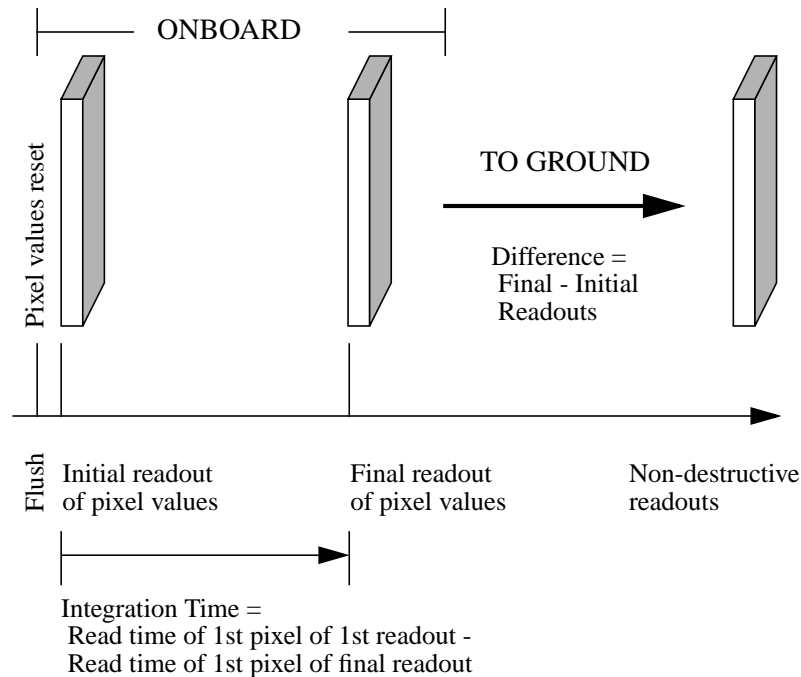
Observers should use the FAST readout mode. No significant advantages results from using SLOW readout mode, and calibrations for that mode were not obtained during Cycles 7 and 7N and are not planned for Cycle 10.

Accumulate Mode

The *Accumulate Readout Mode* (ACCUM) generates the simplest basic exposure. In its simplest incarnation, *two sample readout*, illustrated in Figure 8.1 it is analogous to a WFPC2 readout. This simple two sample readout strategy is the one to use for short integrations of relatively bright objects, and when you are observing in the background limited regime at long wavelengths. This section is therefore a good place to start to get familiar with the concepts inherent in the operation of the NICMOS arrays, including their *non-destructive readout capabilities*. The allowed ACCUM mode integration times are restricted to 173 tabular values. Furthermore, as described on page 192, only a maximum of 32 of these will have matched dark calibration frames.

The first action of an ACCUM exposure is three passes through the detector *resetting* each of the pixels. The *reset* is immediately followed by a fourth pass through the detector *non-destructively reading* and storing the pixel values. This marks the beginning of the integration. The final action is a second non-destructive reading of the detector, which marks the end of the integration. *The returned image is the difference between the second and the first pass pixel values, and the integration time is defined as the time between the first and second read of the first pixel.* The minimum exposure time is ~ 0.6 sec, and the minimum time between successive exposures is ~ 8-12 seconds. It has the minimum time for output amplifier operation which minimizes the amplifier glow contribution to the image (see below). This method does not discriminate against cosmic ray events or check for saturation levels in the image onboard the spacecraft.

Figure 8.1: Basic NICMOS Readout—Simple Two-Sample Readout



Flush time is 0.615s and is followed immediately by the Initial Readout.

Multiple Initial and Final Sample Readout

The observer has the option of requesting *multiple reads* in place of the single initial and final readouts in ACCUM mode. In this case after the detector array is reset it will be followed by 1–25 (specified by the NREAD parameter) reads of the initial pixel values which are averaged onboard to define the initial signal level. After the exposure time has elapsed, the final pixel values are again read NREAD times and averaged onboard. The data downlinked is the difference between the initial and final average signal levels for each pixel. The integration time is defined as the time between the first read of the first pixel in the initial NREAD passes and the first read of the first pixel in the final NREAD passes. The use of multiple reads in ACCUM mode is illustrated in Figure 8.2 for the case of NREAD = 4.

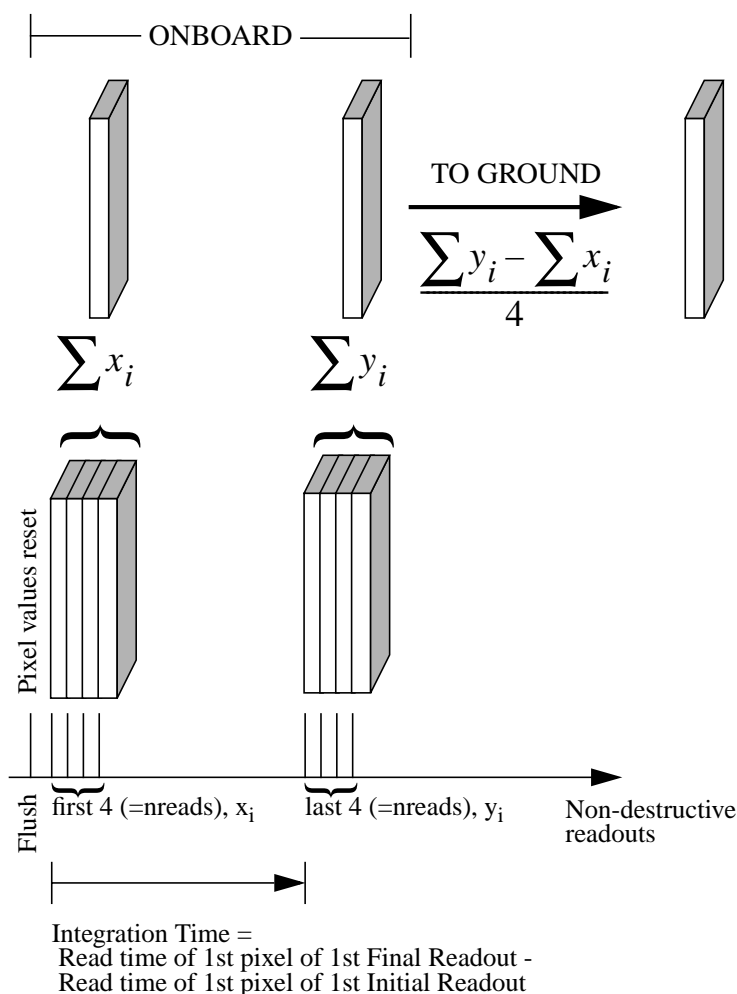


For Cycle 10 only NREAD =1 or 9 is supported (any other values are considered “available”—unsupported—modes).

The advantage of this method is a reduction in the read noise associated with the initial and final reads, which can reduce the noise in intermediate time integrations on faint sources. In theory the read noise should be

reduced by $1/(n)^{1/2}$ where n is the number of reads. However, the amplifier glow (Chapter 7), adds extra signal and associated photon noise close to the corners of the array, which is important when multiple readouts are made. Amplifier glow is an additive noise source large enough that for $NREAD > 9$ there is little further gain in noise. In practice, the maximum improvement in effective read noise over a single initial and final read is no larger than a factor 40-50%, due to the added amplifier glow that each read-out adds to the final noise budget. For integrations where source photon noise or dark current noise exceeds the detector read noise the multiple readouts may not offer much advantage. This option puts a higher burden on the CPU and requires an additional time per readout of 0.3 seconds in FAST mode. This mode does not discriminate against cosmic ray events and does not check for saturation onboard the spacecraft.

Figure 8.2: ACCUM Mode with Four Initial and Final Readouts



Multiple-Accumulate Mode

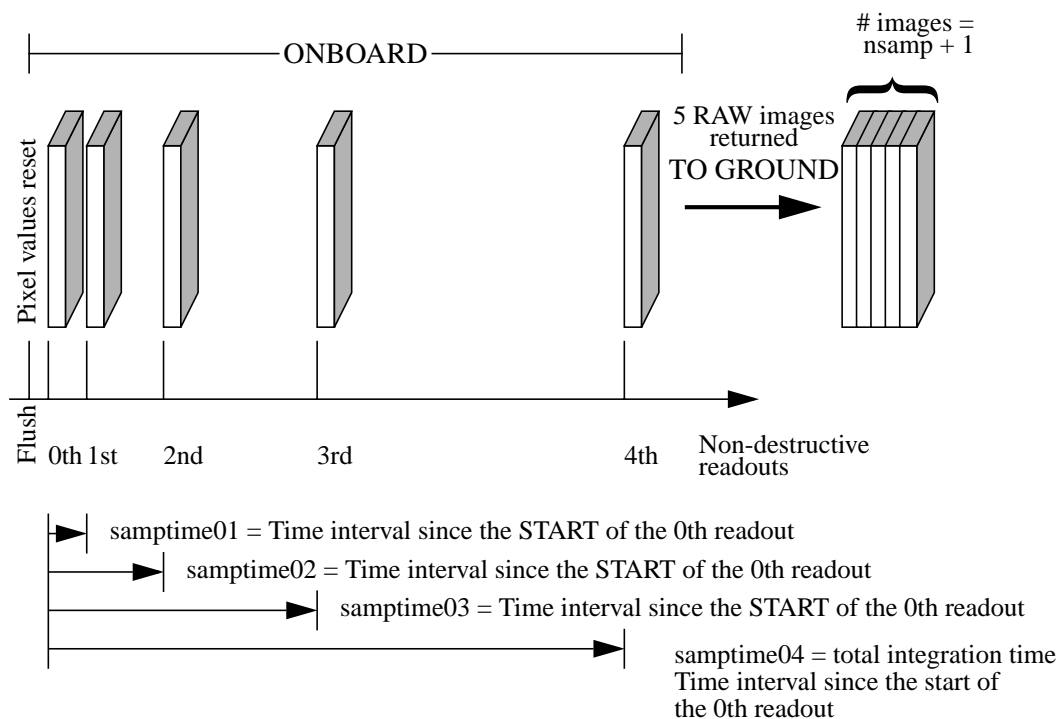
Normally a single integration on a target results in a single 256x256 image at the termination of the exposure. The non-destructive nature of the NICMOS readout offers more elaborate methods of using the instrument which aim to optimize the scientific content of the results. In particular it is possible to read-out images at intermediate stages of an integration and *return both these and the final image to the ground*. In this mode of operation, known as *Multiple-Accumulate* (MULTIACCUM), each intermediate readout can only consist of a single readout. The observer uses this capability by creating a list of times, specified by the SAMP-TIME parameters, at which the detector pixels are read out non-destructively creating images of various integration times. The choice of the times during the integration in which the observer can create these reads is very flexible, for example they might be linearly spaced or logarithmically spaced. Linearly spaced exposures may be useful for very faint targets where cosmic ray filtering is important while logarithmically spaced exposures permit the observation of a very wide dynamic range. The process is shown schematically in Figure 8.3 for the case of logarithmically spaced intervals with NSAMP=4. In MULTIACCUM the detector reset is followed by a single read of the initial pixel values. Then a sequence of non-destructive array readouts are obtained at observer specified times. Up to 25 readouts can be specified spanning a total integration time from 0.203 seconds to 8590.0 seconds. The last read of the detector array ends the exposure and thus the last SAMP-TIME will be equal to the total exposure time. All of the readouts, including the initial readout, are stored and downlinked without any onboard processing. This is different to ACCUM mode as the initial read is also returned and no on board subtraction occurs. For N readouts, this mode requires the storage and transmission (downlink) of $N+1$ times as much data volume for ACCUM mode.

MULTIACCUM mode arguably provides the highest quality scientific data in return. The benefits of obtaining observations in MULTIACCUM mode fall into two areas.

- The dynamic range of the observation is greatly increased. Rather than being limited by the charge capacity of a NICMOS pixel (a few $\times 10^5$ electrons), an observation's dynamic range is in principle limited by the product of the pixel capacity and the ratio of the longest and shortest exposures (8590.0 and 0.203 seconds). In practice, the PSF and internal stray light will probably be the limiting factors.
- An image can be reconstructed by processing of the stack of readouts to cope with the effects of cosmic ray particle events, as well as saturation.

MULTIACCUM provides the best choice for deep integrations or integrations on fields with objects of quite different brightness except when the background signal is so bright that it requires the use of short exposures where the background of the telescope dominates the signal. *In the absence of compelling reasons, observers should use MULTIACCUM for all observations.*

Figure 8.3: Example MULTI-ACCUM with NSAMP = 4



MULTIACCUM Predefined Sample Sequences (SAMP-SEQ)

While it is possible to specify MULTIACCUM observations with nearly any set of up to 25 readout times, such usage results in a requirement to send excessive volumes of commanding information up to HST. Accordingly, STScI and the NICMOS IDT defined a set of sequences which should cover nearly all applications of MULTIACCUM. These are defined in Table 8.2. The observer specifies the name of the sequence and the number of samples to be obtained. The SCAMRR and MCAMRR are to be used when the fastest temporal sampling is desired. The SPARS64 and SPARS256 sequences have relatively few readouts and may be helpful when two or more cameras are operated in parallel (in particular they

generally permit a second and third camera to operate in parallel with a minimal impact on the operation of the primary camera). They are also recommended for observations of fields where only faint targets are present. The STEPXX sequences all start with three rapid readouts and then are logarithmically spaced to provide a large dynamic range up to their defined time (e.g., STEP64 has log steps up to 64 seconds) and then revert to linear spacing. The STEPXX sequences are recommended for observations involving both bright and faint targets, where high dynamic range is required. The use of the MIF sequences is not recommended because the multiple initial and final reads induce additional read-out noise without much advantage over other sequences.

Table 8.2: MULTIACCUM SAMP-SEQs

Sequence Name	Readout Times					Description
SCAMRR	0.203	0.406	0.609	0.812	1.015	Single camera faster possible operation
	1.218	1.421	1.624	1.827	2.030	
	2.233	2.436	2.639	2.842	3.045	
	3.248	3.451	3.654	3.857	4.060	
	4.263	4.466	4.669	4.872	5.075	
MCAMRR	0.303	0.606	0.909	1.212	1.515	Fastest possible operation with 2 or 3 cameras used in parallel
	1.818	2.121	2.424	2.727	3.030	
	3.333	3.636	3.939	4.242	4.545	
	4.848	5.151	5.454	5.757	6.060	
	6.363	6.666	6.969	7.272	7.575	
STEP1	0.303	0.606	0.995	1.993	2.991	Rapid reads up to 1 second then 1 second steps
	3.989	4.987	5.985	6.983	7.981	
	8.979	9.977	10.975	11.973	12.971	
	13.969	14.967	15.965	16.963	17.961	
	18.959	19.957	20.955	21.953	22.951	
STEP2	0.303	0.606	0.995	1.993	3.987	Rapid reads up to 2 seconds then 2 second steps
	5.981	7.975	9.969	11.963	13.957	
	15.951	17.945	19.939	21.933	23.927	
	25.921	27.915	29.909	31.903	33.897	
	35.891	37.885	39.879	41.873	43.867	
STEP8	0.303	0.606	0.995	1.993	3.987	Rapid reads up to 8 seconds then 8second steps
	7.981	15.975	23.969	31.963	39.957	
	47.951	55.945	63.939	71.933	79.927	
	87.921	95.915	103.909	111.903	119.897	
	127.891	135.885	143.879	151.873	159.867	
STEP16	0.303	0.606	0.995	1.993	3.987	Rapid reads up to 16 seconds then 16second steps
	7.981	15.975	31.969	47.963	63.957	
	79.951	95.945	111.939	127.933	143.927	
	159.921	175.915	191.909	207.903	223.897	
	239.891	255.885	271.879	287.873	303.867	

Table 8.2: MULTIACCUM SAMP-SEQs (Continued)

Sequence Name	Readout Times					Description
STEP32	0.303	0.606	0.995	1.993	3.987	Rapid reads up to 32 seconds then 32 second steps
	7.981	15.975	31.969	63.969	95.969	
	127.969	159.969	191.969	223.969	255.969	
	287.969	319.969	351.969	383.969	415.969	
	447.969	479.969	511.969	543.969	575.969	
STEP64	0.303	0.606	0.995	1.993	3.987	Rapid reads up to 64 seconds then 64second steps
	7.981	15.975	31.969	63.969	127.967	
	191.965	255.963	319.961	383.959	447.957	
	511.955	575.953	639.951	703.949	767.947	
	831.945	895.943	959.941	1023.939	1087.937	
STEP128	0.303	0.606	0.995	1.993	3.987	Rapid reads up to 128 seconds then 128 second steps
	7.981	15.975	31.969	63.969	127.967	
	255.961	383.955	511.949	639.943	767.937	
	895.931	1023.925	1151.919	1279.913	1407.907	
	1535.901	1663.895	1791.889	1919.883	2047.877	
STEP256	0.303	0.606	0.995	1.993	3.987	Rapid reads up to 256 seconds then 256 second steps
	7.981	15.975	31.969	63.969	127.967	
	255.961	511.961	767.961	1023.961	1279.961	
	1535.961	1791.961	2047.961	2303.961	2559.961	
	2815.961	3071.961	3327.961	3583.961	3839.961	
MIF512	0.303	0.606	0.909	1.212	1.515	Eight rapid readout at start and end with 7 evenly spaced readouts over 512 seconds
	1.818	2.121	2.424	31.994	63.994	
	127.992	191.990	255.988	319.986	383.984	
	447.982	511.980	512.283	512.586	512.889	
	513.192	513.495	513.798	514.101	514.404	
MIF1024	0.303	0.606	0.909	1.212	1.515	Eight rapid readout at start and end with 7 evenly spaced readouts over 1024 seconds
	1.818	2.121	2.424	63.999	127.997	
	255.991	383.985	511.979	639.973	767.967	
	895.961	1023.955	1024.258	1024.561	1024.864	
	1025.167	1025.470	1025.773	1026.076	1026.379	
MIF2048	0.303	0.606	0.909	1.212	1.515	Eight rapid readout at start and end with 7 evenly spaced readouts over 2048 seconds
	1.818	2.121	2.424	127.995	255.989	
	511.989	767.989	1023.989	1279.989	1535.989	
	1791.989	2047.989	2048.292	2048.595	2048.898	
	2049.201	2049.504	2049.807	2050.110	2050.413	
MIF3072	0.303	0.606	0.909	1.212	1.515	Eight rapid readout at start and end with 7 evenly spaced readouts over 3072 seconds
	1.818	2.121	2.424	127.995	255.989	
	639.988	1023.987	1407.986	1791.985	2175.984	
	2559.983	3071.981	3072.284	3072.587	3072.890	
	3073.193	3073.496	3073.799	3074.102	3074.405	
SPARS64	0.303	0.606	63.994	127.992	191.990	Similar to STEP64 but without the rapid initial readouts
	255.988	319.986	383.984	447.982	511.980	
	575.978	639.976	703.974	767.972	831.970	
	895.968	959.966	1023.964	1087.962	1151.960	
	1215.958	1279.956	1343.954	1407.952	1471.950	

Table 8.2: MULTIACCUM SAMP-SEQs (Continued)

Sequence Name	Readout Times					Description
SPARS256	0.303	0.606	255.996	511.996	767.996	Similar to STEP256 but without the rapid initial read-outs
	1023.996	1279.996	1535.996	1791.996	2047.996	
	2303.996	2559.996	2815.996	3071.996	3327.996	
	3583.996	3839.996	4095.996	4351.996	4607.996	
	4863.996	5119.996	5375.996	5631.996	5887.996	

Trade-offs Between ACCUM and MULTIACCUM

Given that there is so much more information present in a MULTIACCUM dataset than in an ACCUM dataset, it may seem obvious that MULTIACCUM should always be the preferred readout mode. In practise, the trade-off is not always so straightforward.

Because of the fixed read-out patterns available for use in MULTIACCUM mode (the SAMP-SEQs), in order to make an exposure of total integration time a minute or two, it is necessary in most modes to make a significant number of readouts. This leads to a significant volume of data to process. Additionally, the readouts are initially stored in a buffer in the NICMOS flight computer. A maximum of 94 readouts can be stored in this buffer, after which the content of the buffer must be dumped to the Solid State Recorder. A full dump of 94 reads takes about three minutes. The data dumps occur in parallel with the beginning of another set of exposures in most, but not all, circumstances. Thus, during the preparation of the Phase 2 proposals, some observers with very short (1-2 minutes) exposures may consider the trade-offs between ACCUM and MULTIACCUM.

There are a variety of disadvantages to ACCUM mode. First, the ability present in a MULTIACCUM exposure to filter out CR hits which occur during the exposure is lost. We find for NICMOS that typically between 2 and 4 pixels are hit per second per camera by CRs: most of these are low energy and so can be filtered out of a MULTIACCUM exposure by the calibration pipeline software. In ACCUM mode the process of CR removal requires separate exposures, and is a time consuming piece of post-processing as it is for WFPC2. Second, the ability to detect pixel saturation, which again is done automatically for MULTIACCUM observations by the calibration software, can in some circumstances be lost in ACCUM mode. The reason for this is that the time elapsed between the first read for each pixel and the reset immediately prior to the read is approximately 0.2 seconds. During this time, pixels exposed to a bright target will accumulate significant signal, which is then present in the first read. When this is subtracted on-board in ACCUM mode, all the charge

accumulated in the time between reset and read will be subtracted. If the pixel has saturated during the exposure, the difference between initial and final reads will be less than the expected saturation value for the pixel, and thus it may be impossible to recognize that the pixel is saturated. Thus in the case of bright targets, erroneous signal levels may be recorded in ACCUM mode. Third, in ACCUM mode, even if pixel saturation is detected, it is not possible to repair the data obtained in the saturated pixel. In MULTIACCUM mode, pixels which have saturated can be repaired by using the results of previous, unsaturated reads during the same exposure.

In conclusion, in cases where a multitude of short duration exposures must be made per orbit, and data volume is therefore a problem, ACCUM may possibly (but not necessarily) be a good choice. In all other cases it is likely that MULTIACCUM will yield the best results, and we recommend that all observers attempt to use MULTIACCUM.

Read Times and Dark Current Calibration in ACCUM Mode

Because of the effects of shading, and the possibility that the underlying dark current may vary with time since reset, the removal of dark current (for calibration purposes, we implicitly assume shading and amplifier glow is a part of the time variable “dark current”) from data is more complicated than for many other instruments. The most accurate way to remove the dark current from any observation is a measurement of the dark current with an identical integration time. This would also apply to every individual read-out in a MULTIACCUM observation. Of course, this would be prohibitively expensive in on-orbit calibration time. Instead, we have adopted two strategies. First, for ACCUM observations we will make dark current calibration observations for a set of 8 exposure times for a single initial and final read (listed below) and 14 exposure times for 9 initial and final reads. As for WFPC2, only a certain set of exposure times are allowed in ACCUM mode (173 times are specified currently, ranging from 0.57 seconds to 3600 seconds), and in Phase II proposals any user selected exposure time will be rounded down to the nearest available option from the 173 available times. If one of the times listed below is selected (this list will be published with the Phase II Proposal Instructions), then the calibration database used by the calibration pipeline software will contain dark current calibration files which are an exact match to the chosen exposure times. On the other hand, if any other one of the 173 allowed exposure times in ACCUM mode need to be used, the calibration pipeline will interpolate between the various files in the database to determine the dark current for the chosen exposure time. Based on our understanding of the instrument, this is not a very accurate technique and residuals from

poor dark subtraction will be present in the final images. We therefore discourage observers to use ACCUM times other than those listed below (except for target acquisition in coronagraphic observations). If other ACCUM exposure times must be used, observers should also obtain their own calibrations. For MULTIACCUM mode, dark calibrations will be made to match each of the 16 SAMP-SEQs. Finally, we note that SLOW readout mode is not supported and no calibration of this mode will be provided by STScI.

Table 8.3: Preliminary Exposure Times with Dark Current Calibration

Time (seconds) (NREAD=1)	Time (seconds) (NREAD=9)
1.071	9.939
2.038	12.075
4.963	15.157
9.715	18.339
25.714	22.533
58.142	30.274
110.246	44.969
229.680	62.702
	88.335
	114.806
	163.642
	234.240
	365.156
	485.148

Acquisition Mode

Images obtained using the coronagraph in Camera 2 may be taken using any of the detector read-out modes. An ACQ mode observation performs an autonomous on-board acquisition (Mode-2 Acquisition) for subsequent coronagraph images. This mode is described in detail in Chapter 5 (Coronagraphy).

How to Plan an Observation

The chapters in this part provide the details of how to construct a NICMOS observation: exposure time calculations; overheads and orbit time determinations; and a description of observing techniques for dithering, measuring the background, and mapping extended targets.

Exposure Time Calculations

In This Chapter...

Overview / 143

Calculating NICMOS Imaging Sensitivities / 147

WWW Access to the Exposure Time Calculator / 152

In this chapter we provide information needed to estimate exposure times for NICMOS Cycle 10 Phase I proposals. We provide some general comments about NICMOS imaging exposure time issues. We then describe how to use the Web-based NICMOS Exposure Time Calculator (ETC). At the time of this writing, imaging is the only capability implemented on the ETC; we plan to have an ETC for spectroscopic (grism) observations on time for the Cycle 10 Call for Proposals. We use expected instrument performance characteristics under NCS operations. These will be updated as more in-flight information becomes available. The estimation of read noise for multiple initial and final reads also differs significantly from earlier versions of the ETC: we include more realistic values than were hitherto available.

Reference sensitivity curves are also given in Appendix 1 for imaging (including polarizers), and in Chapter 5 for grism spectroscopy.

Overview

We describe some instrument-specific behavior which must be taken into account when estimating required exposure times. The WWW NICMOS ETC provides the most convenient means of estimating count rates and signal-to-noise ratios (SNRs) for imaging observations. The user

provides an estimate of the flux and spectral shape of the source by means of a Web-based form, and sets the instrument configuration parameters (camera number, filter used, independent exposures and the number of initial and final reads for the MULTIACCUM sequence in MIF mode) to be used. The ETC handles either point sources or extended objects with a user-specified diameter.

The user requests either the exposure time required for a user-defined SNR or the expected SNR for a user-defined exposure time. The ETC will then estimate the requested exposure time or SNR when the request is submitted. The results can be used to plan observations. It will also indicate the read noise-limited and saturation-limited exposure times for the object in question.



The WWW NICMOS Exposure Time Calculator (ETC) should be regarded as the tool of choice for estimating integration times for NICMOS observations. The ETC provides the most accurate estimates; its reference tables are constantly updated with the most recent values of the instrument's characteristics as our knowledge of the NICMOS performance under NCS operations improves.

A few comments about the limitations of making exposure time and SNR estimates are in order here.

NICMOS performance will change in Cycle 10 (relative to previous values) because the instrument will be operated at a different temperature with the NCS. This is expected to increase the DQE, but also increase the dark current. The exact performance characteristics are not currently known, and will not be known accurately until the revitalized instrument is tested in flight during SMOV after the NCS is installed. The ETC incorporates our best guess at the likely worst-case instrumental performance at the new operating temperature, and it will be updated after SMOV. We also provide an estimate of the best possible SNR using best-case figures for the DQE and dark current.

The instrumental characteristics used by the ETC are *average* values across the field of view of the camera. The actual sensitivity will vary across the field. The HgCdTe arrays in NICMOS have a fairly substantial spatial variation in their DQE (i.e. flatfield) --- at the shortest wavelengths the pixel-to-pixel variation between the minimum and maximum DQE is as much as a factor of four. This means that imaging sensitivity will vary over the chip. For photon-limited observations it will vary as the square root of the local DQE, and for read noise-limited observations it will vary as the DQE itself. A second source of spatial variation comes from the fact that dark current in these detectors is not constant over the chip: there is a substantial increase in the dark current near the corners of the chip because of amplifier glow.

The ETC will calculate SNR or exposure time as requested, for the requested number of end-point reads. Signal is the number of electrons in the peak pixel, and noise is the standard deviation in a pixel due to photon statistics and instrumental noise. We also provide an estimate of the total SNR (for fixed exposure time) or necessary exposure time (for fixed SNR) for point sources in 0.5", 0.5" and 1" apertures for NIC1, NIC2, and NIC3, respectively. For point sources, the ratio of signal in the peak pixel to the total signal is also provided. For an extended source the point spread function does not enter into the calculation.

For photon-limited observations (limited either by the target count rate or the background), SNR increases as the square root of the total observation time, regardless of how the observation is subdivided into individual exposures. However, some NICMOS observations may be significantly affected by read noise, and the net SNR from the sum of several exposures will depend on the relative contributions of read noise and photon noise.



We stress that there is a limit on how much the read noise can be reduced using multiple initial and final reads: the read noise goes down from about 30 e- with one read at the start and one at the end of the exposure (this corresponds to a 'CCD exposure'), to about 20 e- with 9 initial and 9 final reads. Increasing the number of end-point reads does not bring the read noise of the averaged exposures down any further, due in part to the increased amplifier glow during multiple reads (Chapter 8 and Chapter 9). This sort of behavior is common to all NICMOS detectors.

An empirical rule for the decrease in read noise with number of reads is used in the ETC.

Phenomena such as cosmic ray persistence (Chapter 4) can degrade sensitivity for faint object imaging by increasing the level of background noise. The impact of cosmic ray persistence is not easily quantified because it is non-Gaussian, correlated noise. It is not possible to predict the extent of this effect at the time the observations are planned, so it is not included in the ETC calculations.

Instrumental Factors

Detectors

The detector properties which will affect the sensitivity are simply those familiar to ground-based optical and IR observers, namely dark current and read noise, and the detector quantum efficiency (DQE). Expected characteristics for NICMOS are described in Chapter 8 (Table 8.1).

Optics

NICMOS is a relatively simple instrument in layout, and thus contains a fairly small number of elements which affect the sensitivity. These are the filter transmission, the pixel field of view (determined by the NICMOS optics external to the dewar, in combination with the HST mirrors), the reflectivities of the various external mirrors and the transmission of the dewar window.

The filter transmissions as function of wavelength were measured in the laboratory, and the resulting curves are presented in Appendix 1, convolved with OTA, NICMOS fore-optics and detector's response. There are no appreciable out-of-band leaks in the NICMOS filters (Chapter 4).

NICMOS contains a total of seven mirrors external to the dewar, each of which reduces the signal received at the detector. The mirrors have protected silver coatings (except for the field divider assembly which has a gold coating) for maximum reflectivity, and have 98.5% reflectivity. The dewar window has a transmission of roughly 93%. Therefore, the combination of optical elements is expected to transmit ~84% of the incoming signal from the OTA.

The sensitivity will obviously be affected by the pixel field of view. The smaller the angular size of a pixel, the smaller the fraction of a given source that will illuminate the pixel. Finally, the optical efficiency will be degraded further by the reflectivities of the aluminum with MgF_2 overcoated HST primary and secondary mirrors.

Background Radiation

At long wavelengths the dominant effect limiting the NICMOS sensitivity will be the thermal background emission from the telescope. How large this is depends on the areas of the primary and secondary mirror and their optical configuration, temperatures, and emissivities. At shorter NICMOS wavelengths, sensitivities will be affected by the zodiacal background. Both sources of background are described in Chapter 4. In the WWW NICMOS ETC, the contribution of both backgrounds is included in all computations; also, a choice of low, average or high zodiacal background is provided.

Background radiation will be a slightly worse problem in the case of Multi-Object Spectroscopy (MOS) than in the case of imaging observations. Every pixel on the array will always see the entire background radiation integrated over the grism bandpass. The expected detected background rate per pixel is given in Table 5.5 of Chapter 5.

Calculating NICMOS Imaging Sensitivities

In some situations it may be desirable to go through each step of the calculation. One example would be the case of a source with strong emission lines, where one wants to estimate the contribution of the line(s) to the signal. This could include the case of a strong emission line which happens to fall in the wing of a desired filter's bandpass. To facilitate such calculations, we provide in this section recipes for determining the signal to noise or exposure time by hand.

Signal to noise Calculation

The signal, in e^-/s , generated by a continuum source with a Flux

$$F_j[Jy] = \frac{F_{cont}}{10^{-26} W \cdot m^2 \cdot Hz \cdot pixel}$$

is

$$\begin{aligned} C_c &= F_j \gamma_{opt} \gamma_{det} \gamma_{filt} A_{prim} E \\ &= F_j \eta_c [e^-/sec] \end{aligned}$$

where:

γ_{opt} is the transmittance of the entire optical train up to the detector, excluding the filters;

γ_{det} is the detector quantum efficiency;

γ_{filt} is the filter transmittance;

A_{prim} is the unobscured area of the primary;

E is a constant given by:

$$E = 10^{-26} / (h\lambda)$$

where h is Planck's constant and λ the wavelength. (F_j , γ_{opt} , γ_{det} and γ_{filt} are all frequency dependent). The expression for C_c has to be integrated over the bandpass of the filter, since some of the terms vary significantly with wavelength. The value for η_c is listed for each filter in Table 9.1, Table 9.2, and Table 9.3, so that the signal in e^-/sec can be estimated. It should be noted that to determine C_c more accurately, the source flux F_j should be included in the integral over the filter bandpass, since the source flux is bound to be a function of wavelength. For Table 9.1 to 9.3, this has been done assuming a source effective temperature of 5,000K.

For an emission line with intensity I_{ij} (in $W m^{-2} pixel^{-1}$) falling in the bandpass of the filter, the counts in e^-/s are given by:

$$\begin{aligned} C_{line} &= I_{ij} \gamma_{opt} \gamma_{det,\lambda} \gamma_{filt,\lambda} A_{prim} E \\ &= \epsilon_\lambda I_{ij} [e^-/sec] \end{aligned}$$

where E is defined as before. In this case, the detector quantum efficiency and filter transmission are determined for the wavelength λ of the emission line. The values for ϵ_λ are listed in Table 9.1, 9.2, and 9.3.

The total signal generated by the pixel is the sum of the continuum and line signals calculated above, namely $C_s = C_c + C_l$.

Source signal is superimposed on sky background and thermal background from warm optics. At $\lambda > 1.7 \mu\text{m}$ the background is often much brighter than the source. In such cases the observation is background limited, not read noise limited. There is little point in increasing the number of multiple initial and final reads when the observation is background-limited, though multiple exposures and dithering will help cosmic ray removal and correction of other effects such as persistence from previously-observed bright objects.

The other components of unwanted signal are the read noise, N_r , and the dark current, I_d (in $\text{e}^-/\text{s}/\text{pixel}$). By read noise, we mean the electronic noise in the image after the subtraction of two reads of the same pixel, spaced by the time interval which is the first-order analog of a CCD exposure time.



Proposers should always assume the worst case scenario for the NICMOS dark current to calculate exposure times (see Chapter 8 for an explanation of the best and worst dark current scenarios). This corresponds to adopting a dark current of $\sim 2.0\text{--}2.5 \text{ e}^-/\text{s}/\text{pixel}$.

It is now possible to calculate the signal to noise ratio expected for an exposure of duration t seconds, where a number N_{read} of reads are taken before and after the integration. It is:

$$SNR = \frac{C_s t}{\sqrt{(C_s + B + I_d)t + N_r^2 f(N_{\text{read}})}}$$

Where C_s , the count rate in $\text{e}^-/\text{sec}/\text{pixel}$, is the sum of C_c plus C_{line} , B is the background in $\text{e}^-/\text{sec}/\text{pixel}$ (listed in Table 9.1, 9.2, and 9.3), I_d is the dark current in $\text{e}^-/\text{sec}/\text{pixel}$ and N_r is the read-out noise, in e^-/pixel , for one initial and one final read. We represent the effectiveness of multiple initial and final reads at beating down readnoise by the function $f(N_{\text{read}})$, which is unity for $N_{\text{read}} = 1$, and decreases with the number of reads for $N_{\text{read}} \leq 8$. This function is not well determined at present.

It is important to note that in these equations, the flux to be entered (either F_j or I_{ij} or both) is *not* the total source flux, but the flux falling on a pixel. In the case of an extended source this can easily be worked out from the surface brightness and the size of the pixel. For a point source, it will be necessary to determine the fraction of the total flux which is contained

within the area of one pixel and scale the source flux by this fraction. For Camera 1 in particular, this fraction may be quite small, and so will make a substantial difference to the outcome of the calculation. Appendix 1 reports for each filter the fraction of the PSF falling in the brightest pixel assuming a point source centered on the pixel.

The signal to noise ratio evaluated by a fit over the full PSF for point sources would, of course, be larger than this central pixel SNR; this discrepancy will be largest for the higher resolution cameras and for the longest wavelengths. Both Appendix 1 and the WWW NICMOS ETC provide SNRs and exposure times calculated in reference apertures (0.5" for NIC1 and NIC2, 1" for NIC3) to account for this effect.

Saturation and Detector Limitations

Given a particular filter-detector combination and a requested target flux, there is an exposure time above which the observation ceases to be read noise limited. There is also an exposure time above which the detector starts to saturate. The WWW NICMOS ETC will produce these two fluxes or exposure times (as appropriate) when it performs the requested estimation. The sensitivity plots of Appendix 1 report saturation curves.

Exposure Time Calculation

The other situation frequently encountered is when the required signal to noise is known, and it is necessary to calculate from this the exposure time needed. In this case the same elements must be looked up as described above, and the required time can be calculated as:

$$t = \frac{(SNR)^2(C_s + B + I_d) + \sqrt{(SNR)^4(C_s + B + I_d)^2 + 4(SNR)^2 C_s^2 N_r^2 f(N_{read})}}{2C_s^2}$$

Sensitivity curves for fixed SNRs (SNR=3 and SNR=10) are given in Appendix 1 for both point sources and extended sources.

Table 9.1: NIC1 Filter Sensitivity Parameters (per pixel)

Filter name	η_c [e ⁻ /sec/Jy]	ξ [e ⁻ /sec/(W/m ²)]	B [e ⁻ /sec]
F090M	6.69x10 ⁵	1.41x10 ¹⁸	1.05x10 ⁻²
F095N	3.77x10 ⁴	9.56x10 ¹⁷	5.48x10 ⁻⁴
F097N	4.55x10 ⁴	1.19x10 ¹⁷	6.23x10 ⁻⁴
F108N	5.29x10 ⁴	1.74x10 ¹⁸	7.52x10 ⁻⁴
F110M	1.19x10 ⁶	2.66x10 ¹⁸	1.50x10 ⁻²
F110W	3.48x10 ⁶	3.75x10 ¹⁸	4.11x10 ⁻²
F113N	6.39x10 ⁴	2.03x10 ¹⁸	8.10x10 ⁻⁴
F140W	5.54x10 ⁶	8.60x10 ¹⁸	6.33x10 ⁻²
F145M	1.365x10 ⁶	5.55x10 ¹⁸	1.24x10 ⁻⁴
F160W	3.01x10 ⁶	8.46x10 ¹⁸	3.52x10 ⁻²
F164N	1.33x10 ⁵	6.24x10 ¹⁸	1.34x10 ⁻³
F165M	1.50x10 ⁶	8.00x10 ¹⁸	1.65x10 ⁻²
F166N	1.30x10 ⁵	6.16x10 ¹⁸	1.28x10 ⁻³
F170M	1.57x10 ⁶	8.54x10 ¹⁸	2.37x10 ⁻²
F187N	1.41x10 ⁵	8.17x10 ¹⁸	7.93x10 ⁻³
F190N	1.40x10 ⁵	8.53x10 ¹⁸	9.80x10 ⁻³
POL0S	1.13x10 ⁶	1.21x10 ¹⁸	2.70x10 ⁻²

Table 9.2: NIC2 Filter Sensitivity Parameters (per pixel)

Filter Name	η_c [e ⁻ /sec/Jy]	ξ [e ⁻ /sec/(W/m ²)]	B [e ⁻ /sec]
F110W	4.28x10 ⁶	4.42x10 ¹⁸	0.14
F160W	3.48x10 ⁶	9.80x10 ¹⁸	0.12
F165M	1.75x10 ⁶	9.33x10 ¹⁸	5.57x10 ⁻²
F171M	6.80x10 ⁵	8.76x10 ¹⁸	2.99x10 ⁻²
F180M	6.46x10 ⁵	9.30x10 ¹⁸	5.06x10 ⁻²
F187N	1.66x10 ⁵	9.54x10 ¹⁸	2.72x10 ⁻²
F187W	1.84x10 ⁶	9.83x10 ¹⁸	0.40
F190N	1.61x10 ⁵	9.93x10 ¹⁸	3.38x10 ⁻²
F204M	8.90x10 ⁵	1.24x10 ¹⁹	1.00
F205W	5.38x10 ⁶	1.87x10 ¹⁹	22.8
F207M	1.19x10 ⁶	1.16x10 ¹⁹	2.48
F212N	1.79x10 ⁵	1.17x10 ¹⁹	0.51
F215N	1.64x10 ⁵	1.14x10 ²⁰	0.60
F216N	1.78x10 ⁵	1.22x10 ¹⁹	0.69
F222M	1.22x10 ⁶	1.29x10 ¹⁹	9.26
F237M	1.37x10 ⁶	1.81x10 ¹⁹	35.6
POL0L	8.81x10 ⁵	7.07x10 ¹⁸	1.56

Table 9.3: NIC3 Filter Sensitivity Parameters (per pixel)

Filter Name	η_c [e ⁻ /sec/Jy]	ξ [e ⁻ /sec/(W/m ²)]	B [e ⁻ /sec]
F108N	5.90x10 ⁴	1.92x10 ¹⁸	1.70x10 ⁻²
F110W	3.70x10 ⁶	3.88x10 ¹⁸	1.03
F113N	7.14x10 ⁴	2.18x10 ¹⁸	1.90x10 ⁻²
F150W	6.39x10 ⁶	9.92x10 ¹⁸	2.32
F160W	3.41x10 ⁶	9.70x10 ¹⁸	0.86
F164N	1.46x10 ⁵	6.94x10 ¹⁸	3.29x10 ⁻²
F166N	1.40x10 ⁵	6.81x10 ¹⁸	3.17x10 ⁻²
F175W	8.97x10 ⁶	1.85x10 ¹⁹	103.4
F187N	1.55x10 ⁵	8.86x10 ¹⁸	0.20
F190N	1.62x10 ⁵	9.90x10 ¹⁸	0.25
F196N	1.72x10 ⁵	1.04x10 ¹⁹	0.48
F200N	1.76x10 ⁵	1.06x10 ¹⁹	0.87
F212N	1.76x10 ⁵	1.18x10 ¹⁹	3.75
F215N	1.62x10 ⁵	1.12x10 ¹⁹	4.42
F222M	1.21x10 ⁶	1.30x10 ¹⁹	69.5
F240M	1.76x10 ⁶	1.79x10 ¹⁹	417.9

WWW Access to the Exposure Time Calculator

Using the NICMOS Imaging Exposure Time Calculator¹

The exposure time calculator provides formal estimates resulting from combining several exposures (e.g. several MULTIACCUM sequences in a dithered pattern), without considering the advantages of, e.g., cosmic ray removal that result from dithered exposures.

The URL for the NICMOS imaging exposure time calculator is

1. At the time of this writing, the NICMOS exposure time calculator is still evolving. The user interface will not differ much from the one illustrated here, though some details (especially units and user-supplied target spectra) may change in the final version of the calculator used for Cycle 10 NICMOS proposal preparation.

<http://www.stsci.edu/instruments/nicmos/etc>

The exposure time calculator web interface is shown in Figure 9.1, and a brief description of the different fields appearing in the Web page follows.

Figure 9.1: The NICMOS WWW ETC

NICMOS Imaging Exposure Time Calculator

This form will calculate the count rates and S/N for a simulated bandpass of ONE source in a NICMOS observation. (For [general help](#) on how to use the Exposure Time Calculator or for help on various topics, click on the appropriate highlighted words. You may also like to see the current known [problems](#) with the ETC.)

1. Select one [Detector](#) and an associated [Filter](#):

☒ NIC1

☐ NIC2

☐ NIC3

2. Specify the [exposure parameters](#):

☒ Exposure time needed to obtain a S/N of

☐ S/N reached in an exposure time of seconds

with exposures

4. [Normalize](#) the target's flux:

Point source with:

☒ $V = 1.0$ or

☐ $1.5 \times 10^{-13} \text{ ergs cm}^{-2} \text{ s}^{-1} \text{ Å}^{-1}$ at Angstroms, or

☐ Do not Renormalize Point Source Spectrum. Use only for User Input Spectra or Calibration Spectra

Extended source with a diameter of arcsec with:

☐ $V/\text{arcsec}^2 = 1.0$ or

☐ $1.5 \times 10^{-13} \text{ ergs cm}^{-2} \text{ s}^{-1} \text{ Å}^{-1} \text{ arcsec}^{-2}$ at Angstroms or

☐ Do not Renormalize Extended Source Spectrum. Use only for User Input Spectra or Calibration Spectra

[E\(B-V\)](#) Average Galactic

5. Specify the expected [background levels](#):

Zodiacal Light Earth-shine

Field 1: The user must choose a camera (NIC1, NIC2 or NIC3) and select the desired filter on the Web page.

Field 2: **Either** the exposure time for a user-specified signal to noise ratio **or** the signal to noise ratio resulting from a user-specified cumulative exposure time must be selected². The number of exposures entered will be combined with additive signal, and noise added in quadrature.

2. It must be stressed that given the realities of near infrared observing, there is much to be gained in terms of robustness of data if multiple exposures of a given target are made (see "Chopping and Dithering Patterns", Chapter 11) under similar conditions, preferably in succession. The formal signal to noise ratio is not the only consideration to be borne in mind when devising an observing strategy.

Field 3: The choice of spectral distribution is made in this section. The choices are self-explanatory.

Field 4: The target flux is specified here by indicating a point source magnitude or an extended object integrated magnitude. If a user-supplied spectrum is provided, the spectrum must not be 'normalized': in this case one should explicitly turn off the normalization in this section. Input units of the spectrum that the user provides are wavelength in Angstroms, and flux (F_λ) in $\text{erg cm}^2 \text{s}^{-1} \text{Angstrom}^{-1}$.

Field 5: Expected background levels from zodiacal contribution at 45 degrees from the ecliptic plane, and average earth-shine. A larger range of choices (low, medium, high background) will be added at a later stage.

The '**Submit Calculation**' button can be pressed at any time to calculate the expected exposure times or signal to noise ratios with the chosen values on the page. If the filter for the chosen camera is the BLANK filter, no throughput is assumed, so the signal will be zero in this case, and any requested exposure time will be infinite.

If the user experiences problem with the ETC or with the interpretation of the output of the calculator, the STScI Helpdesk should be contacted and provided the ETC ID that is shown in the user's Web browser. This information may help STScI personnel to retrieve details of the ETC submission in order to assist the user. Files with this information are retained for a short period of time before being purged from the disks at STScI.

Overheads and Orbit Time Determination

In This Chapter...

Table Overview / 155
NICMOS Exposure Overheads / 156
Orbit Use Determination / 159

In this chapter we describe the overheads associated with NICMOS observations to help distribute observations into orbits.

Overview

Once the set of science exposures and any additional target acquisition or calibration exposures required for the science program have been determined, they must be converted into a total number of orbits. Generally, this is a straightforward exercise involving tallying up the overheads on the individual exposures and on the selected pattern (see Chapter 11), packing the exposure and overhead times into individual orbits, and tallying up the results to determine the total orbit request. This process may need to be iterated, in order to seek the most efficient use of the orbit time.

We refer to the CP/Phase I Proposal Instructions for information on the Observatory policies and practices with respect to orbit time requests and for the orbit determination. Below, we provide a summary of the NICMOS

specific overheads, and give an example to illustrate how to calculate orbit requirements for Phase I Proposals.

NICMOS Exposure Overheads

The overheads on exposures are summarized in Table 10.1. All numbers are approximate and, for the observatory level overheads, rounded up to the nearest half minute. These overhead times are to be used (in conjunction with the actual exposure time and the Cycle 10 Phase I Proposal Instructions) to estimate the total time in orbits for NICMOS proposal time requests. After an HST proposal is accepted, the observer will be asked to submit a Phase II proposal to allow scheduling of the approved observations. At that time the observer will be presented with actual, up to date overheads by the scheduling software. Allowing sufficient time for overhead in the Phase I proposal is important; additional time to cover unplanned overhead will not be granted later.

Overheads can be subdivided into two main categories:

- ***Generic (Observatory Level) Overheads:***
 - The first time an object is acquired, the overhead time for the guide star acquisition must be included.
 - In subsequent contiguous orbits the overhead for the guide star re-acquisition must be included; if the observations are occurring in the continuous viewing zone (CVZ, see the CP/Phase I Proposal Instructions), no guide star re-acquisitions are required.
 - The re-acquisitions can be assumed to be accurate to ≤ 10 milli-arcsecs; thus additional target acquisitions or pickups are not needed following a re-acquisition. However, if doing coronagraphy on a single guide star, a target re-acquisition is strongly encouraged (see Chapter 5).
 - Time must be allowed for each deliberate movement of the telescope; e.g., if a target acquisition exposure is being performed on a nearby star and then offsetting to the target or if a series of exposures in which the target is moved relative to the camera (dithers or chops) are being performed, time for the moves must be allowed
- ***NICMOS Specific Overheads:***
 - The 18 second set-up time at the beginning of each orbit or at each different telescope pointing is inclusive of the filter selection. There is no additional set-up time for new telescope pointings due to dithering or chopping with the same instrument configuration.

- Overheads are operating-mode dependent. In particular, the overhead for the BRIGHTOBJ mode is particularly onerous, since this mode resets and reads each pixel, one pixel at a time.
- The target acquisition overhead of $(157 + 2 \times \text{exptime})$ seconds for coronagraphy needs to be accounted for the first time an object is acquired under the coronagraphic spot. No re-acquisition is required for observing the same target in different filters, or from one orbit to the next, if using two guide stars; see Chapter 5 if using a single guide star. 'Exptime' is the exposure time needed to observe the target outside the coronagraphic spot, for centroiding and acquisition under the spot.
- Overhead times for changing cameras are given in Table 10.2. The values in the Table include the time to perform the Small Angle Maneuver (to change from one camera to the other) and the time for Instrument reconfiguration (to change PAM position). In addition, the observer must include 18 seconds for set-up which includes filter selection.
- The amount of time required to chop depends on the chop throw, and whether an on-target guide star re-acquisition is desired. The telescope can maintain lock on the guide stars if the chop throw is smaller than 1-2 arcminutes. If it is larger, then the observer can choose to maintain pointing through the gyros (DROP-TO-GYRO) or re-acquire the guide stars (3 minute overhead per re-acquisition—note that this is not the 5.3-minute orbit re-acquisition) every time the telescope goes back to the target; with the first option the pointing uncertainty is about 1 milliarcsec/second due to telescope drift. The drop-to-gyro option can be adopted for background pointings, where telescope drift is not a concern.
- In most cases, the data management overhead of 3 minutes will be hidden inside the orbit occultation time or placed in parallel with exposures. The latter, however, does not always happen as the software may not find a good location to place the data management (buffer dump) in parallel. Proposers whose observations require them to obtain multiple sets of 94 read-outs are advised to

include the data management overhead for at least half of the times in their orbit computation.

Table 10.1: NICMOS Overheads

Action	Overhead
<i>Generic (Observatory Level)</i>	
Guide star acquisition	Initial acquisition 7.1 minutes re-acquisitions on subsequent orbits = 5.3 minutes per orbit
Spacecraft POSTARG moves	for offsets less than 1 arcminute and more than 10 arcsecs = 1 minute, for offsets between 10 arcsecs and 1 arcsec = 0.5 minute; for offsets less than 1 arcsec in size = 20 seconds
Slew of x arcsecs to new target within an orbit (slew < 2 arcmin, same guide stars)	(x + 20) seconds
Type 2 Slew to new target within an orbit (slew > 2 arcmin, new guide stars)	<1 degree slew: 2.5 min. + 7.1 min. guide star acq. 1 degree < slew <10 degrees: 5.0 min. + 7.1 min. guide star acq. 10 degrees < slew <100 degrees: 13 min. + 7.1 min. guide star acq.
<i>NICMOS Specific Overheads</i>	
Set-up at beginning of each orbit or at each different telescope pointing - always required. (other than dither/chop maneuvering)	18 seconds
Filter change	16 seconds (shortest 10 seconds, longest 16 seconds)
Exposure overheads: ACCUM FAST readout ACCUM SLOW readout(restricted) MULTIACCUM BRIGHTOBJ	(12 + NREAD * 0.6) seconds (15 + NREAD * 3.3) seconds 9 seconds (exptime x 16384 + 10) seconds
Target acquisition (for coronagraphy)	157 seconds + 2 * exptime seconds (includes slew)
Dithering/Chopping of x arcsecs (< 1-2 arcmin)	(x + 10) seconds
Chopping of x arcsec (> 2 arcmin, using drop-to-gyro)	(x + 31) seconds
Chopping of x arcsec (> 2 arcmin, with guide star re-acquisition)	(x + 31) seconds + 3 minutes for each guide star re-acq
Data management (for every 94 read-outs within an orbit)	3 minutes

Table 10.2: Change of Camera Overheads (seconds)

Going From:	Going To:				
	Coronagraph	NIC 1	Intermediate	NIC 2	NIC 3
Coronagraph	0	40	80	125	620
NIC 1	55	0	40	85	580
Intermediate	95	40	0	45	540
NIC 2	150	95	55	0	285
NIC 3	645	590	550	285	0

Orbit Use Determination

The easiest way to learn how to compute total orbit time requests is to work through examples. We provide below one which should be representative of many types of observations. The example describes a thermal IR observation, with the TWO-CHOP pattern.

Observations in the Thermal Regime Using a Chop Pattern and MULTIACCUM

Observations at long wavelengths will be obtained for target A in all three NICMOS cameras. The F187N filter is used in each of the three cameras in turn. The observer requires exposure times of 128 seconds in each exposure, in MULTIACCUM mode. A good sequence for the target is considered to be STEP8 with NSAMP=21. The target is extended and the selected chopping throw is one detector width. Note that this changes the time to chop for each camera.

The declination of the source is -40 degrees, so the visibility period during one orbit is 59 minutes. The orbit requirement is summarized in Table 10.3 on page 160.

Table 10.3: Orbit Determination for Observations of Target A

Action	Time (minutes)	Explanation
<i>Orbit 1</i>		
Initial Guide Star Acquisition	7.1	Needed at start of observation of new target
Science exposure, NIC1 F187N	2.6	128 seconds exposure time on target 27 seconds for MULTIACCUM overhead
Small Angle Maneuver (chop)	0.4	Move off-target by one field of view
Science exposure, NIC1 F187N	2.3	128 seconds exposure time off target 9 seconds for MULTIACCUM overhead
Small Angle Maneuver (chop)	0.4	Move back on-target
Science exposure, NIC1 F187N	2.3	128 seconds exposure time on target 9 seconds for MULTIACCUM overhead
Small Angle Maneuver (chop)	0.4	Move off-target by one field of view
Science exposure, NIC1 F187N	2.3	128 seconds exposure time off target 9 seconds for MULTIACCUM overhead
Small Angle Maneuver (from NIC1 to NIC2) + Reconfigure Instrument	1.4	0.7 min to move on-target in NIC2 plus 0.7 min for instrument reconfiguration (change focus from NIC1 to NIC2).
Science exposure, NIC2 F187N	2.6	128 seconds exposure time on target 27 seconds for MULTIACCUM overhead
Small Angle Maneuver (chop)	0.5	Move off-target by one field of view
Science exposure, NIC2 F187N	2.3	128 seconds exposure time off target 9 seconds for MULTIACCUM overhead
Small Angle Maneuver (chop)	0.5	Move on-target
Science exposure, NIC2 F187N	2.3	128 seconds exposure time on target 9 seconds for MULTIACCUM overhead
Small Angle Maneuver (chop)	0.5	Move off-target by one field of view
Science exposure, NIC2 F187N	2.3	128 seconds exposure time off target 9 seconds for MULTIACCUM overhead
Small Angle Maneuver (from NIC2 to NIC3) + Reconfigure Instrument	4.8	1.0 min to move on-target in NIC3 plus 3.8 min for instrument reconfiguration (change focus from NIC2 to NIC3)
Science exposure, NIC3 F187N	2.6	128 seconds exposure time on target 27 seconds for MULTIACCUM overhead
Small Angle Maneuver (chop)	1.0	Move off-target by one field of view
Science exposure, NIC3 F187N	2.3	128 seconds exposure time off target 9 seconds for MULTIACCUM overhead

Table 10.3: Orbit Determination for Observations of Target A

Action	Time (minutes)	Explanation
Small Angle Maneuver (chop)	1.0	Move on-target
Science exposure, NIC3 F187N	2.3	128 seconds exposure time on target 9 seconds for MULTIACCUM overhead
Small Angle Maneuver (chop)	1.0	Move off-target by one field of view
Science exposure, NIC3 F187N	2.3	128 seconds exposure time off target 9 seconds for MULTIACCUM overhead
DUMP NIC buffer	~3.0	Terminal dump, could go in occultation.

The total time spent on the target is 47.5 minutes, with a visibility period of 59 minutes. Thus, there is room for a slight increase in exposure time without having the observations go into a second orbit. Note that if the observation were of a moving target, the slews to the new targets would be taken up in the tracking overhead, and the small angle maneuvers would all take 0.25 minute, regardless of the camera.

Techniques for Dithering, Background Measurement and Mosaicing

In This Chapter...

Introduction / 164
Strategies For Background Subtraction / 165
Chopping and Dithering Patterns / 167
Examples / 175
Phase II Proposal Instructions for Patterns / 178

In this chapter we deal with techniques for small scale motions to remove localized detector non-uniformities, for mapping areas larger than the size of the field of view of the NICMOS cameras, and the issue of removing the thermal background of the telescope.



Special procedures have been created to enable observers to perform these operations, and these are significantly different than those described in earlier versions of this handbook.

Introduction

Multiple exposures with small offsets in the pointing of the telescope are usually necessary or recommended for NICMOS observations. We distinguish three particular circumstances which may require small offsets:

- **Dithering** to permit the removal of dead or non-calibrated (i.e., non-correctable) pixels on the detectors, and detector's non-uniformities (i.e. sensitivity variations),
- Dithering or **chopping** to measure the background associated with an astronomical source,
- **Mosaicing** to map a source larger than a single detector field of view.

The techniques described in this chapter may be used to accomplish any one or any combination of these goals.

Experience with NICMOS has shown that the background is considerably fainter than was expected prior to deployment (see Chapter 4). The background appears spatially uniform (variations no larger than a few percent across the NIC3 field of view) and does not vary much with time (variations of less than 5% on orbit timescales). The description of the thermal background in Chapter 4, Chapter 9 and the Exposure Time Calculator provide a basis for estimating the relative contributions of source and background. It is strongly advised that provision for direct measurement of the background be included in proposals whenever the background is significant relative to the source(s) of interest. The frequency of such measurements should be about once per orbit, and more frequent measurements should be planned when the background must be measured to high accuracy.



All observations at wavelengths beyond 1.7 μm should consider the need for background measurements.

Background images are obtained by offsetting the telescope from the target to point to an “empty” region of the sky. The ability to routinely offset the telescope pointing is a fundamental operational requirement for NICMOS. Starting in cycle 9, HST programs will use a standard *pattern* syntax, which will replace the old pattern optional parameters, and the even older scan parameters form. The new syntax allows multiple observations to be made at each point in the pattern, if desired. Observers should check the “Phase 2 Proposal Instructions” for the exact syntax of the special requirement that invokes the pattern, and the “pattern parameter form” that describes the motion. For simplicity, a set of pre-defined observing patterns has been built; these patterns combine exposures taken under them into one

or more *associations*. A *pattern*, then, is a set of images of the same astronomical target obtained at pointings offset from each other, e.g. for the purpose of *mapping* an extended target or for creating background images. The *associations* of exposures are created for the purpose of simultaneously processing all the images (through a given filter) from a single *pattern*. Dithered images can thus be easily reassembled into a single image with the effects of minimizing bad pixels, or images taken in the long wavelength regime can be corrected for the thermal contribution, or observations of extended targets combined into a single large *map*.

Two distinct types of telescope motion are defined:

- *Dither*: Individual motions are limited to no more than 40 arcsec. These are intended to be used to perform small dithers, to measure backgrounds for compact sources, and to accomplish sequences of overlapping exposures for the construction of mosaics. Such sequences will be assembled into a single final image by the calibrations pipeline.
- *Chop*: Motions up to 1440 arcsec are permitted. These are intended for the measurement of the background at one or more locations significantly removed from the target pointing. Each non-contiguous background pointing will be assembled into its own final image in addition to the target pointing by the calibration pipeline.

Telescope motions involve overheads for physically moving the telescope and, if necessary, for re-acquiring the guide stars. Therefore, significant time overheads may be incurred by observations which need background subtraction or propose to map extended regions of the sky. A careful estimate of the overheads associated with a specific observation or set of observations is necessary to evaluate the number of orbits required (see Chapter 10).

Strategies For Background Subtraction

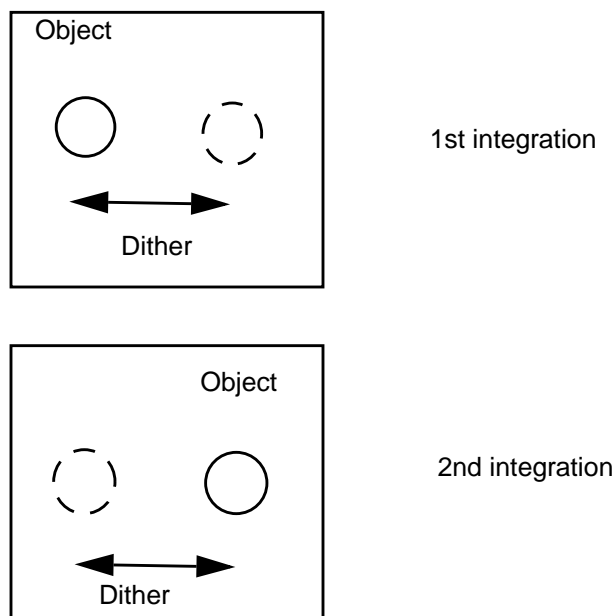
The most efficient strategy for removing the background from a science exposure strongly depends on the nature of the target and of the science to be accomplished. In general, two types of targets can be defined: compact and extended.

Compact Objects

For compact objects, such as point sources, background subtraction can be achieved by moving the target across the camera field of view (see Figure 11.1). A dither pattern, which involves movements of a few arcsec

from one exposure to the next, can then be used. This is an efficient way to build background images, since the target is present in each exposure, and a background image can be created from the stacking and filtering of all exposures.

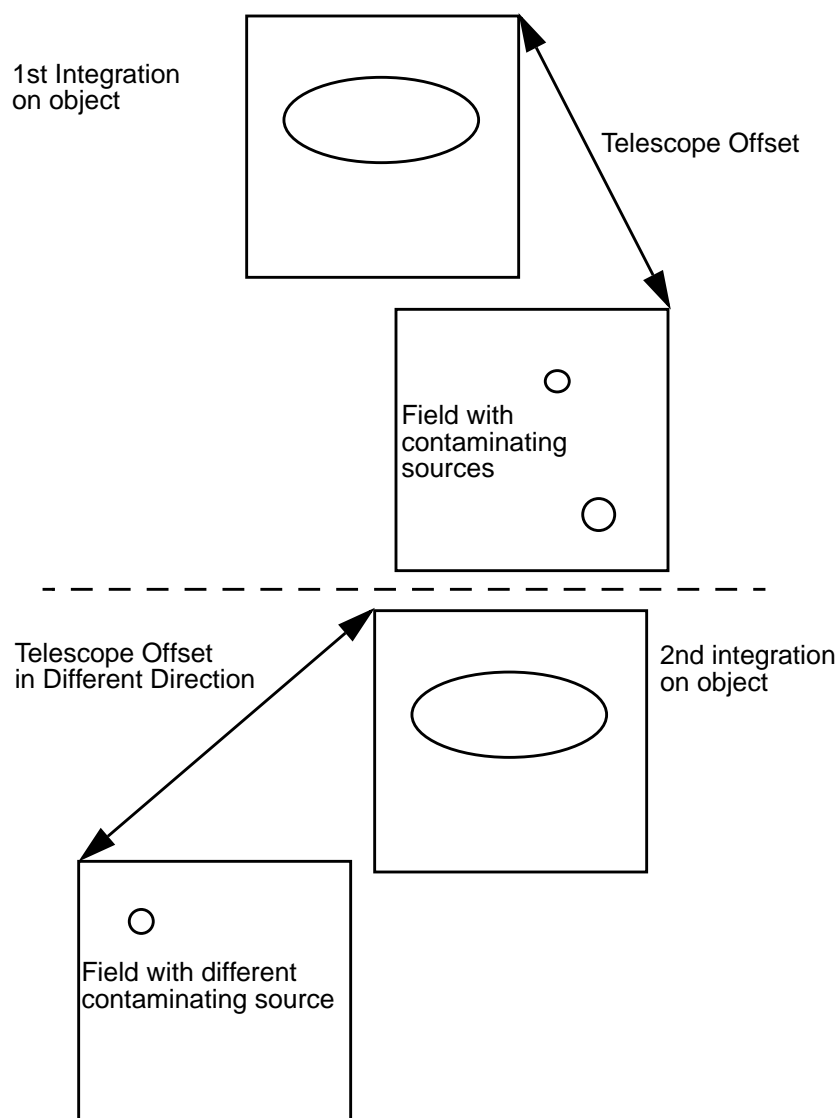
Figure 11.1: Dithering



Extended Objects

For an extended object which occupies a significant portion of the NICMOS field of view, the dithering technique does not apply to building background images. In this case, offsets to an adjacent field (chopping) chosen to be at least one camera field away in an arbitrary (or user specified) direction, are necessary. By offsetting in different directions a stacked and filtered sky image can be created which removes the effect of contaminating objects in the offset fields (see Figure 11.2). As in the case of compact objects, these offsets might be quite small, but for large galaxies for example, they may need to be over considerable distances. The user will have the ability to specify the offset values and directions and the number of offsets, in the Phase II pattern parameters form.

Figure 11.2: Chopping



Chopping and Dithering Patterns

There are a set of fifteen pre-designed patterns available for NICMOS observations. Users may define their own patterns as well, using the Pattern Parameters Form, during phase II development. The pre-defined patterns include four dithering patterns, four chopping patterns, five dither-chop patterns, and two mapping patterns. For each of these, the observer will be able to specify the number of positions desired (2 to 40), the dither size (0 to 40 arcsec), the chop size (0 to 1440 arcsec, also used for mapping), and

the orientation of the pattern with respect to either the detector or the sky. The POS-TARG special requirement will still be available for offsetting the telescope and creating custom-design patterns as well, but there are a number of advantages to using the pre-designed patterns:

- They simplify the specification of complex observations in the Phase II proposal,
- All the observations pertaining to an exposure logsheet line in a pattern result in one association and are simultaneously calibrated and combined in the data calibration pipeline, including background calibration, cosmic ray removal, and flat field averaging. Observations obtained with POS-TARG do not result in associations, and will have to be combined manually by the observer,
- They permit the observation of a mosaic with a fixed position angle without fixing spacecraft roll, which increases the number of opportunities to schedule the observations.

Multiple exposures may be obtained at each position by the use of the number-of-iterations (NEXP) optional parameter. This may be useful for cosmic ray removal. In addition, exposures in different filters at each pattern position can be obtained.

The fifteen patterns are listed in Table 11.1, together with applicable parameters, such as the allowed values for the number of steps in the pattern, the dither size, or the chop size. In addition, the figure number where the pattern is graphically shown is given in column 5 of Table 11.1. Offset sizes and number of steps in a pattern affect the amount of overhead time required to perform an observation (see Chapter 10). The effects of dithering or chopping on an astronomical image are shown in a set of examples in the next section.

Table 11.1: NICMOS Pre-designed Observing Patterns and Parameters

Pattern Name	Num. Pos.	Num. Patts	Dither Size	Chop Size	Orient	See Figure
NIC-SPIRAL-DITH	2-40	NA	0-40	NA	camera	11.3
NIC-SQUARE-WAVE-DITH	2-40	NA	0-40	NA	camera	11.3
NIC-XSTRIP-DITH	2-40	NA	0-40	NA	camera	11.3
NIC-YSTRIP-DITH	2-40	NA	0-40	NA	camera	11.3
NIC-ONE-CHOP	NA	1-40	NA	0-1440	camera	11.4
NIC-TWO-CHOP	NA	1-40	NA	0-1440	camera	11.4
NIC-SPIRAL-DITH-CHOP	NA	1-40	0-40	0-1440	camera	11.5
NIC-XSTRIP-DITH-CHOP	NA	1-40	0-40	0-1440	camera	11.5
NIC-YSTRIP-DITH-CHOP	NA	1-40	0-40	0-1440	camera	11.5
NIC-ONE-SKY-CHOP	NA	1-40	NA	0-1440	sky	10.6
NIC-TWO-SKY-CHOP	NA	1-40	NA	0-1440	sky	10.6
NIC-XSTRIP-DITH-SKY-CHOP	NA	1-40	0-40	0-1440	sky	10.6
NIC-SPIRAL-DITH-SKY-CHOP	NA	1-40	0-40	0-1440	sky	10.6
NIC-MAP	1-40	1-40	0-1440	0-1440	sky	10.6
NIC-SPIRAL-MAP	2-40	NA	0-40	NA	sky	10.6

Note on Orientation:

The new pattern parameter syntax requires additional input on orientation. Specifically, the pattern must be defined in either the POS-TARG (camera) frame or the CELESTIAL (sky) frame. An orientation angle may be specified as well (the usual default is 0°). In the POS-TARG frame, this is the angle of the motion of the target from the first point of the pattern to the second, counterclockwise from the x detector axis (the directions are defined in Figure 6.1). In the CELESTIAL frame, the angle is measured from North through East.

Some of the chopping patterns in Table 11.1 are doubled, they can be specified either as POS-TARG default or CELESTIAL default.

Move the sky or the telescope?

The new pattern syntax attempts to resolve the confusing dichotomy in the old pattern implementation, as to whether the pattern moves the telescope or the target. It does this by providing the two reference frames described above. Patterns done in the POS-TARG reference frame will move the target, just as the “POS-TARG” special requirement does. Patterns done in the CELESTIAL reference frame will move the telescope,

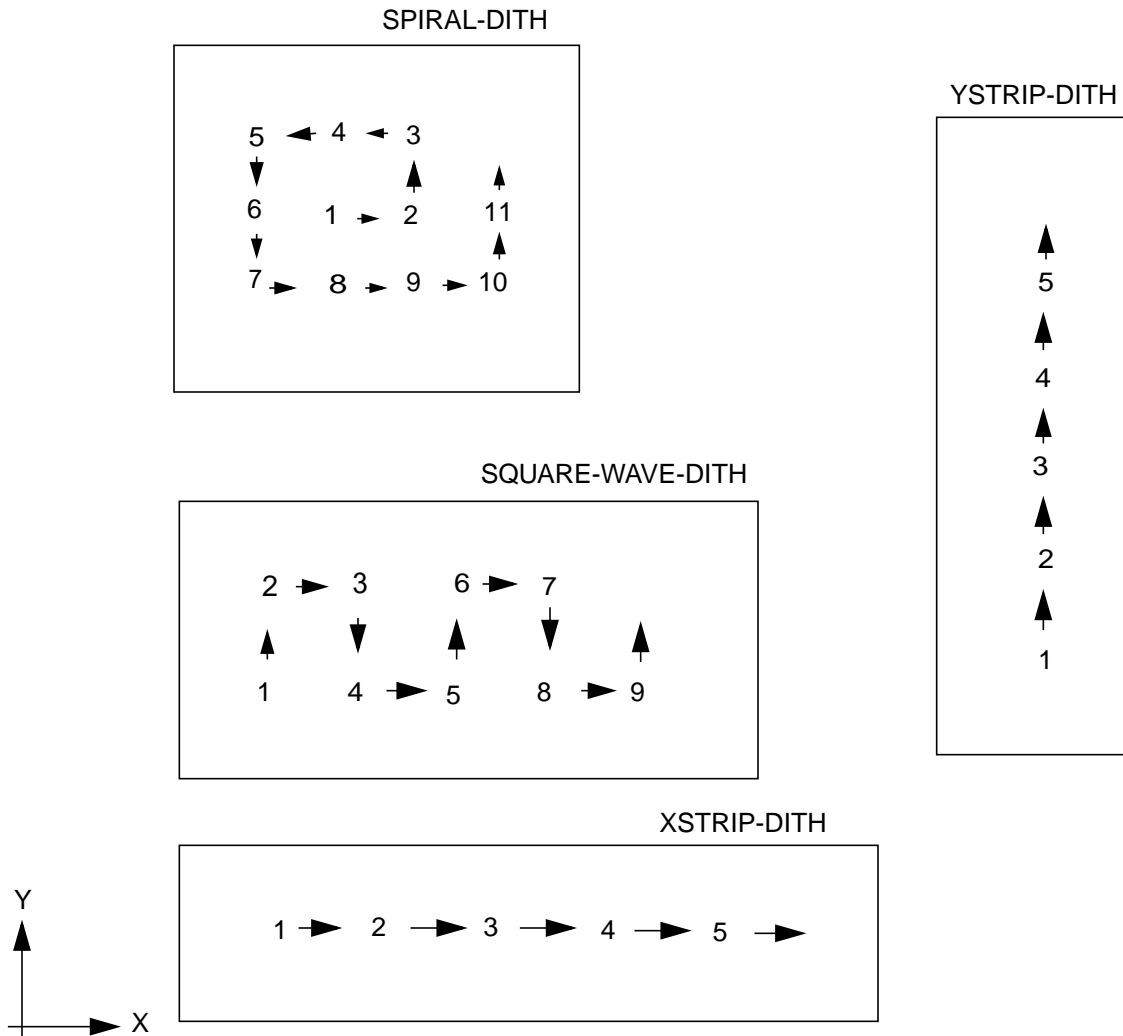
as was done with the original implementation of the NICMOS patterns. The target will move in the opposite direction on the image, in the CELESTIAL frame.

Dither Patterns

The dither patterns are recommended for the background subtraction from observations of point sources (beyond 1.7 microns), and for the reduction of sensitivity variations and bad pixel effects. The four types of canned dither routines are SPIRAL-DITH, SQUARE-WAVE-DITH, XSTRIP-DITH, and YSTRIP-DITH. Most of the names are self-explanatory: the SPIRAL-DITH pattern produces a spiral around the first pointing; the SQUARE-WAVE-DITH pattern covers extended regions by moving along a square-wave shape; the XSTRIP-DITH and YSTRIP-DITH patterns move the target along the x and y directions of the detector, respectively. The difference between the XSTRIP-DITH and the YSTRIP-DITH patterns is that the first moves by default along the grism dispersion (more or less), while the second moves orthogonal to the grism dispersion axis. These patterns are illustrated in Figure 11.3

Note that there is an additional parameter for dithering patterns, to center the pattern on the target. The default is to start the dithering at the target position.

Figure 11.3: Dither Patterns



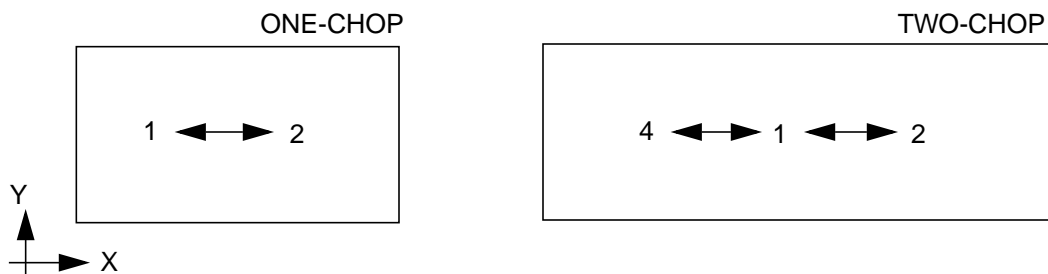
Chop Patterns

The chop patterns are recommended for measuring the background adjacent to extended targets. For each chop pattern, half of the exposures are taken on the target (position 1). There are two basic patterns, ONE-CHOP and TWO-CHOP. The ONE-CHOP pattern produces one image of the target and one image of the background. The TWO-CHOP pattern produces one image (with two exposures) of the target and two background images, with the background fields positioned on opposite sides of the target. These patterns may be repeated if necessary: note that rather than specifying the number of points in the pattern, the observer specifies the number of repeats of the pattern. For example, calling the NIC-TWO-CHOP pattern with number of patterns of 1 will produce four

images, one on the target, one off to one side (default -x detector direction, see next para.), one back on the target, and one off to the other side. If the number of patterns is set to 2, the observer will get eight images, and so forth. Chop patterns are illustrated in Figure 11.4.

Because chopping is best done to empty regions of the sky, we provide a set of chopping patterns that are in the CELESTIAL coordinate system, as well as the standard set (that are in the POS-TARG frame). These have the word SKY in their name, and must have an orientation angle (degrees E from N for the first motion of the pattern) supplied. These should be used when the region around the target contains some objects that should be avoided when measuring the background. SKY patterns are illustrated in Figure 11.6.

Figure 11.4: Chop Patterns

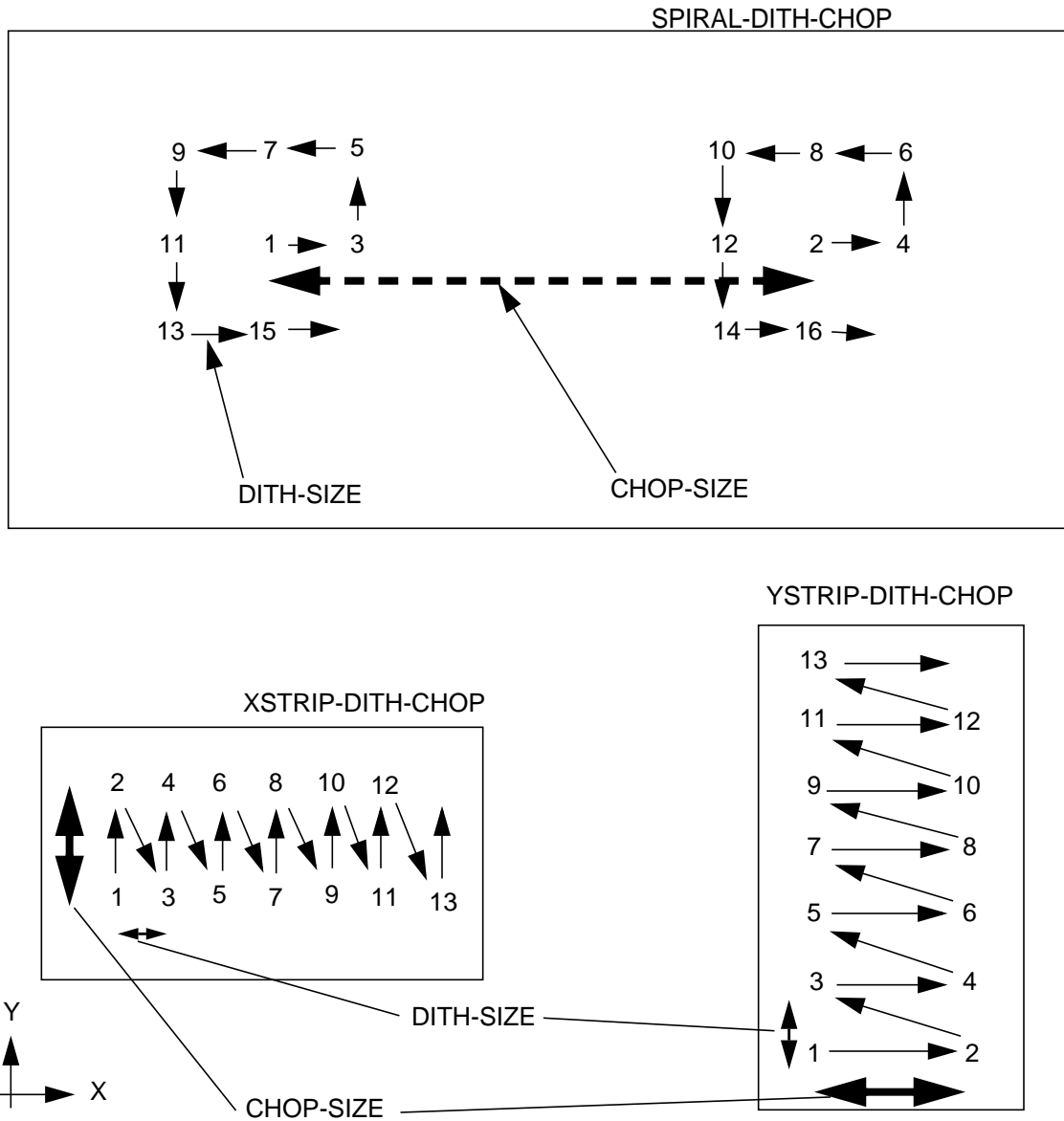


Combined Patterns

The combined patterns permit dithering interleaved with chops to measure the background. They are recommended for simultaneous minimization of detector artifacts and background subtraction, for observations beyond 1.7 microns. Three types of combined patterns are implemented: SPIRAL-DITH-CHOP, XSTRIP-DITH-CHOP, and YSTRIP-DITH-CHOP. Their characteristics are analogous to the dither patterns SPIRAL-DITH, XSTRIP-DITH, and YSTRIP-DITH, respectively, with the addition that each dither step is coupled with a background image obtained by chopping. These combined patterns are shown in Figure 11.5.

In a manner similar to the regular chopping patterns, the combined patterns have “SKY” versions implemented in the CELESTIAL frame. Since these require an orientation angle, there is no YSTRIP-DITH-SKY-CHOP, however: this is redundant with XSTRIP-DITH-SKY-CHOP. These are illustrated in Figure 11.6.

Figure 11.5: Combined Patterns



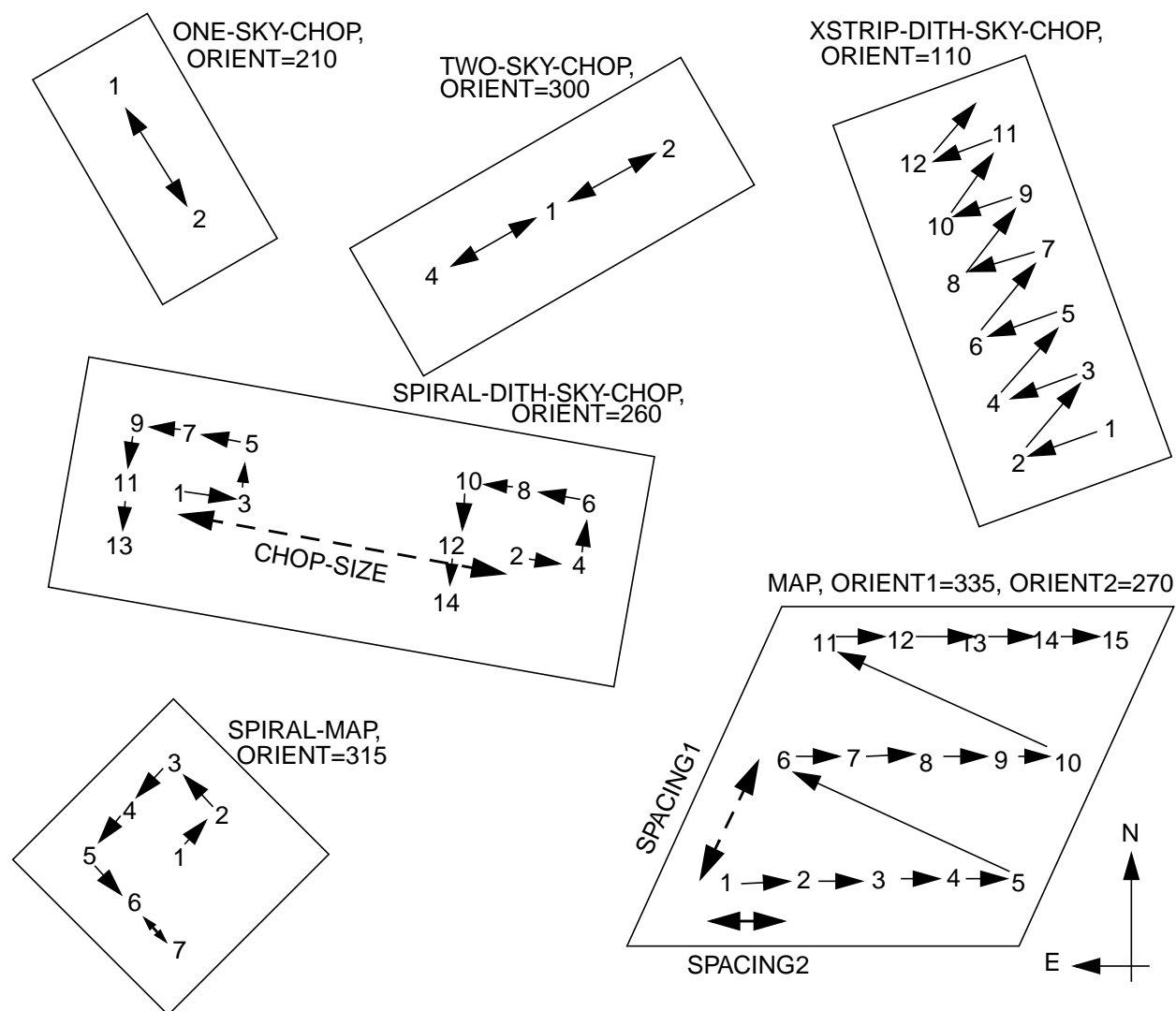
Map Patterns

A new addition to the suite of “canned” patterns are the two MAP sequences. These allow the telescope to be pointed at a regular grid of points, doing a series of exposures at each point. These are done in the CELESTIAL frame, so an orientation angle must be supplied, and the telescope motion on the sky is specified (rather than the target motion relative to the detector, see note above). The SPIRAL-MAP sequence is basically the SPIRAL-DITH sequence in the CELESTIAL frame, and automatically maps the (square or rectangular) region around the target.

The MAP sequence defines an arbitrary parallelogram on the sky. The observer may specify the number of points in each of two directions, and the position angle (E of N) of each direction.

As with the dithering patterns, the observer has the option of specifying whether the target is centered in the pattern or not. The target will be centered in the SPIRAL-MAP pattern if there are 9, 16, 24,... points in the pattern, but will not necessarily be centered otherwise. The observer can specify if the target should be centered along one axis or the other, or both, of the parallelogram defined by the MAP sequence. These are illustrated in Figure 11.6.

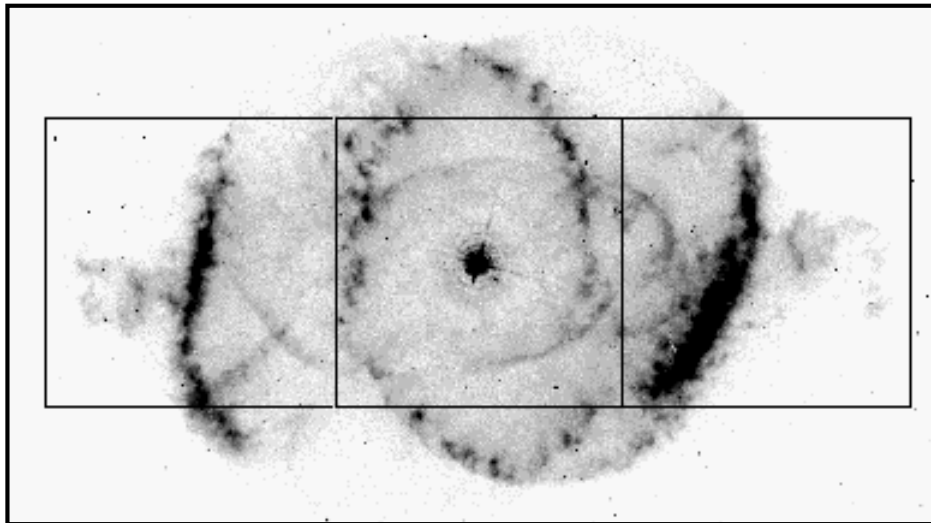
Figure 11.6: Patterns on the sky



Examples

The next few pages show some selected examples of how the patterns work on astronomical observations

Figure 11.7: NIC-TWO-SKY-CHOP pattern.



Spacing (chop throw) = 1 detector width,
 Pattern Orient = 270° ,
 Visit Orient = 225° ,
 (Frame=CELESTIAL)

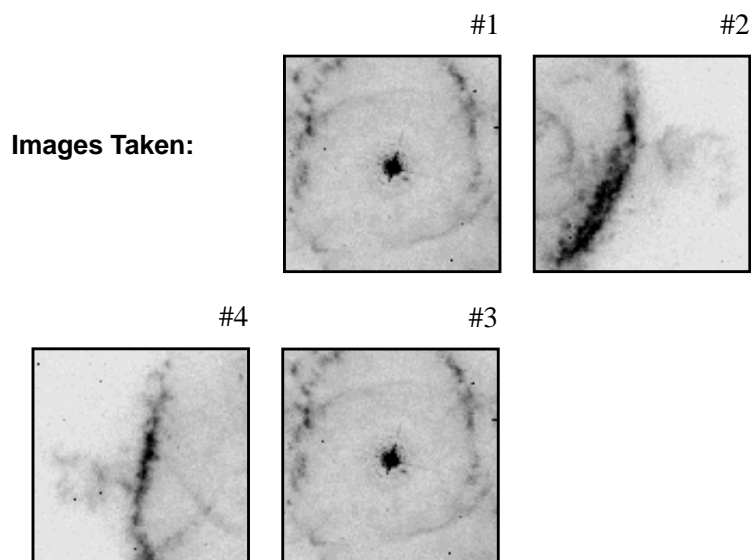
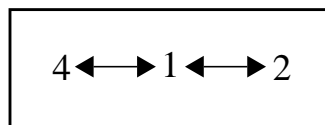
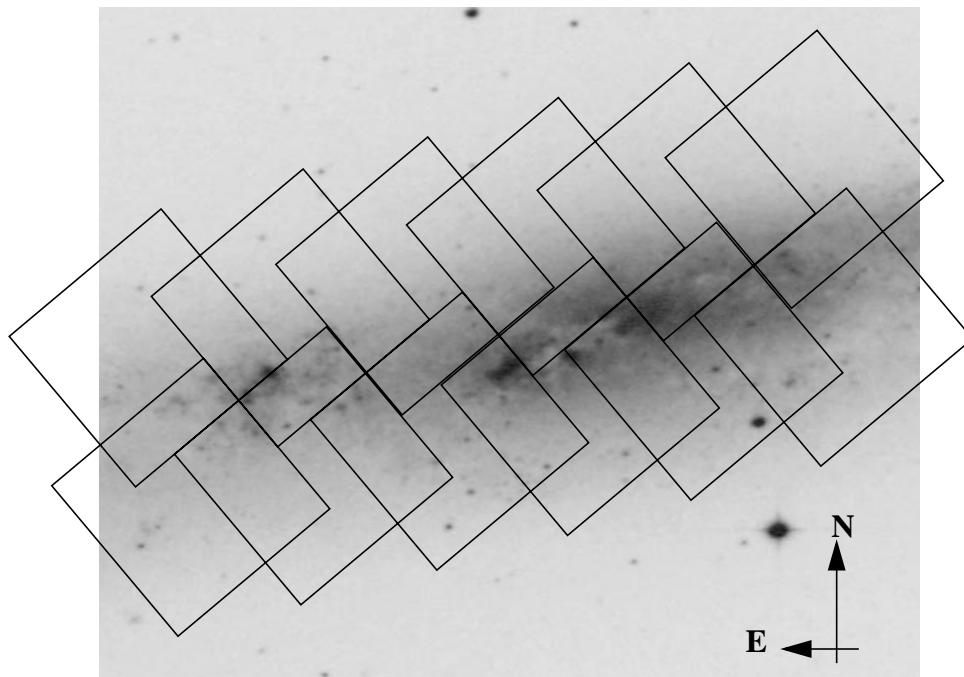


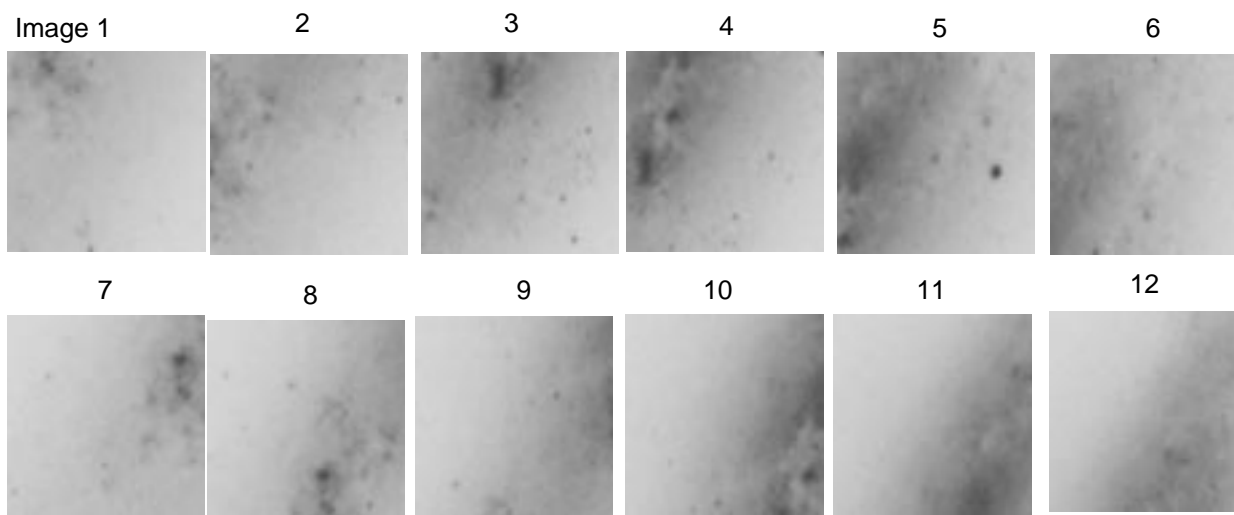
Figure 11.8: NIC-MAP Pattern



Spacing = detector size/ $\sqrt{2}$, Frame= CELESTIAL, Pattern2 Orient = 284° , Pattern1 Orient = 14° ,
No visit level orient specified: nominal roll puts detector Y at position angle 310°

Could cover the area more efficiently with Spacing = $0.866 \times$ detector size, and
Pattern1 Orient = Pattern2 Orient + 60°

In either case, the lack of visit orient specification greatly increases the chance of scheduling the observation.



Phase II Proposal Instructions for Patterns



We discuss the Phase II instructions for patterns in this section in order to illustrate the options available. This is not, however, an exhaustive description and is not the appropriate reference to use when preparing a Phase II proposal. While writing your Phase II you should refer to the Phase II Proposal Instructions, which contain a complete and up-to-date guide.

This section is not crucial for preparing the Phase I proposal, but it may be relevant to know beforehand which parameters will be available, and what values these parameters can have. The pattern parameter form allows for two nested parameters (pattern 2 is performed at each point in pattern 1) but many of the predefined patterns already use this capability: you cannot always “nest” the “canned” patterns. A pattern can apply to a series of exposure logsheet lines, and the entire sequence is done at each point in the pattern. Thus the special requirement `PATTERN n [<exposure list>]` (where `n` is the number of the pattern parameter form to be applied to these observations) should only apply once to any exposure logsheet line, and should only be specified on one exposure in `<exposure list>`. Be very careful not to “call” a line in two different patterns!

The set of exposures resulting from a pattern is sorted by filter, and an association is created for each filter.

Patterns may use the FOM instead of moving the whole telescope, however this is an “available” (not “supported”) mode of observation. The FOM doesn’t necessarily come back to exactly the same place, so artifacts on the mirror may appear to move around. Observers requiring very small, and very rapid offsets (or making observations in parallel to another instrument) may benefit from its use and can discuss this with their Contact Scientist during the Phase II proposal process.

Types of Motions

The `OFFSET` optional parameter defines which type of telescope motion will be performed during a pattern, in order to dither or chop. Telescope motions fall into three categories:

- Small angle maneuvers (SAMs) where FGS Fine Lock guiding is maintained. Such SAMs are typically limited to < 2 arcmin from the point of the initial guide star acquisition. This is the practical limit of the radial extent of the pattern. Often it will be smaller due to guide star availability.

- SAMs without FGS guiding (i.e. GYRO pointing control). These are necessary for larger motions (> 2 arcmin). The telescope will drift at a rate of 1 to 2 milliarcsec per second of time (elapsed time since dropping to gyro-- not exposure time).
- SAMs with RE-ACQuisitions of guide stars at each return to the target position. This can be used to chop between a target and an offset background measurement pointing (which would be observed with GYRO pointing control).

The available options for OFFSET are:

- SAM, the default, will use guide stars whenever possible. If a motion, or the sequence of motions, moves the telescope sufficiently from the original position that guide stars are no longer available, then exposures will be obtained using GYRO control. If a subsequent motion returns the telescope to a point where the original guide stars become available then the guide stars will be RE-ACQuired. This incurs an overhead of ~ 3 minutes for each RE-ACQuisition.
- SAM-NO-REACQ will use guide stars (FGS fine lock) until the *first* instance in the pattern when guide stars become unavailable. The remainder of the pattern will be executed using GYRO control.
- SAM-NO-GYRO will use guide stars for all exposures. If guide stars are not available, the observations will not be scheduled.
- FOM will use the Field Offset Mirror to perform the pattern. See the description above; this is an “available” operating mode, for use only for coordinated parallels.

Calibration Overview

The chapters in this part describe the calibration of NICMOS. These chapters include an overview of the calibration pipeline process; the expected accuracies for data taken in Cycle 10; and the present preliminary plans for calibrating and verifying the instrument's performance.

Calibration Pipeline

In This Chapter...

Overview / 183

NICMOS Pipeline / 187

NICMOS Data Products / 191

This chapter describes the pipeline calibration system developed at STScI. This system provides observers with NICMOS data after various instrumental signatures are removed, conversions to flux units are performed, and patterns of exposures are combined. Several enhancements to the HST ground system have been made to support NICMOS, including the concept of associations of datasets and an improved file format for data storage and distribution. A detailed description of the analysis of HST data in general and NICMOS data in particular can be found in the *HST Data Handbook*.

Overview

All data taken with NICMOS are automatically processed and calibrated by a suite of software programs known as the *pipeline*. The purpose of pipeline processing is to provide data products to observers and the HST Data Archive in a form suitable for most scientific analyses. Pipeline processing is also applied to engineering data and calibration data.

The basic sequence of steps in the STScI pipeline system (also known as OPUS) is:

1. Assemble data received from HST into datasets.
2. Perform a standard level of calibration of the science data.
3. Store both the uncalibrated and calibrated datasets in the Archive and populate the Archive database catalog to support StarView queries.

The pipeline must also handle exceptions (e.g., incomplete data) and perform a general data evaluation and quality control step. Final delivery of data to observers is accomplished by the data distribution mechanisms of the Archive system.

The calibration step has several goals:

- Remove the known instrumental signatures (e.g., flat field and dark current).
- Correct the data for non-linear behavior and convert to physical units (e.g., gain and flux calibration).
- Flag degraded or suspect data values and provide estimates of the statistical uncertainties of each pixel.

While a calibration pipeline may not be able to provide the optimal calibration for a specific observation (which may, in fact, not become available until some time after the data were obtained and calibrated), the goal is to provide data calibrated to a level suitable for initial evaluation and analysis for all users. Observers frequently require a detailed understanding of the calibrations applied to their data and the ability to repeat, often with improved calibration products, the calibration process at their home institution. Further, certain types of image artifacts can appear in NICMOS data, which require processing with specialized tools to remove. To support these goals, the calibration software is available within the **IRAF/STSDAS** system and the calibration reference files (e.g., flat fields) are available from the HST Archive via StarView so that observers have the ability to repeat and customize the calibration processing to meet the specific needs of individual observations.

Associations

To improve the utility of the pipeline processing for the second generation science instruments—NICMOS and STIS—several significant changes were made to the structure of the calibration pipeline. The largest of these changes was to enable the combination of multiple observations during the calibration process. This permits the pipeline to both generate a combined product and to use calibrations obtained contemporaneously with the science observations. This capability is designed to support the cosmic ray event removal, mosaicing, and background subtraction for NICMOS observations. As discussed in Chapter 11, mechanisms exist for compactly requesting such observations in the Phase II proposal.

Concept

The basic element in the HST ground system has historically been the *exposure*. The first generation HST science instruments were commanded to generate single exposures, which result from a recognizably distinct

sequence of commands to the instrument. This creates a flow of data which is assembled into a single *dataset*. Each dataset is given a unique 9 character identifier (an *IPPPSSOOT* in STScI terminology) and is processed by the pipeline, calibrated, and archived separately from all other datasets.

An illustrative (partial) counter example to this procedure is the WFPC2 CRSPLIT proposal instruction. This results in two WFPC2 exposures from a single line on the exposure logsheet (the way in which observers specify commands for HST). However, the HST ground system treats a CRSPLIT as two distinct exposures which are commanded, processed, calibrated, and archived separately. The pipeline does not combine these two images (datasets) to create the single image without cosmic ray events which was the observer's original intention. Currently, the observers (and any future archival researchers) are left to perform this task on their own.

The second generation instruments present many instances in which the combination of data from two or more exposures is necessary to create a scientifically useful data product. Both NICMOS and STIS need to combine exposures to remove cosmic rays and to improve flat fielding (by dithering). For NICMOS, the HST thermal background contributes a significant signal at wavelengths greater than 1.7 μm . Multiple exposures (dithered for small targets and offset onto blank sky—chopped—for extended targets) are necessary to measure and remove this background.

Usage

Associations exist to simplify the use of HST data by observers. This starts from the proposal phase, continues with a more complete calibration process than would be possible without associations, carries into the archiving and retrieval of associated data, and includes the use of HST data by observers within the **IRAF/STSDAS** system.

An *association* is a set of one or more exposures along with an *association table* and, optionally, one or more products. We define the following terms:

- An *exposure* is the atomic unit of HST data.
- A *dataset* is a collection of files having a common rootname (same *IPPPSSOOT*).
- A *product* is a dataset derived from one or more exposures.

The first generation instruments all had a one-to-one correspondence between exposures and datasets. They do not have products. NICMOS and STIS use the association structure as a meta-dataset. Further, they use the information in multiple exposures during the calibration process to create products.

From a high level, an association is a means of identifying a set of exposures as belonging together and being, in some sense, dependent upon one another. The association concept permits these exposures to be

calibrated, archived, retrieved, and reprocessed (within OPUS or **STSDAS**) as a set rather than as individual objects. In one sense, this is a book-keeping operation which has been transferred from the observer to the HST data pipeline and archive.

Associations are defined by optional parameters on a single exposure logsheet line. That is, there is a one-to-one correspondence between proposal logsheet lines and associations (although it is possible to have exposures which are not in associations).

Observers may obtain one or more associations at each of one or more positions on the sky using the NICMOS proposal grammar. Typically usage will be:

- To obtain a sequence of slightly offset exposures (dithering) to improve the flat fielding, avoid bad pixels and cosmic rays, and, for sufficiently compact targets, to remove the thermal background signal.
- Mapping of targets larger than the NICMOS detector's field of view.
- To obtain a sequence of observations in which the telescope is chopped between the target and one or more offset regions of (hopefully blank) sky.

A set of predefined patterns are provided in the proposal instructions for these types of observations or a combination of both types (Chapter 11). The Institute ground system will expand the observer's single line request into multiple exposures each with its own identifying name (*IPPPSSOOT*) and populate the necessary database relations to describe this association for the OPUS system.

Re-engineering

For the second generation science instruments the format of the data products from the pipeline is FITS (Flexible Image Transport System) files with image extensions. The **IRAF/STSDAS** system was modified to operate directly on these files. Each NICMOS image is expressed as a set of five image extensions representing the image, its variance, a bit encoded data quality map, the number of valid samples at each pixel, and the integration time at each pixel. This structure is used at all stages of the calibration process which permits the re-execution of selected elements of the pipeline without starting from the initial point. Finally, the calibration code itself is written in the C programming language (rather than IRAF's SPP language). This greatly simplifies the modification of the pipeline code by users and the development of new NICMOS specific data processing tasks.

NICMOS Pipeline

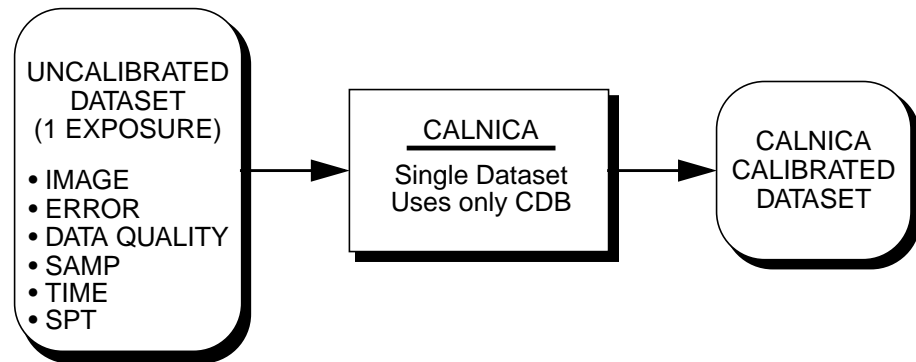
The NICMOS calibration task is divided into two stages: **calnica**, which is used for every individual exposure, and **calnicb**, which is used after **calnica** on those exposures which comprise an association.

Static Calibrations—calnica

The first calibration stage, **calnica**, (Figure 12.1) performs those calibrations which can be done to a single exposure using the configuration information from its telemetry and the Calibration Data Base. Such calibrations are derived from the calibration program (see Chapter 13) and typically change on time scales of months. This is analogous to the WFPC2 calibration process (**calwp2**). **Calnica** performs the following steps:

- Correct for signal present in the zeroth read (in MULTIACCUM data)
- Subtract the bias level (in MULTIACCUM data).
- Flag known bad pixels in the data quality array.
- Calculate a noise model for each pixel.
- Subtract dark current.
- Correct for non-linearity.
- Flat field to bring each pixel to a common gain.
- Convert the image data to count rate units.
- Calculate various image statistics (e.g., median).
- Store photometric calibration information in image header keywords.
- Correct for cosmic ray events and pixel saturation (in MULTIACCUM data).
- Calculate estimates of the background.
- Analyze the internal engineering telemetry for potential problems with the observation.

Figure 12.1: Conceptual calnica Pipeline

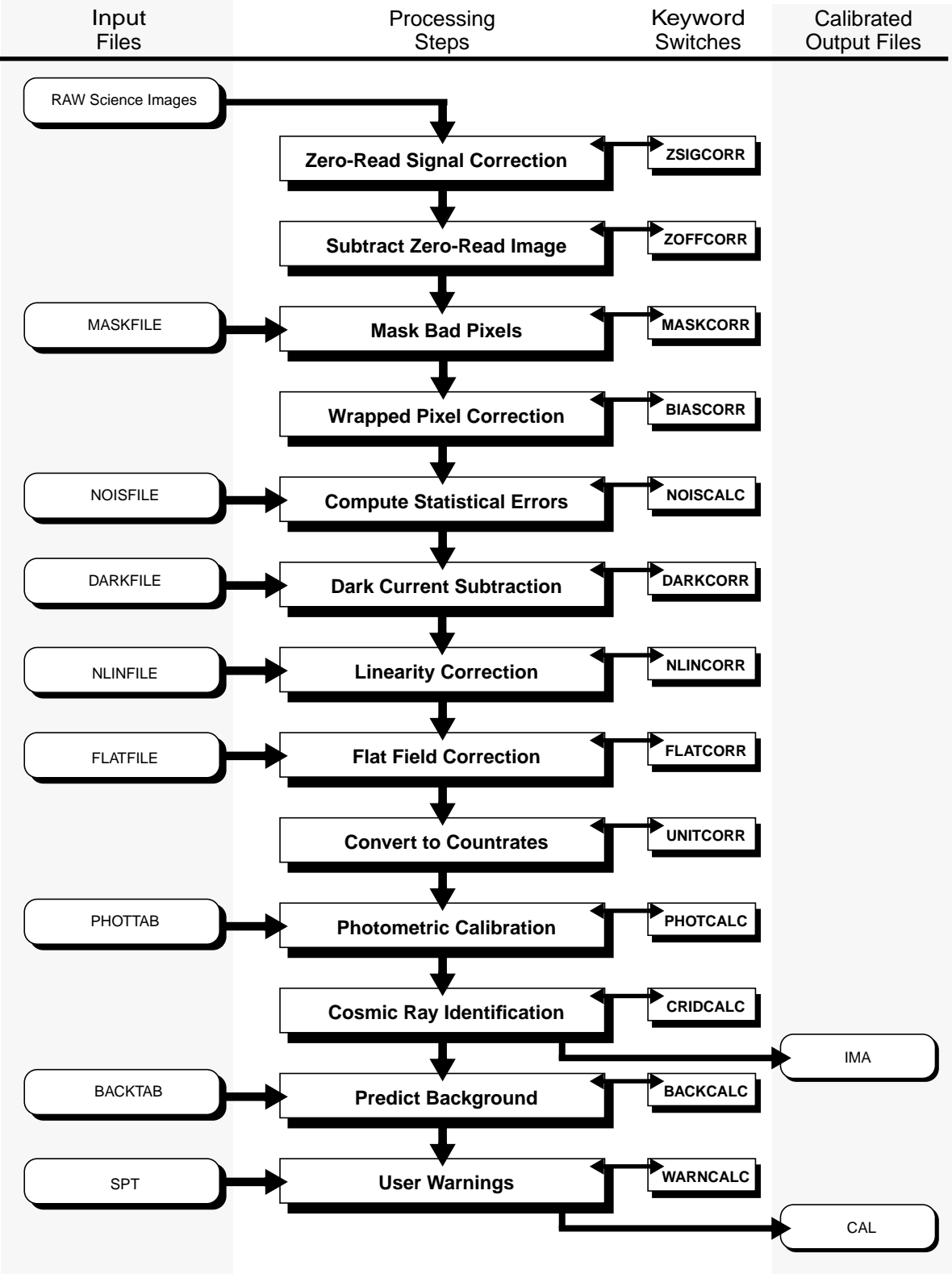


Observers will be given both the uncalibrated (*raw*) data and the processed data for each exposure. For MULTIACCUM observations, partially calibrated data for each readout will be generated (which excludes the cosmic ray and saturation corrections), in addition to a final single image.

To recalibrate NICMOS data, observers will need the **calnica** software (included in the **STSDAS** distribution) and the necessary calibration reference files (available from the HST Data Archive using StarView and from the NICMOS WWW pages).

The data processing flow chart for normal imaging and spectroscopic images is shown in Figure 12.2.

Figure 12.2: Calibration Steps of the calnica Pipeline

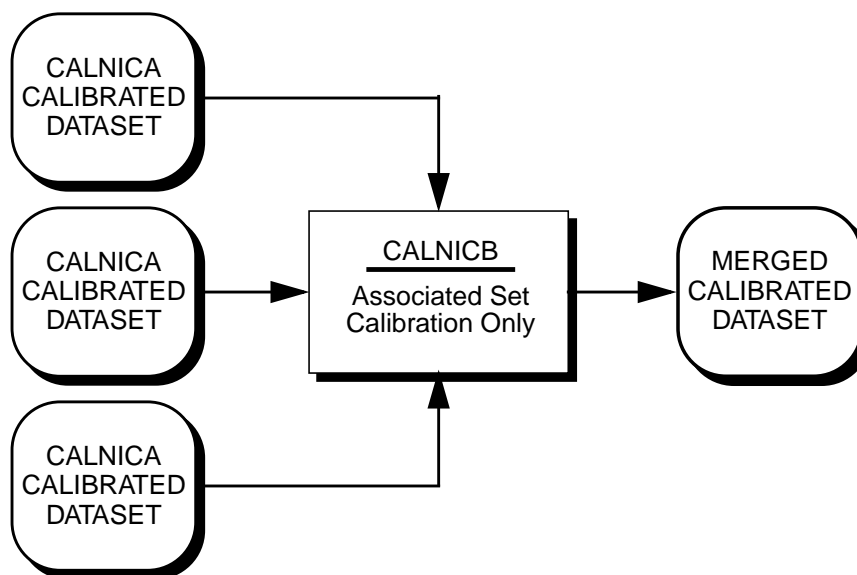


Contemporaneous Observations—calnicb

While previously it has been possible to execute multiple exposures from a single proposal logsheet line (e.g., WFPC2, CR-SPLIT, and NEXP= n constructs), this capability was significantly expanded to support requirements of the second generation science instruments. Typical examples include the removal of cosmic rays, the construction of a mosaic image, and the subtraction of the sky background from a sequence of on-target and off-target observations. These observations are distinguished by the fact that their calibration and processing depends upon other observations obtained *at the same time*.

The **calnicb** part of the pipeline carries out the calibration and merging of associated data frames, each of which has first been processed by **calnica**. In the case shown in Figure 12.3, the associated set has 3 individual datasets that are combined into one merged and calibrated dataset.

Figure 12.3: Conceptual calnicb Pipeline



We refer to these sets of exposures as associations. The **calnicb** task operates on an entire association, and produces one or more products from that set (Figure 12.3). In the case of dither patterns, **calnicb** reads from the headers of the individual exposure files what the telescope offsets were. It then identifies sources in the images, and, starting with the telescope pointing information from the headers as an initial guess, determines what the pointings actually were. It then combines the images into a final mosaic, rejecting from the output any cosmic rays that had not been detected in the individual exposures when they were processed by **calnica**.

The **calnicb** code uses all the data quality information generated by **calnica** to avoid propagating identified cosmic rays, bad pixels, or saturated pixels, into the output mosaic. In the case of chopped images, if multiple images were obtained at each chop position, **calnicb** generates a mosaic for each background position and produces an output product image for each of those. It then combines each of the background images to generate an average background for the target position, removes this background from the mosaic it has generated for the target position, and then saves the result of this operation as the final, background subtracted mosaiced image of the target. When **calnicb** is calculating the offsets between images, it starts with the telescope pointing information as its first guess. If it is unable to match the various images by adjusting this pointing information by more than some limit, the code reverts to using the pointing information alone, on the assumption that there are no sources bright enough to detect in the individual images, or that there are instrumental artifacts that are confusing the offset calculation, or that the telescope suffered a loss of guide star lock during one or more of the exposures resulting in a potentially very large offset being introduced. To date, we have found that all of these things happen very rarely indeed.

NICMOS Data Products

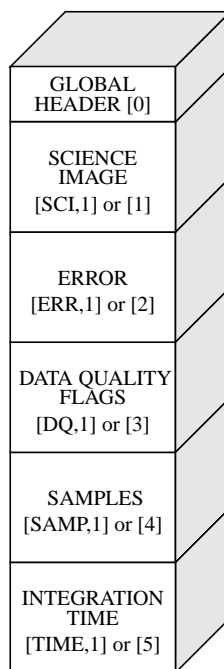
Standard NICMOS Dataset Structure

NICMOS data are represented by five data arrays for each readout. These arrays contain the:

- Science image.
- Error array.
- Quality flags array.
- Samples array.
- Integration time array.

Each downlinked readout is always represented by these five data arrays. In the basic NICMOS data file format, shown in Figure 12.4, each of these data arrays is stored as a separate image extension in the FITS container file. The MULTIACCUM mode (Figure 12.5) produces multiple images. The file structure for such a dataset consists of a lattice of the 5 data arrays that are created for each readout, as shown in Figure 12.5. Compact FITS representations are used to store arrays in which all elements have the same value.

Figure 12.4: Data Format for ACCUM, BRIGHTOBJ and ACQ Modes



Science Image (**SCI**)

The science image contains the information recorded by the NICMOS detector. The data may be represented as counts (i.e., data numbers) or as count rates (i.e., data numbers per second). Generally the latter is desirable since it is easier to interpret in mosaiced datasets and corresponds closely to flux.

Error Array (**ERR**)

The error array contains an estimate of the statistical uncertainty at each pixel. It is expressed as a real number of standard deviations. This is a calculated quantity based on a noise model of the instrument and its environment.

Data Quality Flags Array (**DQ**)

The data quality flags array provides 16 independent flags for each pixel. Each flag has a true (set) or false (unset) state and is encoded as a bit in a 16 bit (short integer) word. Users are advised that this word should *not* be interpreted as an integer.

Samples Array (**SAMP**)

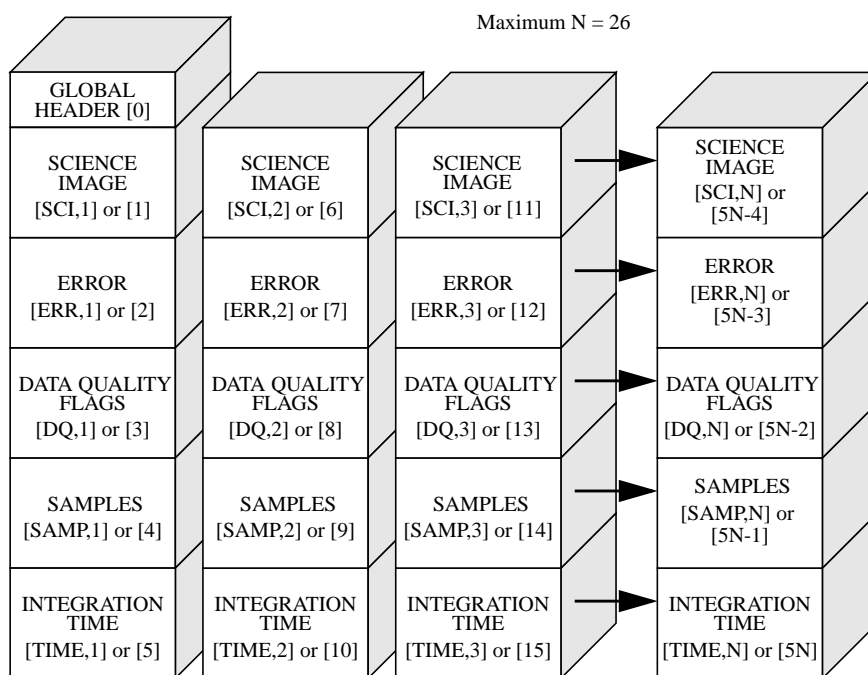
The samples array is used for one of two purposes:

- For data where multiple samples of the array were obtained during the integration (MULTIACCUM mode), the samples array denotes the number of samples for each pixel in the corresponding science image.
- When multiple integrations are combined to produce a single image, the samples array will contain the number of samples retained at each pixel. Note that this implies that the original number of samples information is not propagated forward into combined images.

Integration Time Array (TIME)

The integration time array contains the total integration time at each pixel. While initially a simple parameter in some observing modes, combining datasets into composite mosaics and using the information obtained by multiple non-destructive readouts during an integration requires us to keep track of the actual exposure time for each pixel. This array is useful for simple conversions between counts and count rates.

Figure 12.5: MULTIACCUM Data Format



IRAF Access

The physical format of NICMOS datasets is FITS with image and table extensions. Data is delivered to observers and used within IRAF and **STSDAS** in this format. The FITS image kernel that became available in **IRAF** v2.11 supports the reading and writing of this data format directly.

This permits the use of NICMOS data without conversion (i.e., the **strfits** task is *not* necessary).

Individual FITS image and table extensions are accessed from IRAF tasks by appending to the file name either the index number of the extension, or the combination of the extension name (e.g., SCI, ERR, DQ, SAMP, or TIME) and the extension version number (see Figure 12.4 and Figure 12.5).

Calibration Goals and Plans

In This Chapter...

Expected Calibration Accuracies / 195
Calibration Plans / 197

This chapter describes the expected accuracies which should be reached in the calibration of NICMOS during Cycle 10. Since the NCS-operated NICMOS represents a new instrument, a full new suite of calibrations will be obtained during Cycle 10 to characterize the instrument performance under the new operating conditions. The list of activities which will be performed during the Servicing Mission Orbital Verification 3B (SMOV3B) to enable science with NICMOS is also detailed for reference.

Expected Calibration Accuracies

Remarks

In Table 13.1 we list a provisional summary of our calibration goals for Cycle 10. These goals represent the calibrations and performance achieved by NICMOS during Cycle 7 and 7N. Calibration proposals which will be executed during the SMOV phase and during the Cycle 10 calibration program are aimed at reproducing (and possibly improving on) the same level of calibration obtained during Cycle 7 and 7N. Although observers may plan on NICMOS achieving these levels of performance, uncertainties

still exist, as explained in the next section. Science programs which require superior calibrations should request and justify additional observing time to reach the necessary calibration accuracy.

Areas of Significant Uncertainty

The figures reported in the Table below are drawn directly from the performance and calibrations achieved with NICMOS during its “cryogenic life” (Cycle 7 and Cycle 7N). Uncertainties in the actual performance during Cycle 10 are related to the temperature stability under NCS operations on both orbital and secular timescales. Current requirements set goals of 0.1 K temperature stability on orbital scale and 0.5 K over one year. Other areas of uncertainty include the quality of the transformations and (for a small portion of each Camera’s field of view) the effects of vignetting.

Provisional Cycle 10 Calibration Goals

Table 13.1: Summary of Cycle 10 Calibration Goals

Attribute	Accuracy	Limiting Factor/Notes
Detector dark current and shading	<10 DN	All MULTIACCUM sequences will have good calibrations. A small subset of the available ACCUM mode exposure times will have a direct calibration.
Flat fields	1% broad-band 2-3% narrow-band	Color dependence may limit flats in some cases. The low spatial frequency may only be reliable to $\leq 3\%$.
Photometry	5% photometric zero point 2% relative over FOV 2% stability	Photometric systems, Intrapixel effects, Filter leaks on red sources
PSF and focus	Maintained within 1 mm	Breathing and OTA desorption are approximately equal effects.
Coronagraphic PSF	0.013 arcsec accuracy positioning in the hole	
Polarization	~1% relative intensity 3-5% polarization accuracy	Photometric performance Ghosts/polarizing efficiency
GRISM wavelength calibration	.005 μm	Limited by centroiding of target for wavelength zeropoint determination.
GRISM photometric calibration	20–30% absolute and relative	The figure is quoted without the NIC3 intrapixel sensitivity correction. With this correction, GRISM photometry will be better. Expected accuracy over central 80% of spectral range. Grism C flat field may not achieve this performance.
Astrometry	0.2% plate scale 0.1" to FGS frame	

Calibration Plans

The calibrations available during Cycle 10 will be based on two distinct calibration activities. First, the activity known as SMOV will provide science-enabling and initial calibrations for all NICMOS science modes. Second, the routine Cycle 10 calibration program will provide the necessary observations to achieve the goals set in Table 13.1.

It is important to distinguish between the various goals of these calibration activities. SMOV is intended to demonstrate that the instrument

is functioning as expected, based on both previous experience and expectations under NCS operations, to establish necessary operation parameters (e.g. plate scale), and to begin the calibration and scientific use of NICMOS. In many cases the complete calibration will be conducted during Cycle 10 with SMOV being used to demonstrate that the planned calibrations are in fact feasible. This approach is designed to enable the acquisition of science observations at the earliest possible date, even if the best possible calibrations do not become available until some time later. This contributes to the efficiency with which HST can be operated.

As of this writing, only a preliminary draft of the SMOV activities is known and those activities relevant to NICMOS calibrations are listed in Table 13.2, for reference. The baseline of the SMOV plan for NICMOS consists of 30 activities, of which 24 are calibration-related. Some of these test specific components of the instrument while others characterize its performance within the HST environment. A number of proposals are aimed at testing the detector's temperature stability under NCS operations, and performance changes with temperature variations.

Table 13.2: Planned (preliminary) NICMOS SMOV Activities

Activity Title	Demonstrates or Calibrates
NICMOS Cool-down Dark Performance	Dark performance as a function of temperature
NICMOS Cool-down Flat-Field Performance	Flat-field performance as a function of temperature.
NICMOS Temperature: Setpoint and Stability	Demonstrate detector's temperature stability within 0.1 K on orbital scales
NICMOS Focus Characteristics with Temperature	Demonstrate NICMOS optical alignment repeatability after temperature variations
NICMOS Transfer Function Test	Set optimal detector DC offset voltages.
NICMOS SAA Cosmic-Ray Persistence Test	Measurement of decay time of SAA cosmic ray events.
NICMOS Jitter Test	Demonstrate that the NCS-induced jitter does not degrade NICMOS image quality
NICMOS Target Acquisition Test (Mode 2)	Demonstrate Mode 2 (on-board) acquisitions.
NICMOS to FGS Astrometric Calibration	Establish the locations of the NICMOS detectors within the FGS coordinate system.
NICMOS Plate Scale and Astrometric Calibration	Determine plate scales, relative field rotations, and field distortions for each camera.
NICMOS Fine Optical Alignment	Optimal positioning of the PAM based on grid of small PAM motions.
NICMOS NIC3 Fine Optical Alignment	Optimal positioning of the PAM /FOM for NICMOS camera 3.
NICMOS Focus Monitor	Monitoring of NICMOS best focus position (stability).

Table 13.2: Planned (preliminary) NICMOS SMOV Activities

Activity Title	Demonstrates or Calibrates
NICMOS Point Spread Function Characterization	Characterization of the imaging performance of NICMOS and initial set of PSF observations.
NICMOS Astronomical Persistence Test	Characterize the effect of severe overexposure of the NICMOS detectors. Measurements of decay time for photon persistence.
NICMOS Intflat Ability and Stability	Demonstration of flat fielding capability and stability monitoring.
NICMOS HST Thermal Background Test	Characterization of HST generated thermal background over a broad range of situations.
NICMOS Absolute Photometry Test	Standard star observations across NICMOS wavelength range. Updates SLTV throughput calibration.
NICMOS Differential Photometry Test	Inter-camera photometric precision and stability test obtained from observations of a star at 25 positions.
NICMOS Detector Noise and Dark Characterization, Cosmic Ray Test	Characterization of detector noise and dark current. Comparison and bootstrap from Cycle 7N warm-up. Re-verification of CR rate.
NICMOS Coronagraphic Performance Verification	Optical characterization of coronagraphic stray light rejection and PSF of the obscured star.
NICMOS Geometric Stability Test	Stability of the coronagraphic spot, measurements of detector's lateral motions in the NIC2 focal plane.
NICMOS Grisms Absolute Sensitivity	Determine Grisms sensitivity. Compare with Cycle 7 performance.
NICMOS Grisms Wavelength Calibration	Derive wavelength calibrations for Grisms. Compare with Cycle 7 performance.

Appendices

The chapters in this part provide reference material in support of NICMOS observations. Included are filter throughputs and sensitivity curves, infrared flux units and lists of infrared lines. Finally, we give a description of the BRIGHTOBJ readout more, which is unsupported in Cycle 10.

Imaging Reference Material

This chapter provides basic information and sensitivity plots for the imaging and polarimetric filters. The corresponding information for the grism elements is provided in Chapter 5. The spectral characteristics of the NICMOS flight filters were measured at cryogenic temperature and normal incidence at Ball Aerospace. All filters had their spectral transmission measured from 0.5 to 2.7 microns with a step of 0.001 microns. For each filter, we provide the following information:

1. A plot of the filter throughput, which convolves the filter transmission curve with the OTA, the NICMOS foreoptics and the predicted detector's response under NCS operations. A listing of the central, mean, and peak wavelengths, of the wavelength range, filter width, transmission peak, and the fraction of the PSF contained in one pixel (assuming the source is centered on the pixel) is also given.
2. Sensitivity curves for each filter. The curves are calculated for both an extended and a point source, assuming in both cases a flat spectrum [in $F(\lambda)$]. The curves give the flux as a function of time needed to reach $S/N=3$ and $S/N=10$, respectively (continuous and dotted lines). For the extended sources, the flux is given in Jy/arcsec^2 and the S/N is calculated per pixel; for the point sources, the flux is given in Jy, and the S/N is calculated in a 0.5" radius aperture (NIC1 and NIC2) or 1" radius aperture (NIC3). The continuous lines correspond to the best scenario for dark current ($0.5 \text{ e}^-/\text{s}$), while the dotted lines correspond to the worst case scenario ($2.5 \text{ e}^-/\text{s}$). In all cases, the adopted read-out noise is $\sim 30 \text{ e}^-$ and the DQE is that expected for operations at 75 K (see Chapter 8). The sky background, as listed in Chapter 9, is included in all computations. The saturation limit as a function of time is also shown (dashed line); for the extended sources, we have computed the flux which saturates the pixel (the aperture), while for point sources we have computed the flux needed to saturate the brightest pixel (assuming the source is centered on the pixel). The range of times given goes from 0.2 to $\sim 3,000$ seconds, although we advise observers not to use

exposures longer than about 1/3-1/2 orbit ($t < 1500$ -1600 seconds, see Chapter 3).



Proposers should always assume the worst case scenario for the NICMOS dark current (see Chapter 8) to calculate exposure times.

Camera 1, Filter F090M

Figure A1.1: F090M Throughput

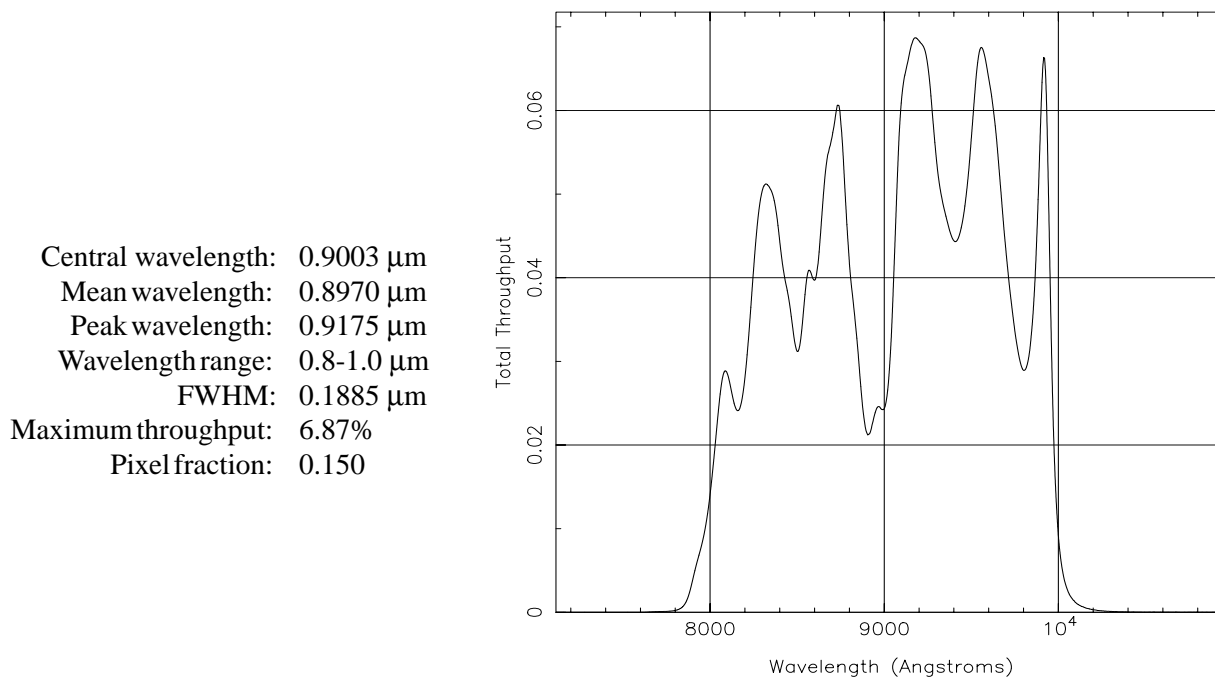
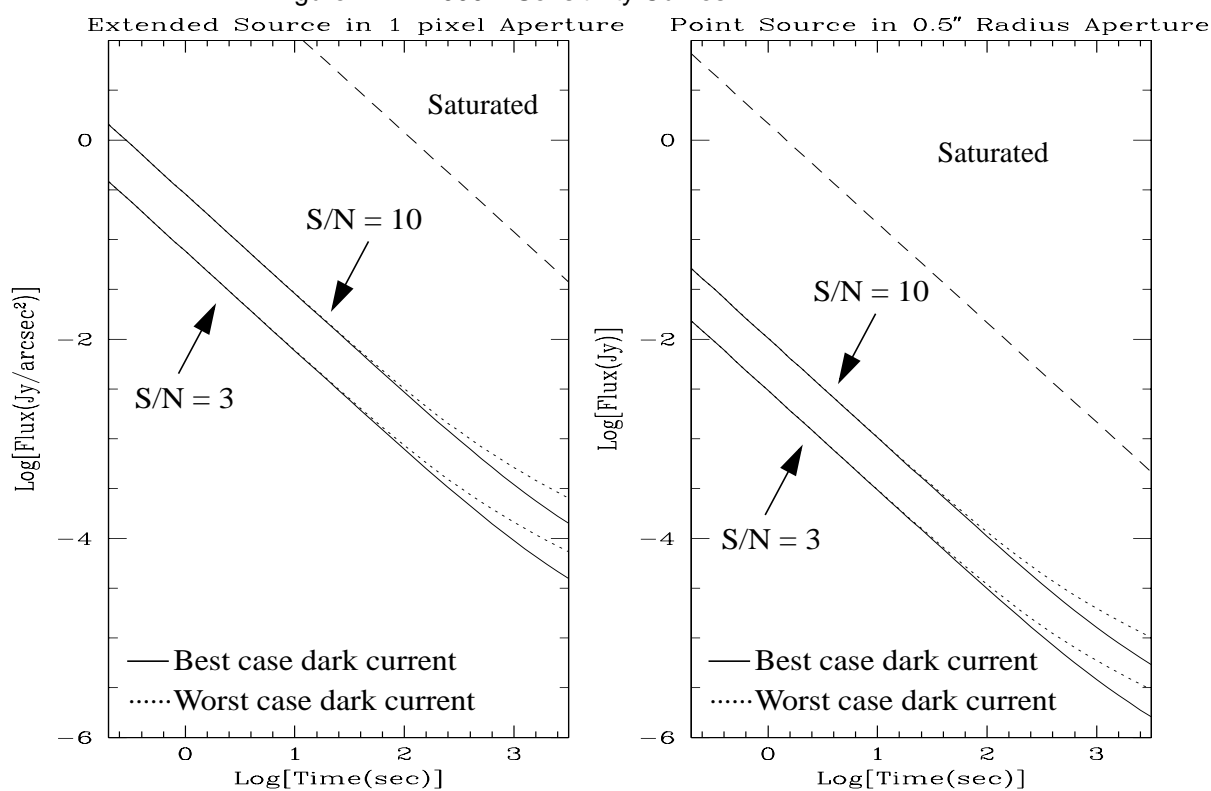


Figure A1.2: F090M Sensitivity Curves



Camera 1, Filter F095N

Figure A1.3: NIC1, F095N Throughput

Notes:

[S III] line.

Central wavelength: 0.9538 μm
 Mean wavelength: 0.9536 μm
 Peak wavelength: 0.9508 μm
 Wavelength range: 1%
 FWHM: 0.0088 μm
 Maximum throughput: 5.66%
 Pixel fraction: 0.136

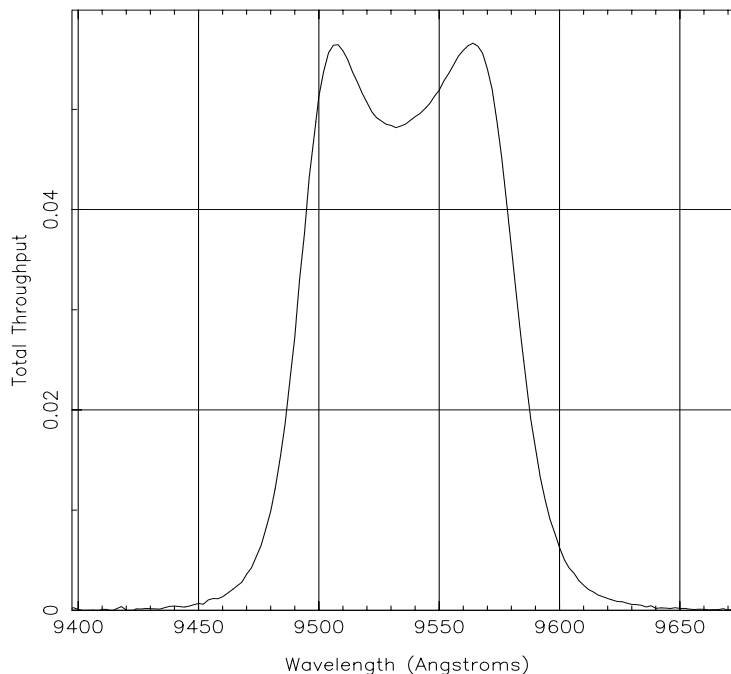
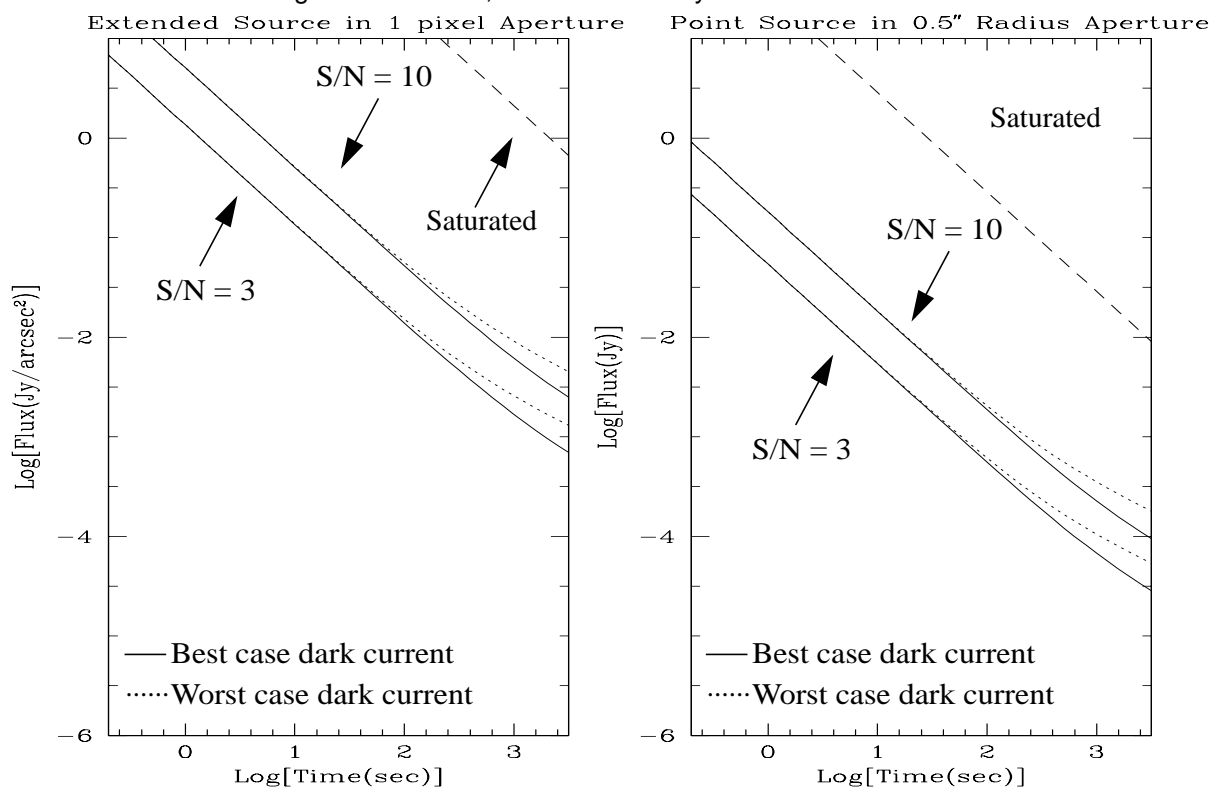


Figure A1.4: NIC1, F095N Sensitivity Curves



Camera 1, Filter F097N

Figure A1.5: NIC1, F097N Throughput

Notes:

[S III] continuum.

Central wavelength: 0.9717 μm
 Mean wavelength: 0.9715 μm
 Peak wavelength: 0.9740 μm
 Wavelength range: 1%
 FWHM: 0.0094 μm
 Maximum throughput: 6.73%
 Pixel fraction: 0.131

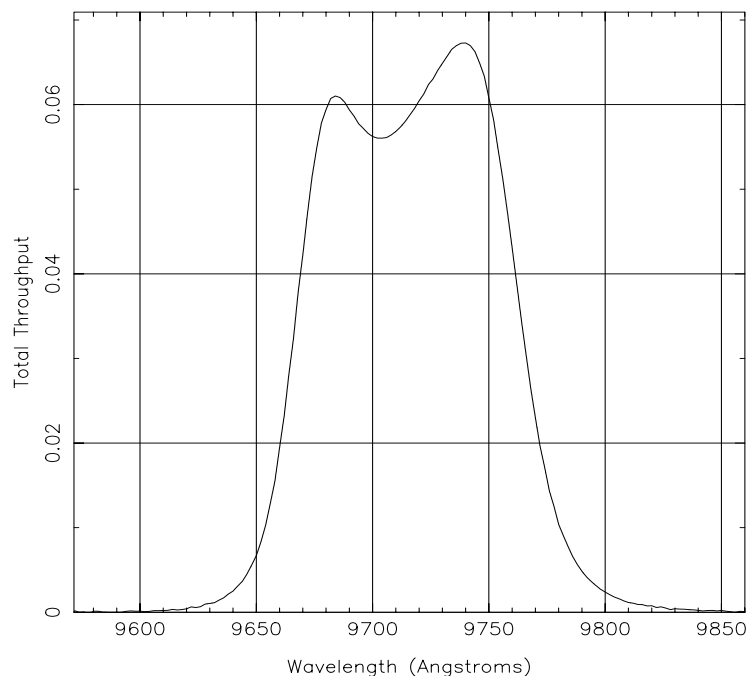
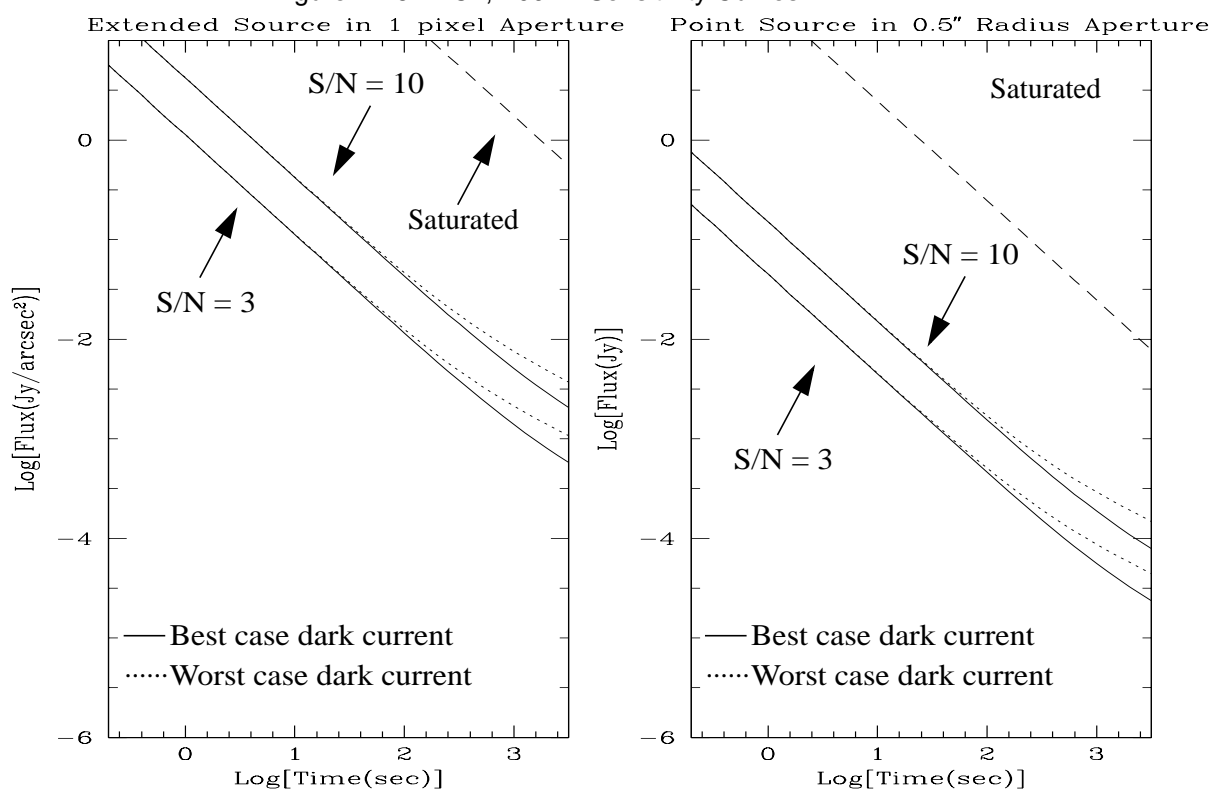


Figure A1.6: NIC1, F097N Sensitivity Curves



Camera 1, Filter F108N

Figure A1.7: NIC1, F108N Throughput

Notes:

[He I] line.

See also "Camera 3, Filter F108N"

Central wavelength: 1.0817 μm
 Mean wavelength: 1.0816 μm
 Peak wavelength: 1.0790 μm
 Wavelength range: 1%
 FWHM: 0.0094 μm
 Maximum throughput: 8.14%
 Pixel fraction: 0.111

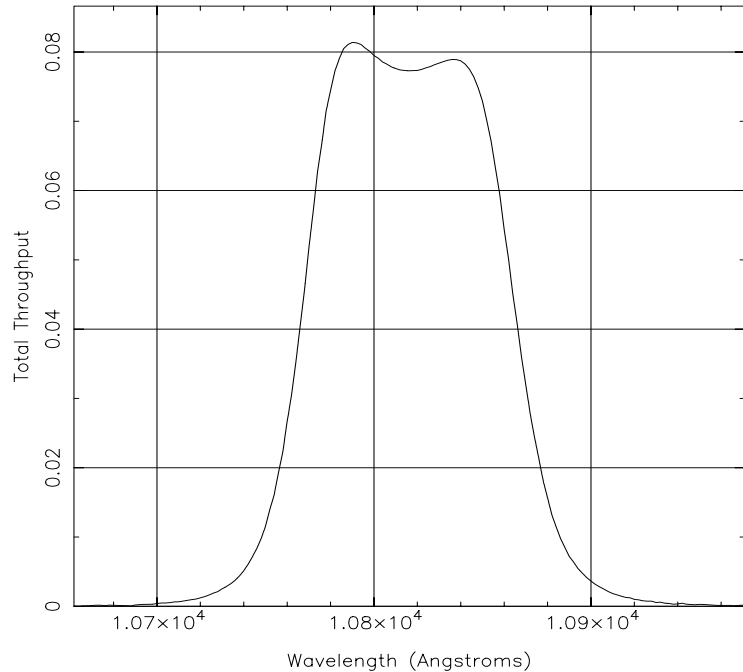
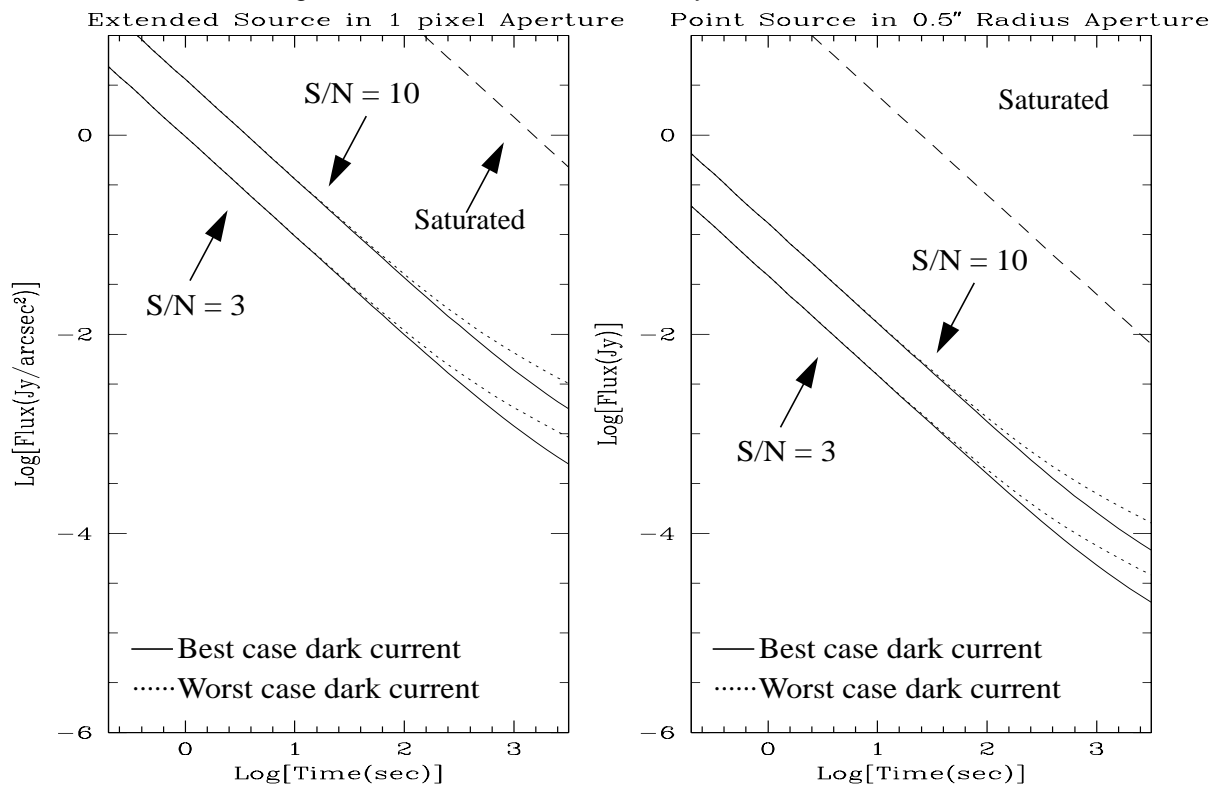


Figure A1.8: NIC1, F108N Sensitivity Curves



Camera 1, Filter F110M

Figure A1.9: NIC1, F110M Throughput

Notes:

See also “Camera 1, Filter F110W”.

Central wavelength: 1.1013 μm
 Mean wavelength: 1.1003 μm
 Peak wavelength: 1.1295 μm
 Wavelength range: 1.0-1.2 μm
 FWHM: 0.1995 μm
 Maximum throughput: 10.46%
 Pixel fraction: 0.108

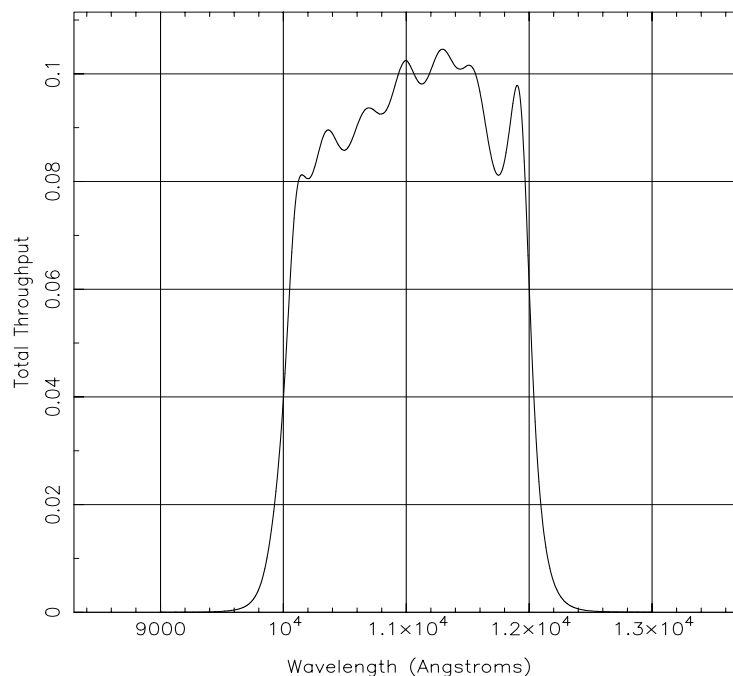
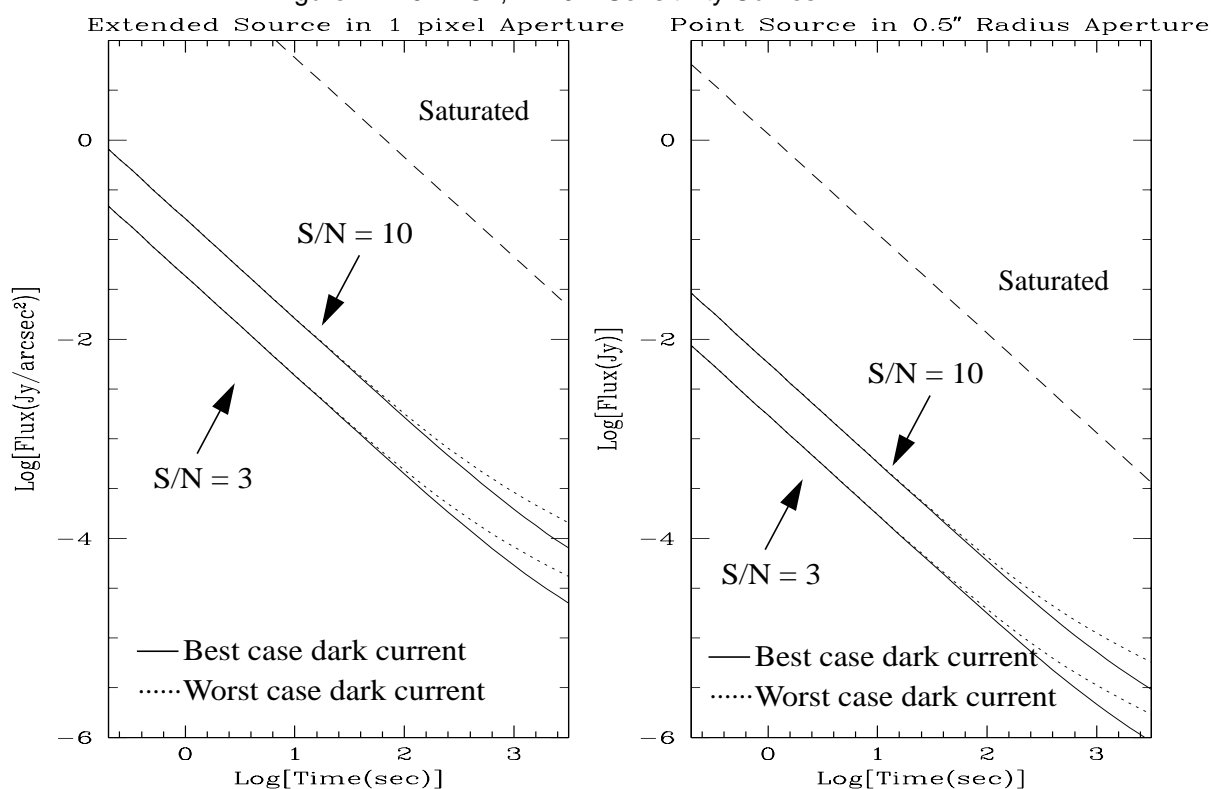


Figure A1.10: NIC1, F110M Sensitivity Curves



Camera 1, Filter F110W

Figure A1.11: NIC1, F110W Throughput

Notes:

See also “Camera 2, Filter F110W” and
“Camera 3, Filter F110W”.

Central wavelength: 1.0985 μm
 Mean wavelength: 1.1022 μm
 Peak wavelength: 1.2760 μm
 Wavelength range: 0.8-1.35 μm
 FWHM: 0.5920 μm
 Maximum throughput: 13.37%
 Pixel fraction: 0.113

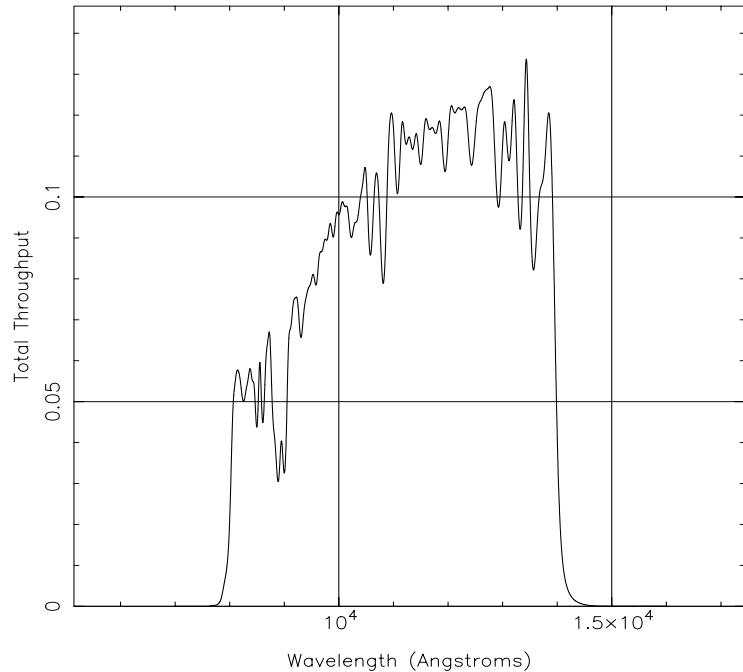
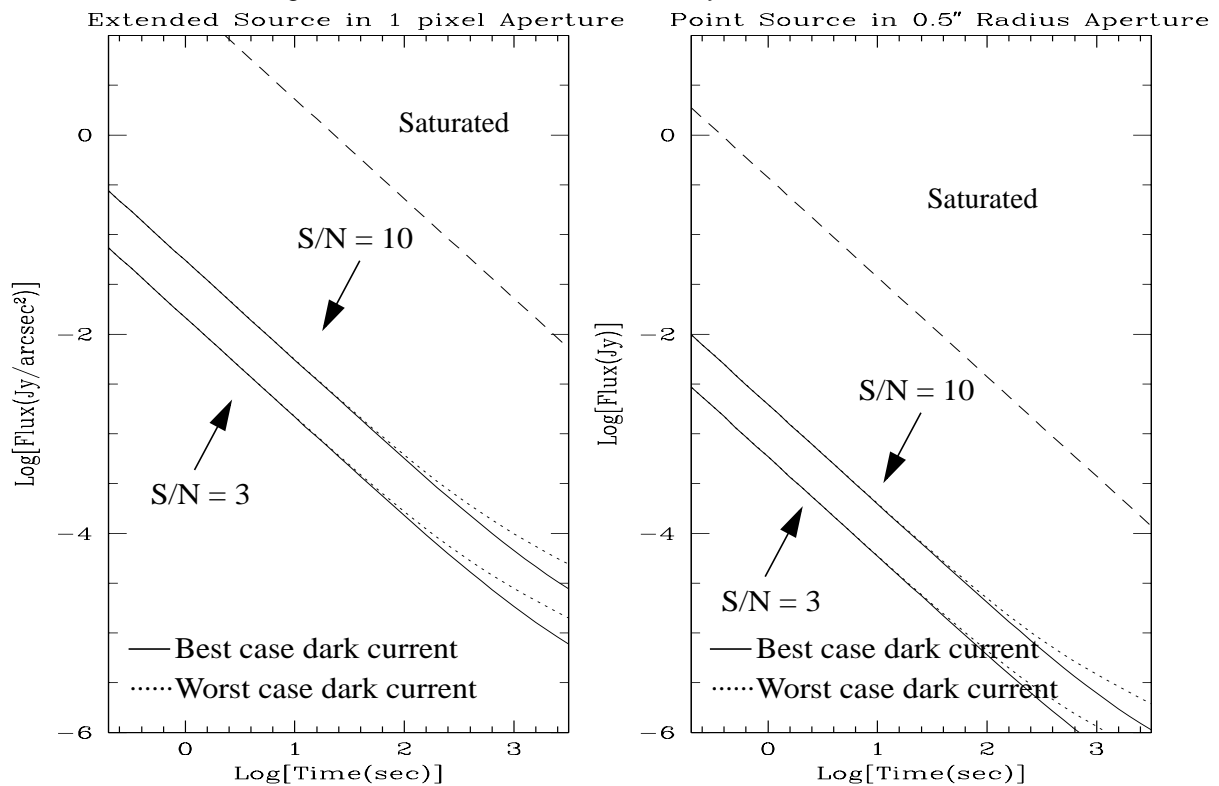


Figure A1.12: NIC1, F110W Sensitivity Curves



Camera 1, Filter F113N

Figure A1.13: NIC1, F113N Throughput

Notes:

[He I] continuum.

See also "Camera 3, Filter F113N".

Central wavelength: 1.1297 μm
 Mean wavelength: 1.1298 μm
 Peak wavelength: 1.1312 μm
 Wavelength range: 1%
 FWHM: 0.0110 μm
 Maximum throughput: 9.52%
 Pixel fraction: 0.102

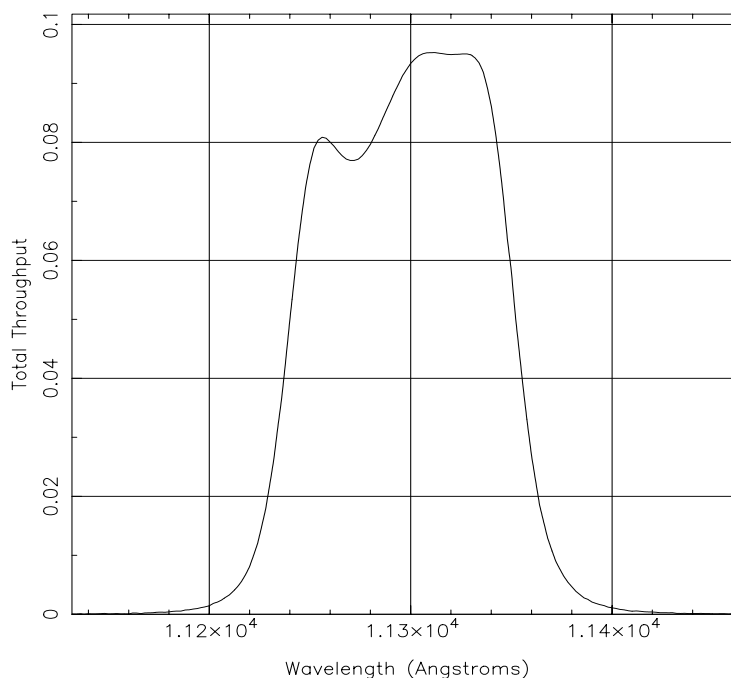
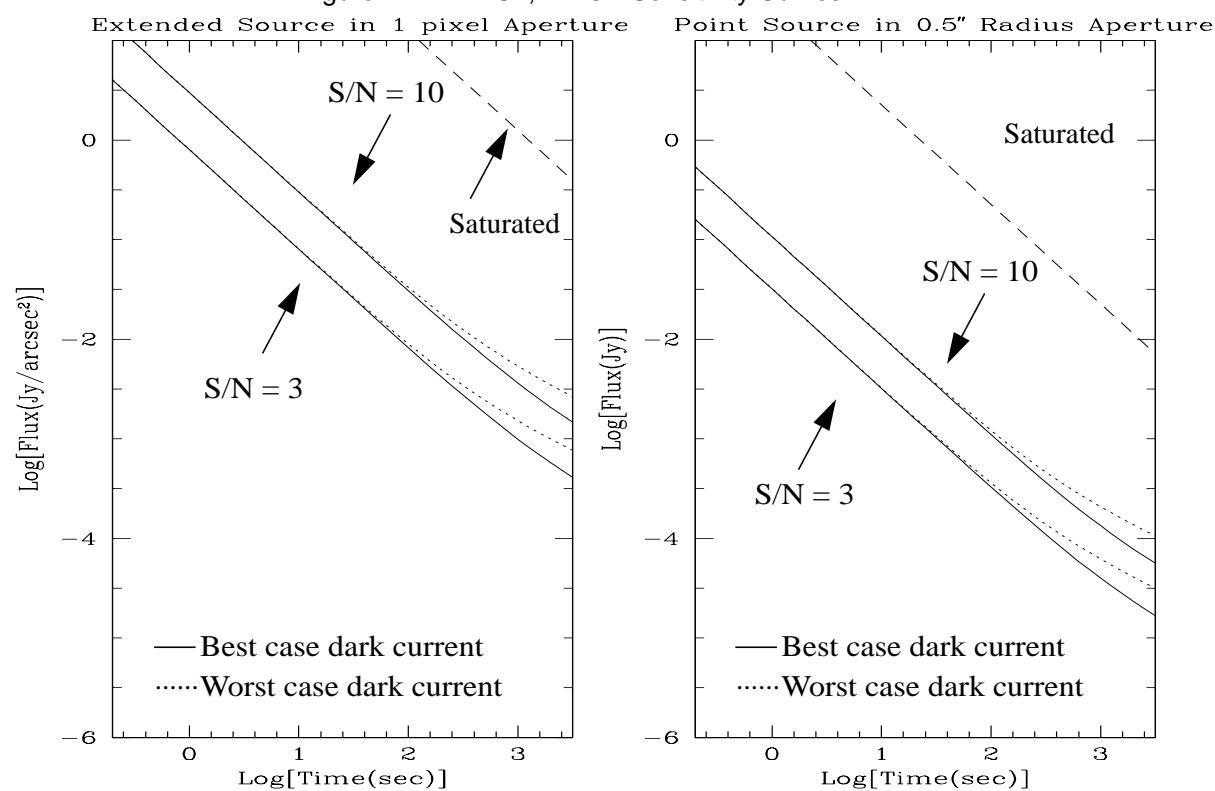


Figure A1.14: NIC1, F113N Sensitivity Curves



Camera 1, Filter F140W

Figure A1.15: NIC1, F140W Throughput

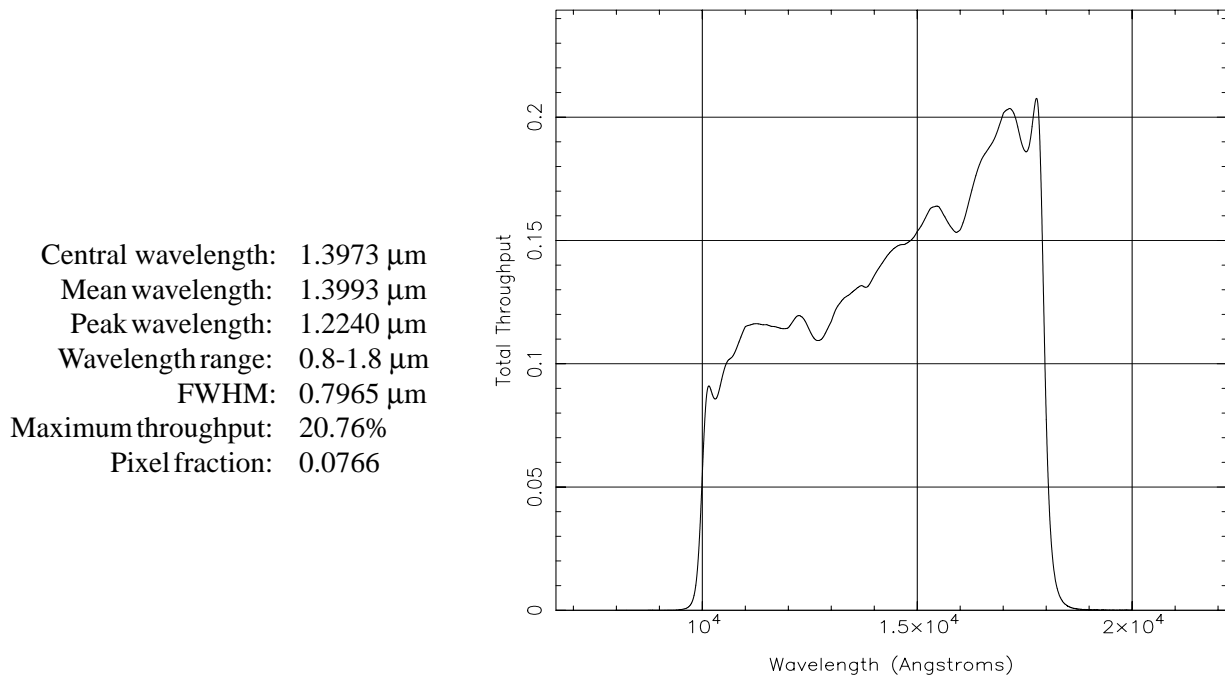
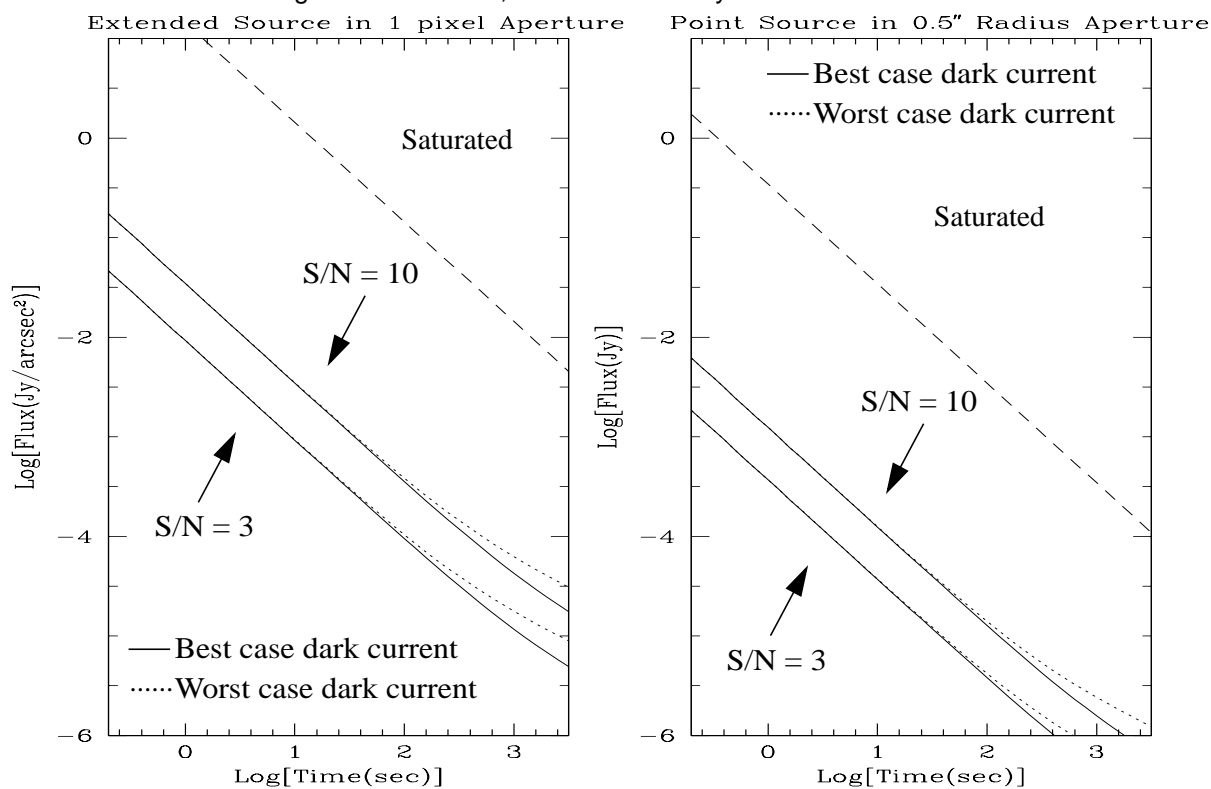


Figure A1.16: NIC1, F140W Sensitivity Curves



Camera 1, Filter F145M

Figure A1.17: NIC1, F145M Throughput

Notes:

H₂O band.

Central wavelength: 1.4513 μm
 Mean wavelength: 1.4524 μm
 Peak wavelength: 1.5100 μm
 Wavelength range: 1.35-1.55 μm
 FWHM: 0.1965 μm
 Maximum throughput: 16.35%
 Pixel fraction: 0.0640

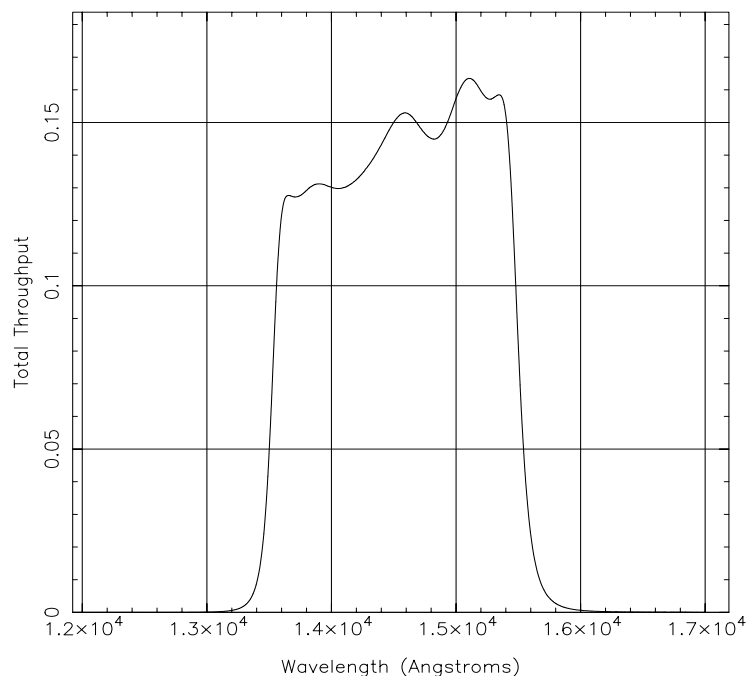
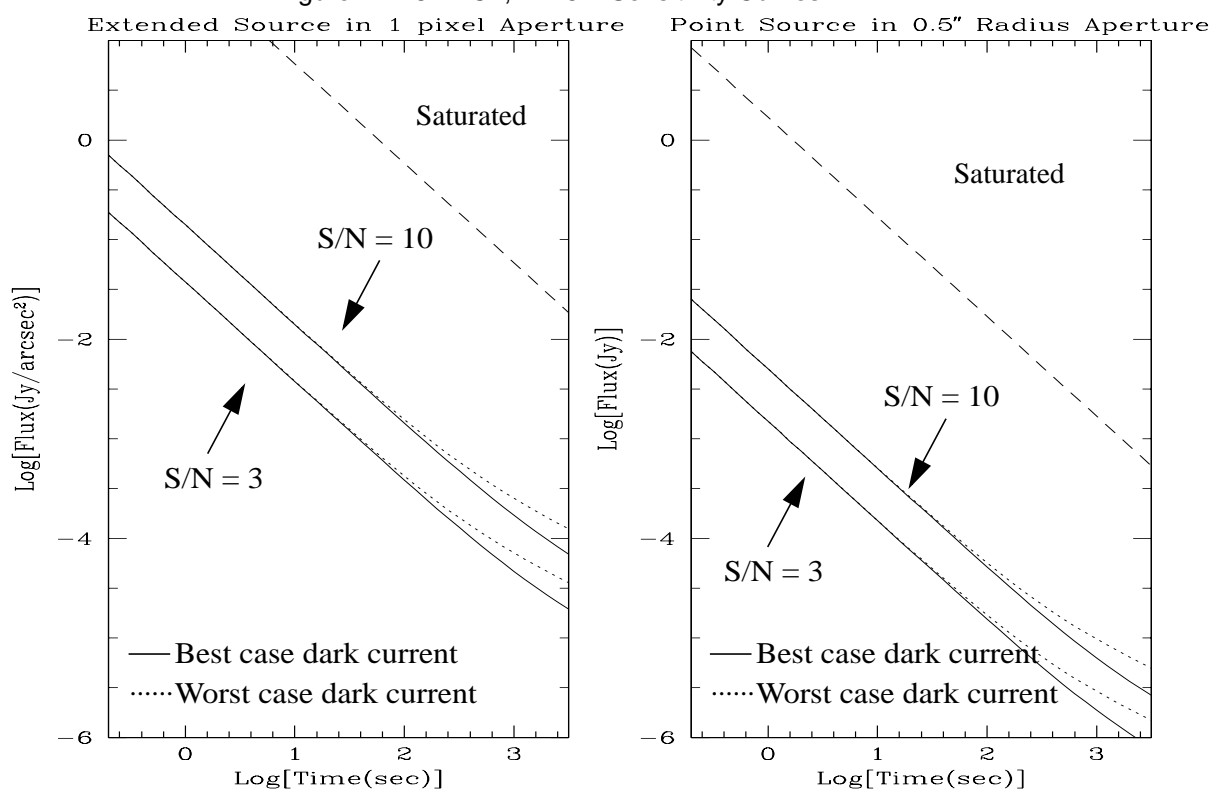


Figure A1.18: NIC1, F145M Sensitivity Curves



Camera 1, Filter F160W

Figure A1.19: NIC1, F160W Throughput

Notes:

Minimum background.

See also “Camera 2, Filter F160W” and “Camera 3, Filter F160W”.

Central wavelength: 1.5960 μm
 Mean wavelength: 1.5947 μm
 Peak wavelength: 1.5830 μm
 Wavelength range: 1.35-1.75 μm
 FWHM: 0.4000 μm
 Maximum throughput: 20.91%
 Pixel fraction: 0.0562

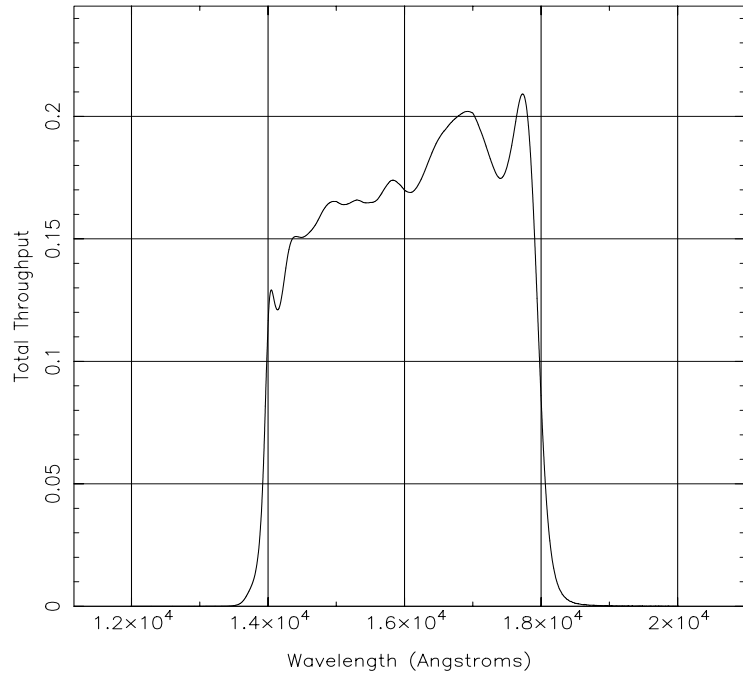
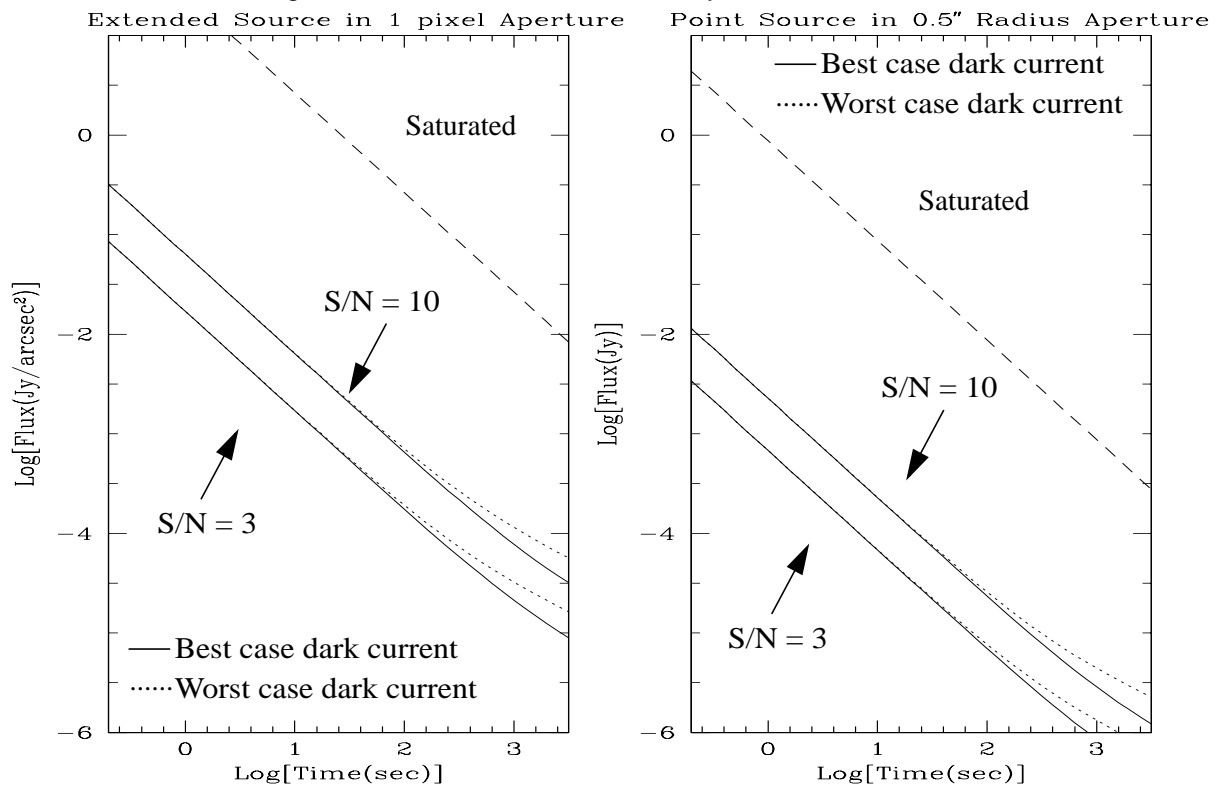


Figure A1.20: NIC1, F160W Sensitivity Curves



Camera 1, Filter F164N

Figure A1.21: NIC1, F164N Throughput

Notes:

[Fe II] line.

See also "Camera 3, Filter F164N".

Central wavelength: 1.6353 μm
 Mean wavelength: 1.6354 μm
 Peak wavelength: 1.6378 μm
 Wavelength range: 1%
 FWHM: 0.0166 μm
 Maximum throughput: 17.96%
 Pixel fraction: 0.0534

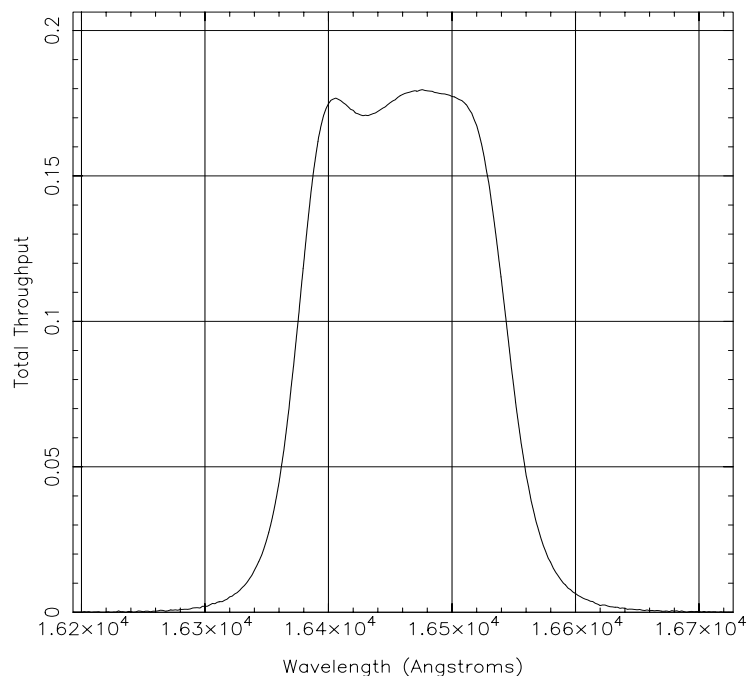
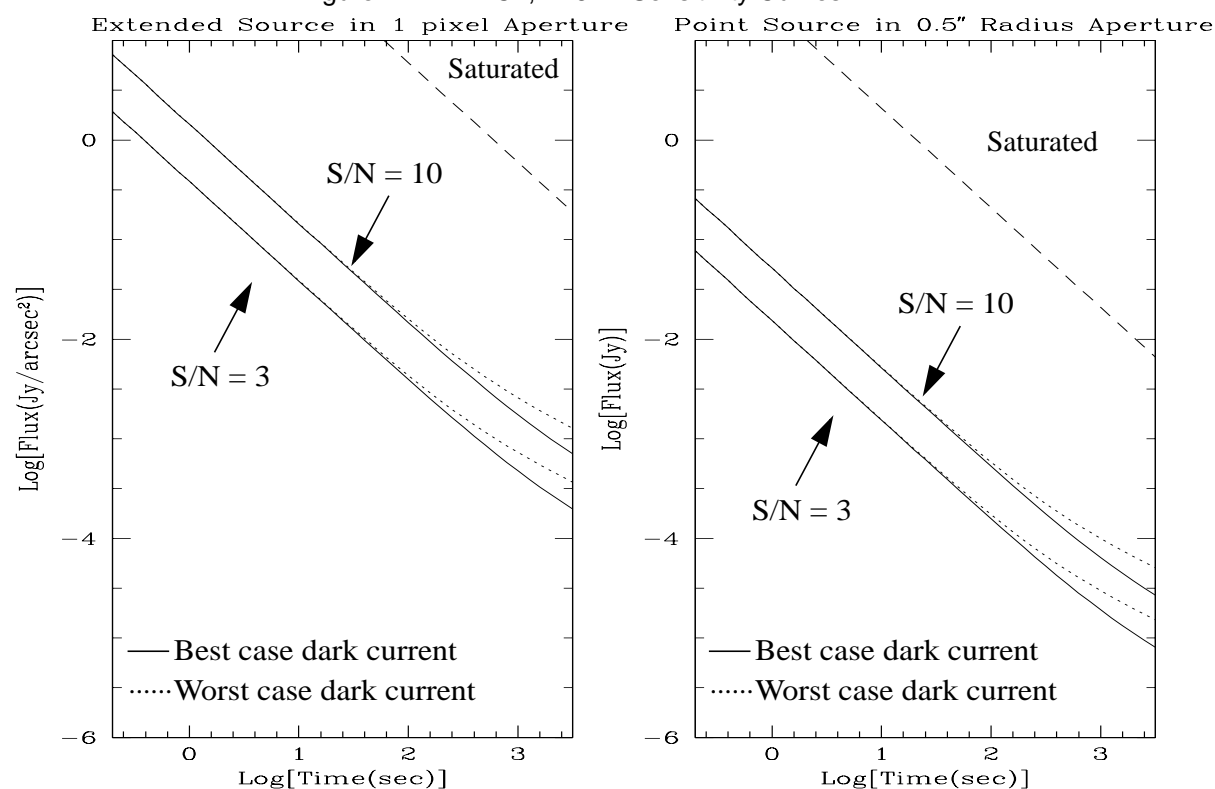


Figure A1.22: NIC1, F164N Sensitivity Curves



Camera 1, Filter F165M

Figure A1.23: NIC1, F165M Throughput

Notes:

H₂O continuum.

See also “Camera 2, Filter F165M”.

Central wavelength: 1.6438 μm
 Mean wavelength: 1.6446 μm
 Peak wavelength: 1.5735 μm
 Wavelength range: 1.55-1.75 μm
 FWHM: 0.1985 μm
 Maximum throughput: 20.44%
 Pixel fraction: 0.0521

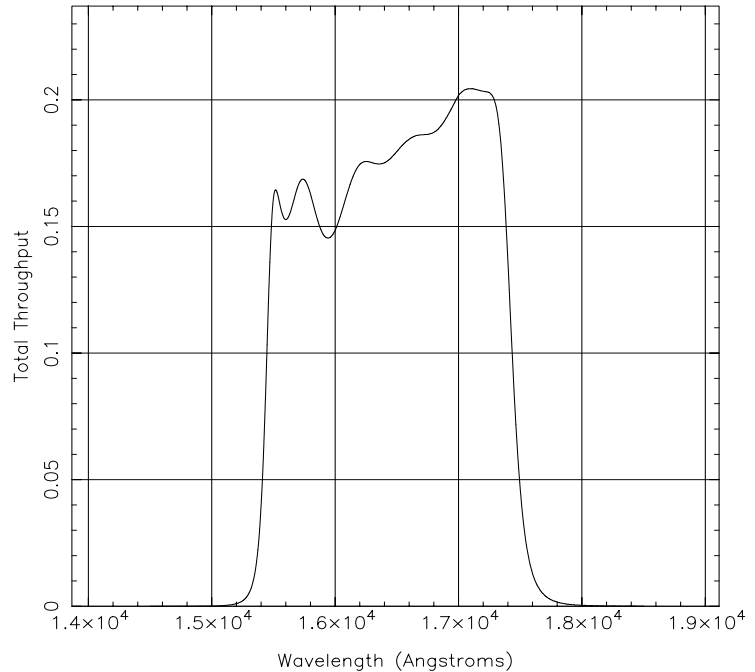
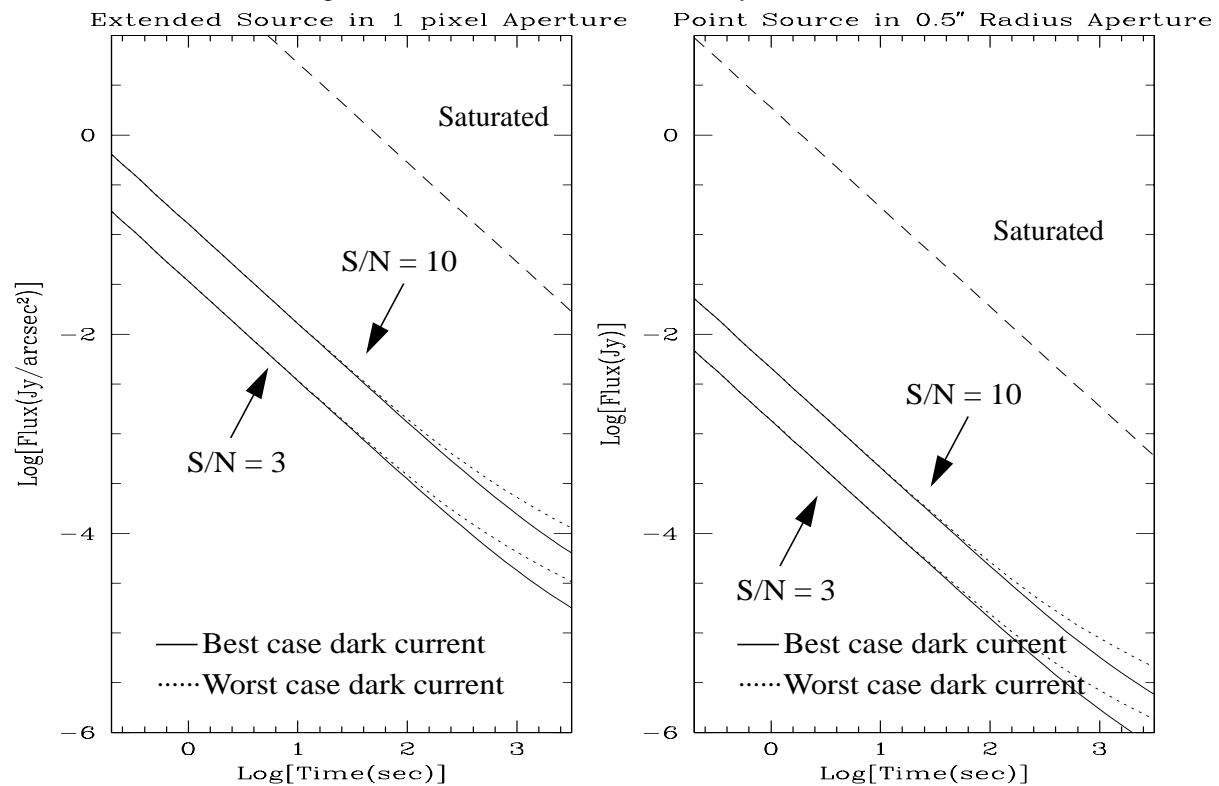


Figure A1.24: NIC1, F165M Sensitivity Curves



Camera 1, Filter F166N

Figure A1.25: NIC1, F166N Throughput

Notes:

[Fe II] continuum.

See also "Camera 3, Filter F166N".

Central wavelength: 1.6606 μm
 Mean wavelength: 1.6606 μm
 Peak wavelength: 1.6622 μm
 Wavelength range: 1% μm
 FWHM: 0.0168 μm
 Maximum throughput: 18.27%
 Pixel fraction: 0.0505

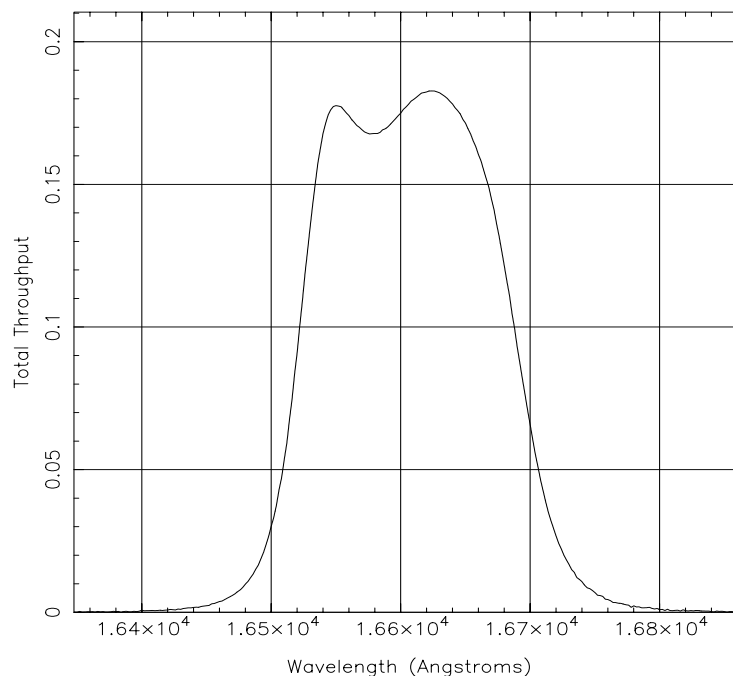
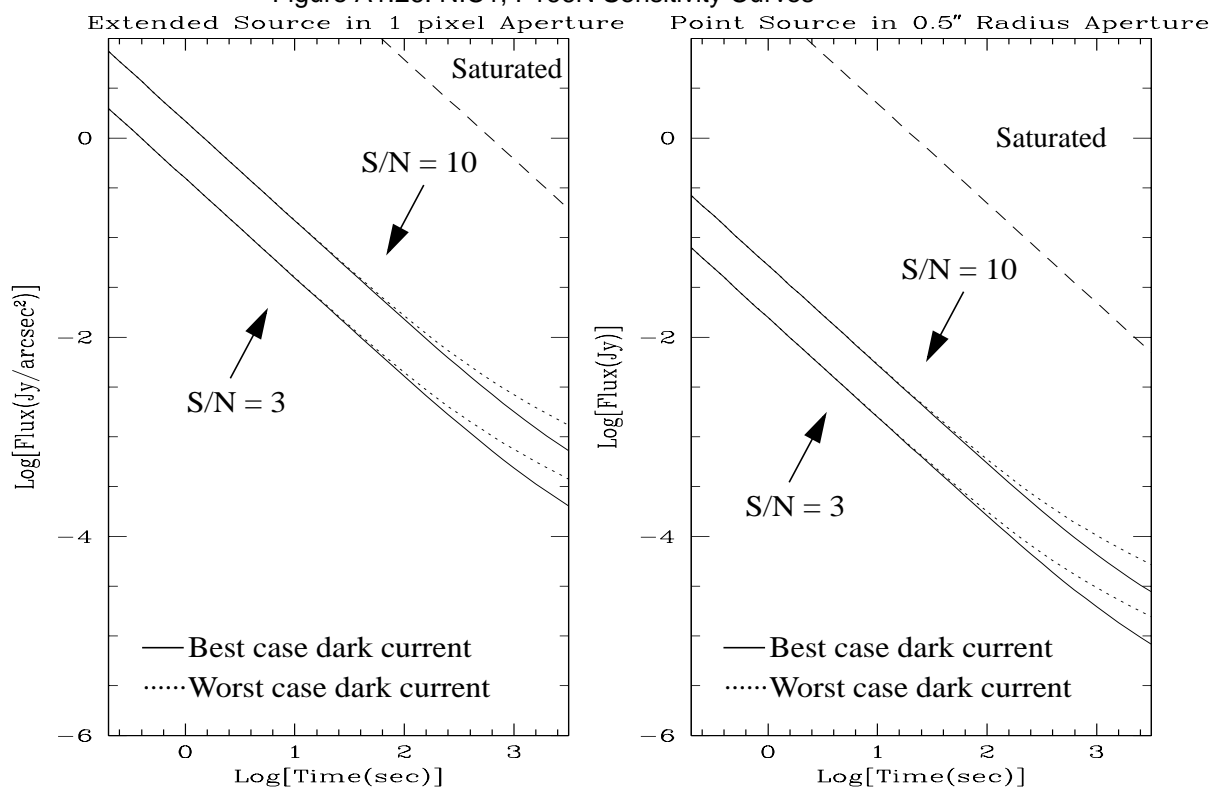


Figure A1.26: NIC1, F166N Sensitivity Curves



Camera 1, Filter F170M

Figure A1.27: NIC1, F170M Throughput

Notes:

See also “Camera 2, Filter F171M”.

Central wavelength: 1.7025 μm
 Mean wavelength: 1.7032 μm
 Peak wavelength: 1.6330 μm
 Wavelength range: 1.6-1.8 μm
 FWHM: 0.2030 μm
 Maximum throughput: 21.08%
 Pixel fraction: 0.0481

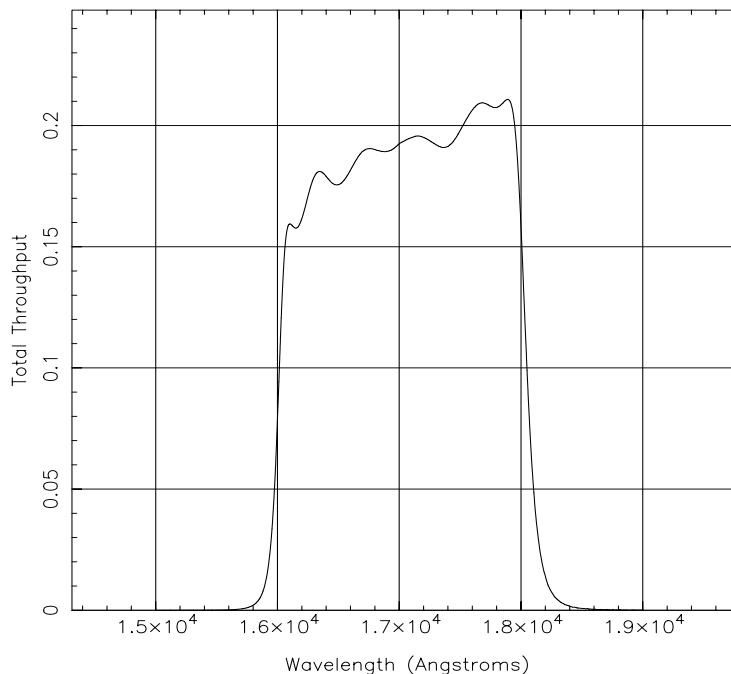
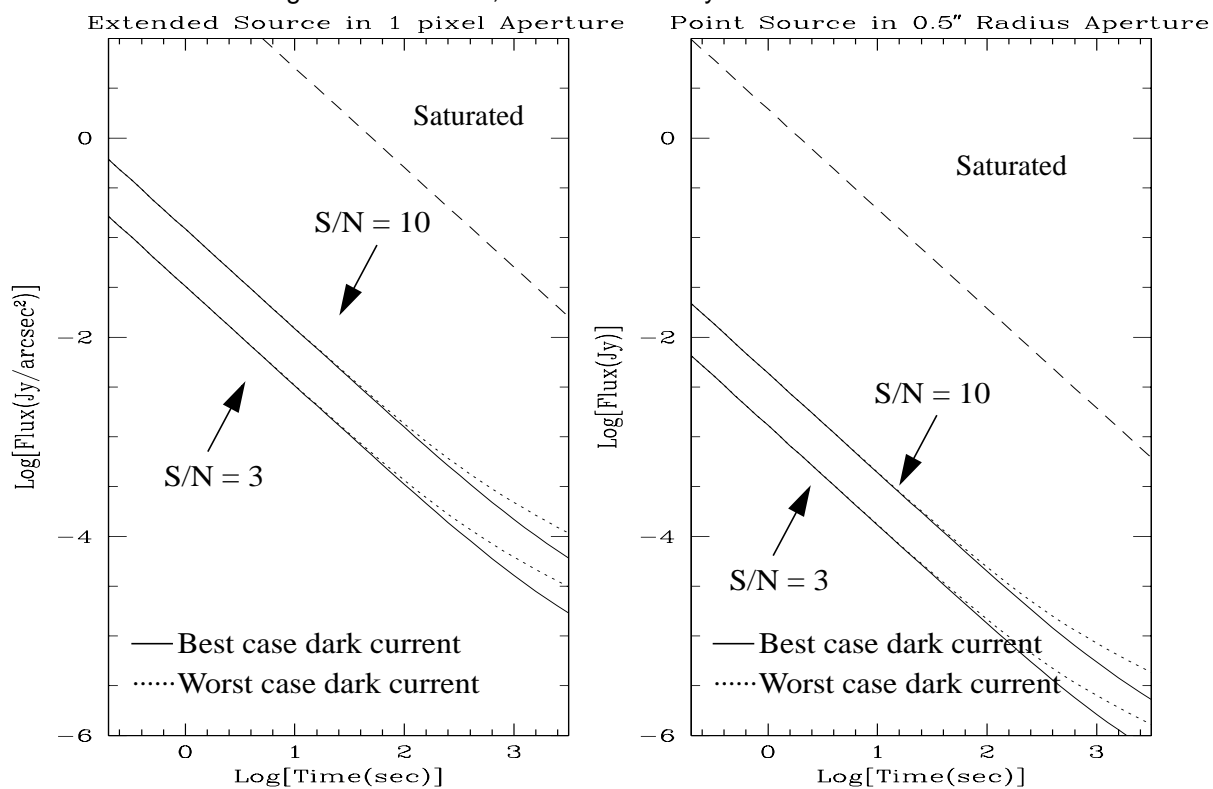


Figure A1.28: NIC1, F170M Sensitivity Curves



Camera 1, Filter F187N

Figure A1.29: NIC1, F187N Throughput

Notes:

Paschen α .

See also “Camera 2, Filter F187N” and “Camera 3, Filter F187N”.

Central wavelength: 1.875 μm
 Mean wavelength: 1.8748 μm
 Peak wavelength: 1.8756 μm
 Wavelength range: 1%
 FWHM: 0.0188 μm
 Maximum throughput: 20.60%
 Pixel fraction: 0.0411

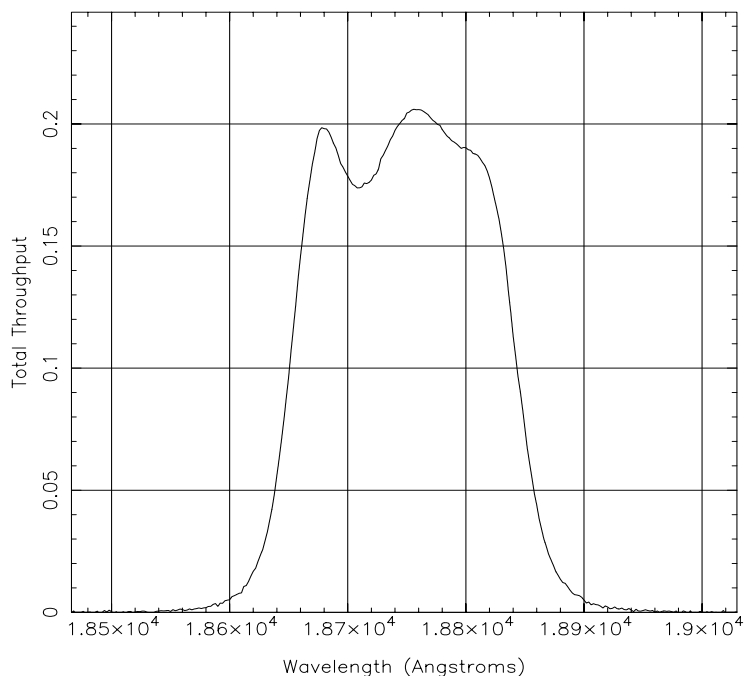
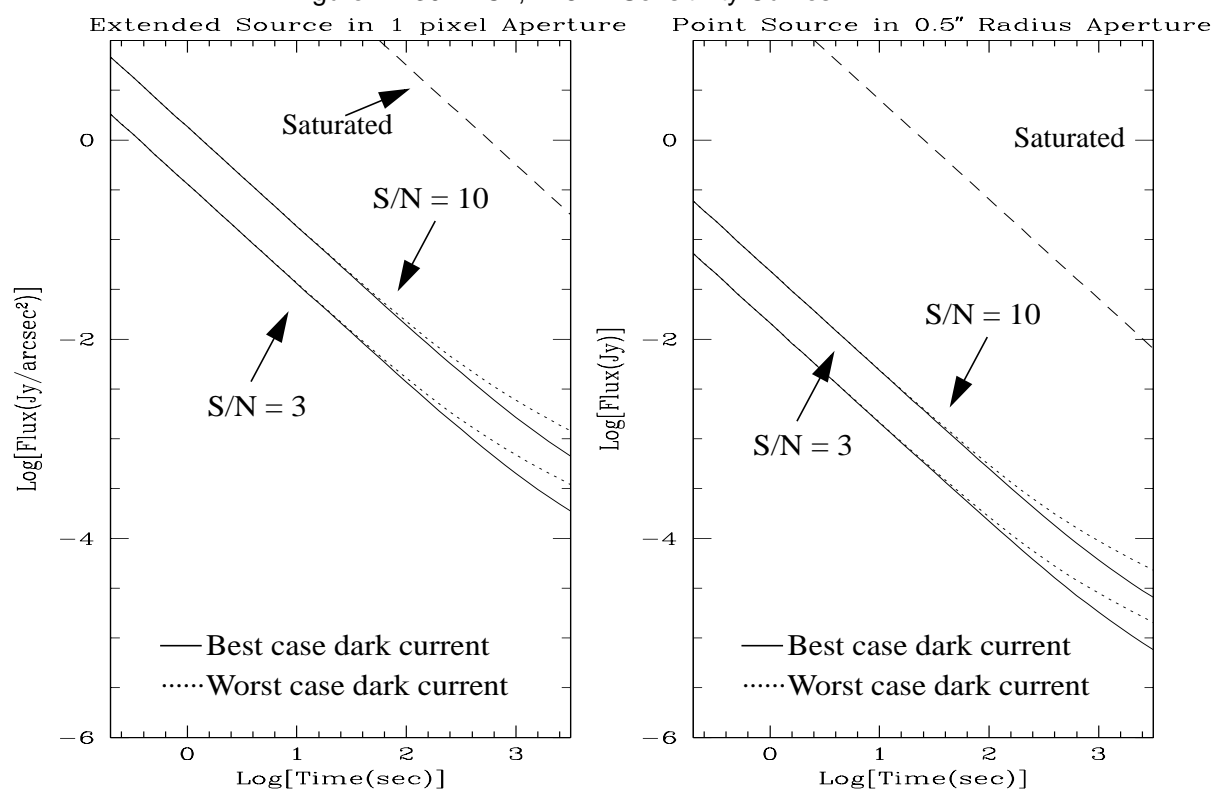


Figure A1.30: NIC1, F187N Sensitivity Curves



Camera 1, Filter F190N

Figure A1.31: NIC1, F190N Throughput

Notes:

Paschen α continuum.

See also “Camera 2, Filter F190N” and “Camera 3, Filter F190N”.

Central wavelength: 1.8987 μm
 Mean wavelength: 1.8986 μm
 Peak wavelength: 1.8942 μm
 Wavelength range: 1%
 FWHM: 0.0174 μm
 Maximum throughput: 21.08%
 Pixel fraction: 0.0401

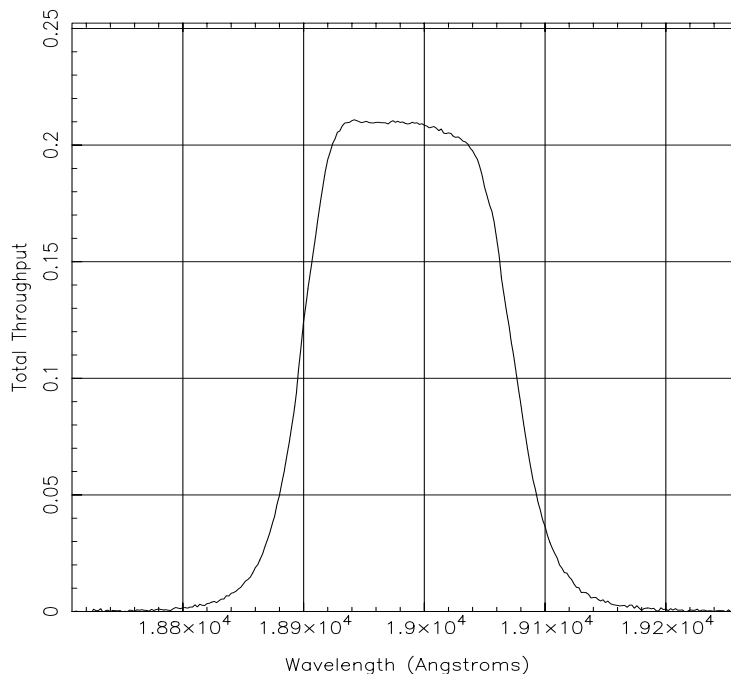
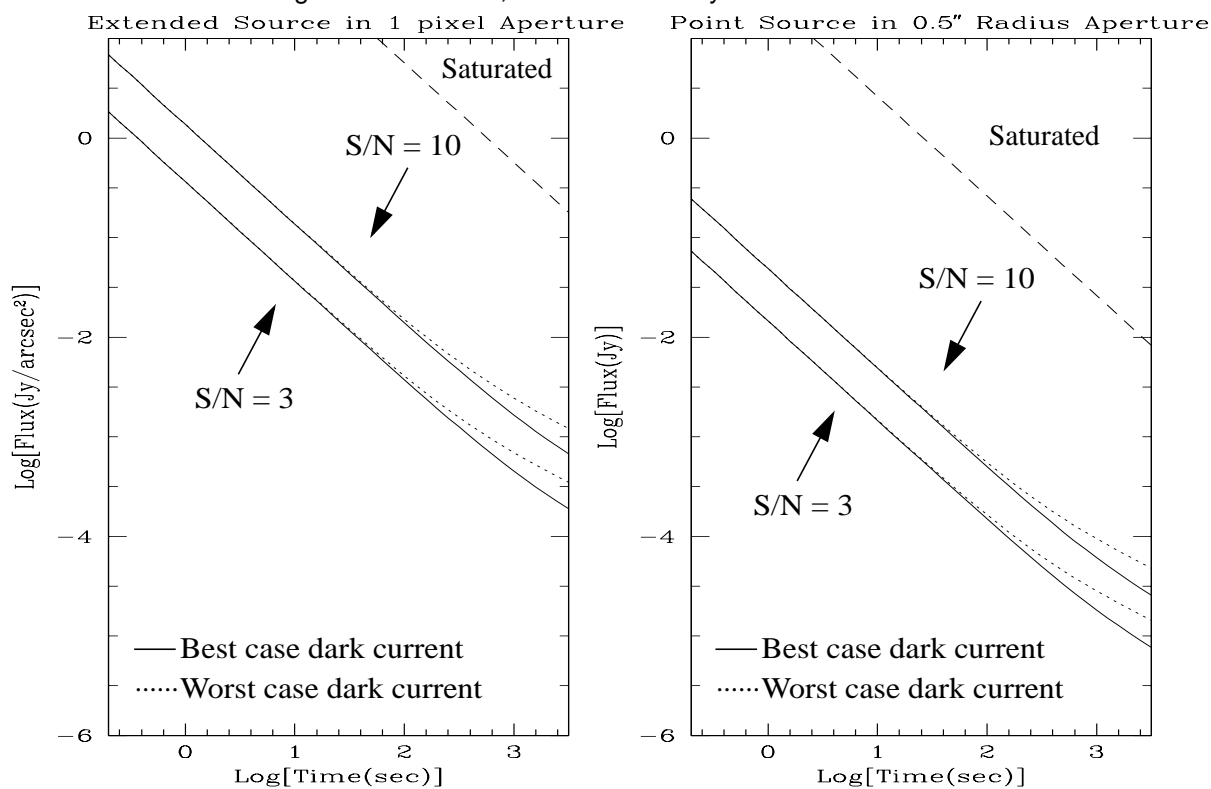


Figure A1.32: NIC1, F190N Sensitivity Curves



Camera 1, Polarizer POL0S

Figure A1.33: NIC1, POL0S Throughput

Central wavelength: $1.0450\ \mu\text{m}$
 Mean wavelength: $1.0384\ \mu\text{m}$
 Peak wavelength: $1.0245\ \mu\text{m}$
 Wavelength range: $0.8\text{--}1.3\ \mu\text{m}$
 FWHM: $0.4750\ \mu\text{m}$
 Maximum throughput: 4.95%
 Pixel fraction: 0.048

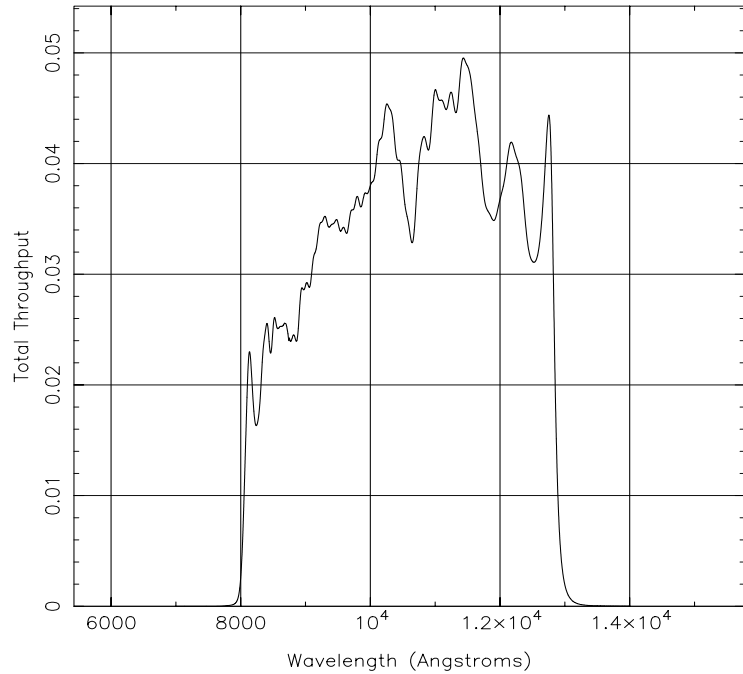
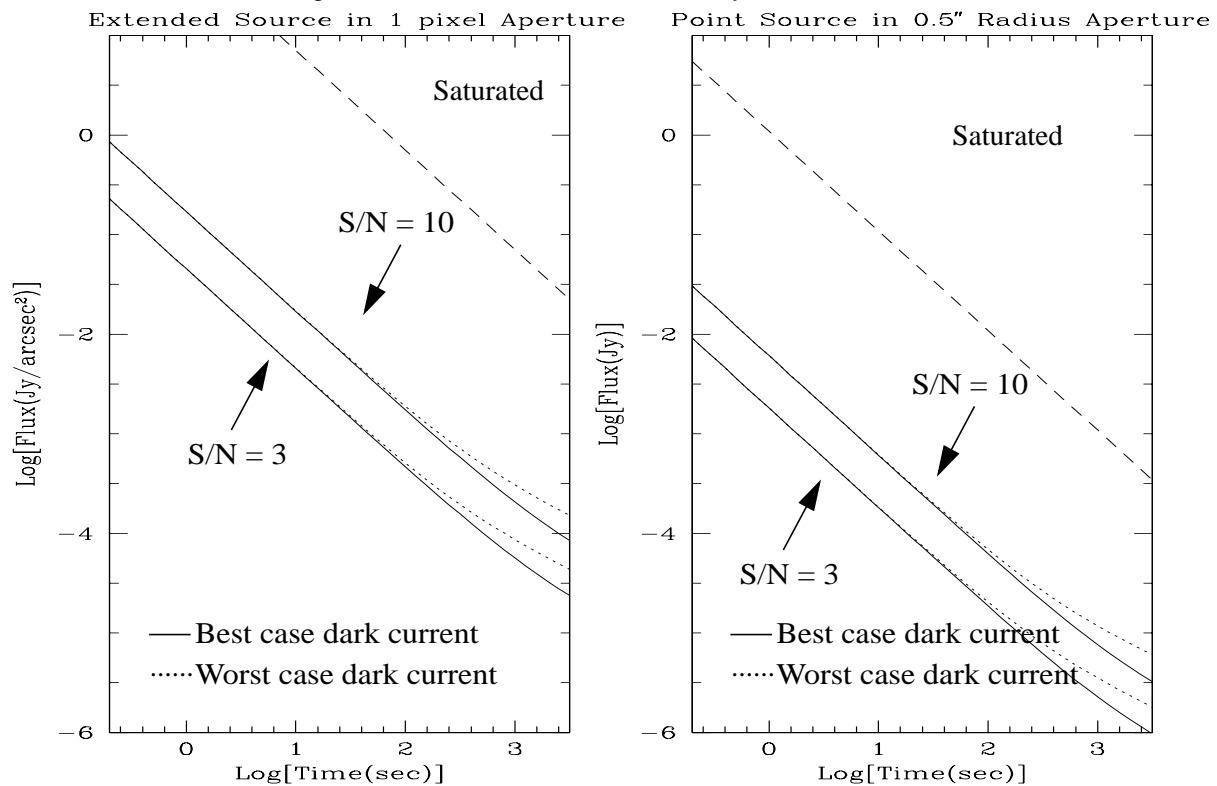


Figure A1.34: NIC1, POL0S Sensitivity Curves



Camera 2, Filter F110W

Figure A1.35: NIC2, F110W Throughput

Notes:

See also “Camera 1, Filter F110W” and “Camera 3, Filter F110W”.

Central wavelength: 1.0998 μm
 Mean wavelength: 1.1035 μm
 Peak wavelength: 1.2035 μm
 Wavelength range: 0.8-1.4 μm
 FWHM: 0.5915 μm
 Maximum throughput: 16.39%
 Pixel fraction: 0.288

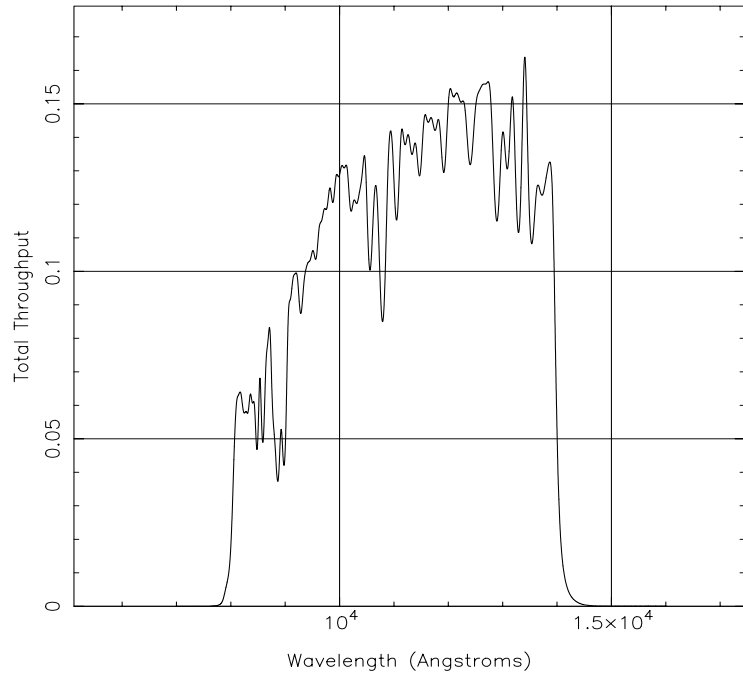
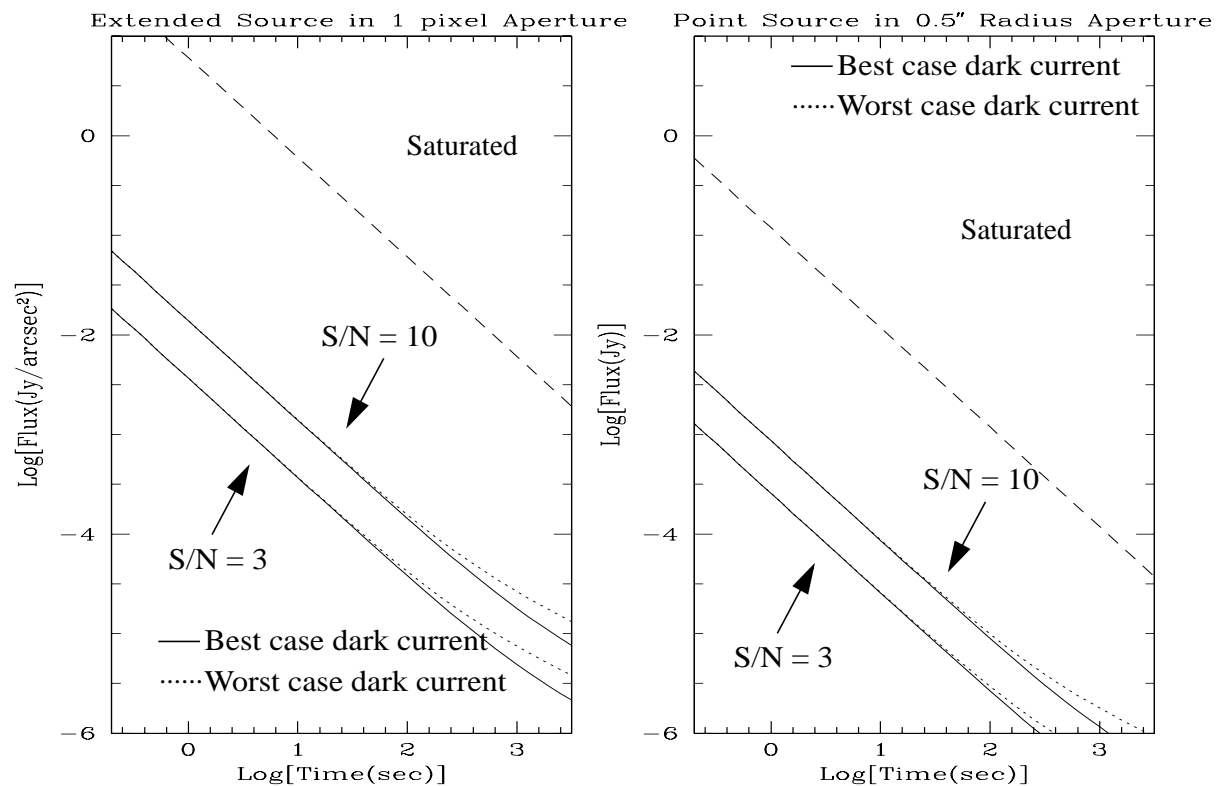


Figure A1.36: NIC2, F110W Sensitivity Curves



Camera 2, Filter F160W

Figure A1.37: NIC2, F160W Throughput

Notes:

Minimum background.

See also “Camera 1, Filter F160W” and
“Camera 3, Filter F160W”.

Central wavelength: 1.5940 μm
 Mean wavelength: 1.5931 μm
 Peak wavelength: 1.5820 μm
 Wavelength range: 1.4-1.8 μm
 FWHM: 0.4030 μm
 Maximum throughput: 24.02%
 Pixel fraction: 0.159

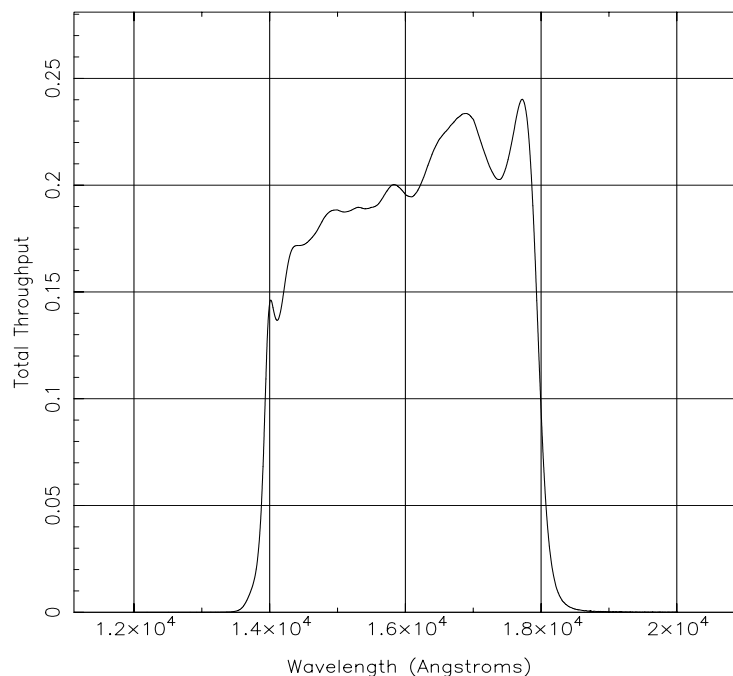
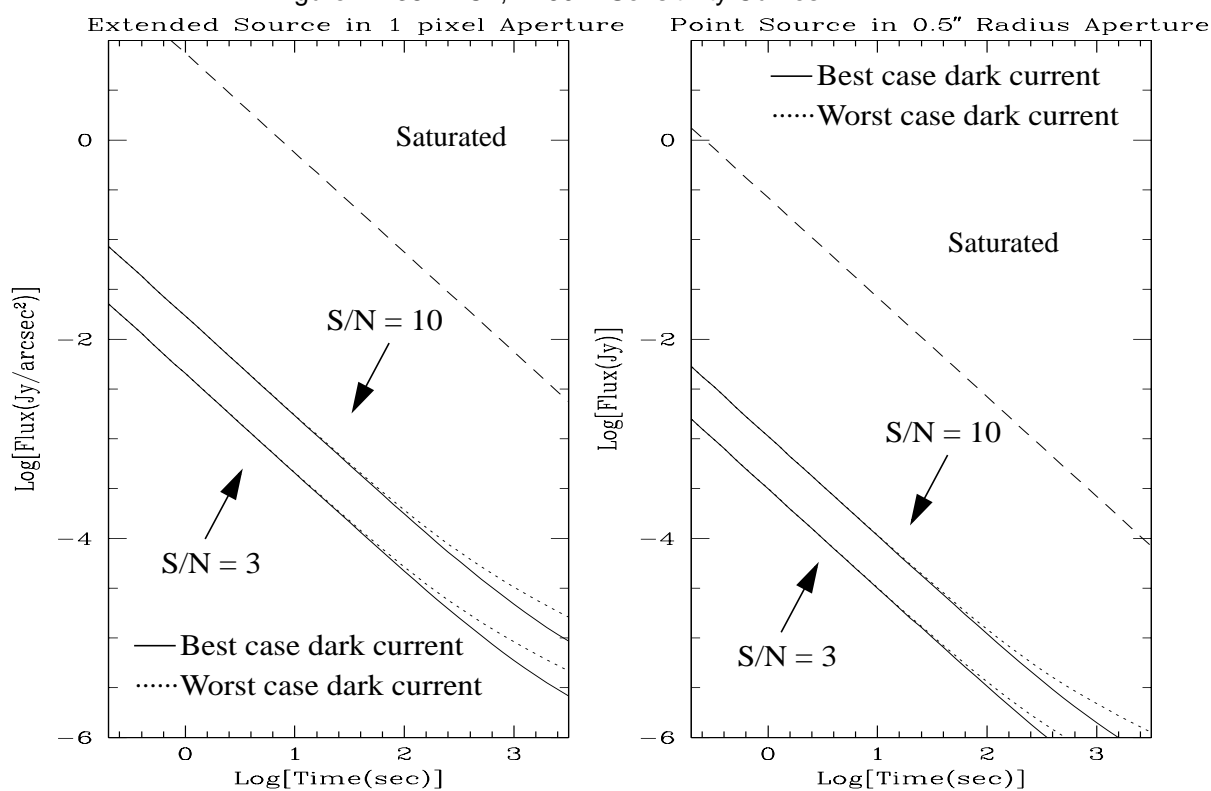


Figure A1.38: NIC2, F160W Sensitivity Curves



Camera 2, Filter F165M

Figure A1.39: NIC2, F165M Throughput

Notes:

Planetary continuum.

See also “Camera 1, Filter F165M”.

Central wavelength: 1.6463 μm
 Mean wavelength: 1.6473 μm
 Peak wavelength: 1.5540 μm
 Wavelength range: 1.55-1.75 μm
 FWHM: 0.1985 μm
 Maximum throughput: 24.07%
 Pixel fraction: 0.149

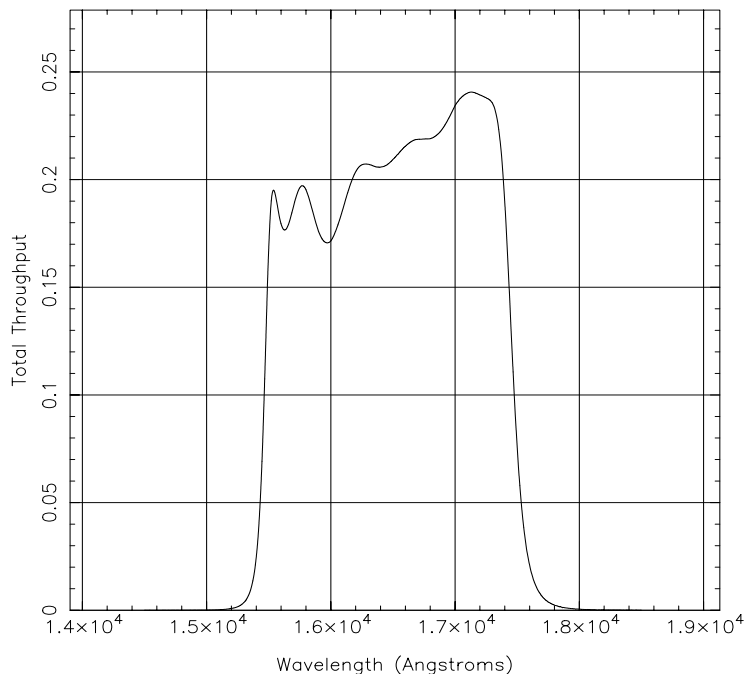
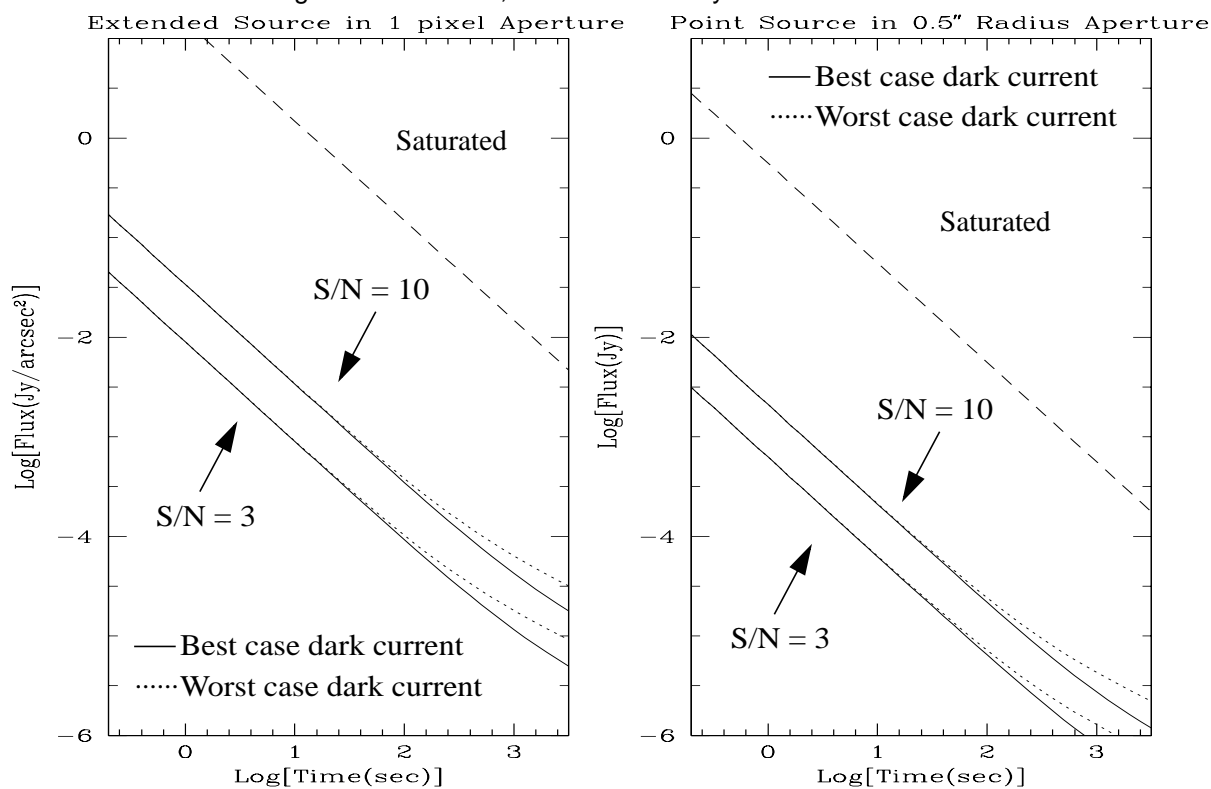


Figure A1.40: NIC2, F165M Sensitivity Curves



Camera 2, Filter F171M

Figure A1.41: NIC2, F171M Throughput

Notes:

HCO₂ and C₂ continuum.

Central wavelength: 1.7206 μm
 Mean wavelength: 1.7209 μm
 Peak wavelength: 1.7224 μm
 Wavelength range: 1.68-1.75 μm
 FWHM: 0.0712 μm
 Maximum throughput: 23.19%
 Pixel fraction: 0.138

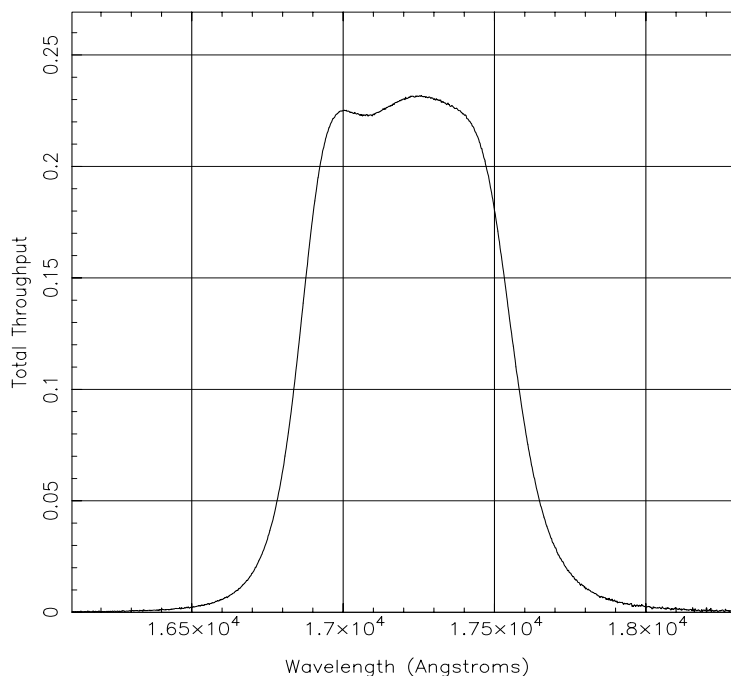
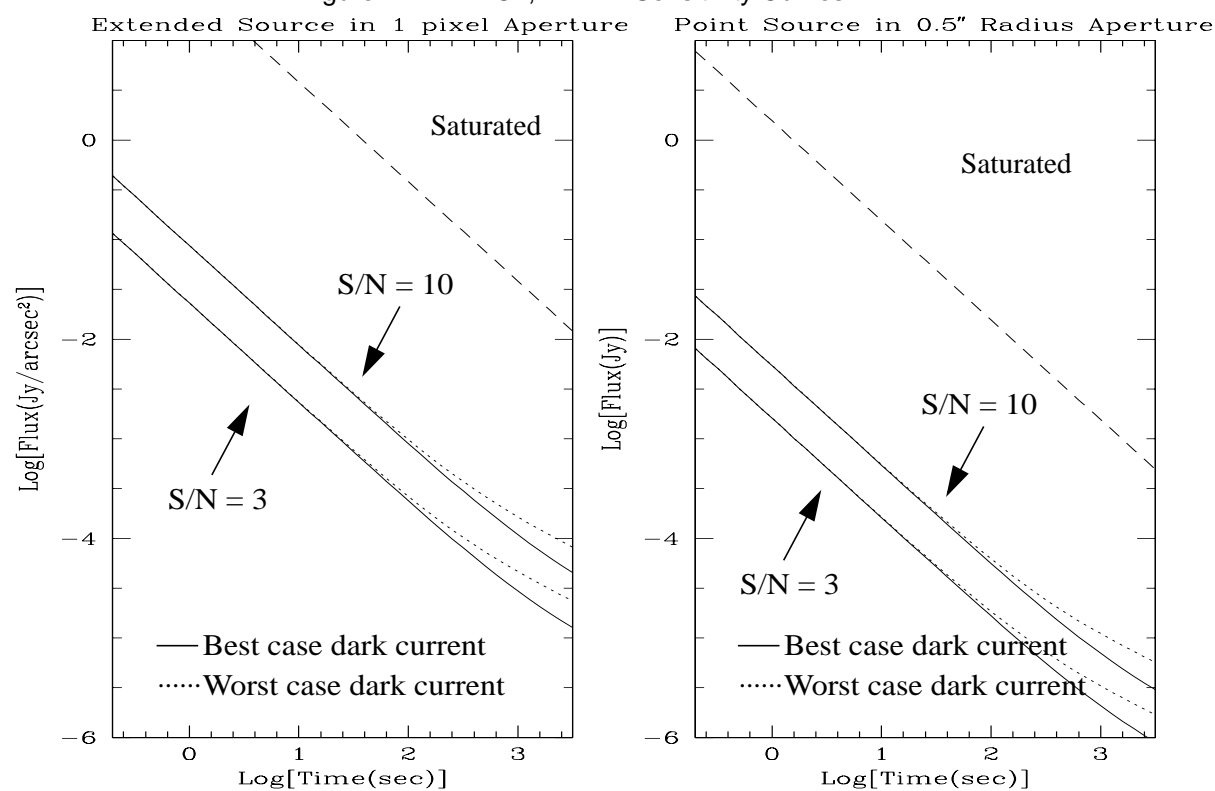


Figure A1.42: NIC2, F171M Sensitivity Curves



Camera 2, Filter F180M

Figure A1.43: NIC2, F180M Throughput

Notes:

HCO₂ and C₂.

Thermal background important.

Central wavelength: 1.7968 μm
 Mean wavelength: 1.7971 μm
 Peak wavelength: 1.8108 μm
 Wavelength range: 1.765-1.83 μm
 FWHM: 0.0684 μm
 Maximum throughput: 23.68%
 Pixel fraction: 0.128

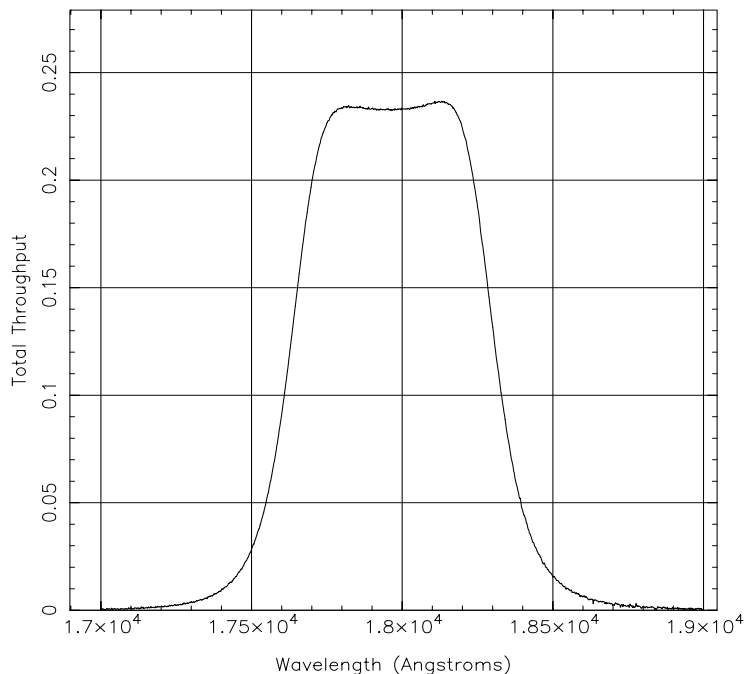
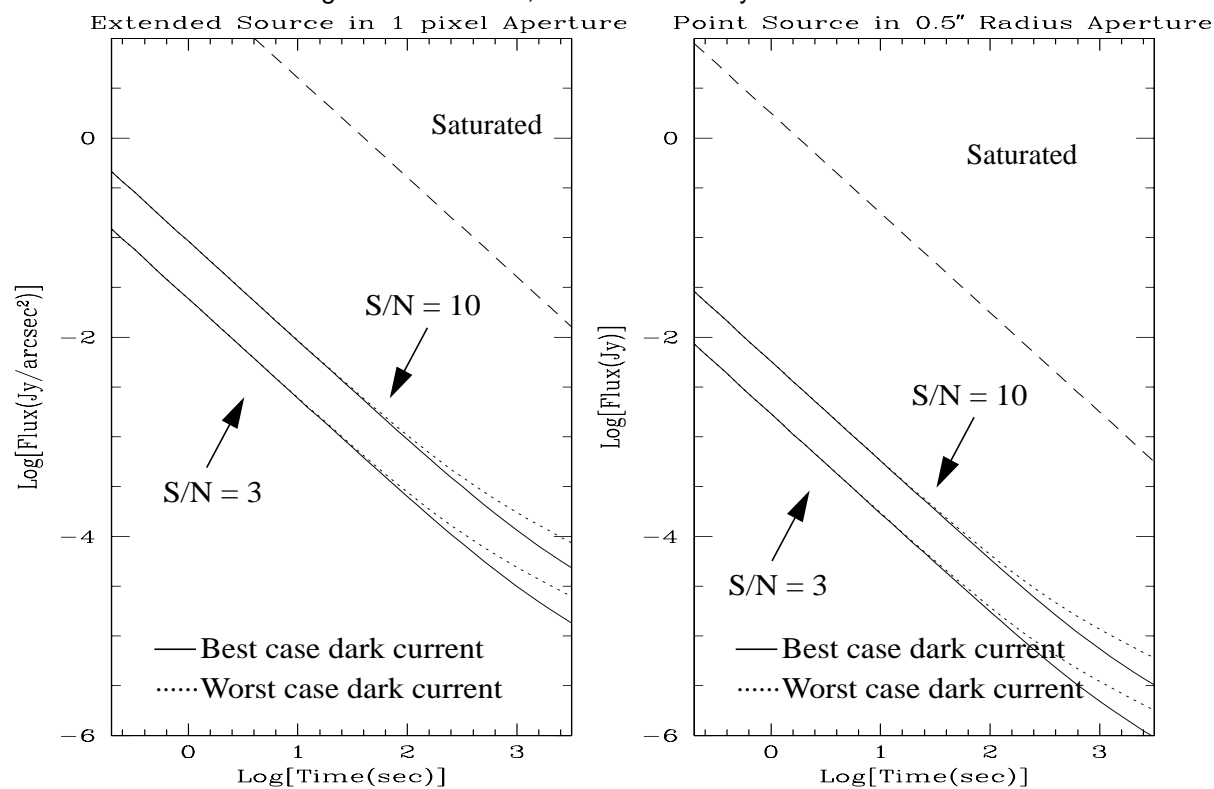


Figure A1.44: NIC2, F180M Sensitivity Curves



Camera 2, Filter F187N

Figure A1.45: NIC2 F187N Throughput

Notes:

Paschen α .

See also “Camera 1, Filter F187N” and “Camera 3, Filter F187N”.

Central wavelength: 1.8740 μm
 Mean wavelength: 1.8738 μm
 Peak wavelength: 1.8746 μm
 Wavelength range: 1%
 FWHM: 0.0192 μm
 Maximum throughput: 23.33%
 Pixel fraction: 0.119

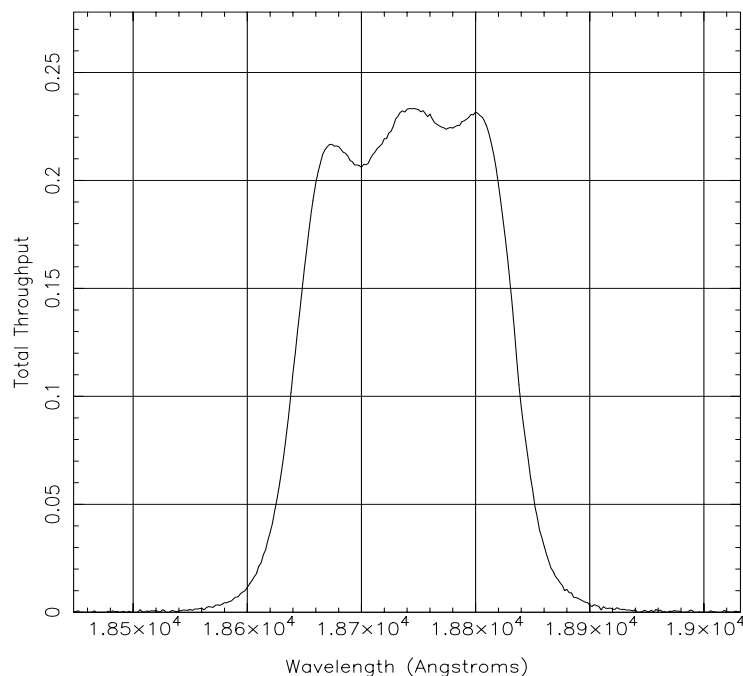
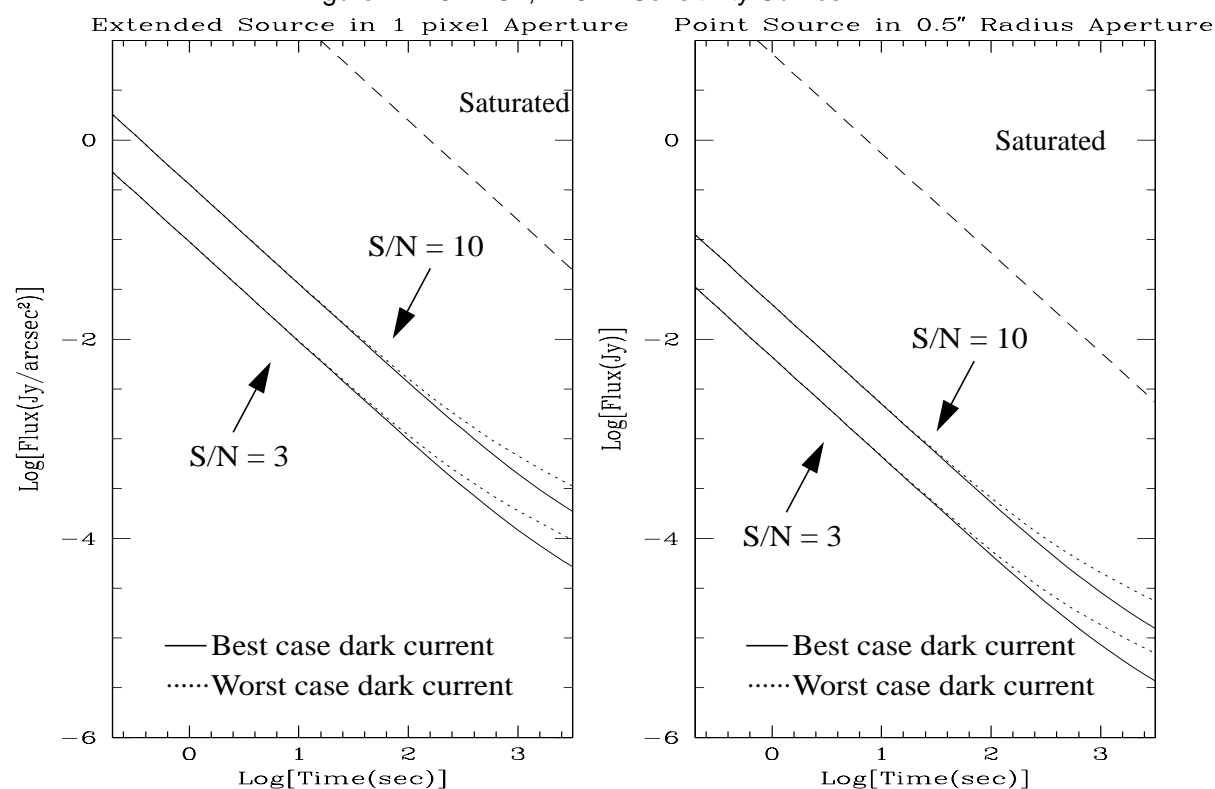


Figure A1.46: NIC2, F187N Sensitivity Curves



Camera 2, Filter F187W

Figure A1.47: NIC2, F187W Throughput

Notes:

Thermal Background important.

Central wavelength: $1.8722\ \mu\text{m}$
 Mean wavelength: $1.8708\ \mu\text{m}$
 Peak wavelength: $1.8930\ \mu\text{m}$
 Wavelength range: $1.75\text{--}2.35\ \mu\text{m}$
 FWHM: $0.2436\ \mu\text{m}$
 Maximum throughput: 22.84%
 Pixel fraction: 0.117

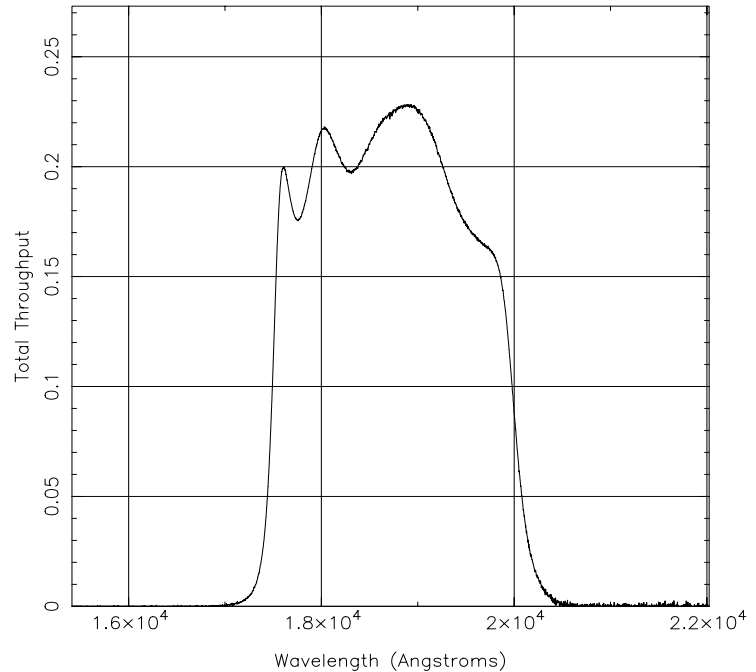
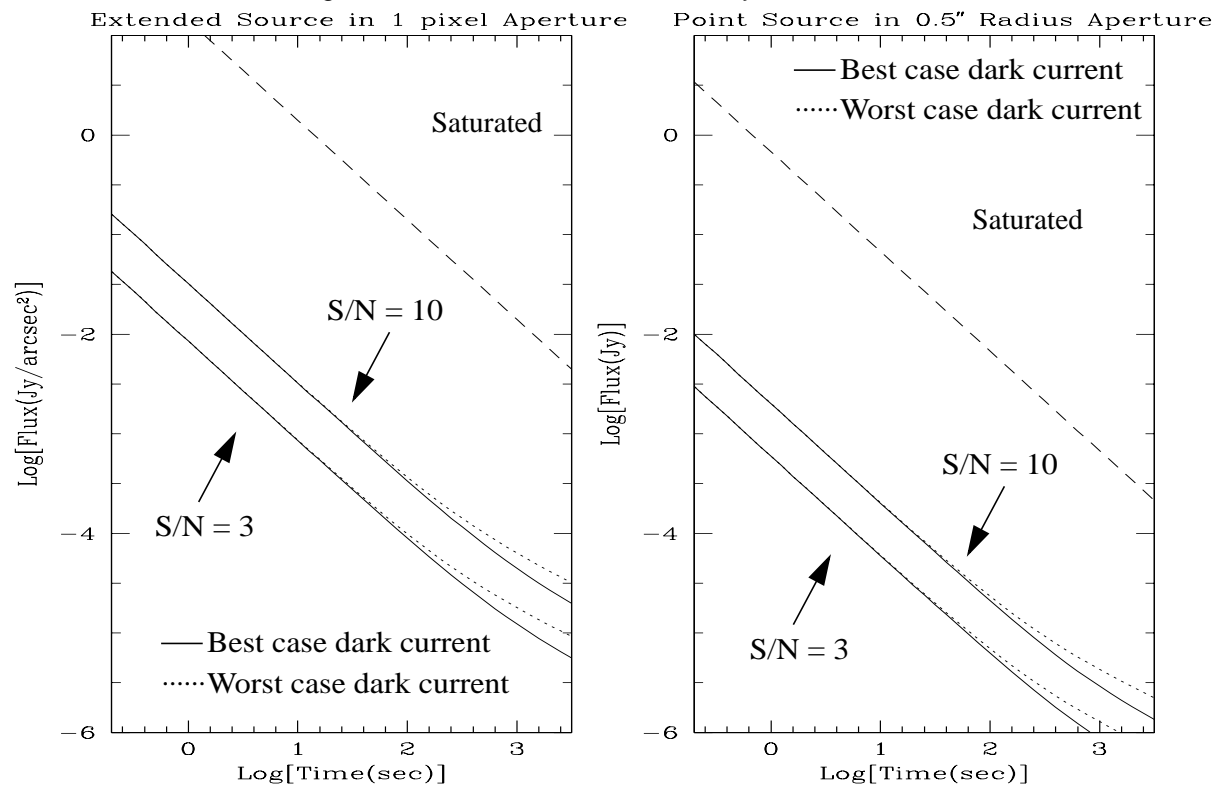


Figure A1.48: NIC2, F187W Sensitivity Curves



Camera 2, Filter F190N

Figure A1.49: NIC2, F190N Throughput

Notes:

Paschen α continuum.

See also “Camera 1, Filter F190N” and
“Camera 3, Filter F190N”,

Central wavelength: 1.9005 μm
 Mean wavelength: 1.9003 μm
 Peak wavelength: 1.9004 μm
 Wavelength range: 1%
 FWHM: 0.0174 μm
 Maximum throughput: 24.37%
 Pixel fraction: 0.116

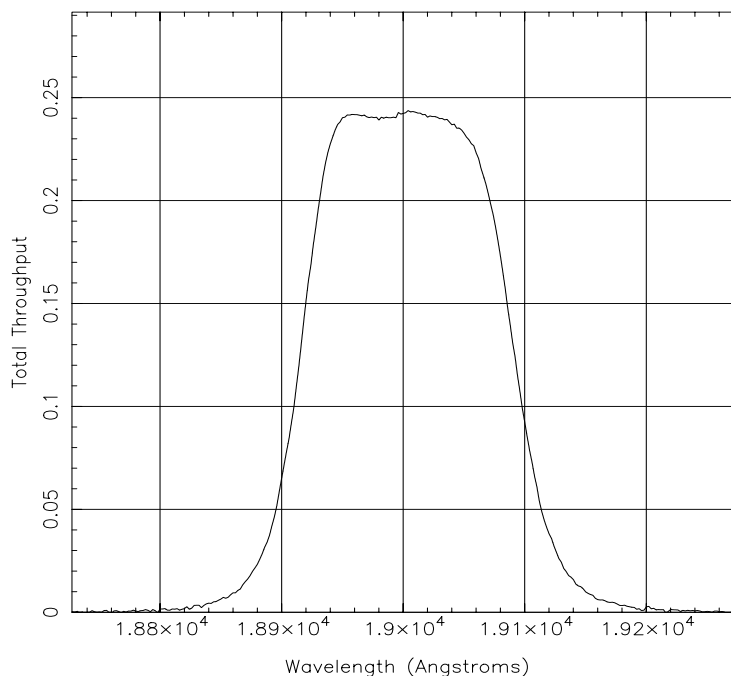
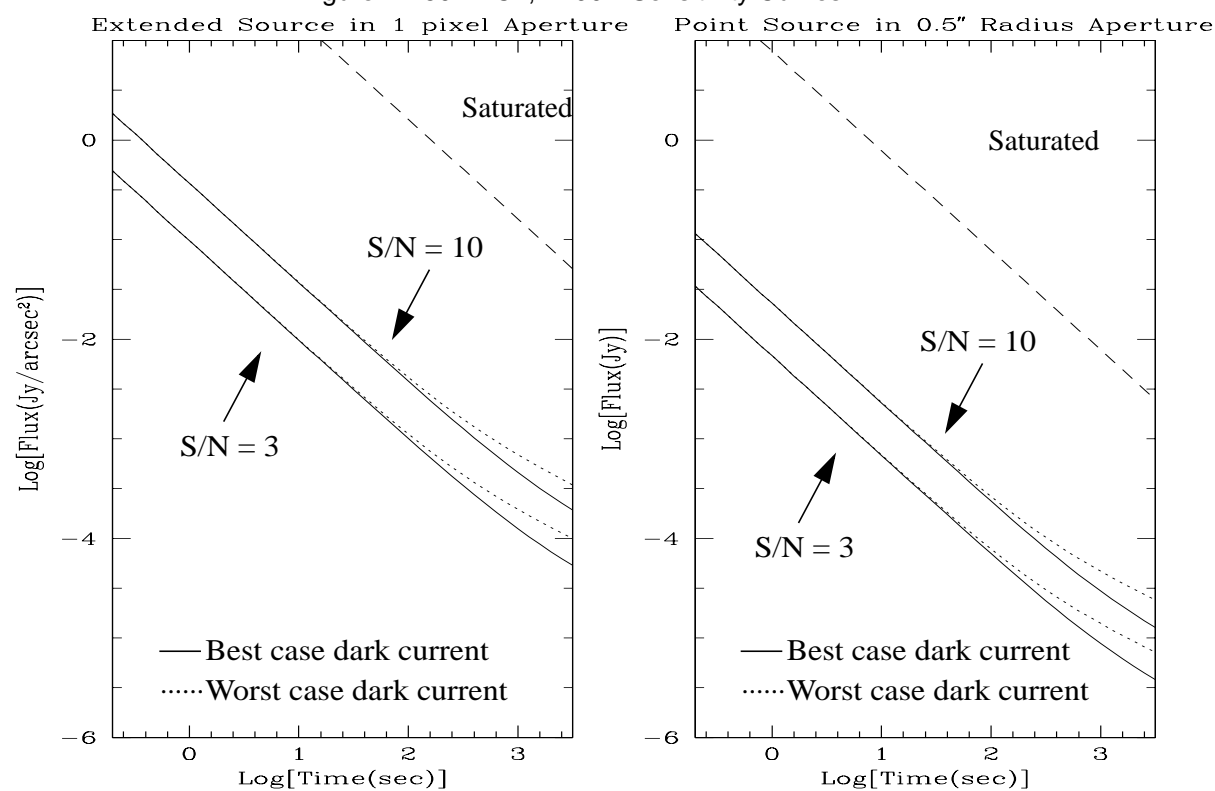


Figure A1.50: NIC2, F190N Sensitivity Curves



Camera 2, Filter F204M

Figure A1.51: NIC2, F204M Throughput

Notes:

Methane band.

Thermal background important.

Central wavelength: $2.0313 \mu\text{m}$
 Mean wavelength: $2.0327 \mu\text{m}$
 Peak wavelength: $2.0342 \mu\text{m}$
 Wavelength range: $1.99\text{--}2.09 \mu\text{m}$
 FWHM: $0.105 \mu\text{m}$
 Maximum throughput: 26.90%
 Pixel fraction: 0.104

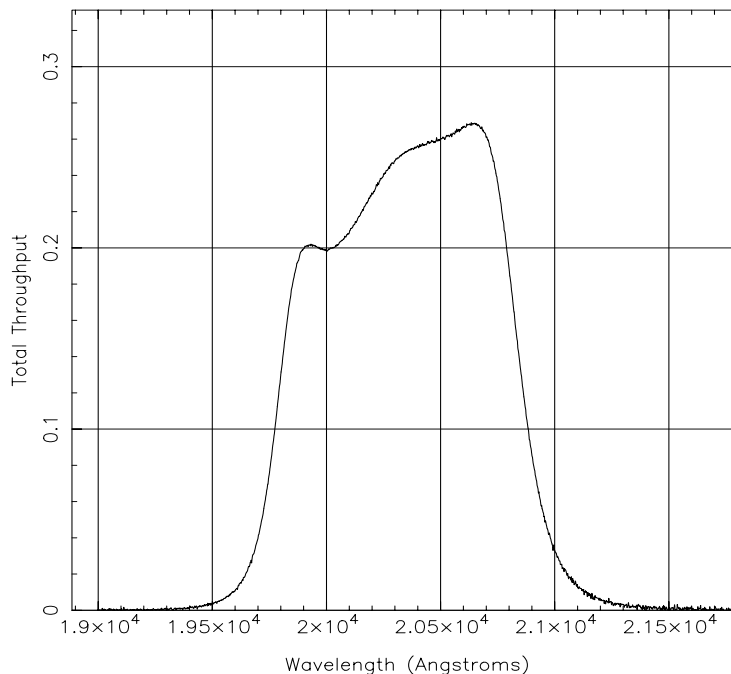
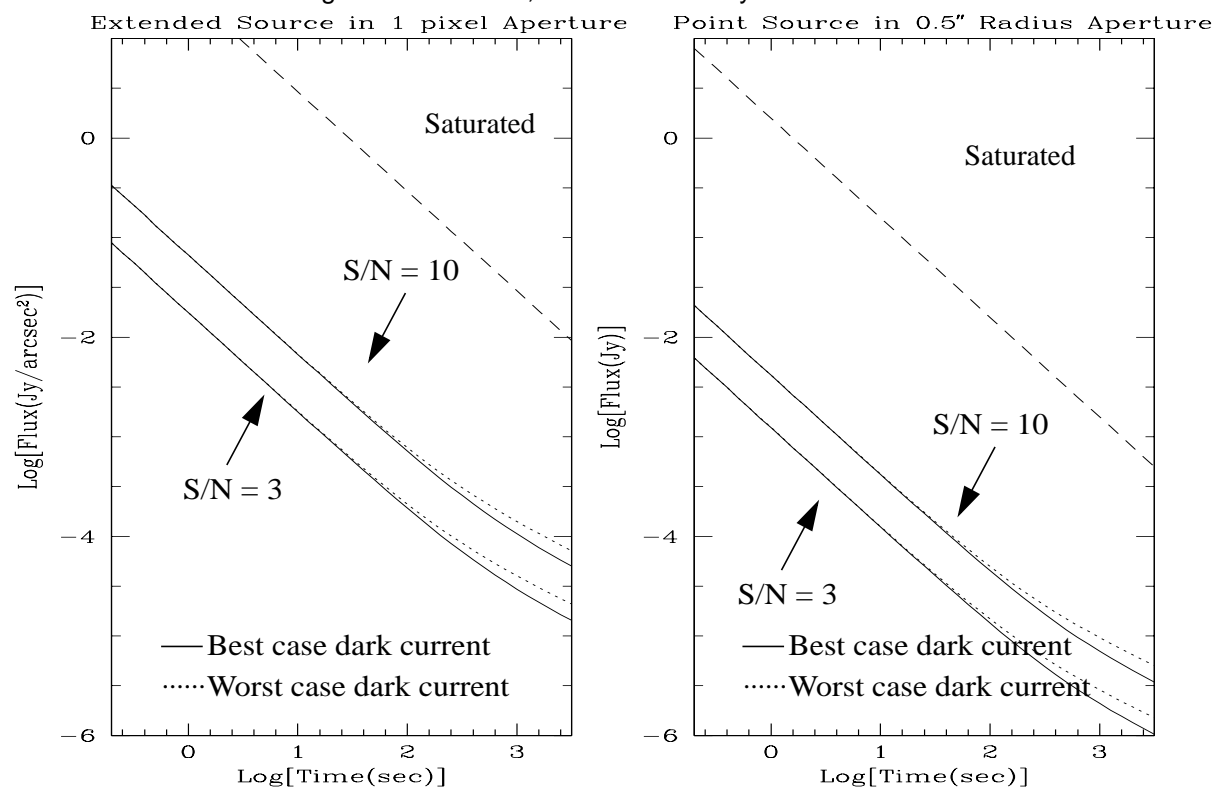


Figure A1.52: NIC2, F204M Sensitivity Curves



Camera 2, Filter F205W

Figure A1.53: NIC2, F205W Throughput

Notes:

Thermal background important.

Central wavelength: 2.0428 μm
 Mean wavelength: 2.0406 μm
 Peak wavelength: 1.9560 μm
 Wavelength range: 1.75-2.35 μm
 FWHM: 0.6125 μm
 Maximum throughput: 34.56%
 Pixel fraction: 0.107

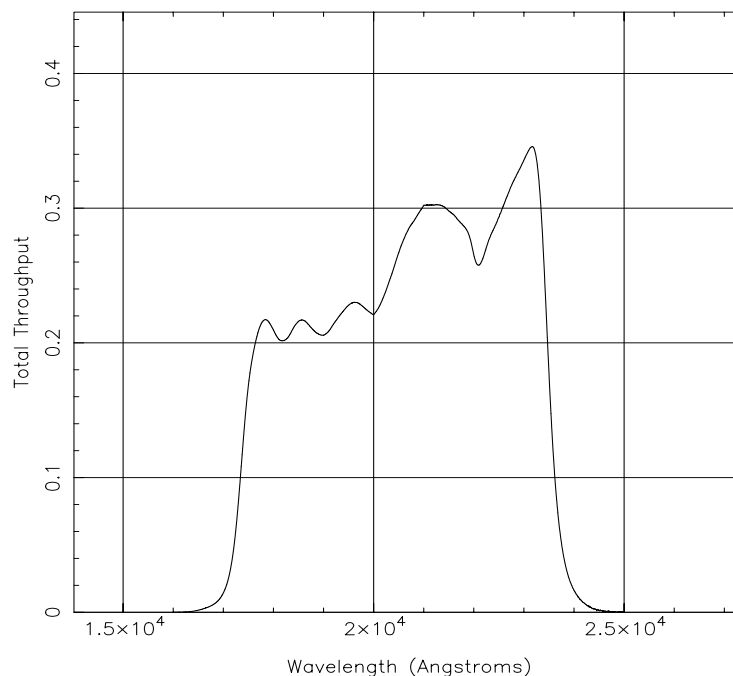
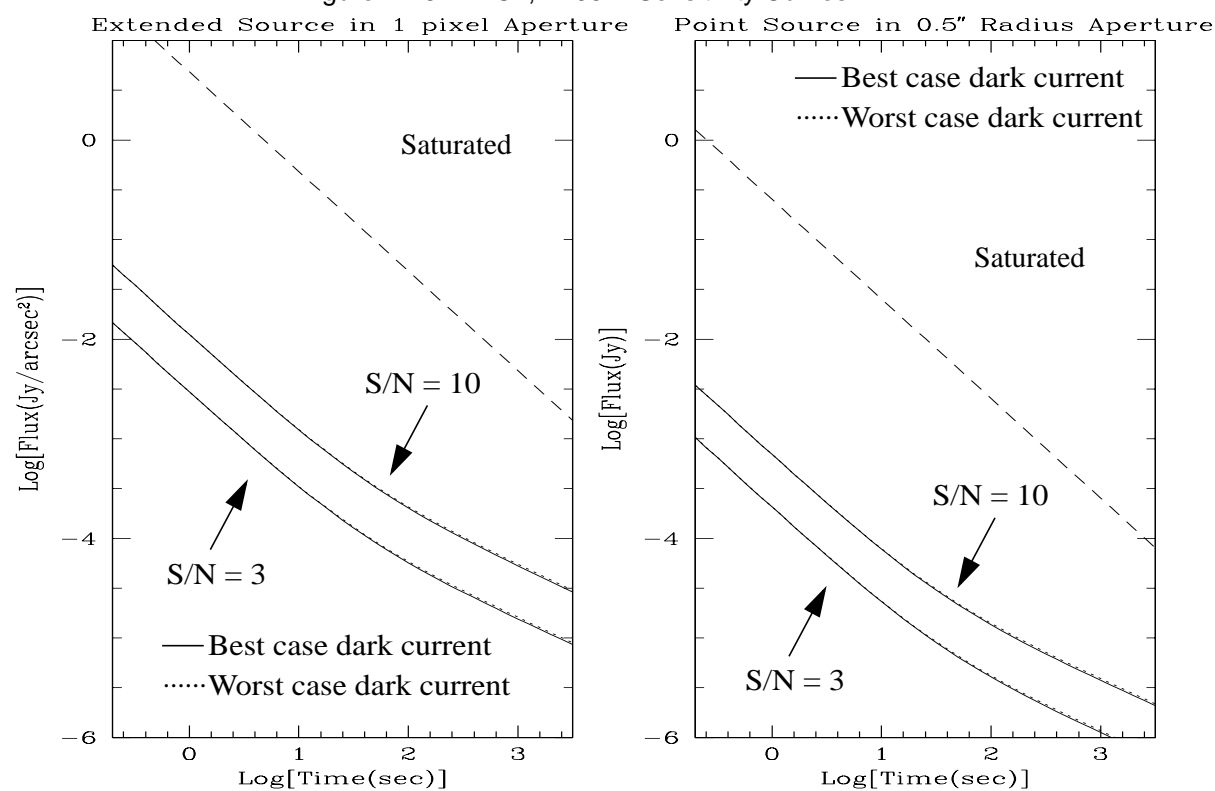


Figure A1.54: NIC2, F205W Sensitivity Curves



Camera 2, Filter F207M

Figure A1.55: NIC2, F207M Throughput

Notes:

Thermal background important.

Central wavelength: 2.0827 μm
 Mean wavelength: 2.0786 μm
 Peak wavelength: 2.0252 μm
 Wavelength range: 2.0-2.15 μm
 FWHM: 0.1522 μm
 Maximum throughput: 25.46%
 Pixel fraction: 0.0976

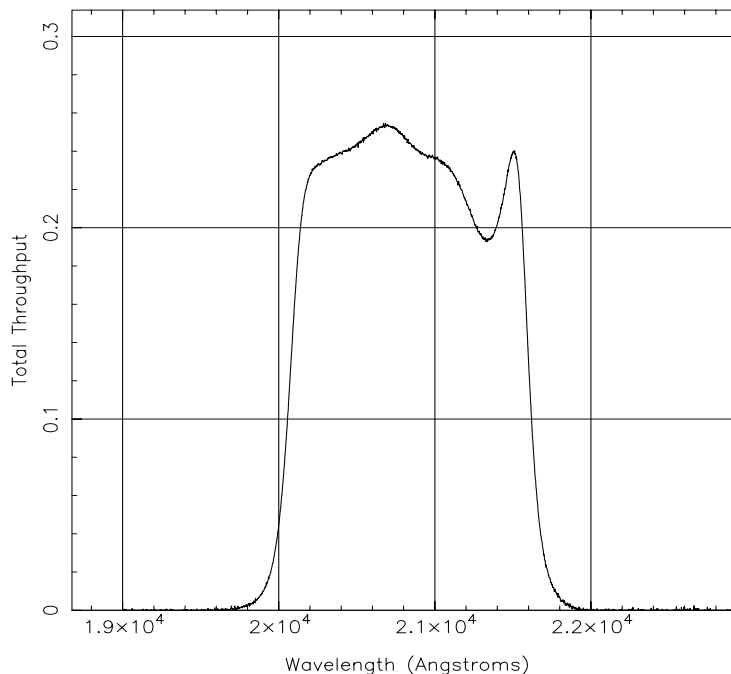
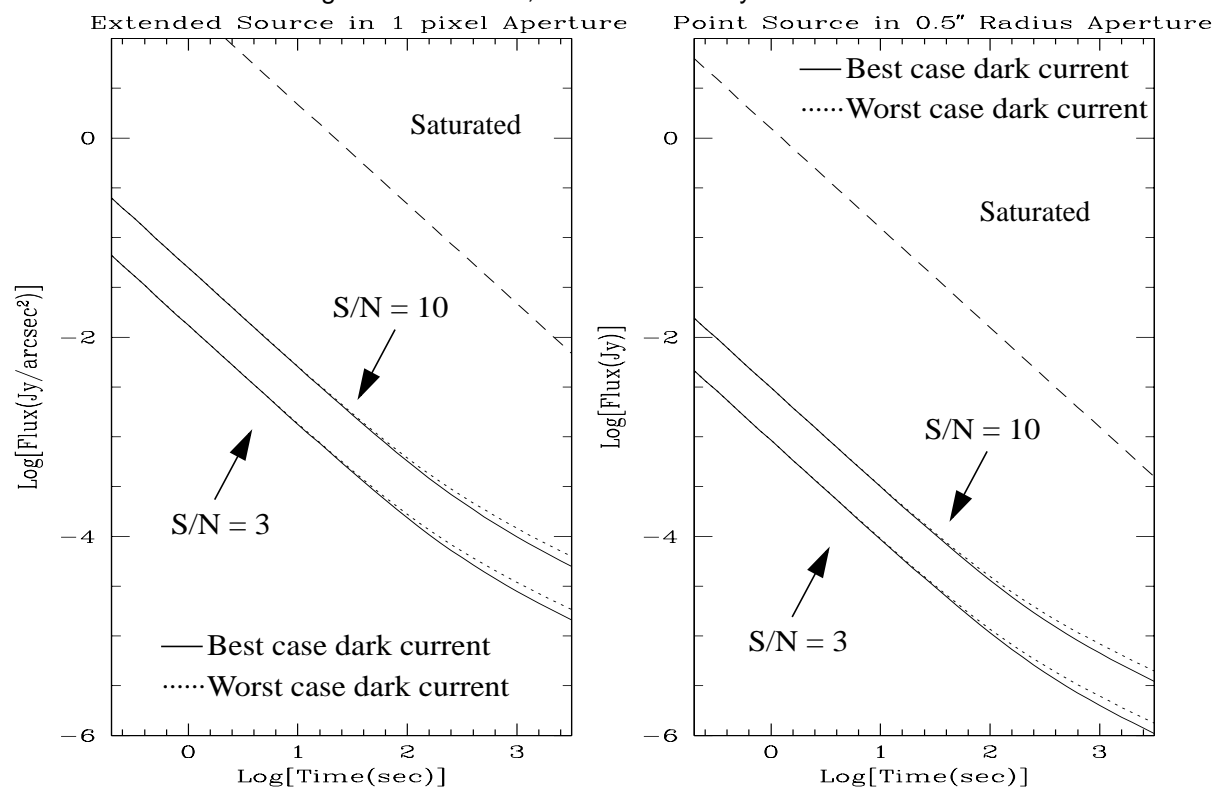


Figure A1.56: NIC2, F207M Sensitivity Curves



Camera 2, Filter F212N

Figure A1.57: NIC2, F212N Throughput

Notes:

H₂ line.

Thermal background important.

See also "Camera 3, Filter F212N".

Central wavelength: 2.1211 μm
 Mean wavelength: 2.1213 μm
 Peak wavelength: 2.1228 μm
 Wavelength range: 1%
 FWHM: 0.0206 μm
 Maximum throughput: 26.03%
 Pixel fraction: 0.0953

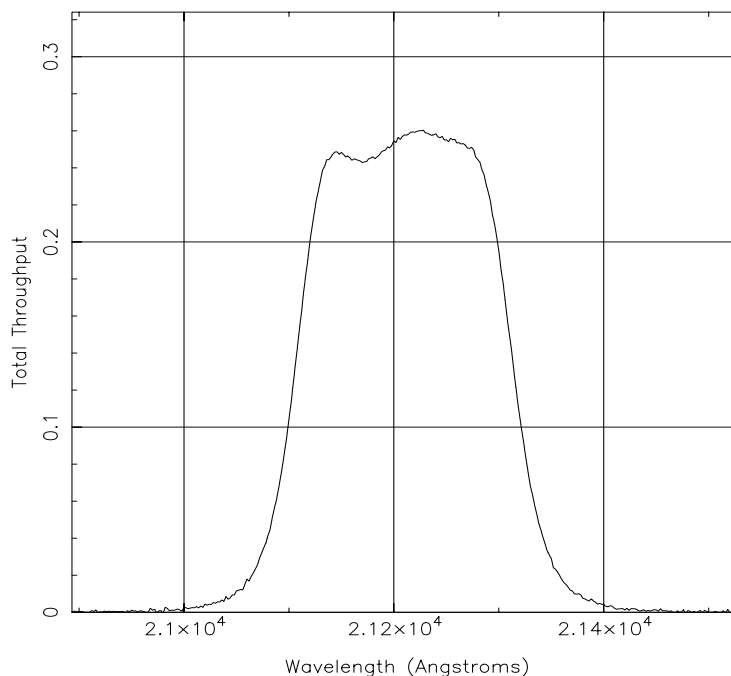
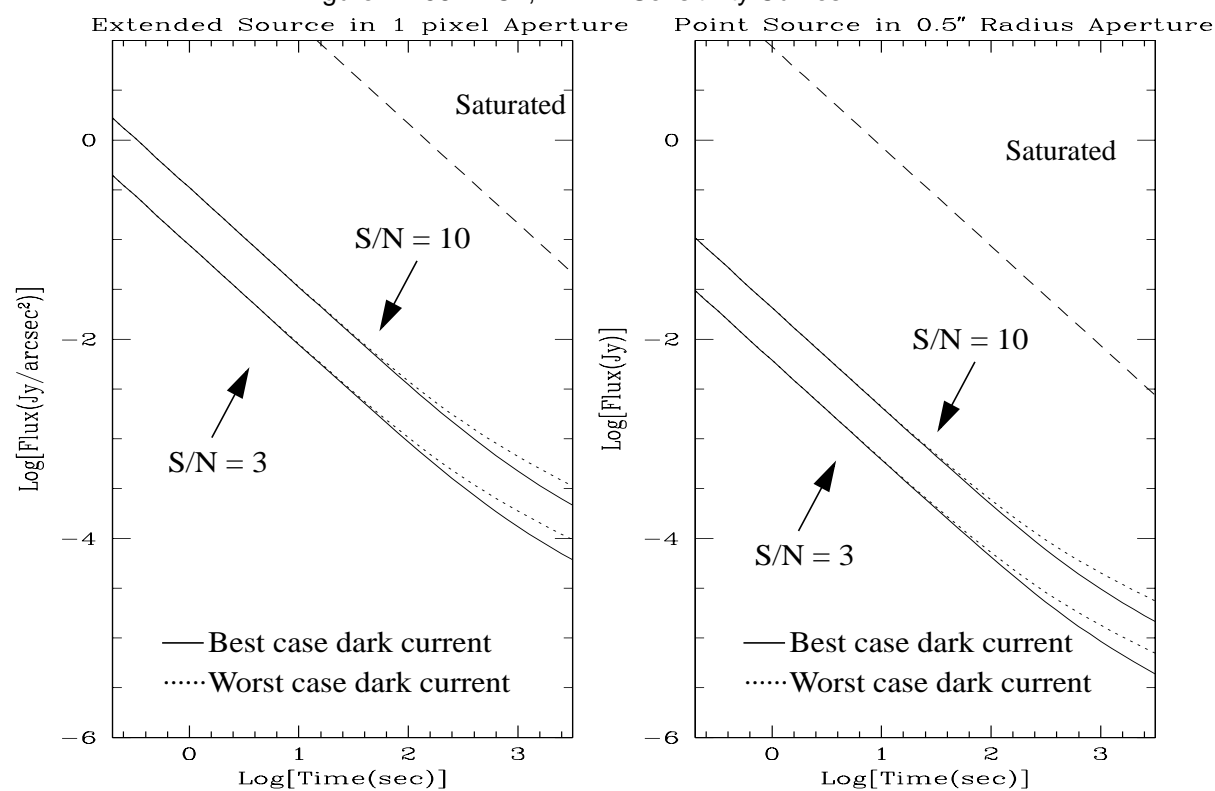


Figure A1.58: NIC2, F212N Sensitivity Curves



Camera 2, Filter F215N

Figure A1.59: NIC2, F215N Throughput

Notes:

N_2 + Brackett γ continuum.

Thermal background important.

Central wavelength: 2.1488 μm
 Mean wavelength: 2.1487 μm
 Peak wavelength: 2.1562 μm
 Wavelength range: 1% μm
 FWHM: 0.0200 μm
 Maximum throughput: 25.40%
 Pixel fraction: 0.0933

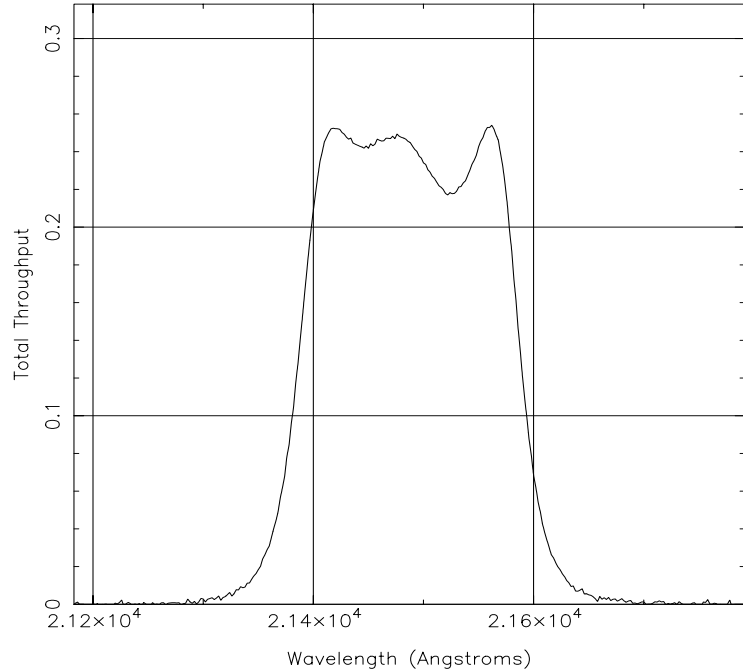
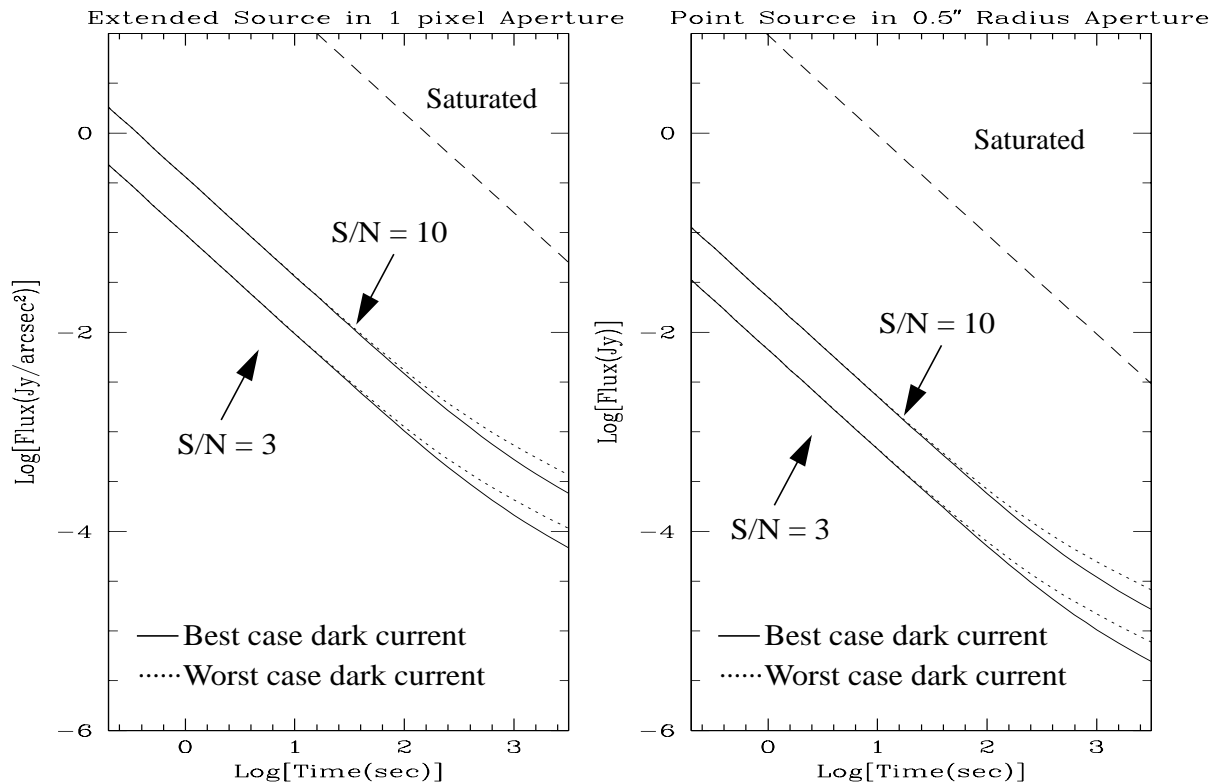


Figure A1.60: NIC2, F215N Sensitivity Curves



Camera 2, Filter F216N

Figure A1.61: NIC2, F216N Throughput

Notes:

Brackett γ line.

Thermal background important.

Central wavelength: 2.1642 μm
 Mean wavelength: 2.1641 μm
 Peak wavelength: 2.1668 μm
 Wavelength range: 1%
 FWHM: 0.0208 μm
 Maximum throughput: 26.35%
 Pixel fraction: 0.0915

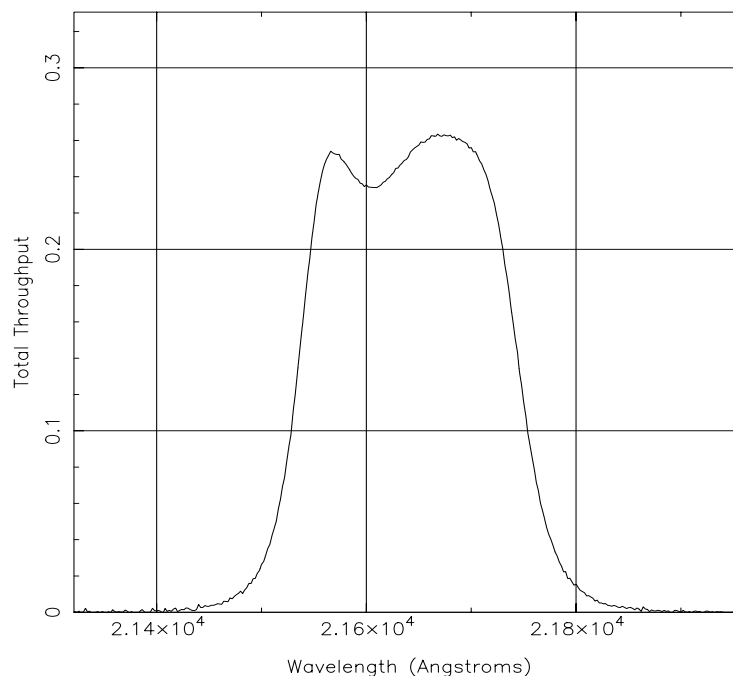
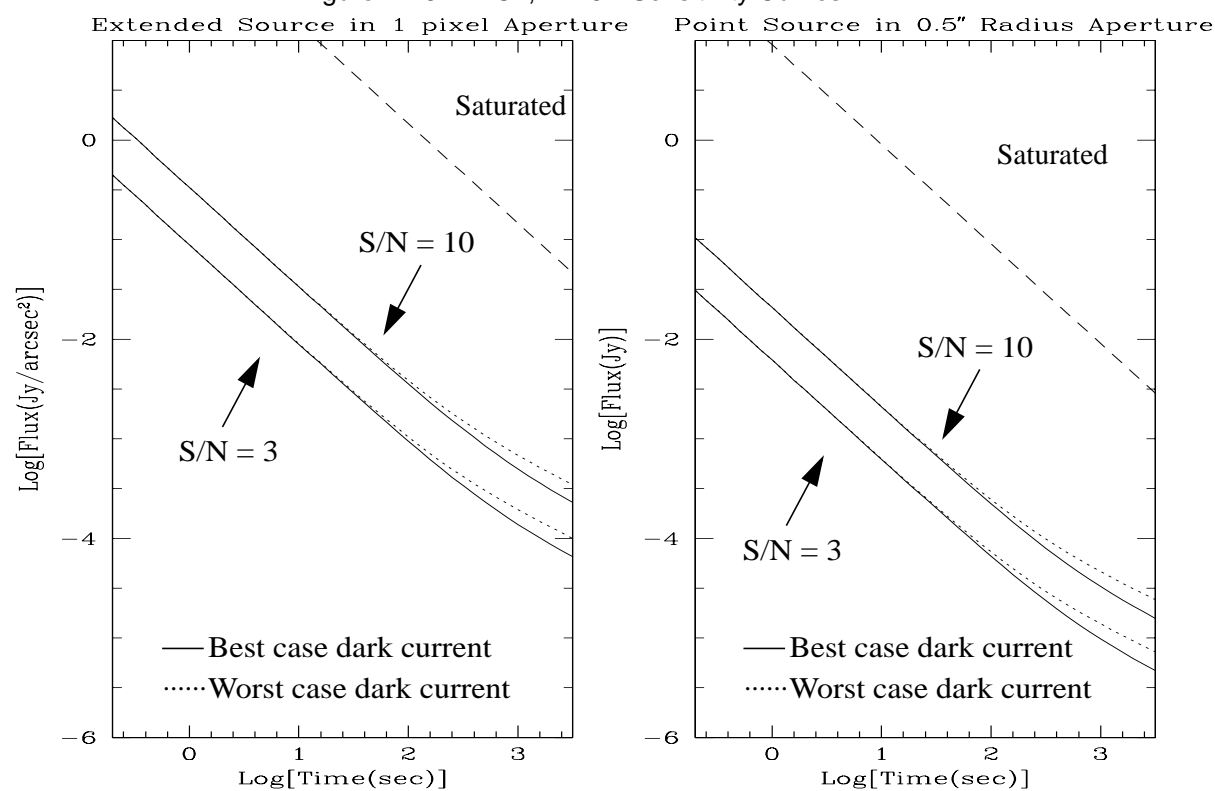


Figure A1.62: NIC2, F216N Sensitivity Curves



Camera 2, Filter F222M

Figure A1.63: NIC2, F222M Throughput

Notes:

CO continuum.

Thermal background important.

See also “Camera 3, Filter F222M”.

Central wavelength: 2.2160 μm
 Mean wavelength: 2.2164 μm
 Peak wavelength: 2.1804 μm
 Wavelength range: 2.15-2.3 μm
 FWHM: 0.1432 μm
 Maximum throughput: 26.71%
 Pixel fraction: 0.0881

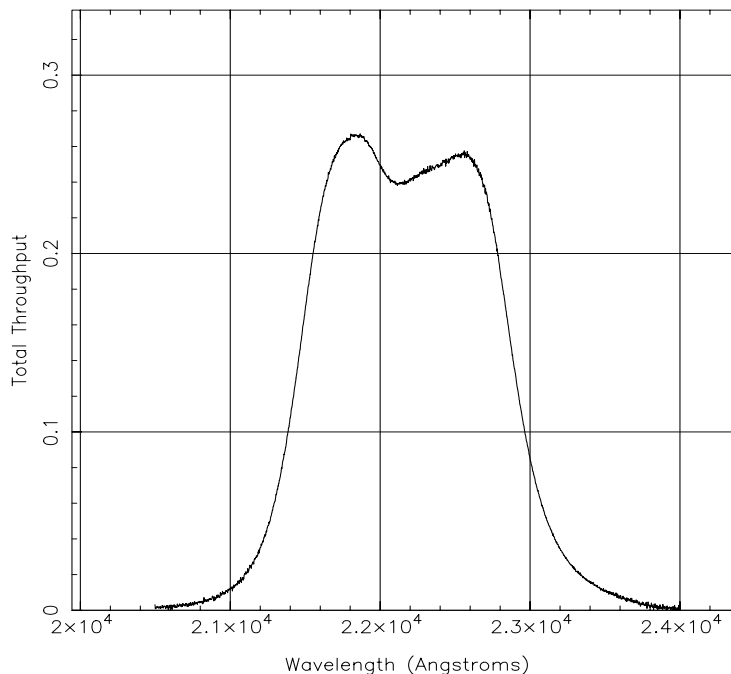
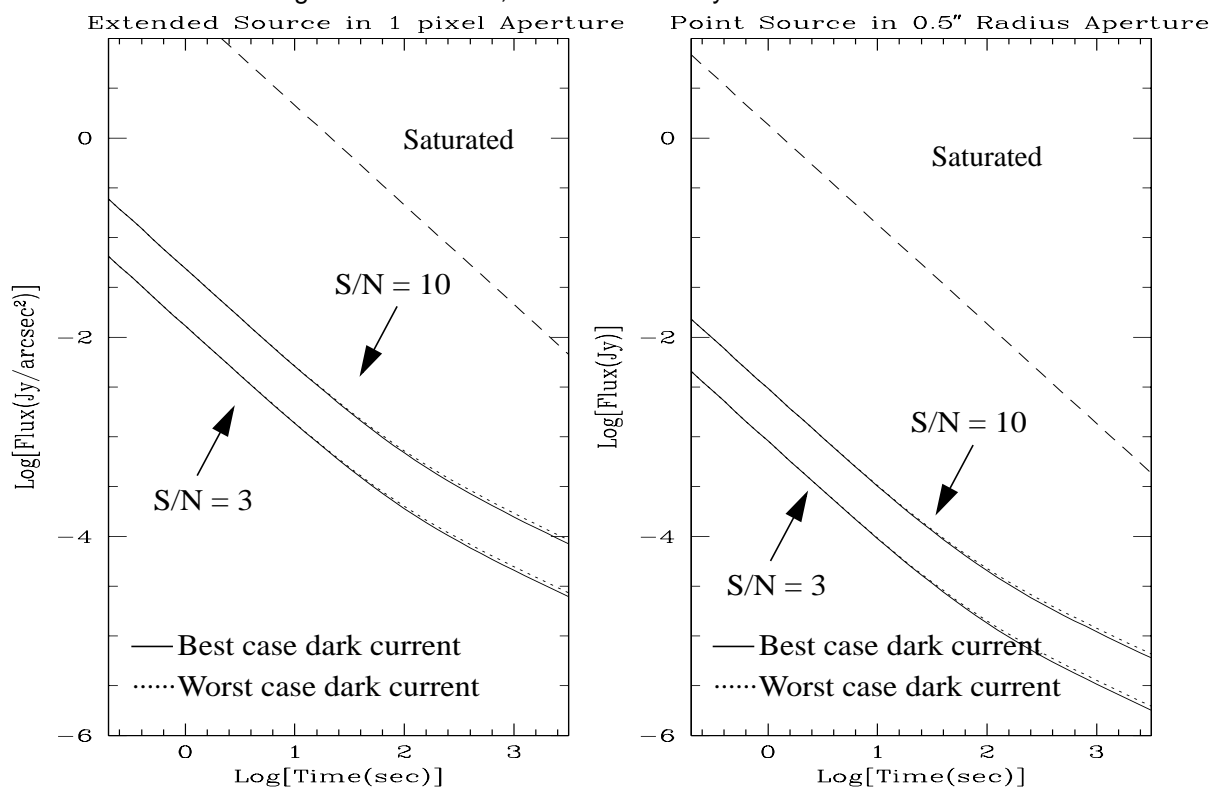


Figure A1.64: NIC2, F222M Sensitivity Curves



Camera 2, Filter F237M

Figure A1.65: NIC2, F237M Throughput

Notes:

CO.

Thermal background important.

See also "Camera 3, Filter F240M".

Central wavelength: 2.3677 μm
 Mean wavelength: 2.3694 μm
 Peak wavelength: 2.3852 μm
 Wavelength range: 2.3-2.45 μm
 FWHM: 0.1546 μm
 Maximum throughput: 32.85%
 Pixel fraction: 0.0797

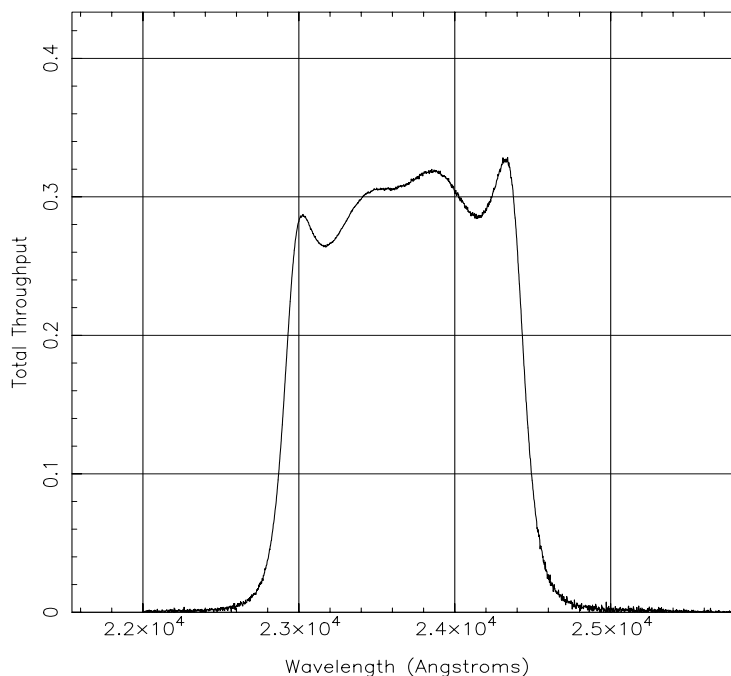
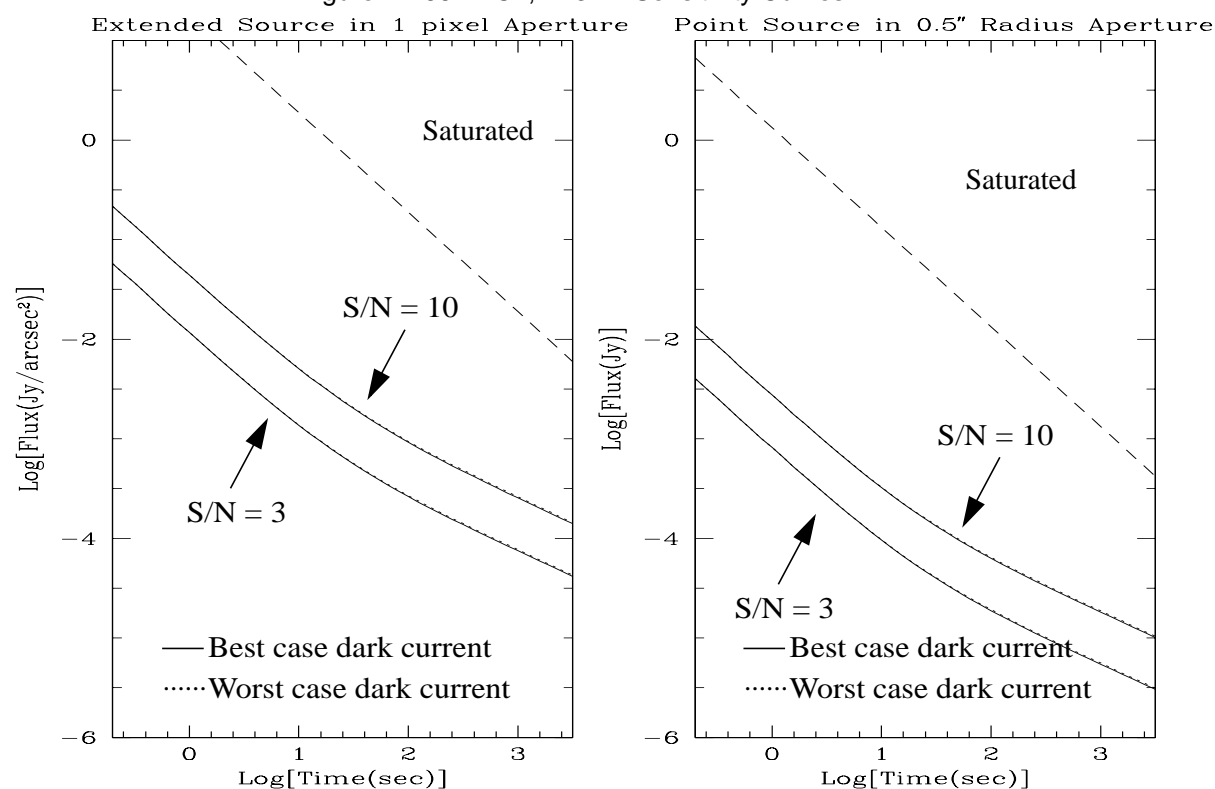


Figure A1.66: NIC2, F237M Sensitivity Curves



Camera 2, Polarizer POL0L

Figure A1.67: NIC2, POL0L Throughput

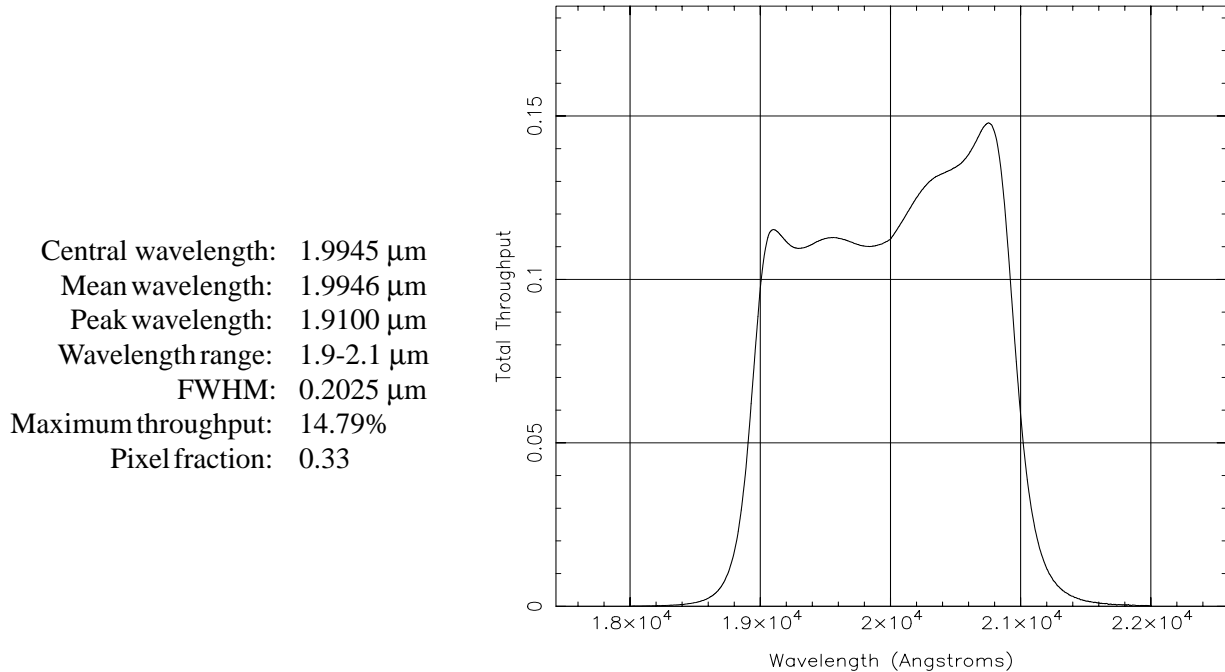
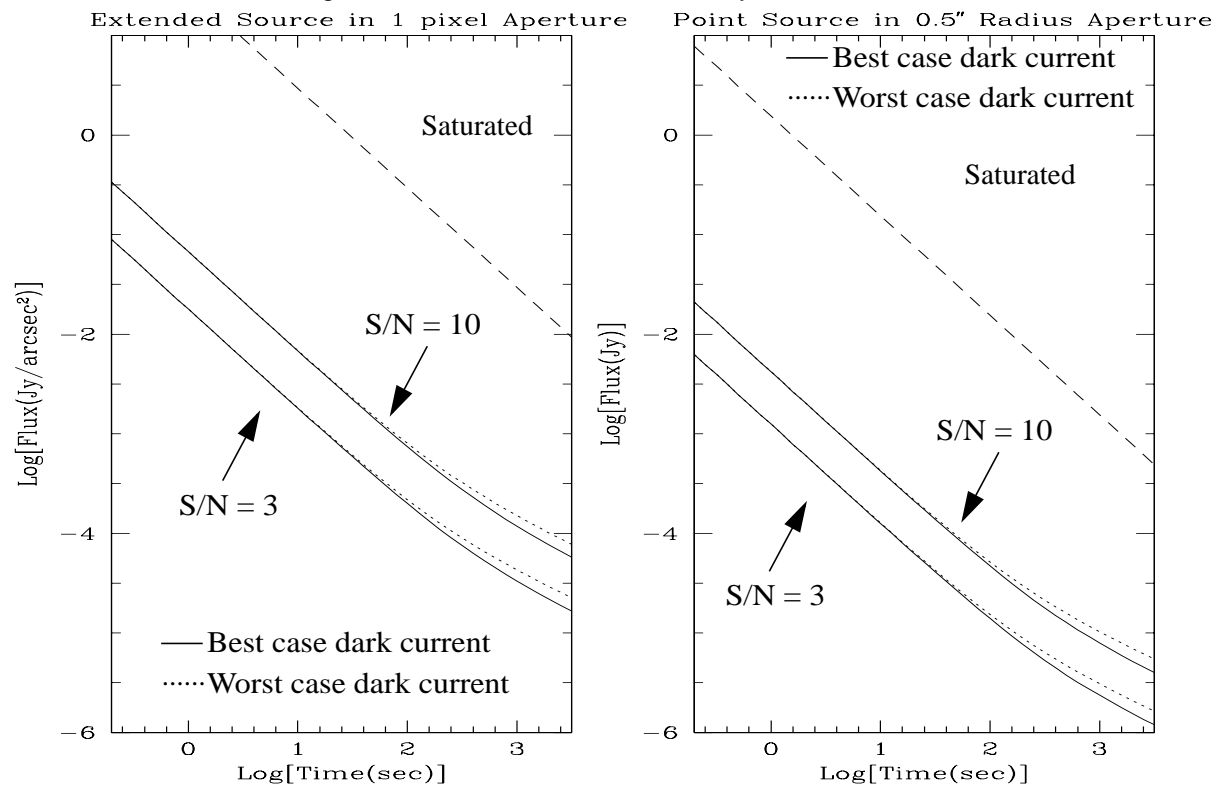


Figure A1.68: NIC2, POL0L Sensitivity Curves



Camera 3, Filter F108N

Figure A1.69: NIC3, F108N Throughput

Notes:

[He I] line.

See also "Camera 1, Filter F108N".

Central wavelength: 1.0800 μm
 Mean wavelength: 1.0799 μm
 Peak wavelength: 1.0776 μm
 Wavelength range: 1%
 FWHM: 0.0096 μm
 Maximum throughput: 8.91%
 Pixel fraction: 0.582

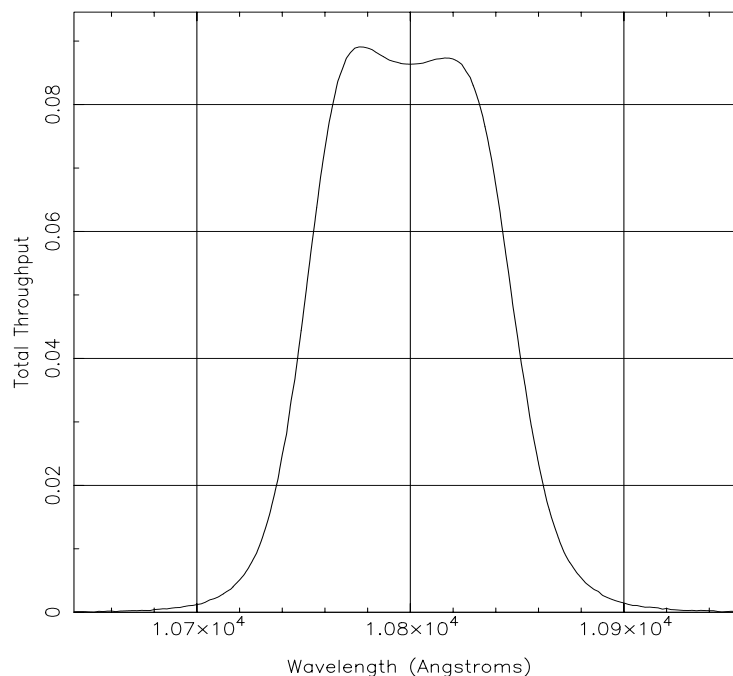
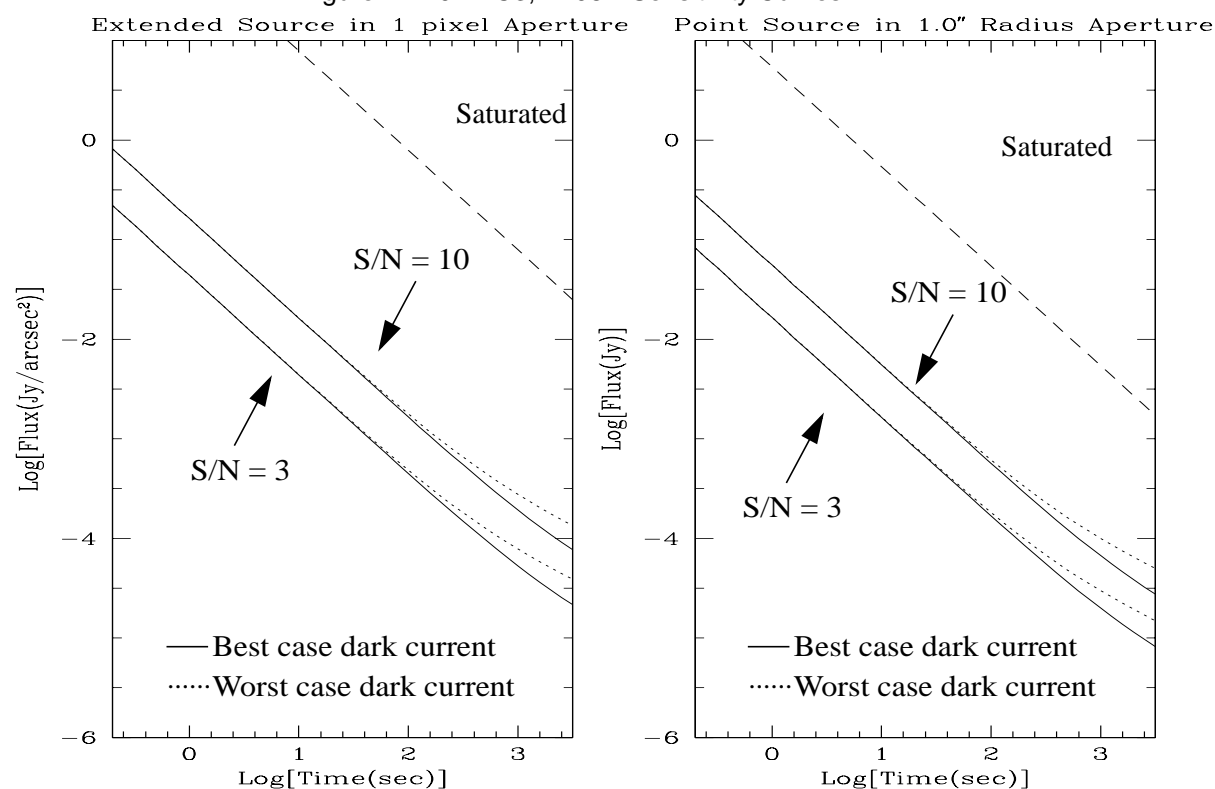


Figure A1.70: NIC3, F108N Sensitivity Curves



Camera 3, Filter F110W

Figure A1.71: NIC3, F110W Throughput

Notes:

See also “Camera 1, Filter F110W” and “Camera 2, Filter F110W”.

Central wavelength: 1.0998 μm
 Mean wavelength: 1.1035 μm
 Peak wavelength: 1.2035 μm
 Wavelength range: 0.8-1.4 μm
 FWHM: 0.5915 μm
 Maximum throughput: 14.36%
 Pixel fraction: 0.590

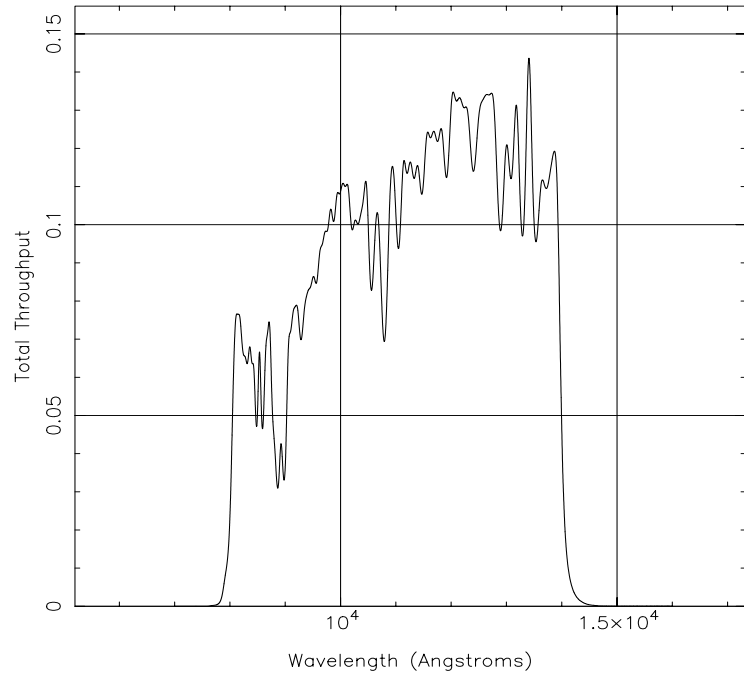
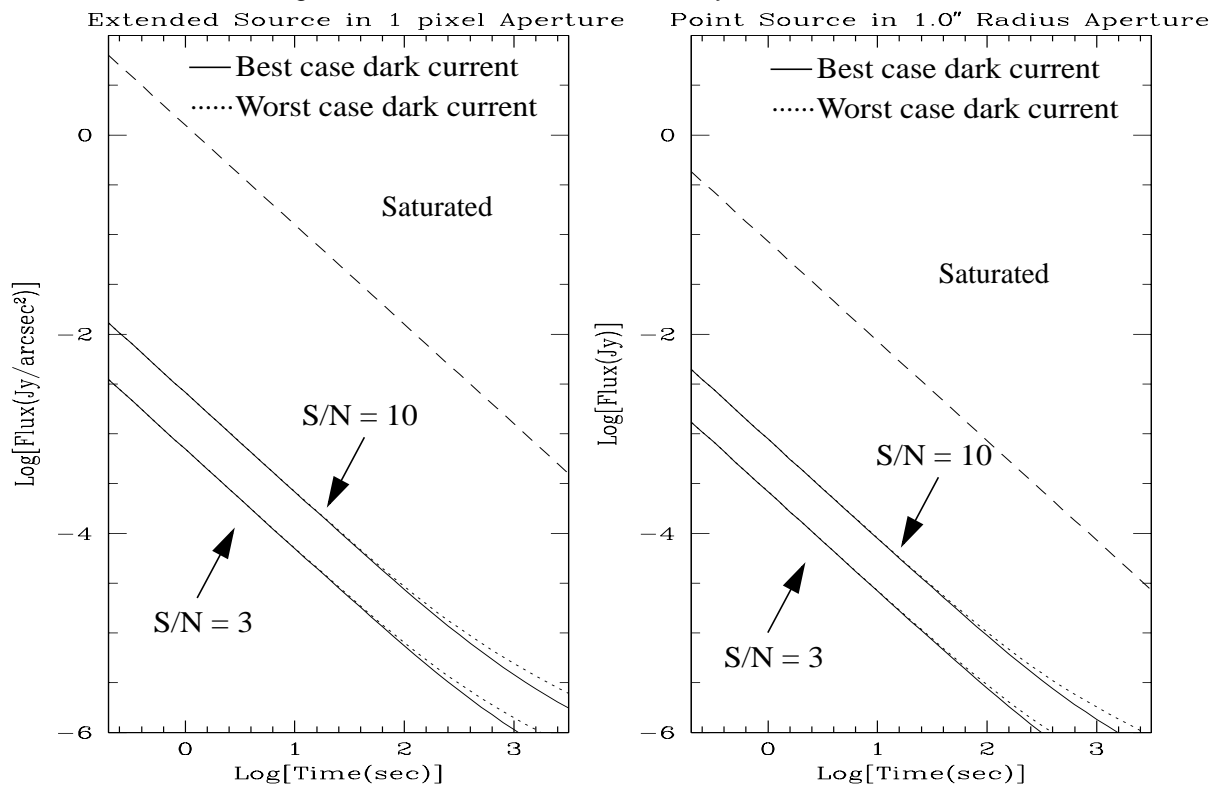


Figure A1.72: NIC3, F110W Sensitivity Curves



Camera 3, Filter F113N

Figure A1.73: NIC3, F113N Throughput

Notes:

[He I] continuum.

See also "Camera 1, Filter F113N".

Central wavelength: 1.1283 μm
 Mean wavelength: 1.1283 μm
 Peak wavelength: 1.1316 μm
 Wavelength range: 1%
 FWHM: 0.0110 μm
 Maximum throughput: 10.62%
 Pixel fraction: 0.579

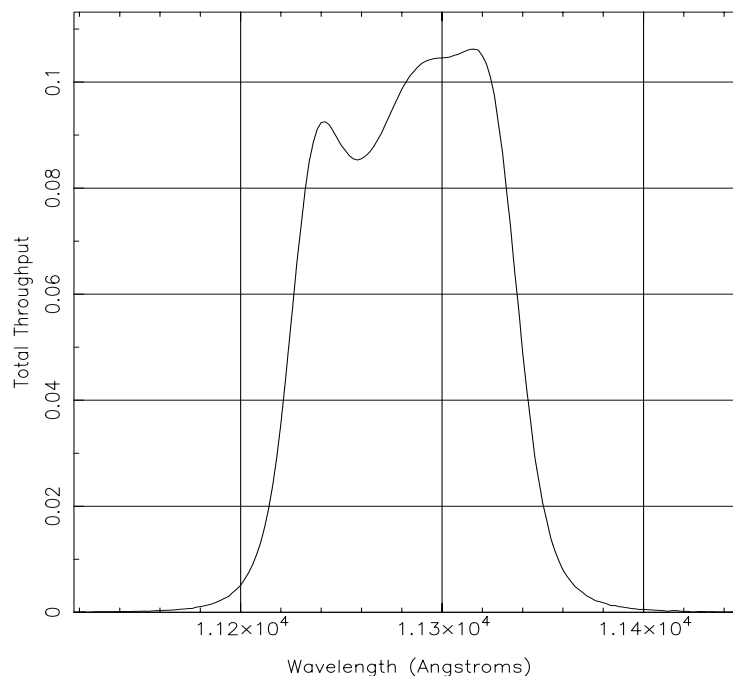
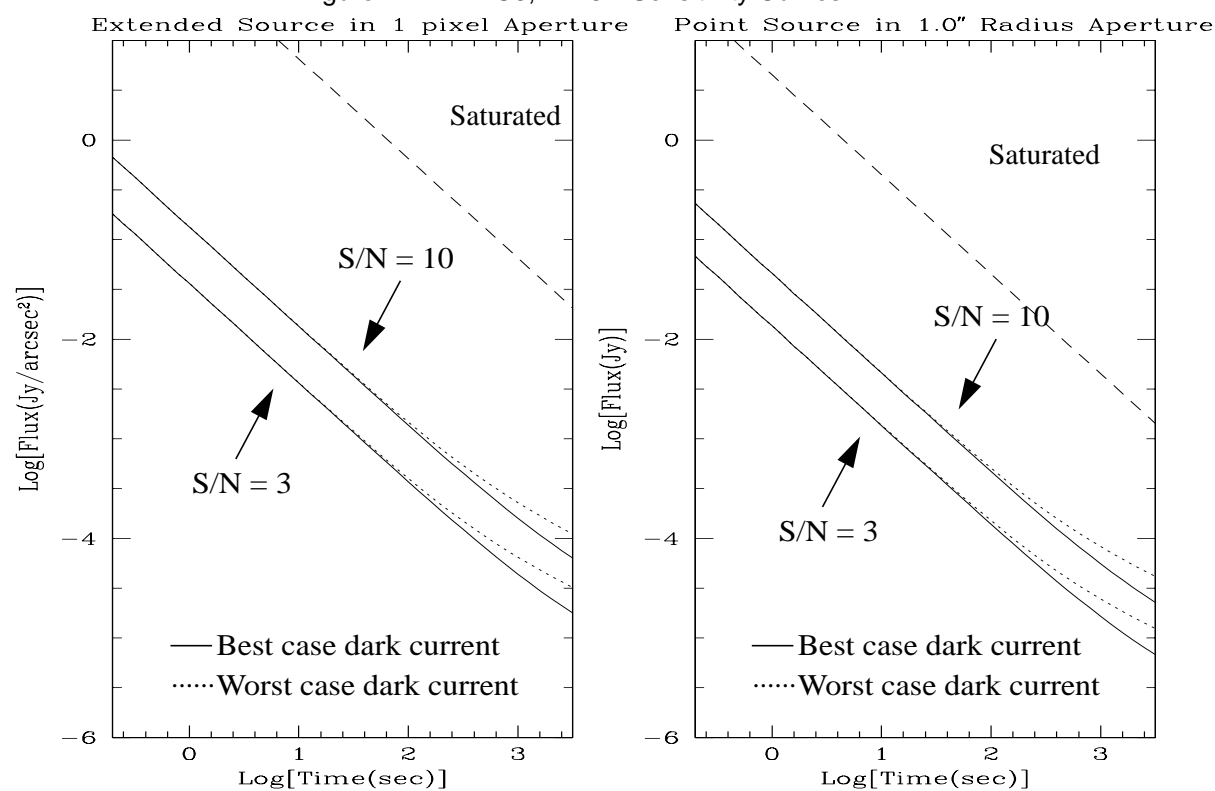


Figure A1.74: NIC3, F113N Sensitivity Curves



Camera 3, Filter F150W

Figure A1.75: NIC3, F150W Throughput

Notes:

Grism B continuum.

Thermal background important.

Central wavelength: 1.5035 μm
 Mean wavelength: 1.5069 μm
 Peak wavelength: 1.6355 μm
 Wavelength range: 1.1-1.9 μm
 FWHM: 0.8020 μm
 Maximum throughput: 24.20%
 Pixel fraction: 0.534

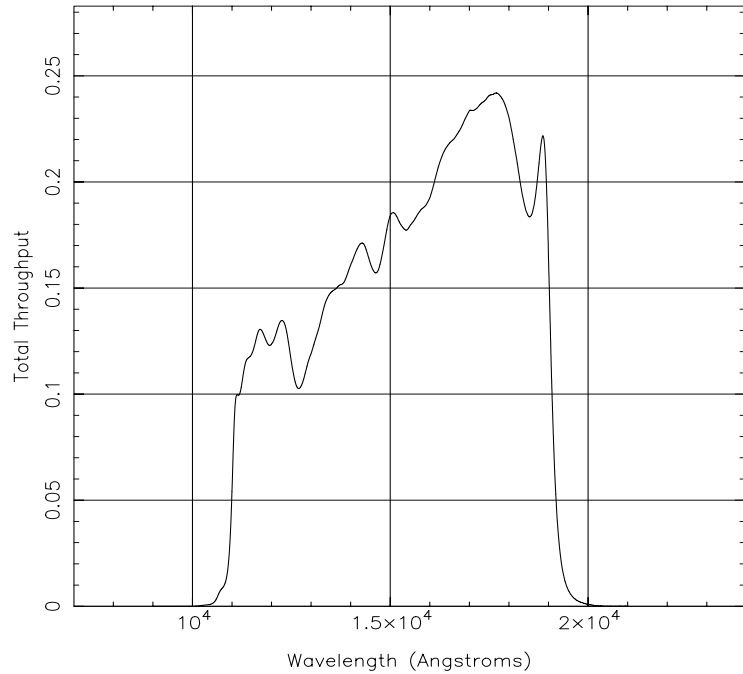
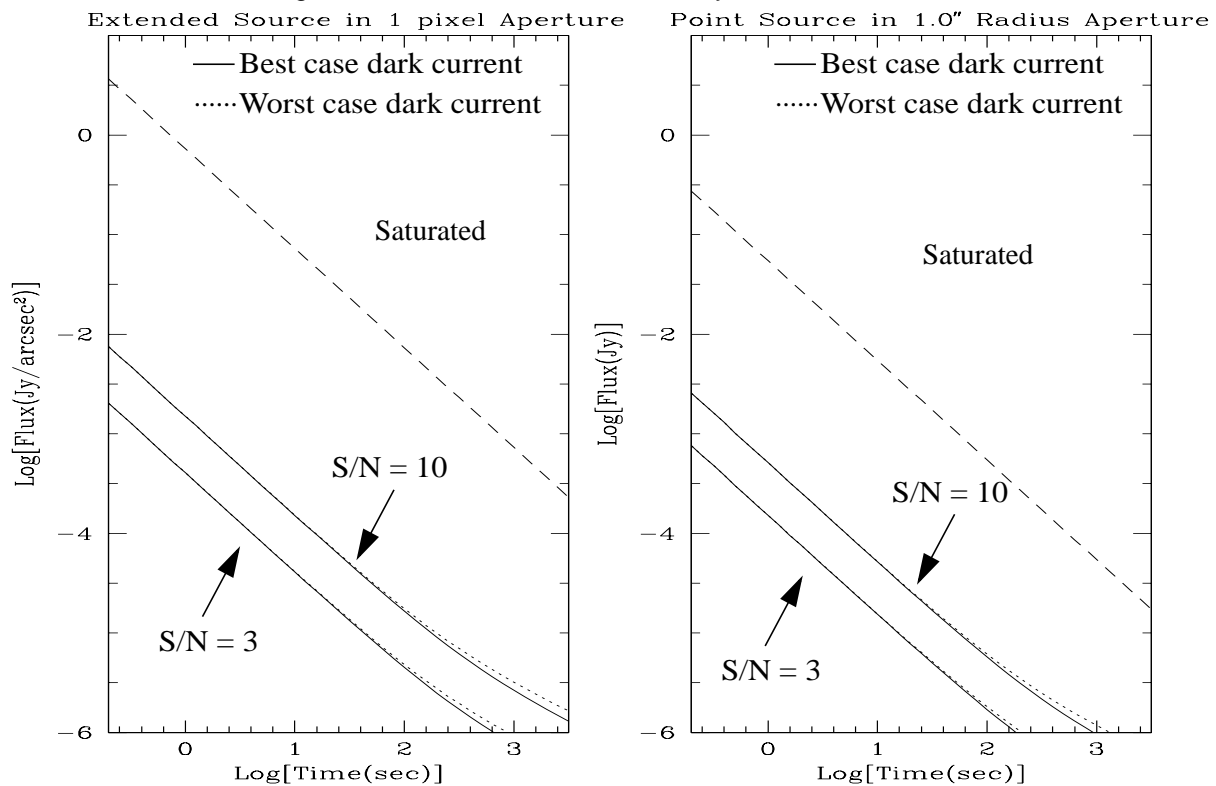


Figure A1.76: NIC3, F150W Sensitivity Curves



Camera 3, Filter F160W

Figure A1.77: NIC3, F160W Throughput

Notes:

Minimum background.

See also “Camera 1, Filter F160W” and
“Camera 2, Filter F160W”.

Central wavelength: 1.5940 μm
 Mean wavelength: 1.5931 μm
 Peak wavelength: 1.5820 μm
 Wavelength range: 1.4-1.8 μm
 FWHM: 0.4030 μm
 Maximum throughput: 23.15%
 Pixel fraction: 0.524

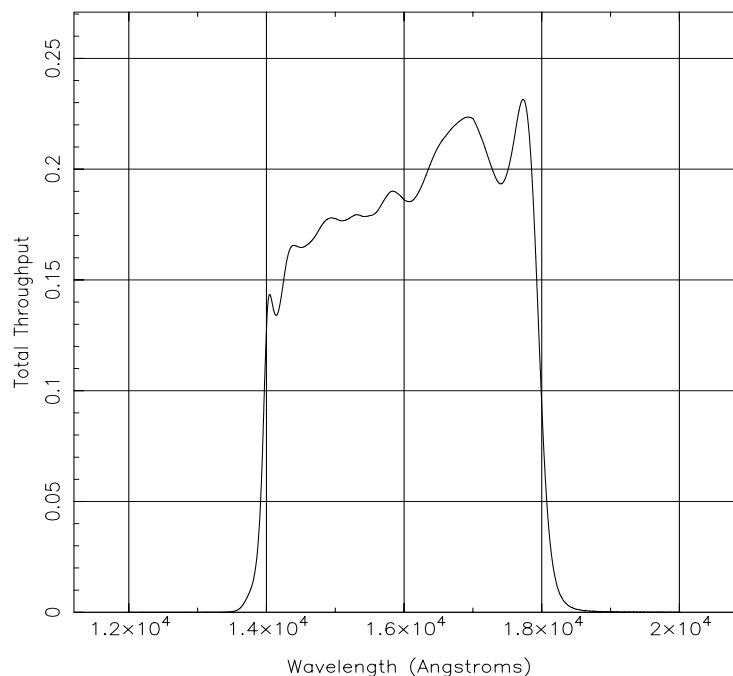
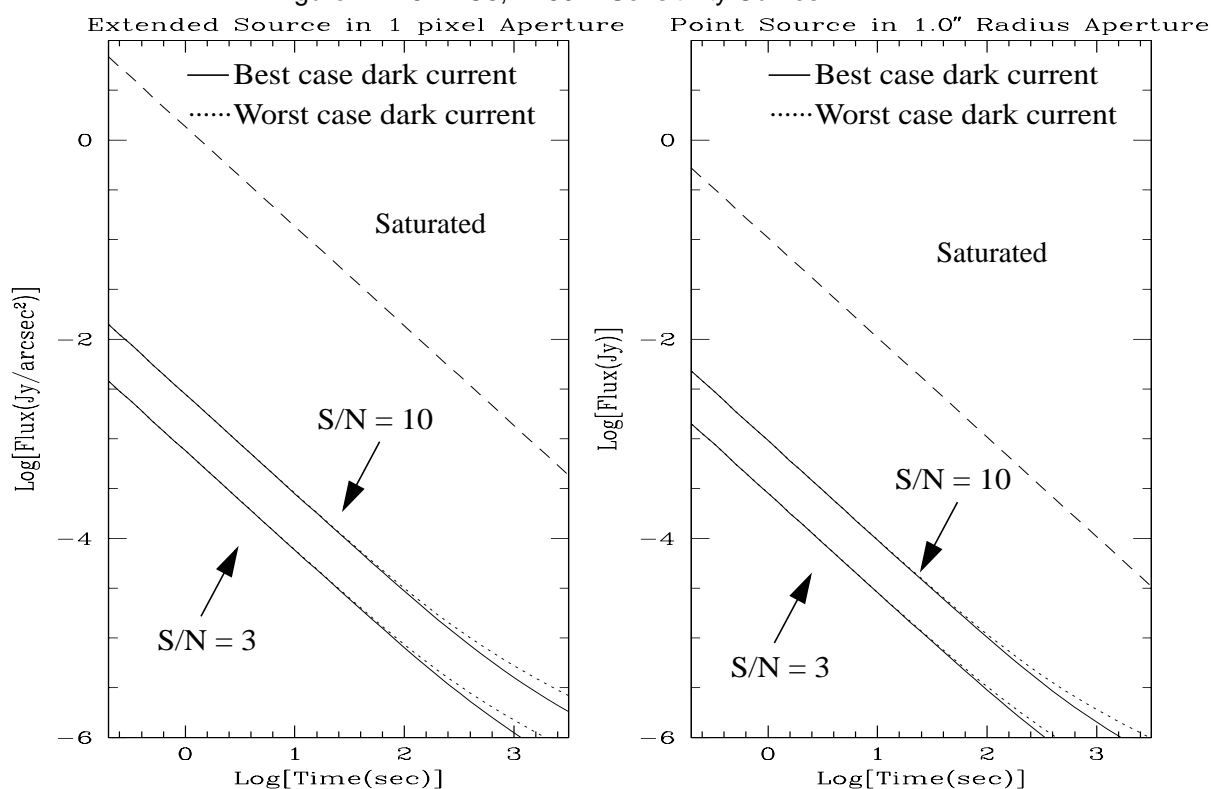


Figure A1.78: NIC3, F160W Sensitivity Curves



Camera 3, Filter F164N

Figure A1.79: NIC3, F164N Throughput

Notes:

[Fe II] line.

See also "Camera 1, Filter F164N".

Central wavelength: 1.646 μm
 Mean wavelength: 1.6460 μm
 Peak wavelength: 1.6476 μm
 Wavelength range: 1%
 FWHM: 0.0170 μm
 Maximum throughput: 19.77%
 Pixel fraction: 0.523

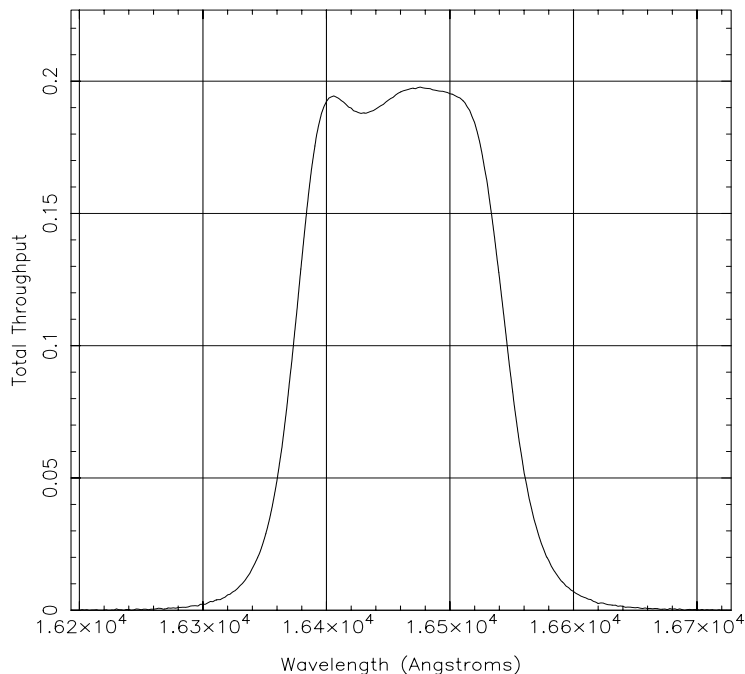
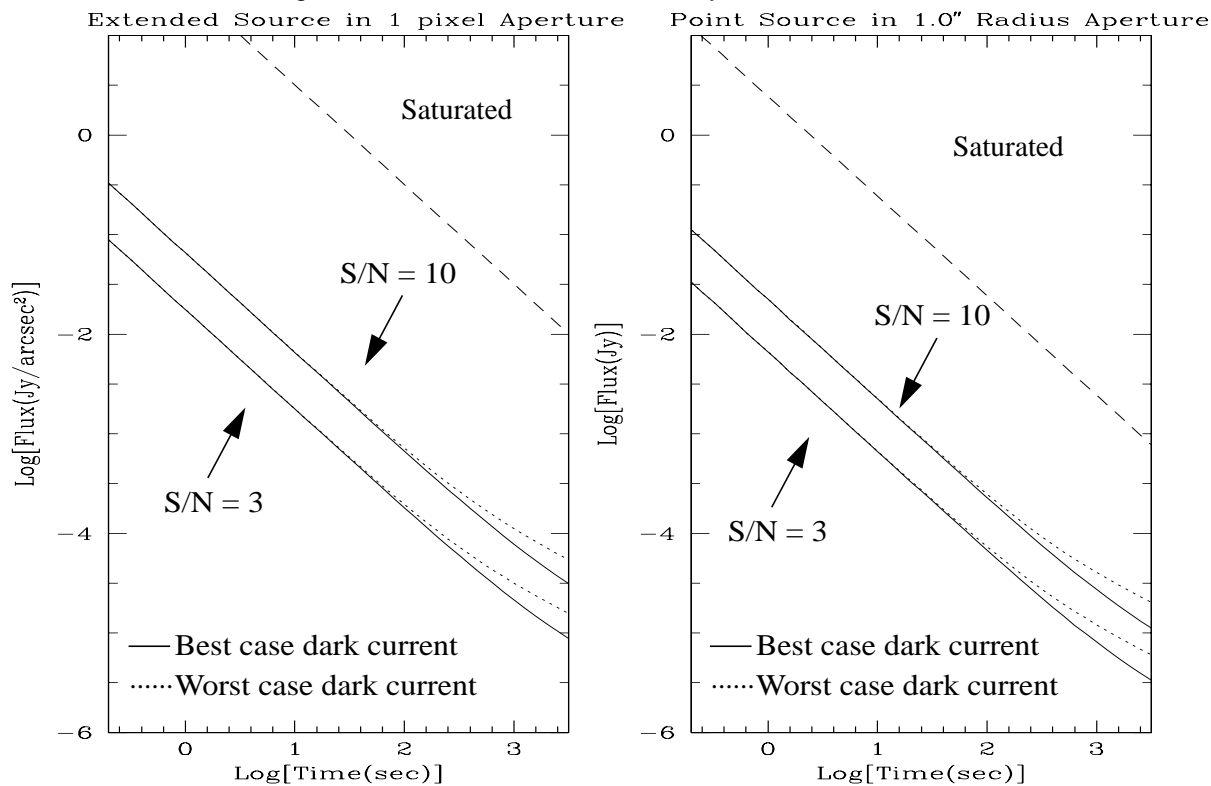


Figure A1.80: NIC3, F164N Sensitivity Curves



Camera 3, Filter F166N

Figure A1.81: NIC3, F166N Throughput

Notes:

[Fe II] continuum.

See also "Camera 1, Filter F166N".

Central wavelength: 1.6582 μm
 Mean wavelength: 1.6582 μm
 Peak wavelength: 1.6602 μm
 Wavelength range: 1%
 FWHM: 0.0164 μm
 Maximum throughput: 19.99%
 Pixel fraction: 0.513

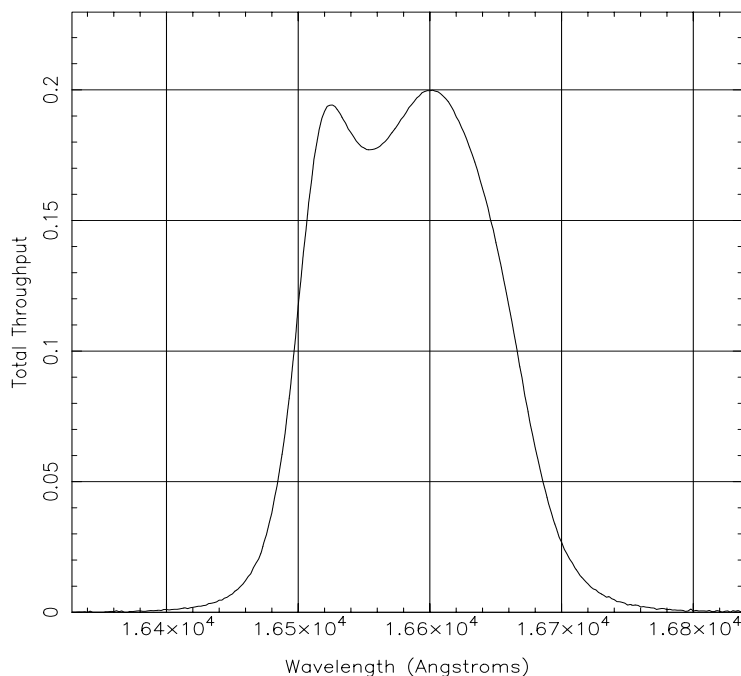
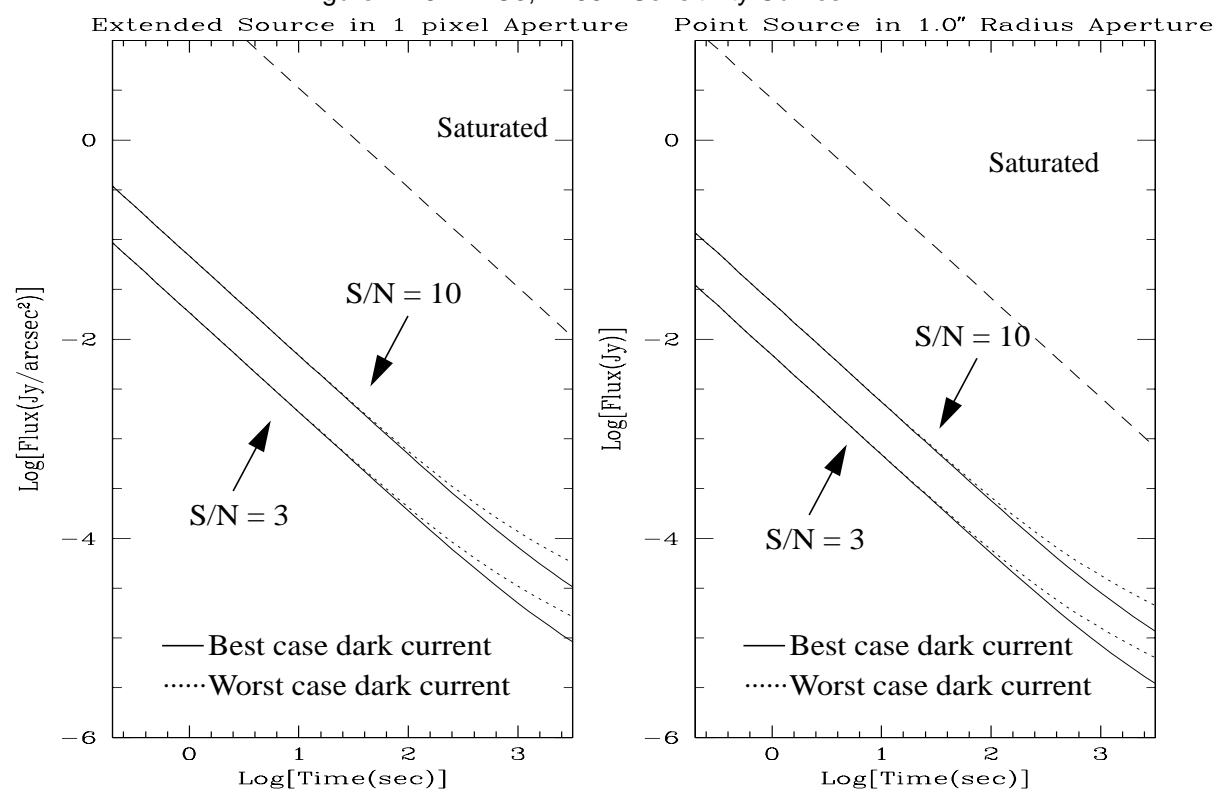


Figure A1.82: NIC3, F166N Sensitivity Curves



Camera 3, Filter F175W

Figure A1.83: NIC3, F175W Throughput

Notes:

Thermal background important.

Central wavelength: 1.7530 μm
 Mean wavelength: 1.7508 μm
 Peak wavelength: 1.9070 μm
 Wavelength range: 1.2-2.3 μm
 FWHM: 1.0940 μm
 Maximum throughput: 33.94%
 Pixel fraction: 0.486

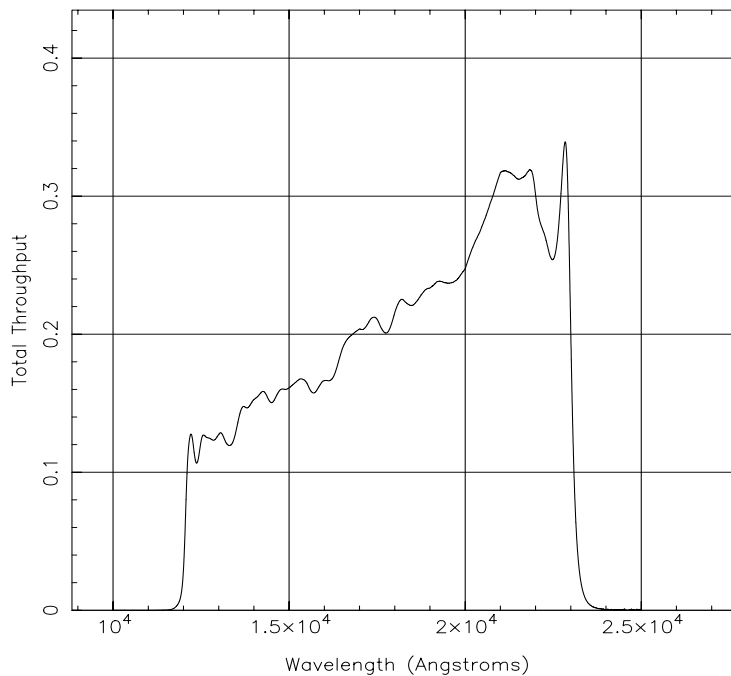
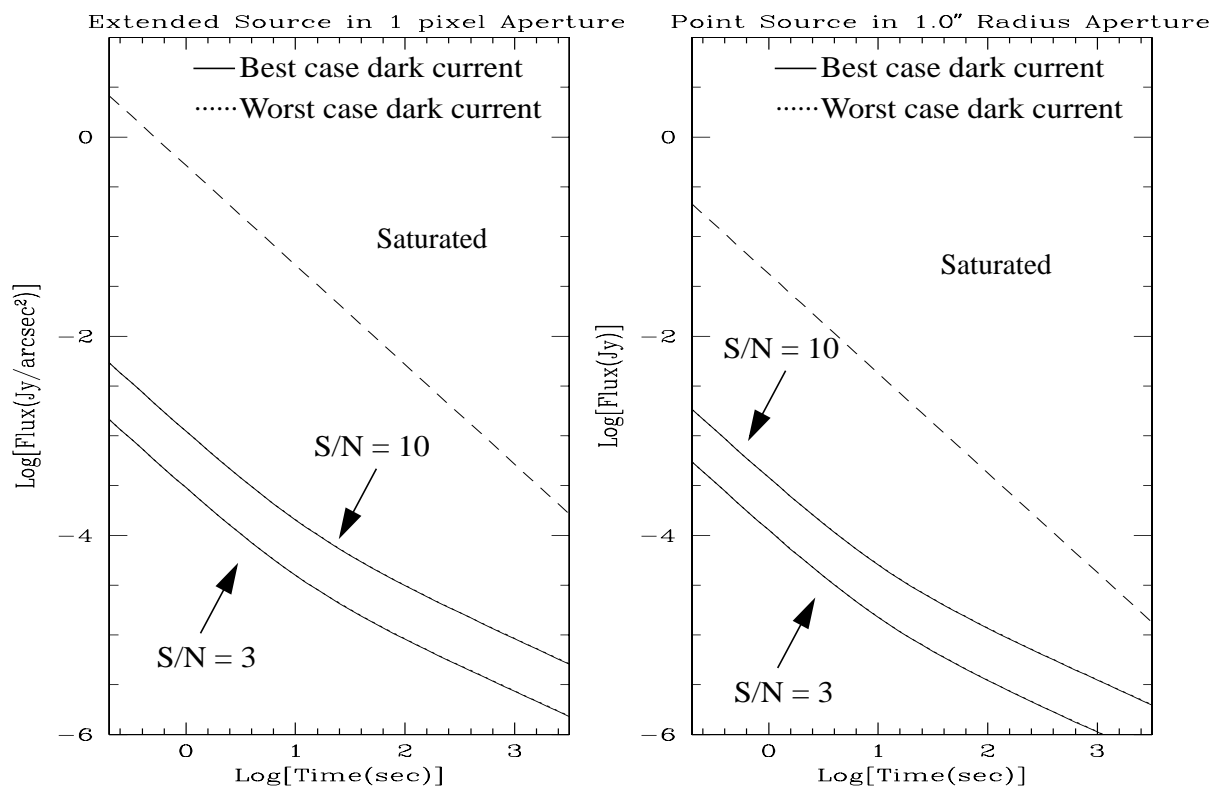


Figure A1.84: NIC3, F175W Sensitivity Curves



Camera 3, Filter F187N

Figure A1.85: NIC3, F187N Throughput

Notes:

Paschen α line.

See also “Camera 1, Filter F187N” and
“Camera 2, Filter F187N”.

Central wavelength: 1.8740 μm
 Mean wavelength: 1.8738 μm
 Peak wavelength: 1.8746 μm
 Wavelength range: 1%
 FWHM: 0.0192 μm
 Maximum throughput: 22.64%
 Pixel fraction: 0.471

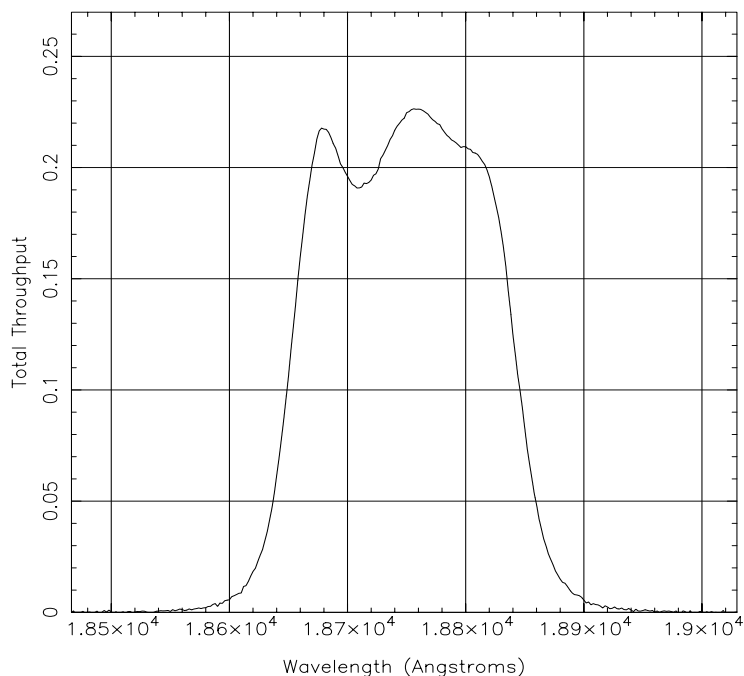
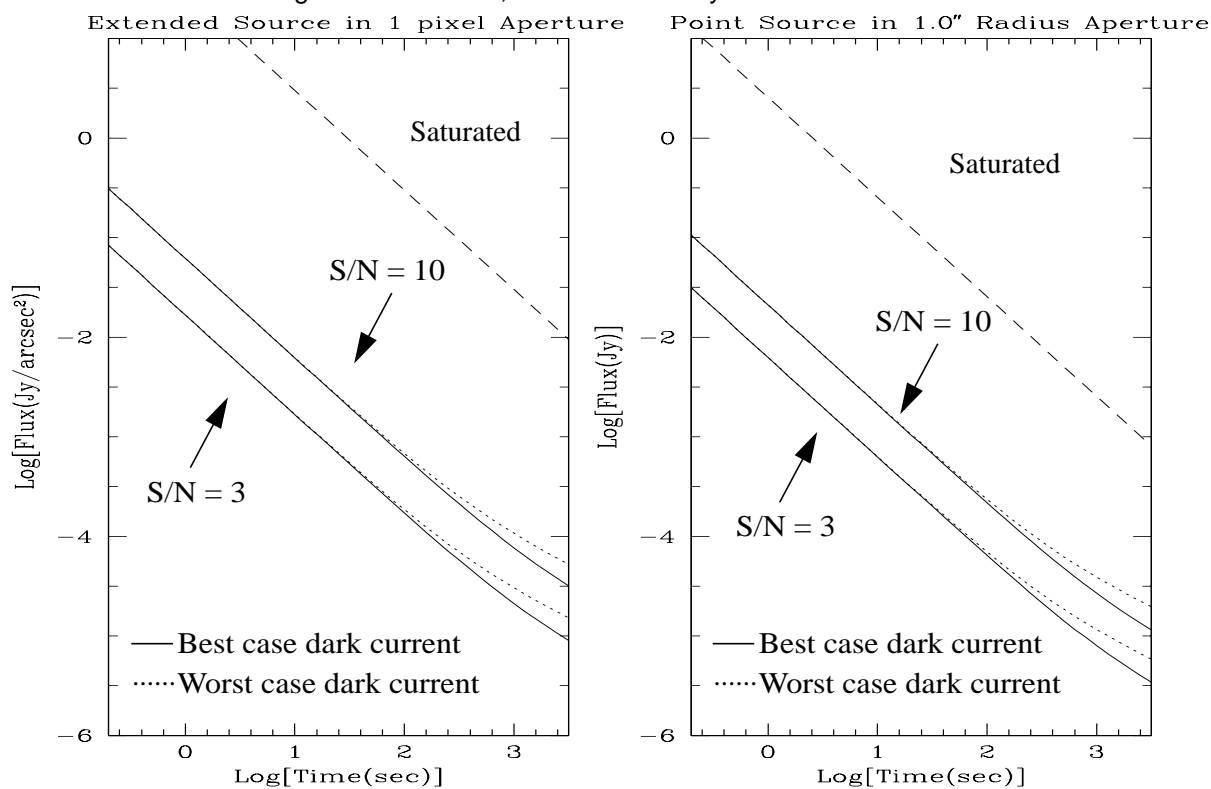


Figure A1.86: NIC3, F187N Sensitivity Curves



Camera 3, Filter F190N

Figure A1.87: NIC3, F190N Throughput

Notes:

Paschen α continuum.

See also “Camera 1, Filter F190N” and “Camera 2, Filter F190N”.

Central wavelength: 1.9005 μm
 Mean wavelength: 1.9003 μm
 Peak wavelength: 1.9004 μm
 Wavelength range: 1%
 FWHM: 0.0174 μm
 Maximum throughput: 24.41%
 Pixel fraction: 0.466

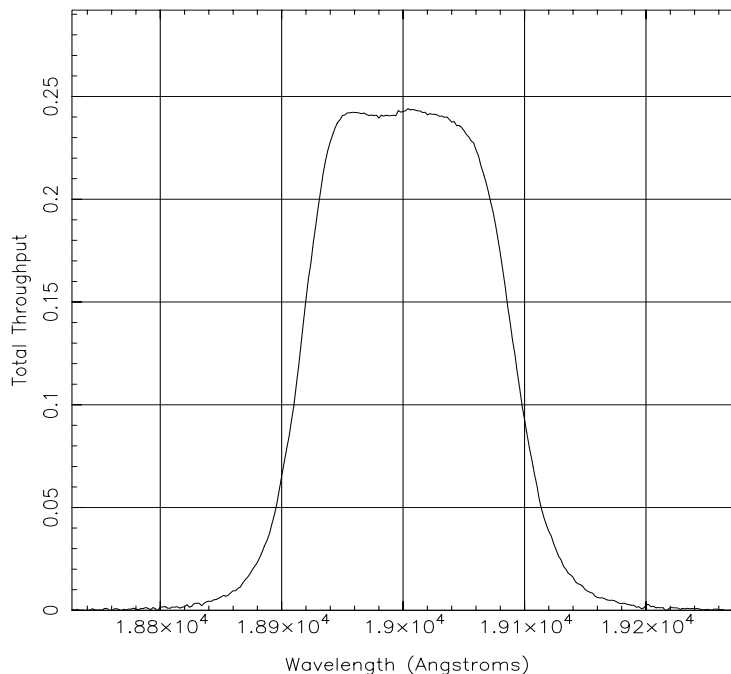
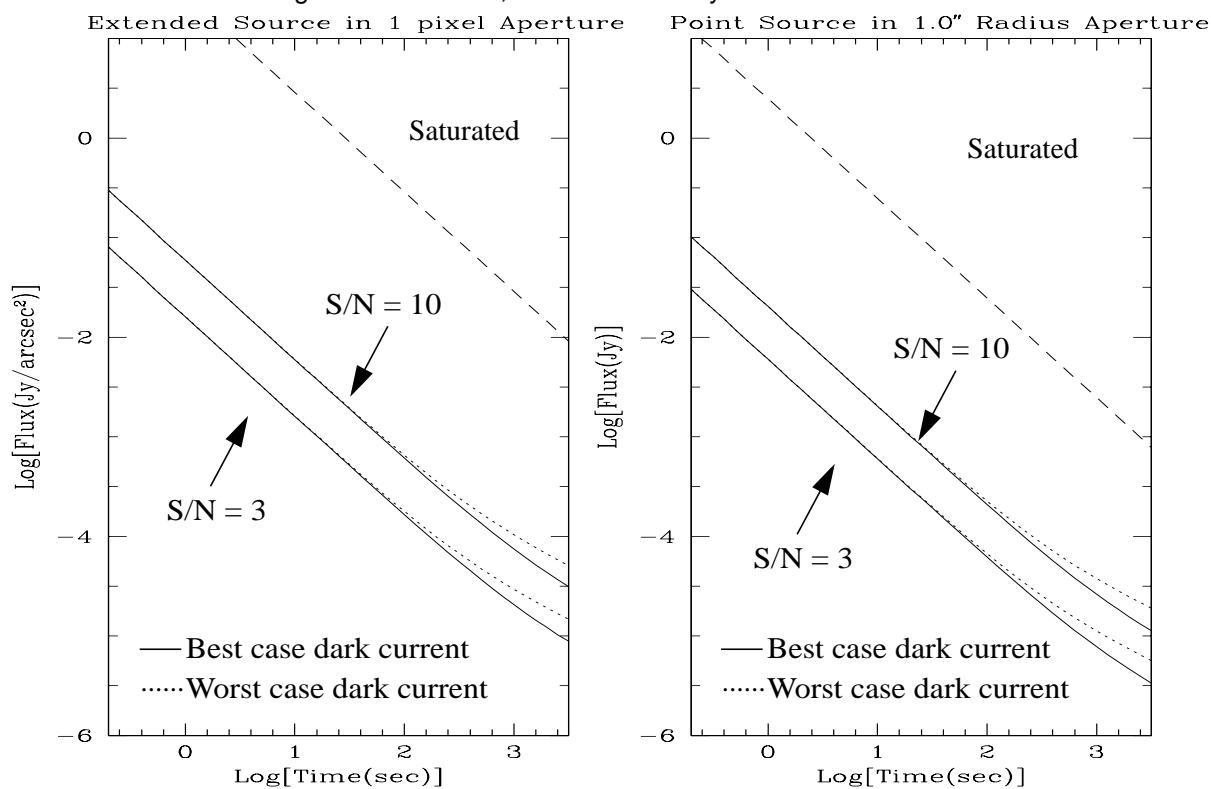


Figure A1.88: NIC3, F190N Sensitivity Curves



Camera 3, Filter F196N

Figure A1.89: NIC3, F196N Throughput

Notes:

[Si VI].

Thermal background important.

Central wavelength: 1.9641 μm
 Mean wavelength: 1.9639 μm
 Peak wavelength: 1.9698 μm
 Wavelength range: 1%
 FWHM: 0.0186 μm
 Maximum throughput: 25.33%
 Pixel fraction: 0.450

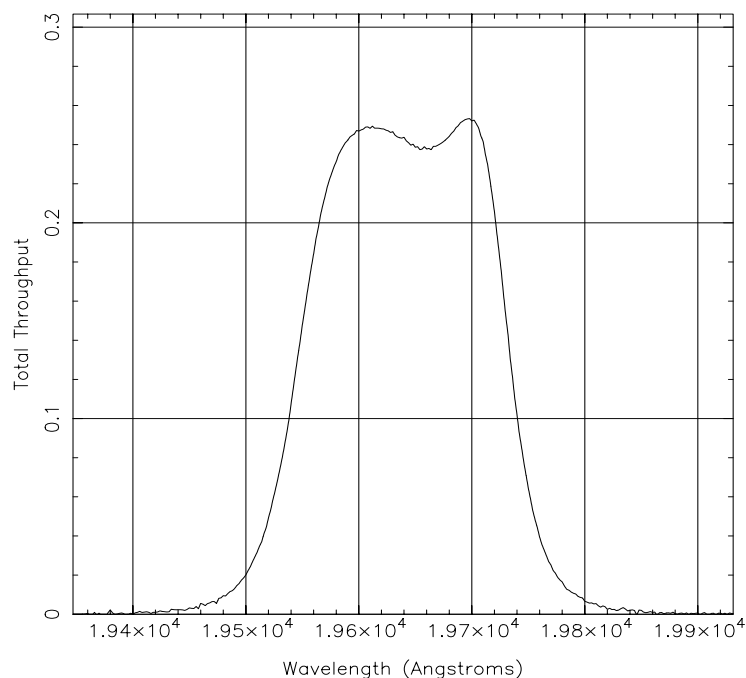
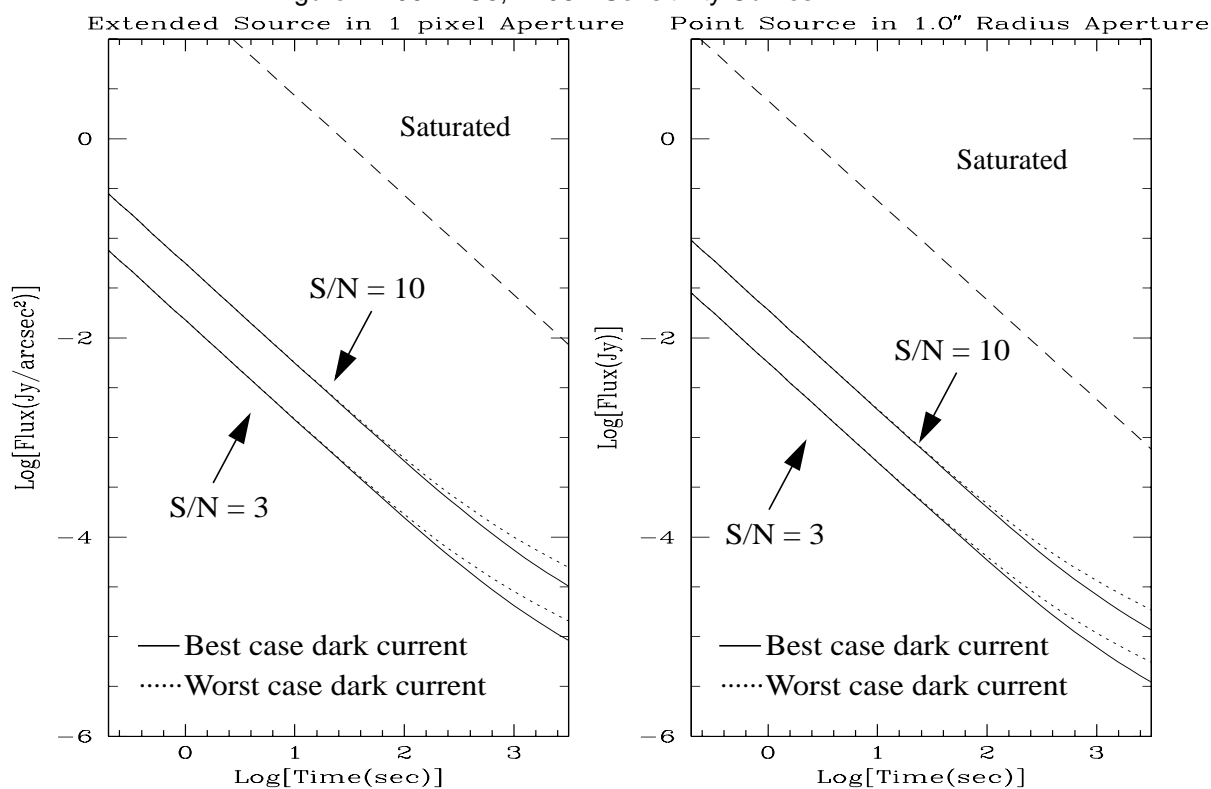


Figure A1.90: NIC3, F196N Sensitivity Curves



Camera 3, Filter F200N

Figure A1.91: NIC3, F200N Throughput

Notes:

[Si VI] continuum.

Thermal background important.

Central wavelength: $1.9973 \mu\text{m}$
 Mean wavelength: $1.9974 \mu\text{m}$
 Peak wavelength: $1.9996 \mu\text{m}$
 Wavelength range: 1%
 FWHM: $0.0206 \mu\text{m}$
 Maximum throughput: 24.59%
 Pixel fraction: 0.445

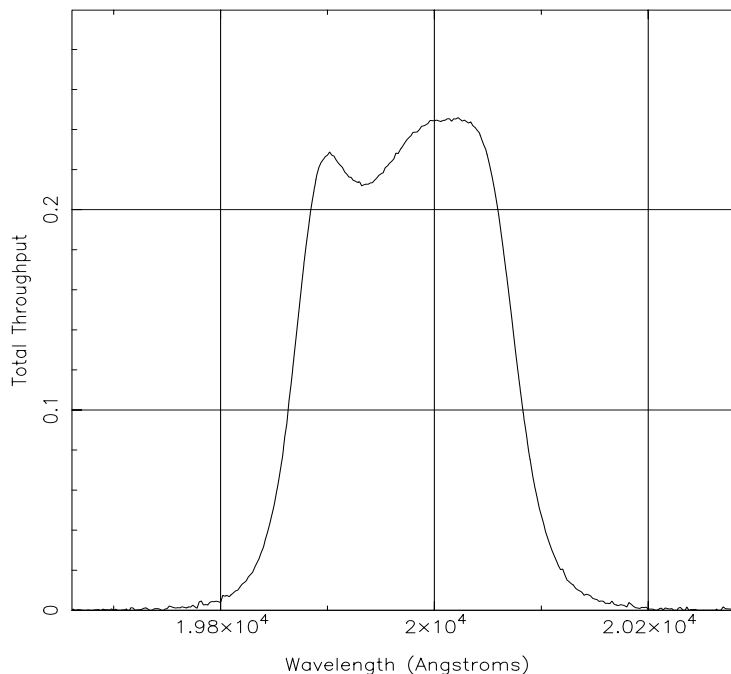
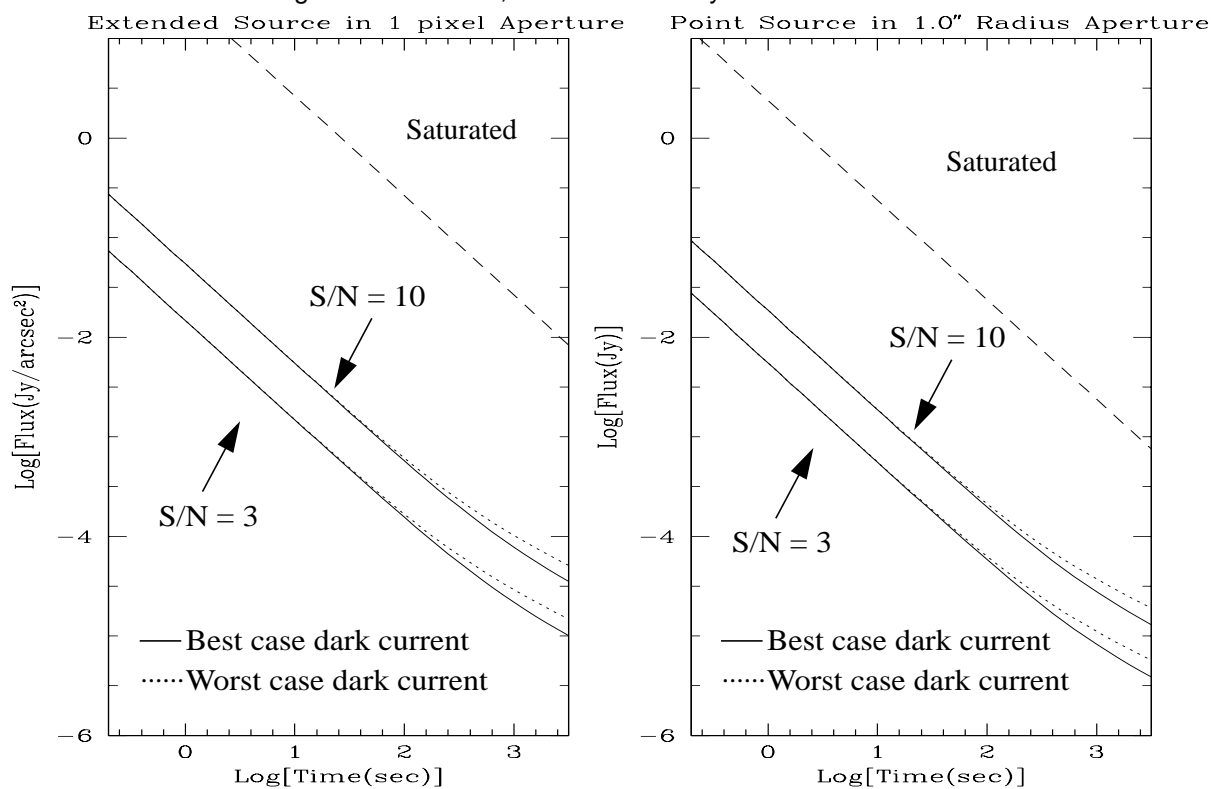


Figure A1.92: NIC3, F200N Sensitivity Curves



Camera 3, Filter F212N

Figure A1.93: NIC3, F212N Throughput

Notes:

H₂ line.

Thermal background important.

See also "Camera 2, Filter F212N".

Central wavelength: 2.1211 μm
 Mean wavelength: 2.1213 μm
 Peak wavelength: 2.1228 μm
 Wavelength range: 1%
 FWHM: 0.0206 μm
 Maximum throughput: 25.70%
 Pixel fraction: 0.418

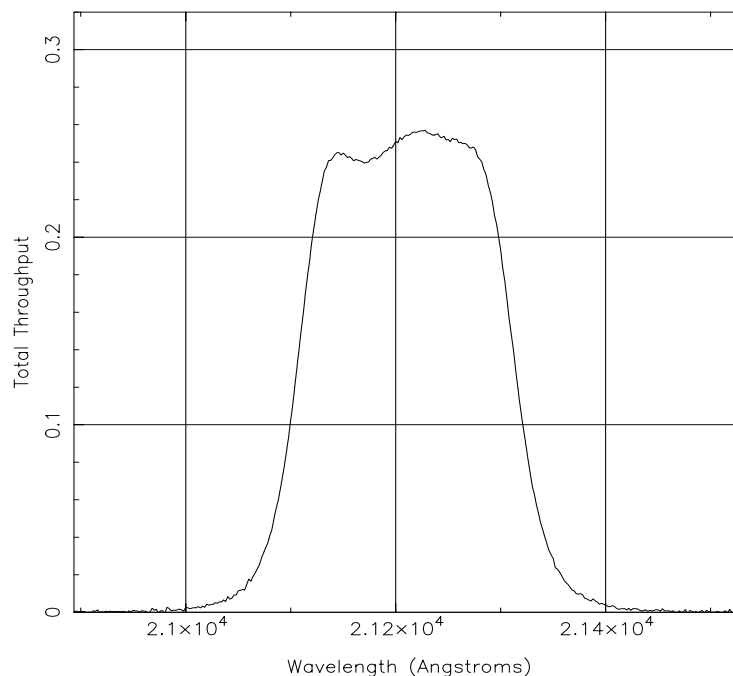
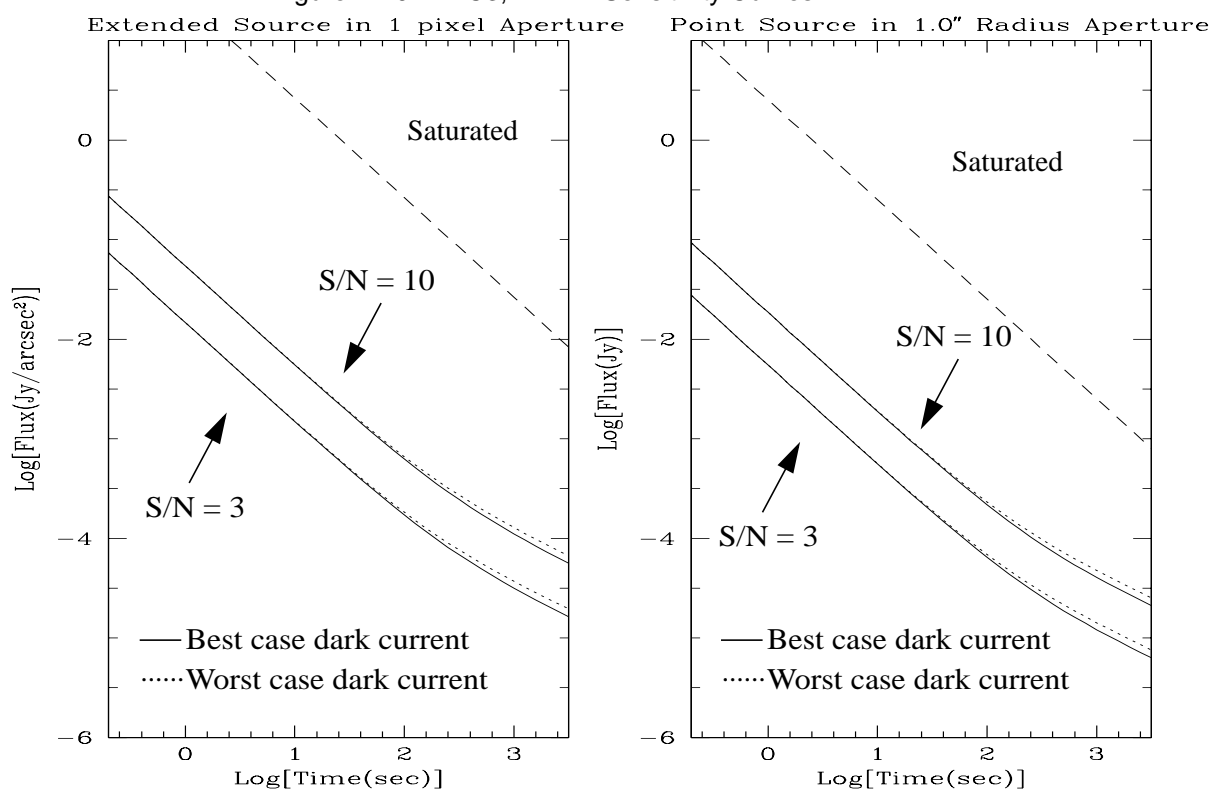


Figure A1.94: NIC3, F212N Sensitivity Curves



Camera 3, Filter F215N

Figure A1.95: NIC3, F215N Throughput

Notes:

H₂ continuum.

Thermal background important.

See also "Camera 2, Filter F215N".

Central wavelength: 2.1488 μm
 Mean wavelength: 2.1487 μm
 Peak wavelength: 2.1562 μm
 Wavelength range: 1%
 FWHM: 0.0200 μm
 Maximum throughput: 25.10%
 Pixel fraction: 0.413

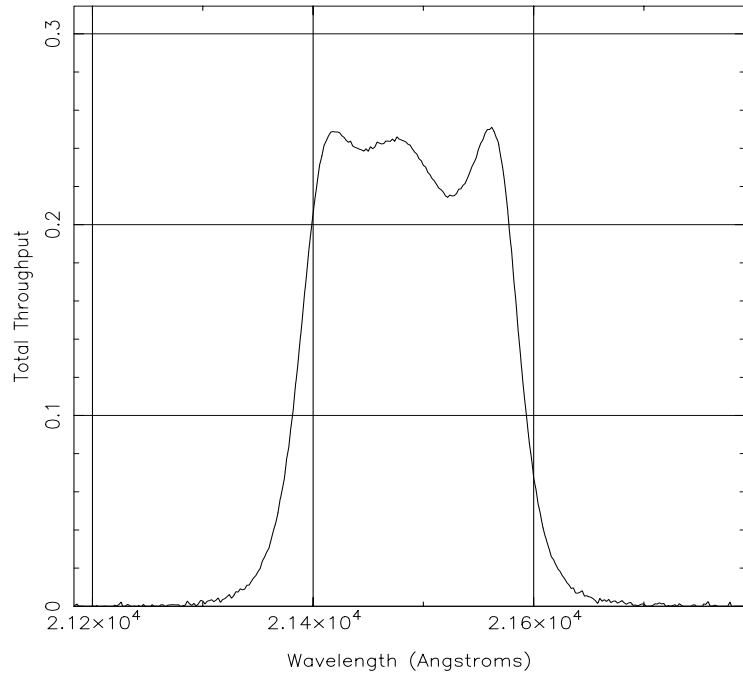
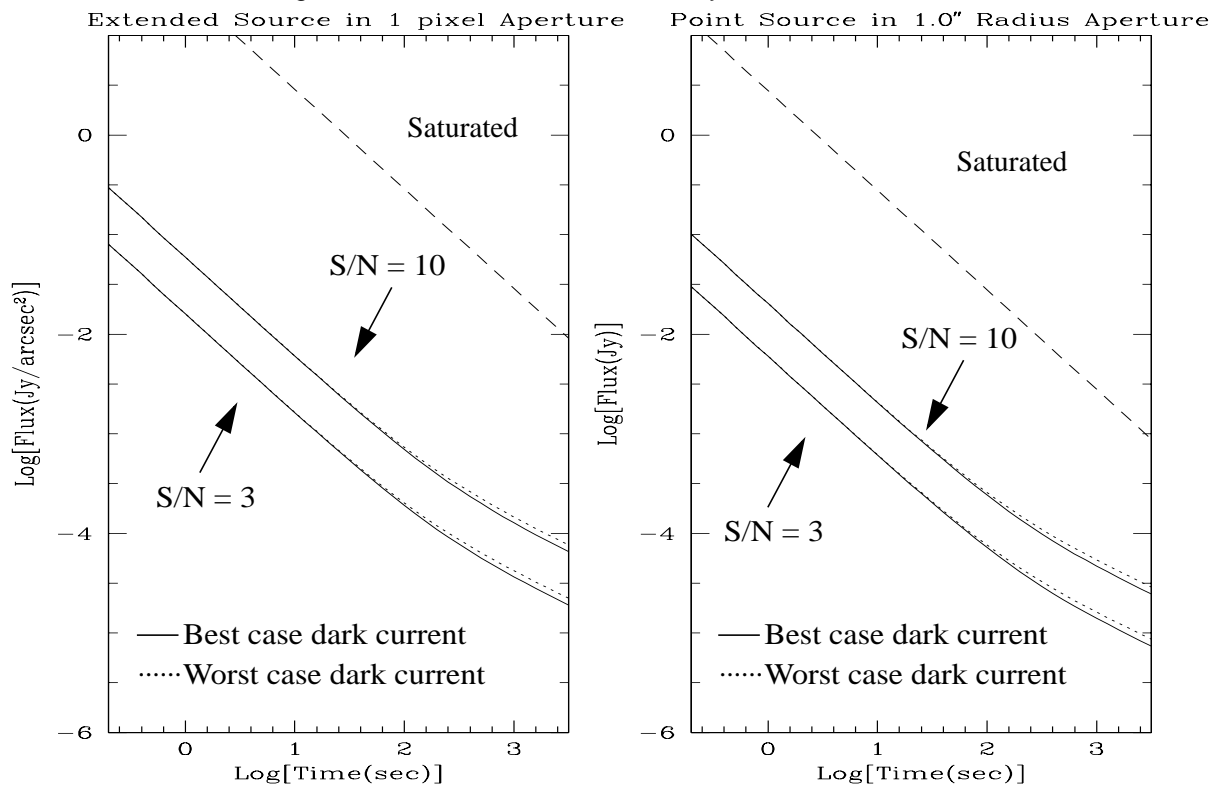


Figure A1.96: NIC3, F215N Sensitivity Curves



Camera 3, Filter F222M

Figure A1.97: NIC3, F222M Throughput

Notes:

CO continuum.

Thermal background important.

See also "Camera 2, Filter F222M".

Central wavelength: 2.216 μm
 Mean wavelength: 2.216 μm
 Peak wavelength: 2.18 μm
 Wavelength range: 2.15-2.3 μm
 FWHM: 0.1432 μm
 Maximum throughput: 26.52%
 Pixel fraction: 0.397

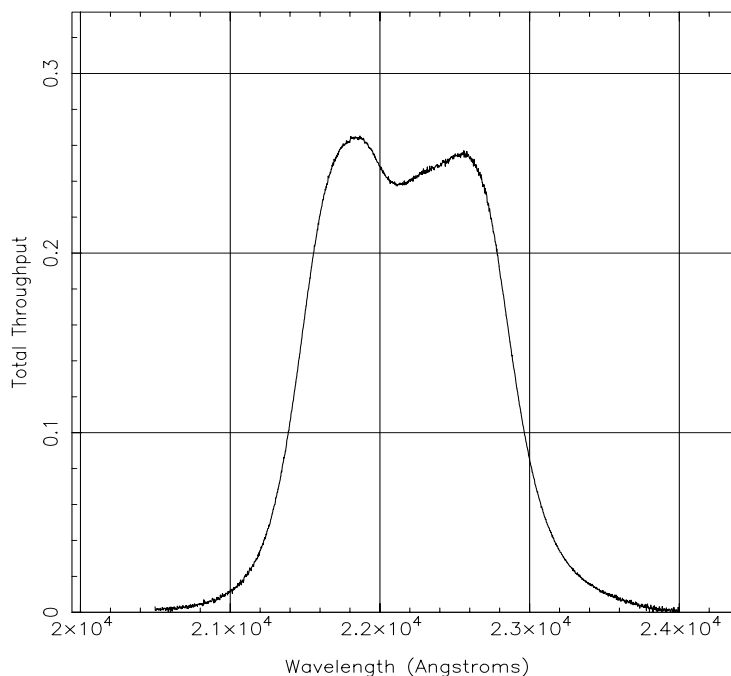
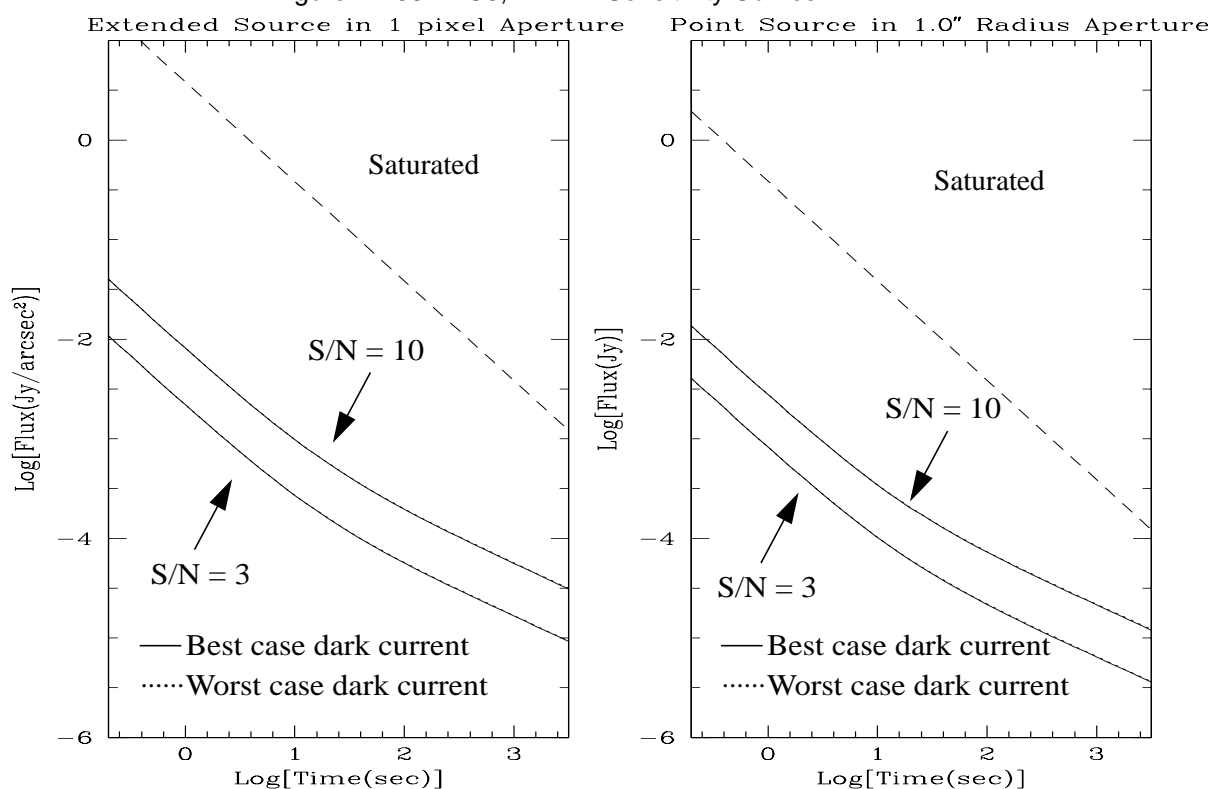


Figure A1.98: NIC3, F222M Sensitivity Curves



Camera 3, Filter F240M

Figure A1.99: NIC3, F240M Throughput

Notes:

CO band.

Thermal background important.

Central wavelength: 2.3978 μm
 Mean wavelength: 2.3977 μm
 Peak wavelength: 2.3155 μm
 Wavelength range: 2.3-2.5 μm
 FWHM: 0.1975 μm
 Maximum throughput: 32.78%
 Pixel fraction: 0.363

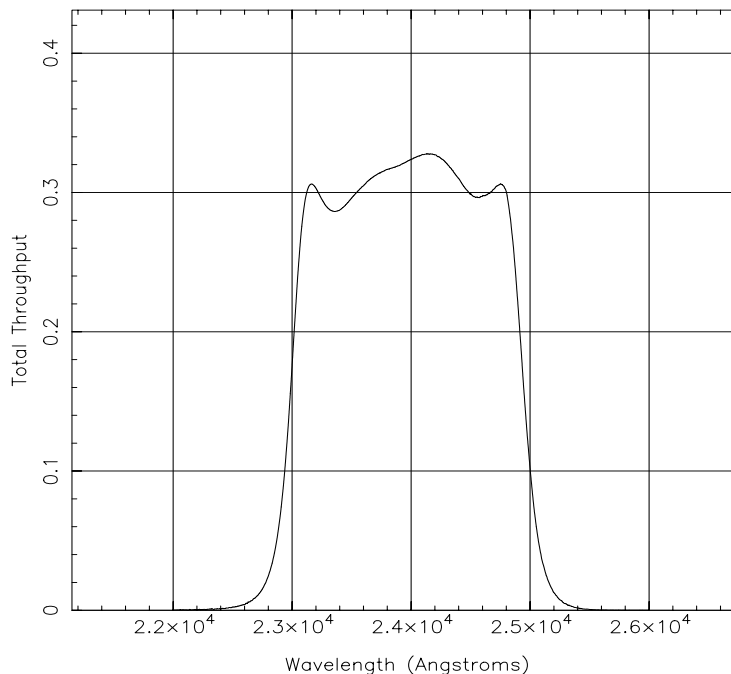
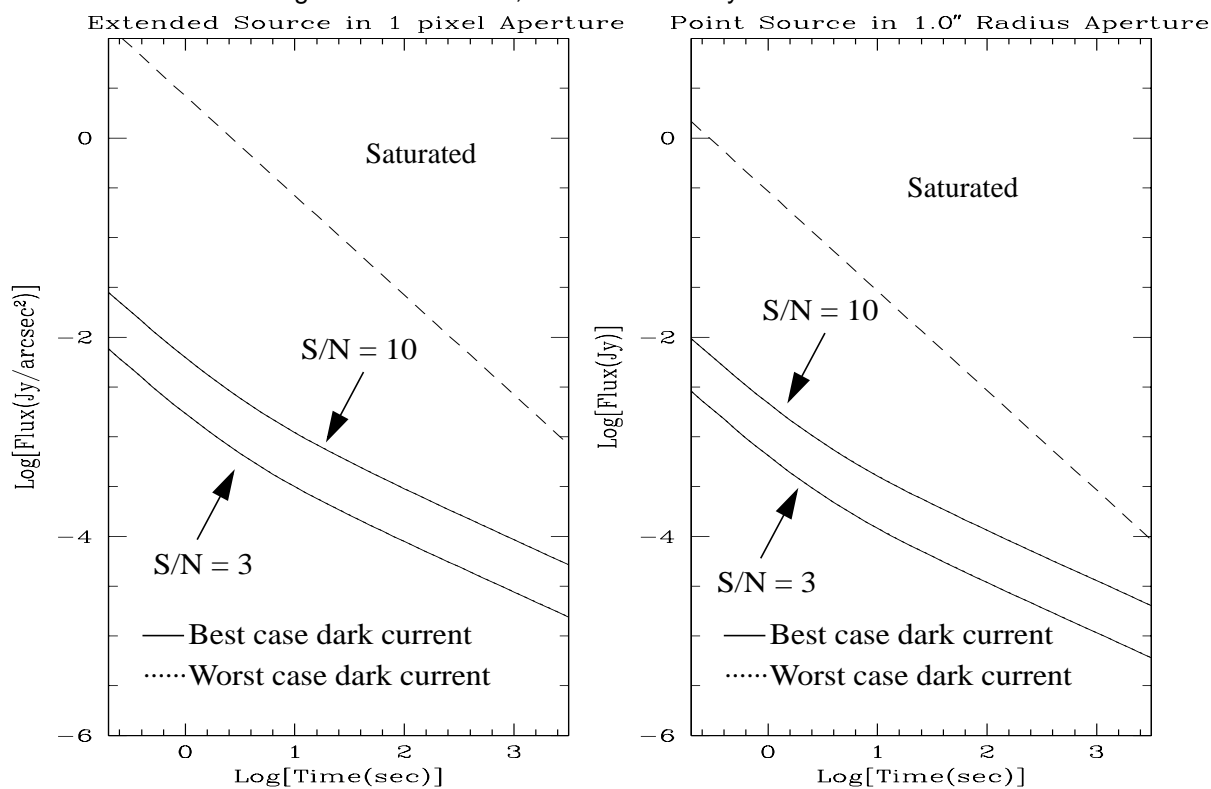


Figure A1.100: NIC3, F240M Sensitivity Curves



Flux Units and Line Lists

In This Appendix...

Infrared Flux Units / 255

Formulae / 258

Look-up Tables / 259

Examples / 266

Infrared Line Lists / 266

In this chapter we provide a variety of background material that may be useful when preparing proposals. This material includes a discussion of the flux and surface brightness units often used in the infrared, which may not be familiar to some users, plus a large compilation of spectral lines that may be encountered in the infrared, and which are either in the NICMOS waveband or which are related to lines which are.

Infrared Flux Units

In the infrared, as in the optical, the means of reporting source brightnesses and the units employed have varied considerably. In recent years, however, magnitude systems have been used less frequently, and the most popular unit for expressing brightnesses, both for point source fluxes and surface brightnesses, is steadily becoming the Jansky. We have adopted the Jansky as the standard flux unit for NICMOS in our documentation and in observer-oriented software. Here we provide some simple formulae and tables to facilitate the conversion from other units into Jy. A Unit Conversion Tool is also available in the NICMOS WWW site, under Software.

Some History

Infrared astronomy really began in the 1960s, when the vast majority of astronomy was still carried out in the visual region. Flux measurements were routinely reported in the UBV magnitude system, and to attempt to integrate IR astronomy into this system, Johnson (Ap.J., **134**, 69) defined the first IR magnitude system. This involved four new photometric bands, the J, K, L and M bands which were centered on wavelengths of 1.3, 2.2, 3.6 and 5.0 microns. These bands were defined not only by the filter bandpasses, but also by the wavebands of the ‘windows’ of high transmission through the atmosphere. In this system, all measurements were referred to the Sun, which was assumed to be a G2V star with an effective temperature of 5785K, and was taken to have a V-K color of roughly +2.2. From his own measurements in this system, Johnson determined Vega to have a K magnitude of +0.02 and K-L=+0.04.

Until the early 1980s IR astronomical observations were restricted to spectra or single channel photometry, and most photometry was reported in systems at least loosely based on Johnson’s system, though with the addition of a new band at 1.6 microns known as the H band and the development of two bands in place of the one formerly defined by Johnson as the L band, a new definition of the L band centered on 3.4 microns, and a rather narrower band known as L’ centered on 3.74 microns.

As the new science of infrared astronomy rapidly expanded its wavelength coverage, many new photometric bands were adopted, both for ground-based observations and for use by the many balloon- and rocket-borne observations and surveys. The differing constraints presented by these different environments for IR telescopes resulted in systems with disappointingly little commonality or overlap, and today the IR astronomer is left with a plethora of different systems to work with.

The IRAS survey results, which were published in 1986, presented observations made photometrically in four bands in the mid- and far-infrared, and mid-infrared spectra, and all were presented in units of Janskys, rather than defining yet another new magnitude system. Since then, IR data from many sites around the world have been increasingly commonly presented in Janskys (Jy), or in Jy/arcsec^2 in the case of surface brightness data. IRAS maps are often presented in units of MJy/steradian.

Ground-based mid-IR photometry is usually carried out using the N and Q photometric bands, which are themselves defined more by the atmospheric transmission than by any purely scientific regard. *IRAS*, freed of the constraints imposed by the atmosphere, adopted its own 12 micron and 25 micron bands, which were extremely broad and therefore offered high sensitivity. Similarly, NICMOS, being above the atmosphere, is not forced to adopt filter bandpasses (See Chapter 4 and Appendix 1) like those used at ground-based observatories, but instead has filters constrained purely by the anticipated scientific demands. Thus in practice NICMOS

does not have filters matched to any of the standard ground-based photometric bands.

Units for NICMOS and Available Software

In order to facilitate proposal preparation by observers, STScI is making available a number of computer programs to assist with signal to noise ratio and integration time calculations. Given the multitude of units and systems that have been used for IR photometry (magnitudes, Janskys, $\text{Wm}^{-2}\mu\text{m}^{-1}$, $\text{Wcm}^{-2}\mu\text{m}^{-1}$, $\text{erg sec}^{-1}\text{cm}^{-2}\mu\text{m}^{-1}$) and for surface brightness measurements ($\text{Janskys arcsec}^{-2}$, $\text{MJy steradian}^{-1}$, $\text{magnitudes arcsec}^{-2}$), presenting these data to observers could become somewhat cumbersome. Additionally, given the lack of any *standard* IR filters (as explained above), in order to express brightnesses in magnitudes we would have to adopt our own NICMOS magnitude system, and observers would have to transform ground-based photometry into the NICMOS bands. We have therefore adopted a single standard set of flux units, Janskys for all photometry and spectroscopy, and $\text{Janskys arcsec}^{-2}$ for all surface brightness measurements in all NICMOS documentation and observer-oriented software. The NICMOS calibration pipeline software delivers results calibrated in $\text{Janskys arcsec}^{-2}$, as well as the more familiar HST unit of $\text{erg s}^{-1}\text{cm}^{-2}\text{\AA}^{-1}$.

We are aware that some observers do not routinely use these units, and therefore below we give a set of simple formulae to use to convert between systems, and some conversion tables. In addition, we have made available, via the NICMOS World Wide Web pages at STScI, software to perform conversions between different systems and units. The Unit Conversion Tool is available at the URL:

http://www.stsci.edu/instruments/nicmos/NICMOS_tools/nicmos_tools.html

Formulae

Converting Between F_v and F_λ

One Jansky (Jy) is defined as $10^{-26} \text{Wm}^{-2} \text{Hz}^{-1}$, so it is a unit of measurement of the spectral flux density, F_v .

For F_v in Jy, use the following formula:

$$F_\lambda = \beta F_v / \lambda^2$$

where λ is the wavelength in microns (μm), and β is a constant chosen from Table 2.1 and depending on the units of F_λ . (This is simply derived, using the fact that $dv/d\lambda = c/\lambda^2$.)

Table A2.1: Constants for Converting F_λ and F_v

F_λ measured in	β
$\text{Wm}^{-2} \mu\text{m}^{-1}$	3×10^{-12}
$\text{Wcm}^{-2} \mu\text{m}^{-1}$	3×10^{-16}
$\text{erg sec}^{-1} \text{cm}^{-2} \mu\text{m}^{-1}$	3×10^{-9}
$\text{erg sec}^{-1} \text{cm}^{-2} \text{\AA}^{-1}$	3×10^{-13}

Remember that $1 \text{W} = 10^7 \text{erg sec}^{-1}$, and $1 \mu\text{m} = 10^4 \text{\AA}$.

Conversion Between Fluxes and Magnitudes

The spectral flux density F_v can be calculated from its magnitude as

$$F_v = 10^{-m/2.5} F_0$$

where m is the magnitude and F_0 the zero-point flux for the given photometric band. We list the central wavelengths and zero-point fluxes for the more commonly encountered photometric bands below in Table 2.2. The CIT system was originally based on Beckwith et al (1976, Ap.J., **208**, 390); the UKIRT system is in fact based on the original CIT system, but with adjustments made largely owing to different filter bandpasses. It should be noted that for a given photometric band there will be small differences in the effective wavelength and zero-point flux from one observatory to another, and for astronomical objects with radically different colors, so these figures can only be treated as approximate.

Table A2.2: Effective Wavelengths and Zero-points for Photometric Bands

Band	$\lambda[\mu\text{m}]$	$F_0[\text{Jy}]$ (CIT)	$F_0[\text{Jy}]$ (UKIRT)
V	0.56	3540	3540
R	0.70	2870	-
I	0.90	2250	-
J	1.25	1670	1600
H	1.65	980	1020
K	2.2	620	657
L	3.4	280	290
L'	3.74	-	252
M	4.8	150	163
N	10.1	37	39.8
Q	20.0	10	10.4

Conversion Between Surface Brightness Units

Surface brightnesses are generally measured in Janskys arcsec^{-2} , MJy steradian^{-1} or magnitudes arcsec^{-2} . If you have a surface brightness S_v in MJy steradian^{-1} , then you can use:

$$S_v[\text{Jy arcsec}^{-2}] = S_v[\text{MJy ster}^{-1}] \times 2.35 \times 10^{-5}.$$

If you have S_v in magnitudes arcsec^{-2} , you can simply use the formula and zero-points as given in the previous section for point sources.

Look-up Tables

In this section we provide look-up tables to facilitate rapid, approximate conversion between the different systems mentioned in the preceding section.

For both integrated source fluxes and surface brightnesses, we provide tables of conversions between systems at the wavelengths of the four commonly used photometric bands which cover the NICMOS operating waveband of 0.8–2.5 microns. We are adopting here the CIT system defined in Table 2.2.

By using Table 2.3 it is possible to estimate the CIT magnitude corresponding to any flux in Jy, by using the property that multiplying or dividing the flux by one hundred adds or subtracts five magnitudes.

Table A2.3: F_V to Magnitude Conversion

F_V [Jy]	I	J	H	K
10.0	5.88	5.56	4.98	4.48
8.0	6.12	5.80	5.22	4.72
6.0	6.44	6.11	5.53	5.04
5.0	6.63	6.31	5.73	5.23
4.0	6.88	6.55	5.97	5.48
3.0	7.19	6.86	6.29	5.79
2.5	7.39	7.06	6.48	5.99
2.0	7.63	7.30	6.73	6.23
1.5	7.94	7.62	7.04	6.54
1.25	8.14	7.81	7.24	6.74
1.0	8.38	8.06	7.48	6.98
0.8	8.62	8.30	7.72	7.22
0.6	8.94	8.61	8.03	7.54
0.5	9.13	8.81	8.23	7.73
0.4	9.38	9.05	8.47	7.98
0.3	9.69	9.36	8.79	8.29
0.25	9.89	9.57	8.98	8.49
0.2	10.13	9.8	9.23	8.73
0.15	10.44	10.12	9.54	9.04
0.125	10.64	10.31	9.74	9.24
0.1	10.88	10.56	9.98	9.48

Table A2.4: I- Band Flux Conversion

F_v [Jy]	I [mag]	F_λ [Wm ⁻² mm ⁻¹]	F_λ [W cm ⁻² μm ⁻¹]	F_λ [erg s ⁻¹ cm ⁻² Å ⁻¹]
2250	0.0	8.32x10 ⁻⁹	8.32x10 ⁻¹³	8.32x10 ⁻¹⁰
894	1.0	3.312x10 ⁻⁹	3.312x10 ⁻¹³	3.312x10 ⁻¹⁰
356	2.0	1.319x10 ⁻⁹	1.319x10 ⁻¹³	1.319x10 ⁻¹⁰
142	3.0	5.25x10 ⁻¹⁰	5.25x10 ⁻¹⁴	5.25x10 ⁻¹¹
56.4	4.0	2.09x10 ⁻¹⁰	2.09x10 ⁻¹⁴	2.09x10 ⁻¹¹
22.5	5.0	8.32x10 ⁻¹¹	8.32x10 ⁻¹⁵	8.32x10 ⁻¹²
8.94	6.0	3.312x10 ⁻¹¹	3.312x10 ⁻¹⁵	3.312x10 ⁻¹²
3.56	7.0	1.319x10 ⁻¹¹	1.319x10 ⁻¹⁵	1.319x10 ⁻¹²
1.42	8.0	5.25x10 ⁻¹²	5.25x10 ⁻¹⁶	5.25x10 ⁻¹³
0.564	9.0	2.09x10 ⁻¹²	2.09x10 ⁻¹⁶	2.09x10 ⁻¹³
0.225	10.0	8.32x10 ⁻¹³	8.32x10 ⁻¹⁷	8.32x10 ⁻¹⁴
0.0894	11.0	3.312x10 ⁻¹³	3.312x10 ⁻¹⁷	3.312x10 ⁻¹⁴
0.0356	12.0	1.319x10 ⁻¹³	1.319x10 ⁻¹⁷	1.319x10 ⁻¹⁴
0.0142	13.0	5.25x10 ⁻¹⁴	5.25x10 ⁻¹⁸	5.25x10 ⁻¹⁵
0.00564	14.0	2.09x10 ⁻¹⁴	2.09x10 ⁻¹⁸	2.09x10 ⁻¹⁵
0.00225	15.0	8.32x10 ⁻¹⁵	8.32x10 ⁻¹⁹	8.32x10 ⁻¹⁶
8.94x10 ⁻⁴	16.0	3.312x10 ⁻¹⁵	3.312x10 ⁻¹⁹	3.312x10 ⁻¹⁶
3.56x10 ⁻⁴	17.0	1.319x10 ⁻¹⁵	1.319x10 ⁻¹⁹	1.319x10 ⁻¹⁶
1.42x10 ⁻⁴	18.0	5.25x10 ⁻¹⁶	5.25x10 ⁻²⁰	5.25x10 ⁻¹⁷
5.64x10 ⁻⁵	19.0	2.09x10 ⁻¹⁶	2.09x10 ⁻²⁰	2.09x10 ⁻¹⁷
2.25x10 ⁻⁵	20.0	8.32x10 ⁻¹⁷	8.32x10 ⁻²¹	8.32x10 ⁻¹⁸
8.94x10 ⁻⁶	21.0	3.312x10 ⁻¹⁷	3.312x10 ⁻²¹	3.312x10 ⁻¹⁸
3.56x10 ⁻⁶	22.0	1.319x10 ⁻¹⁷	1.319x10 ⁻²¹	1.319x10 ⁻¹⁸
1.42x10 ⁻⁶	23.0	5.25x10 ⁻¹⁸	5.25x10 ⁻²²	5.25x10 ⁻¹⁹
5.64x10 ⁻⁷	24.0	2.09x10 ⁻¹⁸	2.09x10 ⁻²²	2.09x10 ⁻¹⁹
2.25x10 ⁻⁷	25.0	8.32x10 ⁻¹⁹	8.32x10 ⁻²³	8.32x10 ⁻²⁰
8.94x10 ⁻⁸	26.0	3.312x10 ⁻¹⁹	3.312x10 ⁻²³	3.312x10 ⁻²⁰

Table A2.5: J-band Flux Conversion

F_v [Jy]	J [mag]	F_λ [Wm ⁻² mm ⁻¹]	F_λ [Wcm ⁻² μm ⁻¹]	F_λ [erg cm ⁻² s ⁻¹ Å ⁻¹]
1670	0.0	3.21x10 ⁻⁹	3.21x10 ⁻¹³	3.21x10 ⁻¹⁰
665	1.0	1.28x10 ⁻⁹	1.28x10 ⁻¹³	1.28x10 ⁻¹⁰
265	2.0	5.08x10 ⁻¹⁰	5.08x10 ⁻¹⁴	5.08x10 ⁻¹¹
106	3.0	2.02x10 ⁻¹⁰	2.02x10 ⁻¹⁴	2.02x10 ⁻¹¹
42.0	4.0	8.06x10 ⁻¹¹	8.06x10 ⁻¹⁵	8.06x10 ⁻¹²
16.7	5.0	3.21x10 ⁻¹¹	3.21x10 ⁻¹⁵	3.21x10 ⁻¹²
6.65	6.0	1.28x10 ⁻¹¹	1.28x10 ⁻¹⁵	1.28x10 ⁻¹²
2.65	7.0	5.08x10 ⁻¹²	5.08x10 ⁻¹⁶	5.08x10 ⁻¹³
1.06	8.0	2.02x10 ⁻¹²	2.02x10 ⁻¹⁶	2.02x10 ⁻¹³
0.420	9.0	8.06x10 ⁻¹³	8.06x10 ⁻¹⁷	8.06x10 ⁻¹⁴
0.167	10.0	3.21x10 ⁻¹³	3.21x10 ⁻¹⁷	3.21x10 ⁻¹⁴
0.0665	11.0	1.28x10 ⁻¹³	1.28x10 ⁻¹⁷	1.28x10 ⁻¹⁴
0.0265	12.0	5.08x10 ⁻¹⁴	5.08x10 ⁻¹⁸	5.08x10 ⁻¹⁵
0.0106	13.0	2.02x10 ⁻¹⁴	2.02x10 ⁻¹⁸	2.02x10 ⁻¹⁵
0.00420	14.0	8.06x10 ⁻¹⁵	8.06x10 ⁻¹⁹	8.06x10 ⁻¹⁶
0.00167	15.0	3.21x10 ⁻¹⁵	3.21x10 ⁻¹⁹	3.21x10 ⁻¹⁶
6.65x10 ⁻⁴	16.0	1.28x10 ⁻¹⁵	1.28x10 ⁻¹⁹	1.28x10 ⁻¹⁶
2.65x10 ⁻⁴	17.0	5.08x10 ⁻¹⁶	5.08x10 ⁻²⁰	5.08x10 ⁻¹⁷
1.06x10 ⁻⁴	18.0	2.02x10 ⁻¹⁶	2.02x10 ⁻²⁰	2.02x10 ⁻¹⁷
4.20x10 ⁻⁵	19.0	8.06x10 ⁻¹⁷	8.06x10 ⁻²¹	8.06x10 ⁻¹⁸
1.67x10 ⁻⁵	20.0	3.21x10 ⁻¹⁷	3.21x10 ⁻²¹	3.21x10 ⁻¹⁸
6.65x10 ⁻⁶	21.0	1.28x10 ⁻¹⁷	1.28x10 ⁻²¹	1.28x10 ⁻¹⁸
2.65x10 ⁻⁶	22.0	5.08x10 ⁻¹⁸	5.08x10 ⁻²²	5.08x10 ⁻¹⁹
1.06x10 ⁻⁶	23.0	2.02x10 ⁻¹⁸	2.02x10 ⁻²²	2.02x10 ⁻¹⁹
4.20x10 ⁻⁷	24.0	8.06x10 ⁻¹⁹	8.06x10 ⁻²³	8.06x10 ⁻²⁰
1.67x10 ⁻⁷	25.0	3.21x10 ⁻¹⁹	3.21x10 ⁻²³	3.21x10 ⁻²⁰
6.65x10 ⁻⁸	26.0	1.28x10 ⁻¹⁹	1.28x10 ⁻²³	1.28x10 ⁻²⁰

Table A2.6: H-band Flux Conversion

F_v [Jy]	H [mag]	F_λ [Wm ⁻² μm ⁻¹]	F_λ [Wcm ⁻² mm ⁻¹]	F_λ [erg s ⁻¹ cm ⁻² Å ⁻¹]
980	0.0	1.08x10 ⁻⁹	1.08x10 ⁻¹³	1.08x10 ⁻¹⁰
390	1.0	4.3x10 ⁻¹⁰	4.3x10 ⁻¹⁴	4.3x10 ⁻¹¹
155	2.0	1.712x10 ⁻¹⁰	1.712x10 ⁻¹⁴	1.712x10 ⁻¹¹
61.8	3.0	6.814x10 ⁻¹¹	6.814x10 ⁻¹⁵	6.814x10 ⁻¹²
24.6	4.0	2.713x10 ⁻¹¹	2.713x10 ⁻¹⁵	2.713x10 ⁻¹²
9.8	5.0	1.08x10 ⁻¹¹	1.08x10 ⁻¹⁵	1.08x10 ⁻¹²
3.9	6.0	4.3x10 ⁻¹²	4.3x10 ⁻¹⁶	4.3x10 ⁻¹³
1.55	7.0	1.712x10 ⁻¹²	1.712x10 ⁻¹⁶	1.712x10 ⁻¹³
0.618	8.0	6.814x10 ⁻¹³	6.814x10 ⁻¹⁷	6.814x10 ⁻¹⁴
0.246	9.0	2.713x10 ⁻¹³	2.713x10 ⁻¹⁷	2.713x10 ⁻¹⁴
0.098	10.0	1.08x10 ⁻¹³	1.08x10 ⁻¹⁷	1.08x10 ⁻¹⁴
0.039	11.0	4.3x10 ⁻¹⁴	4.3x10 ⁻¹⁸	4.3x10 ⁻¹⁵
0.0155	12.0	1.712x10 ⁻¹⁴	1.712x10 ⁻¹⁸	1.712x10 ⁻¹⁵
0.00618	13.0	6.814x10 ⁻¹⁵	6.814x10 ⁻¹⁹	6.814x10 ⁻¹⁶
0.00246	14.0	2.713x10 ⁻¹⁵	2.713x10 ⁻¹⁹	2.713x10 ⁻¹⁶
9.8x10 ⁻⁴	15.0	1.08x10 ⁻¹⁵	1.08x10 ⁻¹⁹	1.08x10 ⁻¹⁶
3.9x10 ⁻⁴	16.0	4.3x10 ⁻¹⁶	4.3x10 ⁻²⁰	4.3x10 ⁻¹⁷
1.55x10 ⁻⁴	17.0	1.712x10 ⁻¹⁶	1.712x10 ⁻²⁰	1.712x10 ⁻¹⁷
6.18x10 ⁻⁵	18.0	6.814x10 ⁻¹⁷	6.814x10 ⁻²¹	6.814x10 ⁻¹⁸
2.46x10 ⁻⁵	19.0	2.713x10 ⁻¹⁷	2.713x10 ⁻²¹	2.713x10 ⁻¹⁸
9.8x10 ⁻⁶	20.0	1.08x10 ⁻¹⁷	1.08x10 ⁻²¹	1.08x10 ⁻¹⁸
3.9x10 ⁻⁶	21.0	4.3x10 ⁻¹⁸	4.3x10 ⁻²²	4.3x10 ⁻¹⁹
1.55x10 ⁻⁶	22.0	1.712x10 ⁻¹⁸	1.712x10 ⁻²²	1.712x10 ⁻¹⁹
6.18x10 ⁻⁷	23.0	6.814x10 ⁻¹⁹	6.814x10 ⁻²³	6.814x10 ⁻²⁰
2.46x10 ⁻⁷	24.0	2.713x10 ⁻¹⁹	2.713x10 ⁻²³	2.713x10 ⁻²⁰
9.8x10 ⁻⁸	25.0	1.08x10 ⁻¹⁹	1.08x10 ⁻²³	1.08x10 ⁻²⁰
3.9x10 ⁻⁸	26.0	4.3x10 ⁻²⁰	4.3x10 ⁻²⁴	4.3x10 ⁻²¹

Table A2.7: K-band Flux Conversion

F_v [Jy]	K [mag]	F_λ [Wm ⁻² mm ⁻¹]	F_λ [Wcm ⁻² mm ⁻¹]	F_λ [erg s ⁻¹ cm ⁻² Å ⁻¹]
620	0.0	3.84x10 ⁻¹⁰	3.84x10 ⁻¹⁴	3.84x10 ⁻¹¹
247	1.0	1.53x10 ⁻¹⁰	1.53x10 ⁻¹⁴	1.53x10 ⁻¹¹
98.3	2.0	6.09x10 ⁻¹¹	6.09x10 ⁻¹⁵	6.09x10 ⁻¹²
39.1	3.0	2.43x10 ⁻¹¹	2.43x10 ⁻¹⁵	2.43x10 ⁻¹²
15.6	4.0	9.66x10 ⁻¹²	9.66x10 ⁻¹⁶	9.66x10 ⁻¹³
6.20	5.0	3.84x10 ⁻¹²	3.84x10 ⁻¹⁶	3.84x10 ⁻¹³
2.47	6.0	1.53x10 ⁻¹²	1.53x10 ⁻¹⁶	1.53x10 ⁻¹³
0.983	7.0	6.09x10 ⁻¹³	6.09x10 ⁻¹⁷	6.09x10 ⁻¹⁴
0.391	8.0	2.43x10 ⁻¹³	2.43x10 ⁻¹⁷	2.43x10 ⁻¹⁴
0.156	9.0	9.66x10 ⁻¹⁴	9.66x10 ⁻¹⁸	9.66x10 ⁻¹⁵
0.0620	10.0	3.84x10 ⁻¹⁴	3.84x10 ⁻¹⁸	3.84x10 ⁻¹⁵
0.0247	11.0	1.53x10 ⁻¹⁴	1.53x10 ⁻¹⁸	1.53x10 ⁻¹⁵
0.00983	12.0	6.09x10 ⁻¹⁵	6.09x10 ⁻¹⁹	6.09x10 ⁻¹⁶
0.00391	13.0	2.43x10 ⁻¹⁵	2.43x10 ⁻¹⁹	2.43x10 ⁻¹⁶
0.00156	14.0	9.66x10 ⁻¹⁶	9.66x10 ⁻²⁰	9.66x10 ⁻¹⁷
6.20x10 ⁻⁴	15.0	3.84x10 ⁻¹⁶	3.84x10 ⁻²⁰	3.84x10 ⁻¹⁷
2.47x10 ⁻⁴	16.0	1.53x10 ⁻¹⁶	1.53x10 ⁻²⁰	1.53x10 ⁻¹⁷
9.83x10 ⁻⁵	17.0	6.09x10 ⁻¹⁷	6.09x10 ⁻²¹	6.09x10 ⁻¹⁸
3.91x10 ⁻⁵	18.0	2.43x10 ⁻¹⁷	2.43x10 ⁻²¹	2.43x10 ⁻¹⁸
1.56x10 ⁻⁵	19.0	9.66x10 ⁻¹⁸	9.66x10 ⁻²²	9.66x10 ⁻¹⁹
6.20x10 ⁻⁶	20.0	3.84x10 ⁻¹⁸	3.84x10 ⁻²²	3.84x10 ⁻¹⁹
2.47x10 ⁻⁶	21.0	1.53x10 ⁻¹⁸	1.53x10 ⁻²²	1.53x10 ⁻¹⁹
9.83x10 ⁻⁷	22.0	6.09x10 ⁻¹⁹	6.09x10 ⁻²³	6.09x10 ⁻²⁰
3.91x10 ⁻⁷	23.0	2.43x10 ⁻¹⁹	2.43x10 ⁻²³	2.43x10 ⁻²⁰
1.56x10 ⁻⁷	24.0	9.66x10 ⁻²⁰	9.66x10 ⁻²⁴	9.66x10 ⁻²¹
6.20x10 ⁻⁸	25.0	3.84x10 ⁻²⁰	3.84x10 ⁻²⁴	3.84x10 ⁻²¹
2.47x10 ⁻⁸	26.0	1.53x10 ⁻²⁰	1.53x10 ⁻²⁴	1.53x10 ⁻²¹

Table A2.8: Surface Brightness Conversion

mag / arcsec ²	I-Band		J-Band		H-Band		K-Band	
	Jy / arcsec ²	MJy / steradian	Jy / arcsec ²	MJy / steradian	Jy / arcsec ²	MJy / steradian	Jy / arcsec ²	MJy / steradian
0.0	0.6251	2.66x10 ⁴	0.4630	1.97x10 ⁴	0.2726	1.16x10 ⁴	0.1720	7320
1.0	0.2491	1.06x10 ⁴	0.1847	7860	0.1083	4610	0.0688	2930
2.0	0.0989	4210	0.0736	3130	0.0430	1830	0.0273	1160
3.0	0.0395	1680	0.0294	1250	0.0172	730	0.0109	462
4.0	0.0157	667	0.0117	496	0.0068	291	0.0043	184
5.0	0.0062	266	0.0046	197	0.0027	116	0.0172	732
6.0	0.0025	106	0.0018	78.6	0.0011	46.1	6.88x10 ⁻⁴	29.3
7.0	9.89x10 ⁻⁴	42.1	7.36x10 ⁻⁴	31.3	4.30x10 ⁻⁴	18.3	2.73x10 ⁻⁴	11.6
8.0	3.95x10 ⁻⁴	16.8	2.94x10 ⁻⁴	12.5	1.72x10 ⁻⁴	7.3	1.09x10 ⁻⁴	4.62
9.0	1.57x10 ⁻⁴	6.67	1.17x10 ⁻⁴	4.96	6.84x10 ⁻⁵	2.91	4.32x10 ⁻⁵	1.84
10.0	6.25x10 ⁻⁵	2.66	4.63x10 ⁻⁵	1.97	2.73x10 ⁻⁵	1.16	1.72x10 ⁻⁵	0.732
11.0	2.49x10 ⁻⁵	1.06	1.85x10 ⁻⁵	0.786	1.08x10 ⁻⁵	0.461	6.88x10 ⁻⁶	0.293
12.0	9.89x10 ⁻⁶	0.421	7.36x10 ⁻⁶	0.313	4.30x10 ⁻⁶	0.183	2.73x10 ⁻⁷	0.116
13.0	3.95x10 ⁻⁶	0.168	2.94x10 ⁻⁶	0.125	1.72x10 ⁻⁶	0.073	1.09x10 ⁻⁷	0.0462
14.0	1.57x10 ⁻⁶	0.0667	1.17x10 ⁻⁶	0.0496	6.84x10 ⁻⁷	0.0291	4.32x10 ⁻⁸	0.0184
15.0	6.25x10 ⁻⁷	0.0266	4.63x10 ⁻⁷	0.0197	2.73x10 ⁻⁷	0.0116	1.72x10 ⁻⁸	0.00732
16.0	2.49x10 ⁻⁷	0.0106	1.85x10 ⁻⁷	0.00786	1.08x10 ⁻⁷	0.00461	6.88x10 ⁻⁹	0.00293
17.0	9.89x10 ⁻⁸	0.00421	7.36x10 ⁻⁸	0.00313	4.30x10 ⁻⁸	0.00183	2.73x10 ⁻⁹	0.00116
18.0	3.95x10 ⁻⁸	0.00168	2.94x10 ⁻⁸	0.00125	1.72x10 ⁻⁸	7.3x10 ⁻⁴	1.09x10 ⁻⁹	4.62x10 ⁻⁴
19.0	1.57x10 ⁻⁸	6.67x10 ⁻⁴	1.17x10 ⁻⁸	4.96x10 ⁻⁴	6.84x10 ⁻⁹	2.91x10 ⁻⁴	4.32x10 ⁻¹⁰	1.84x10 ⁻⁴
20.0	6.25x10 ⁻⁹	2.66x10 ⁻⁴	4.63x10 ⁻⁹	1.97x10 ⁻⁴	2.73x10 ⁻⁹	1.16x10 ⁻⁴	1.72x10 ⁻¹⁰	7.32x10 ⁻⁵
21.0	2.49x10 ⁻⁹	1.06x10 ⁻⁴	1.85x10 ⁻⁹	7.86x10 ⁻⁵	1.08x10 ⁻⁹	4.61x10 ⁻⁵	6.88x10 ⁻¹¹	2.93x10 ⁻⁵
22.0	9.89x10 ⁻¹⁰	4.21x10 ⁻⁵	7.36x10 ⁻¹⁰	3.13x10 ⁻⁵	4.30x10 ⁻¹⁰	1.83x10 ⁻⁵	2.73x10 ⁻¹¹	1.16x10 ⁻⁵
23.0	3.95x10 ⁻¹⁰	1.68x10 ⁻⁵	2.94x10 ⁻¹⁰	1.25x10 ⁻⁵	1.72x10 ⁻¹⁰	7.3x10 ⁻⁶	1.09x10 ⁻¹¹	4.62x10 ⁻⁶
24.0	1.57x10 ⁻¹⁰	6.67x10 ⁻⁶	1.17x10 ⁻¹⁰	4.96x10 ⁻⁶	6.84x10 ⁻¹¹	2.91x10 ⁻⁶	4.32x10 ⁻¹²	1.84x10 ⁻⁶
25.0	6.25x10 ⁻¹¹	2.66x10 ⁻⁶	4.63x10 ⁻¹¹	1.97x10 ⁻⁶	2.73x10 ⁻¹¹	1.16x10 ⁻⁶	1.72x10 ⁻¹²	7.32x10 ⁻⁷
26.0	2.49x10 ⁻¹¹	1.06x10 ⁻⁶	1.85x10 ⁻¹¹	7.86x10 ⁻⁷	1.08x10 ⁻¹¹	4.61x10 ⁻⁷	6.88x10 ⁻¹³	2.93x10 ⁻⁷

Examples

1. Given a source with a flux of 0.9mJy at 1350Å, convert this flux to erg s⁻¹cm⁻²Å⁻¹. From section 3, Table 2.1, we see that the conversion constant β is 3×10^{-13} and the wavelength is $1350\text{Å} = 0.135\mu\text{m}$. Thus:

$$F_{\lambda} = 3 \times 10^{-13} \times 9 \times 10^{-4} / 0.135^2 = 1.48 \times 10^{-14} \text{erg s}^{-1} \text{cm}^{-2} \text{Å}^{-1}$$

2. Given a V magnitude of 15.6, and knowledge that V-K=2.5 in the UKIRT system, estimate the flux in Jy at K. Since V-K=2.5 we know that K=13.1. From Table 2.2, the zero-point flux in the UKIRT system for K is 657Jy. Thus the 2.2μm flux is:
Thus the 2.2μm flux is:
3. $F_V = 10^{-13.1/2.5} \times 657 = 3.8 \times 10^{-3} \text{Jy}$
4. Given a surface brightness of 21.1 magnitudes arcsec⁻² at J, convert this into Jy arcsec⁻². Taking the zero-point for the J band from Table 2.2, we determine that the surface brightness is:
5. $10^{-21.1/2.5} \times 1670 = 6.06 \times 10^{-6} \text{Jy arcsec}^{-2}$
6. Given a flux at 0.9μm of $2.3 \times 10^{-7} \text{Jy}$, estimate the I magnitude. $2.3 \times 10^{-7} \text{Jy}$ is less than $2.3 \times 10^{-1} \text{Jy}$ by three powers of a hundred, or 15 magnitudes. From Table 2.3 we see that 0.25Jy is equivalent to an I-band magnitude of 9.89. Thus 2.3×10^{-7} is roughly 15 magnitudes fainter than this, or of order I=24.9.

Infrared Line Lists

We present here lists of some of the more important atomic and molecular lines in the infrared. It is by no means exhaustive.

Table A2.9: Recombination Lines of Atomic Hydrogen: Paschen Series^a

Transition (N _u - N _l)	Vacuum Wavelength (microns)	Vacuum Frequency (cm ⁻¹)	I/I(Hbeta) T _e =N _e =10 ⁴
4-3	1.8756	5531.55	0.332
5-3	1.2822	7799.33	0.162
6-3	1.0941	9139.8	0.0901
7-3	1.0052	9948.1	

a. Intensities from Hummer & Storey, MNRAS 224, 801.

Table A2.10: Recombination Lines of Atomic Hydrogen: Brackett Series

Transition (N_u-N_l)	Vacuum Wavelength (microns)	Frequency (cm^{-1})	$I/(H\beta)$ $T_e=10^4$
5-4	4.5225	2467.765	0.0777
6-4	2.6259	3808.25	
7-4	2.1661	4616.61	0.0275
8-4	1.9451	5141.14	0.0181
9-4	1.8181	5500.8	0.0126
10-4	1.7367	5758.1	0.00909
11-4	1.6811	5948.45	0.00679
12-4	1.6412	6093.22	0.00521
13-4	1.6114	6205.9	0.00409
14-4	1.5885	6295.3	0.00327
15-4	1.5705	6367.4	0.00266
16-4	1.5561	6426.4	0.00220
17-4	1.5443	6475.3	0.00184
18-4	1.5346	6516.3	0.00156
19-4	1.5265	6551.0	0.00133
20-4	1.5196	6580.7	0.00116
series limit	1.459	6855.	

Table A2.11: HeI and HeII Lines

ID	Transition	λ (μm)
HeI	7F-3D,3Fo-3D	1.0031
HeI	7F-3D,1Fo-1D	1.0034
HeII	14-6	1.0049
HeII	5-4	1.0133
HeI	6D-3P,3dD-3Po	1.0314
HeII	13-6	1.0422
HeI	6S-3P,3S-3Po	1.0668
HeI	2P-2S,3Po-3S,GU=3	1.0832
HeI	2P-2S,3Po-3P,GU=1	1.0832
HeI	2P-2S,3Po-3S,GU=5	1.0833
HeI	2P-2S,3Po-3S,GU=9	1.0833
HeI	6P-3D,1Po-1d	1.0905
HeI	6F-3D,3Fo-3D	1.0916
HeI	6F-3D,1Fo-1D	1.0920
HeII	12-6	1.0938
HeI	6P-3D,3Po-3D	1.0997
HeI	5P-3S,1Po-1S	1.1016
HeI	6D-3P,1D-1Po	1.1048
HeII	7LIMIT	1.1164
HeI	6S-3P,1S-1Po	1.1229
HeII	7-5	1.1628
HeII	11-6	1.1677
HeI	5D-3P,3D-3Po	1.1972
HeII	21-7	1.2256
HeII	22-7	1.2418
HeI	4P-3S,3Po-3S	1.2531
HeII	20-7	1.2719
HeI	5P-3D,1Po-1D	1.2759
HeI	5F-3D,3Fo-3D	1.2789
HeII	10-6	1.2817
HeI	5S-3P,3S-3Po	1.2850

Table A2.11: HeI and HeII Lines

ID	Transition	λ (μm)
HeII	19-7	1.2914
HeI	5D-3P,1D-1Po	1.2971
HeI	5F-3D,1Fo-1D	1.2976
HeI	5P-3D,3Po-3D	1.2988
HeII	18-7	1.3150
HeI	5S-3P,1S-1Po	1.3415
HeII	17-7	1.3442
HeII	15-7	1.4273
HeII	8LIMIT	1.4578
HeII	9-6	1.4765
HeII	14-7	1.4882
HeI	4P-3S,1Po-1S	1.5088
HeII	13-7	1.5719
HeII	25-8	1.6241
HeII	24-8	1.6400
HeII	23-8	1.6584
HeII	22-8	1.6799
HeII	12-7	1.6926
HeI	4D-3P,3D-3Po	1.7007
HeII	21-8	1.7053
HeII	20-8	1.7355
HeII	19-8	1.7717
HeII	18-8	1.8167
HeII	9LIMIT	1.8450
HeI	4P-3D,1Po-1D	1.8561
HeII	6-5	1.8639
HeI	4F-3D,3Fo-3D	1.8691
HeI	4F-3D,1Fo-1d	1.8702
HeII	17-8	1.8725
HeII	8-6	1.8753
HeII	11-7	1.8770

Table A2.11: HeI and HeII Lines

ID	Transition	λ (μm)
HeI	8S-4P,3S-3Po	1.9068
HeI	4D-3P,1D-1Po	1.9094
HeI	4P-3D,3Po-3D	1.9548
HeII	15-8	2.0379
HeI	6P-4S,3Po-3S	2.0430
HeI	2P-2S,1Po-1S	2.0587
HeI	4S-3P,3S-3Po	2.1126
HeI	3pP-4sS	2.1132
HeI	4S-3P,1S-1Po	2.1138
HeII	25-9	2.1195
HeII	24-9	2.1469
HeI	7S-4P,3S-3Po	2.1500
HeI	7F-4D,3Fo-3D	2.1614
HeI	4dD-7fF	2.1617
HeI	7F-4D,1Fo-1D	2.1623
HeII	14-8	2.1653
HeI	4-7	2.166
HeII	23-9	2.1786
HeI	7D-4P,1D-1Po	2.1847
HeII	10-7	2.1891
HeII	22-9	2.2155
HeI	7S-4P,1S-1Po	2.2290
HeII	21-9	2.2601
HeII	10LIMIT	2.2778
HeI	6P-4S,1Po-1S	2.3069
HeII	20-9	2.314
HeII	13-8	2.348
HeII	19-9	2.3788
HeII	18-9	2.4606
HeI	6D-4P,3D-3Po	2.4734

Table A2.12: CO Vibration-rotation Band-heads^a

Transition (N_u-N_l)	$^{12}\text{C}^{16}\text{O}$ Vacuum Wavelength (microns)	Frequency (cm^{-1})	$^{13}\text{C}^{16}\text{O}$ Vacuum Wavelength (microns)	Frequency (cm^{-1})
2-0	2.2935	4360.1	2.3448	4264.7
3-1	2.3227	4305.4	2.3739	4212.4
4-2	2.3535	4250.8	2.4037	4160.3
5-3	2.3829	4196.5	2.4341	4108.3
6-4	2.4142	4142.2	2.4652	4056.4
7-5	2.4461	4088.2	2.4971	4004.7
8-6	2.4787	4034.3		
9-7	2.5122	3980.5		
3-0	1.5582	6417.8		
4-1	1.5780	6337.2		
5-2	1.5982	6257.2		
6-3	1.6187	6177.7		
7-4	1.6397	6098.8		
8-5	1.6610	6020.5		

a. All of the $\Delta v = 2$ bandheads occur near $J=50$.

Table A2.13: Important H₂ Lines^a

Line Name		Wavel (μm)	Freq (cm^{-1})	g(J)	Eupper (K)	A ($10\text{e}^{-7}\text{s}$)	LTE I(line)/I(1-0S(1))			
							1000K	2000K	3000K	4000K
1-0	S(0)	2.2235	4497.41	5	6471	2.53	0.27	0.21	0.19	0.19
1-0	S(1)	2.1218	4712.91	21	6956	3.47	1.00	1.00	1.00	1.00
1-0	S(2)	2.0338	4917.01	9	7584	3.98	0.27	0.37	0.42	0.44
1-0	S(3)	1.9576	5108.40	33	8365	4.21	0.51	1.02	1.29	1.45
1-0	S(4)	1.8920	5282.52	13	9286	4.19	0.082	0.26	0.39	0.47
1-0	S(5)	1.8358	5447.25	45	10341	3.96	0.096	0.52	0.91	1.21
1-0	S(6)	1.7880	5592.9	17	11522	3.54	0.010	0.10	0.21	0.31
1-0	S(7)	1.7480	5720.8	57	12817	2.98	0.008	0.15	0.40	0.65
1-0	S(8)	1.7147	5831.9	21	14221	2.34	0.001	0.022	0.074	0.14
1-0	S(9)	1.6877	5925.1	69	15722	1.68	0.025	0.11	0.22	
1-0	S(10)	1.6665	6000.0	25	17311	1.05	0.003	0.015	0.034	
1-0	S(11)	1.6504	6059.0	81	18979	0.53	0.002	0.014	0.037	
1-0	Q(1)	2.4066	4155.25	9	6149	4.29	1.05	0.70	0.61	0.57
1-0	Q(2)	2.4134	4143.47	5	6471	3.03	0.30	0.23	0.22	0.21
1-0	Q(3)	2.4237	4125.87	21	6956	2.78	0.70	0.70	0.70	0.70
1-0	Q(4)	2.4375	412.57	9	7586	2.65	0.15	0.21	0.23	0.24
1-0	Q(5)	2.4548	4073.72	33	8365	2.55	0.24	0.49	0.62	0.70
1-0	Q(6)	2.4756	4039.5	13	9286	2.45	0.036	0.12	0.17	0.21
1-0	Q(7)	2.5001	3999.9	45	10341	2.34	0.042	0.11	0.40	0.53
3-2	S(0)	2.5014	3997.73	5	17387	3.88	0.001	0.007	0.016	
3-2	S(1)	2.3864	4190.33	21	17818	5.14	0.006	0.035	0.087	
3-2	S(2)	2.2870	4372.49	9	18386	5.63	0.002	0.014	0.037	
3-2	S(3)	2.2014	4542.57	33	19086	5.63	0.006	0.043	0.12	
3-2	S(4)	2.1280	4699.32	13	19912	5.22	0.001	0.012	0.036	
3-2	S(5)	2.0656	4841.3	45	20856	4.50	0.003	0.023	0.088	
3-2	S(6)	2.0130	4967.7	17	21911	3.57	0.006	0.021		
3-2	S(7)	1.9692	5078.1	57	23069	2.54	0.001	0.010	0.038	
4-3	S(3)	2.3446	4265.4	21						
4-3	S(4)	2.2668	4411.5	9						

Table A2.13: Important H₂ Lines^a (Continued)

Line Name		Wavel (μm)	Freq (cm^{-1})	g(J)	Eupper (K)	A ($10\text{e}^{-7}\text{s}$)	LTE I(line)/I(1-0S(1))			
							1000K	2000K	3000K	4000K
4-3	S(5)	2.201	4543.5	33						
5-4	S(5)	2.3555	4245.4	45						
5-4	S(7)	2.2510	4442.5	57						
2-0	S(0)	1.2383	8075.3	5	12095	1.27	0.001	0.012	0.028	0.043
2-0	S(1)	1.1622	8604.2	21	12550	1.90	0.004	0.061	0.15	0.23
2-0	S(2)	1.1382	8785.5	9	13150	2.38	0.001	0.025	0.070	0.12
2-0	S(3)	1.1175	8948.6	33	13890	2.77	0.002	0.074	0.24	0.43
2-0	S(4)	1.0998	9092.4	13	14764	3.07	0.021	0.078	0.15	
2-0	S(5)	1.0851	9215.5	45	15763	3.28	0.001	0.048	0.21	0.44
2-9	Q(1)	1.2383	8075.3	9	11789	1.94	0.003	0.037	0.082	0.12
2-0	Q(2)	1.2419	8051.9	5	12095	1.38	0.001	0.012	0.029	0.045
2-0	Q(3)	1.2473	8017.2	21	12550	1.29	0.002	0.039	0.098	0.24
2-0	Q(4)	1.2545	7971.1	9	13150	1.27	0.001	0.012	0.033	0.056
2-0	Q(5)	1.2636	7913.3	33	13890	1.23	0.001	0.024	0.093	0.17
2-0	O(2)	1.2932	7732.6	1	11635	3.47	0.001	0.008	0.016	0.024
2-0	O(3)	1.3354	7488.3	9	11789	1.61	0.003	0.028	0.063	0.094
2-0	O(4)	1.3817	7237.5	5	12095	1.03	0.001	0.008	0.020	0.030
2-0	O(5)	1.4322	6982.5	21	12550	0.698	0.001	0.018	0.046	0.074

a. Energy levels calculated using Dabrowski & Herzberg, Can J Phys 62, 1639 (1984). Einstein coefficients from Turner et al. ApJ Suppl 35, 281 (1977).

Bright Object Mode

In This Appendix...

Bright Object Mode / 275

Bright Object Mode



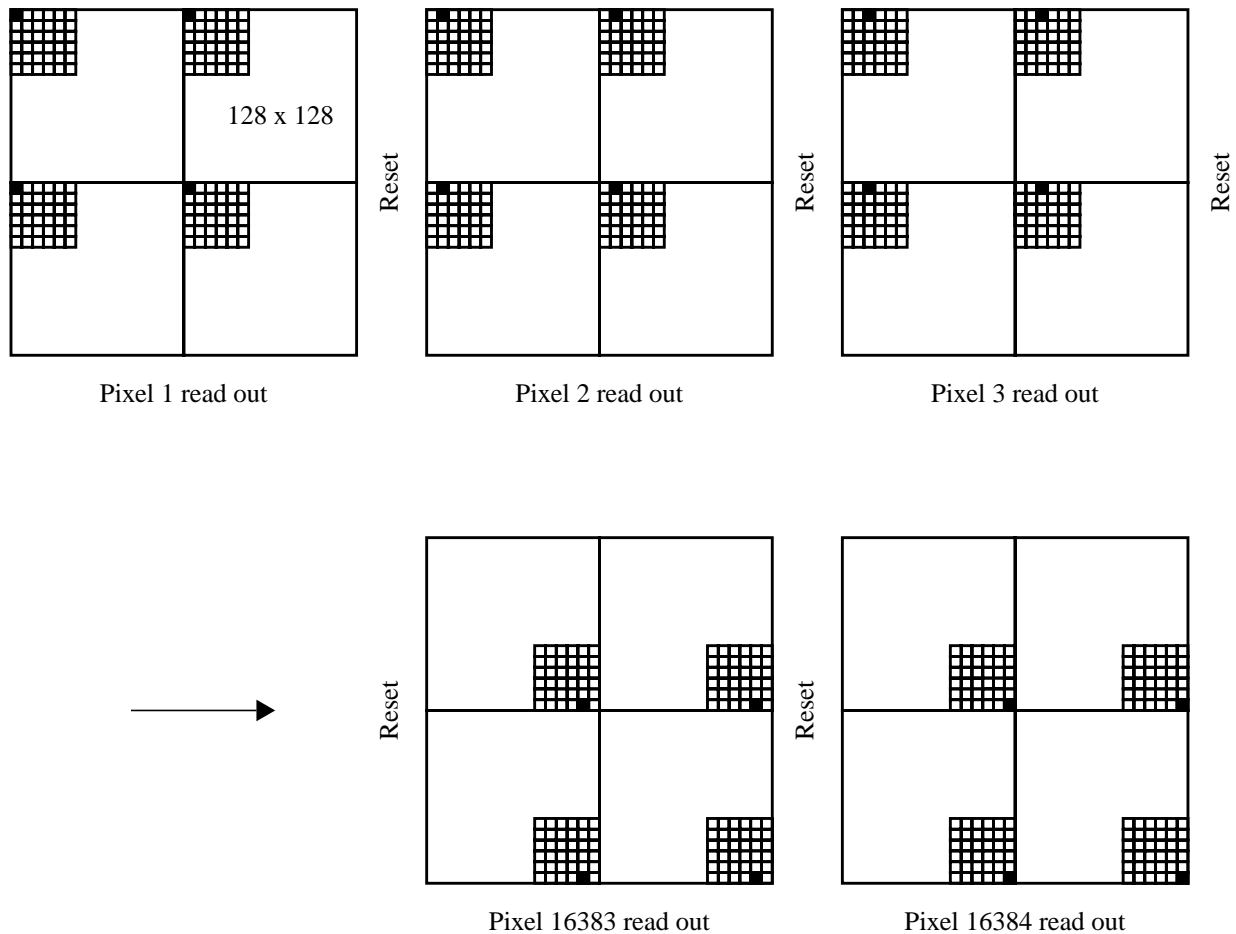
The use of this read-out mode is recommended only for the purpose of determining the centroid of very bright targets which must be acquired under the coronagraphic spot, when any other configuration (e.g., MULTIACCUM or ACCUM with narrow-band filters) saturates the detector. Any other use is strongly discouraged, because of the strong non-linearity of this mode.

The time taken to read through a quadrant on the array sets a fundamental limit on the fastest electron collection rate which can be achieved by resetting all the pixels. An inherent consequence of the methods of operating the NICMOS array detectors in the ACCUM and MULTIACCUM modes is therefore that there is a minimum possible exposure time, ~ 0.6 seconds (0.203 for MULTIACCUM), set by the time required to read the array. For a very bright object, such as the disk of Jupiter, the time between the reset of a pixel, and its final read is sufficiently long that the pixel saturates. Although the detector arrays are multiplexed by division into four quadrants, each pixel in a 128 x 128 pixel quadrant must be sampled in some order (note that there is no transfer of charge as is done in a CCD).

The solution adopted to this problem for NICMOS is the provision of a *bright object mode* which enables targets to be observed which are ~600 times brighter than is possible in the other modes without saturating. In BRIGHTOBJ mode, an ACCUM sequence of operations is performed on *one* pixel in each quadrant at a time. That is, the pixel is reset, read, integrated, and read again with the difference between the final and initial

readouts being stored as the measured signal and the interval between the reads being the exposure time. This process is repeated sequentially for all pixels in each quadrant. Users can think of this as integrating on a single pixel at a time. The smallest integration time which can be used is 1.024 milliseconds. Figure 3.1 illustrates the operation of bright object mode. Initially the detector is reset and the first pixel (solid shading) in each quadrant is read. A reset is then made and the second pixel in each quadrant is read. The process continues until all 16,384 pixels in each quadrant have been read.

Figure A3.1: Bright Object Mode Operation



The time required to take a BRIGHTOBJ mode exposure can be rather long. Since photons are only collected in one pixel per quadrant at a time, the time associated with obtaining the frame is $10.0 + (EXPTIME \times 16384)$ where *EXPTIME* is the integration time per pixel (i.e. the observation time is approximately $(128^2) \times$ the exposure time). For example, if an integration time of 0.1 seconds is used to observe a bright target then the actual time required to complete the observation

would be around 27 minutes! This means that allowing for acquisition time only two such exposures could be obtained in a single target visibility period. However, it is not always so serious. In the case of Jupiter for example the integration times required per pixel are only of the order of milliseconds and so the total integration time will only be around 20 seconds.

The longest exposure time which is possible in BRIGHTOBJ mode is 0.261 seconds, requiring 4278 seconds in total. Thus it is possible, in the worst case, for a single BRIGHTOBJ mode exposure to use more than an orbit. In general observers are strongly advised to consider the trade-off between relatively long BRIGHTOBJ mode exposures (which take the longest time) and short ACCUM mode exposures (perhaps using a narrow filter).

The advantage of this mode of operation is the ability to acquire objects significantly brighter than the normal saturation limit of the detector.

The disadvantages are several:

- The zeropause in this mode is strongly non-linear, such non-linearity has not been characterized (nor are there plans to do so). Observations obtained with this mode are not calibrated and possibly not easily calibratable).
- Some observations will take a long time. BRIGHTOBJ mode exposures are therefore very sensitive to the quality of the pointing of HST. They should not be obtained using GYRO guiding mode. In addition, if the object changes (planetary rotation) or if the telescope pointing changes it will affect different parts of the image differently.
- The D.C. offset of the detector output is not removed in this mode of operation. In general, the signal is very high and the offset does not matter. In some cases it will and this can be a detriment to the signal accuracy.
- There is also no cosmic ray correction or saturation detection in this mode of operation. Although they are still susceptible to cosmic rays, events should be very rare as the integration time *per pixel* is very short.

Index

A

ACCUM 15, 30
 dark current calibration 138
 data format 191
 function of 128
 minimum time 130
 mode, described 28, 130
 multiple reads 130
accumulate mode, see "ACCUM"
accuracy
 expected 195
ACQ 29, 31, 77, 79
 data format 191
 function of 128
 mode, described 139
active control law 27
afterimages 66
amplifier glow 111, 138
 described 123
 non-linearity 123
aperture
 defining 103
 NIC1 through NIC3-FIX 104
 NIC2-ACQ 78
 NIC2-CORON 77, 78
archive
 calibrated data 183
 reference files 184
array
 comparison to CCD 30
 dataset 191
 read 129
 reset 129
 TIME 193

array reset 129
artifacts
 amplifier glow 123
 shading 121
ASCS (Aft Shroud Cooling System)
 see also "cooling system"
associations 165, 184, 185
 datasets 184
atomic lines 266
attached parallel 31

B

background 13, 18
 ground-based 67
 infrared 67
 low sky 72
 radiation 96
 in exposure calculations 146
 spectroscopy 96
 stability 197
 thermal 67, 111, 146, 159, 196
 zodiacal 68, 146
 zodiacal light 67
bad pixels
 detector 111
bandpass
 see "filter"
Becklin-Neugebauer object 50
bleeding 30
breathing 64
bright object limitations 65
bright object mode, see "BRIGHTOBJ"
bright targets 79
BRIGHTOBJ 29

- calibration of mode 16
- data format 191
- exposure times 276
- function of 128
- mode, described 275

C

calibration

- activities 197
- calnica 187
- calnicb 190
- coronagraphy 197
- cycle 10 program 197
- cycle 7 goals 197
- described 183
- detector performance 197
- expected accuracy 195
- photometric 197
- point spread function 197
- reference files 184
- software 187

- calnica 187

- calnicb 190

camera

- attached parallel 31, 32
- changing, overhead 157
- field of view 23
- filters 40
- focus 55
- image quality 55
- orientation 24
- resolution 23
- spatial resolution
 - NIC1 24
 - NIC2 24
 - NIC3 24
- spectroscopy, camera 3 93

- camera 1 through camera 3

- see "camera" and "filter"

CCD

- compared to NICMOS array 30

- CELESTIAL 169, 172

- chop 164, 165, 185

- overhead 157

- patterns

- ONE-CHOP 171

- TWO-CHOP 171

- CO lines 266

- cold baffling 75

- cold pixels 124

- combined patterns

- SPIRAL-DITH-CHOP 172

- XSTRIP-DITH-CHOP 172

- YSTRIP-DITH-CHOP 172

- confocal 19

- continuous viewing zone 72

- conversion tool 255

- cooling system 3, 17, 20, 25

- aft shroud cooling system 27

- bayonet couplings 26

- capillary pumped loop 26

- circulator loop 25, 26, 27

- circulator pump 27

- compressor pump 26

- cooling coil 27

- cryocooler

- electronic support module 25, 27

- flex lines 26, 27

- heat exchanger 25, 26, 27

- multi-layer insulation

- power conversion electronics

- coordinate system

- NICMOS 104, 105

- coronagraphy 18, 156

- coronagraphic hole 77

- coronagraphic mask 24

- expected accuracy 197

- target acquisition

- overhead 157

- coronagraphy

- aperture 104

- cold mask 18

- coronagraphic hole 14

- image contrast, PSF centering 81

- observations 15, 16

- occulting spot 18

- target acquisition 139

- cosmic rays 14, 65, 66

- effect 65

- uncertainty 196
- CPL 27
- CPL (Capillary Pumped Loop)
 - see also "cooling system"
- cryocooler
 - see also "cooling system" 26
- CVZ
 - see "continuous viewing zone"
- Cycle 7
 - calibration goals 197

D

- dark current 111, 148
 - bump 111, 112
 - calibration in ACCUM or MULTIACCUM 138
 - detector 12, 28, 111
 - exposure times 139
- data
 - associations 184
 - calibration process 183
 - data negative limit 78
 - dataset 185
 - dataset structure 191
 - described 184, 191
 - error array 192
 - format 191
 - integration time array 193
 - quality 192
 - readout, overhead 157
 - samples array 192
 - science image 192
- dataset 185
- detector
 - array reset 129
 - arrays 107, 119
 - artifacts 121
 - bad pixels 111
 - bias 129
 - bright object limitations 29
 - characteristics 110
 - dark current 12, 28, 111, 138, 148, 197
 - described 28, 107
 - DQE 12, 111
 - dynamic range 29, 111, 120

- flat fields 197
- HgCdTe 28, 109
- linearity 111, 120
- non-destructive read 30
- non-linearity 29
- operations 28
- photovoltaic 107
- quadrants 107
- quantum efficiency 111
- readnoise 111, 119
- readout modes 28, 127
- readout noise 12, 29
- response 111, 120
- saturation 111, 120
- shading 30, 138, 197
- temperature 12, 27
 - stability 198
- throughput 49
- dewar 19, 21, 22, 25, 27
 - aft end 19, 21
 - cold mask 63
 - shifts 64
 - wiggling 64
 - cooling coil 19
 - cryogenic liquid 25
 - deformation 12, 19
 - fore end 19
 - inner shell 20
 - optical baffles 19
 - solid nitrogen 19, 21
 - thermal short 11, 20
- diffraction
 - rings 63
 - spikes 63
- diffraction limited 23, 39
- dispersion direction 99
- dither 14, 164, 165, 185
 - patterns 15
 - SPIRAL-DITH 170
 - SQUARE-WAVE-DITH 170
 - XSTRIP-DITH 170
 - YSTRIP-DITH 170
- documentation
 - World Wide Web 10
- DQE 114, 144, 203

DROP-TO-GYRO 157

dynamic range
detector 111

E

earthshine 72

electronic bars 124

emission lines
exposure times 147

emissivity 70

encircled energy 13, 61

epsilon diagrams 96

error array 191
described 192

ESM (Electronic Support Module)
see also "cooling system" 25

ETC
see "exposure time calculator"

exclusion

F164N, camera 3 244

F175W, camera 3 246

F187N, camera 3 247

F190N, camera 3 248

F196N, camera 3 249

F200N, camera 3 250

F212N, camera 3 251

F215N, camera 3 252

F222M, camera 3 253

F240M, camera 3 254

grisms 96–??

polarizers 88–??

exposure 143, 184, 185

see "data" and "imaging"

exposure time calculator 143, 152

extended objects 144

point sources 144

signal to noise 145

exposure times

background radiation 145

BRIGHTOBJ 276

calculating 149

dark current 139

emission line contribution 147

instrument parameters 149

instrumental factors 145

signal-to-noise, calculating 147

F

F090M through F237M
see "filter"

FAST

readout mode 138

readout mode, described 129

FET

see "field effect transistor"

FGS 24

field effect transistor 108

field of view

cameras 23

field offset mirror

optical path 22

PSF 64

file

data formats 191

filter 12

available, list of 40

bandpasses 42, 44, 46

camera 1 41

camera 2 43

camera 3 45

described 23, 40

F090M, camera 1 205

F095N, camera 1 206

F097N, camera 1 207

F108N, camera 1 208

F108N, camera 3 239

F110M, camera 1 209

F110W, camera 1 210

F110W, camera 3 240

F113N, camera 1 211

F113N, camera 3 241

F11W, camera 2 222

F140W, camera 1 212

F145M, camera 1 213

F150W, camera 3 242

F160W, camera 1 214

F160W, camera 2 223

F160W, camera 3 243

F164N, camera 1 215

F164N, camera 3 244

F165M, camera 1 216
 F165M, camera 2 224
 F166N, camera 1 217
 F170M, camera 1 218
 F171M, camera 2 225
 F175W, camera3 246
 F180M, camera 2 226
 F187N, camera 1 219
 F187N, camera 2 227
 F187N, camera 3 247
 F187W, camera 2 228
 F190N, camera 1 220
 F190N, camera 2 229
 F190N, camera 3 248
 F196N, camera 3 249
 F200N, camera 3 250
 F204M, camera 2 230
 F205W, camera 2 231
 F207M, camera 2 232
 F212N, camera 2 233
 F212N, camera 3 251
 F215N, camera 2 234
 F215N, camera 3 252
 F216N, camera 2 235
 F222M, camera 2 236
 F222M, camera 3 253
 F237M, camera 2 237
 F240M, camera 3 254
 filter wheel 39
 G141 99
 G206 99
 leak 47
 nomenclature 40
 polarimetry 88
 sensitivities 47
 sensitivity curves, polarizers 88
 sensitivity parameters 150–152
 spectroscopy 40, 96
 transmission 146
 filters 39
 FITS
 NICMOS data format 191
 flatfield
 color dependant 52
 peak-to-peak variation 114

 response 113, 117, 118
 sensitivity variations 14
 flexible image transport system 186
 flux
 Jansky 5, 258
 magnitude
 systems 256
 magnitudes
 zero point 72
 standard stars 48
 unit conversion 72, 258
 examples 266
 units 5, 72, 255, 258
 focus
 camera 1 55
 camera 2 55
 history 53
 NIC3 20
 out-of-focus operations 60
 pupil alignment mechanism 52
 FOM 179
 see "field offset mirror"
 FOS 20

G

GASP
 Guide Star Astrometric Support Package
 31
 ghosts 66
 glint 76, 83
 glow
 amplifier 123
 grisms 14, 24
 available 45
 background radiation 146
 described 93
 resolving power 18
 spectroscopy 18, 93
 grot 125
 guide star
 acquisition overhead 156
 reacquisition overhead 156
 GYRO 179
 gyros 157, 179

H

helium lines 266
 Help Desk
 contacting 9
 history 11
 HOST (HST Orbital Systems Test) 27
 hot pixels 65, 124
 hydrogen lines 266

I

IDT "Instrument Development Team" iii
 image
 DQ 192
 ERR 192
 quality 12, 55
 SAMP 192
 SCI 192
 science 191
 strehl ratios 55
 imaging
 described 17, 103
 filters 40
 infrared 18
 polarimetry 18
 sensitivity limits 18
 instrument 104
 camera orientation 24
 coordinate system 104
 design 20
 F ratio 23
 field divider 23
 field of view 23
 field offset mirror 22
 filters 5, 12
 optical train 52
 optical train. 23
 optics 22
 overview 20
 pixel Size 23
 pupil alignment mechanism 22
 setup time, overhead 156
 integration time array 191
 described 193
 intrapixel sensitivity 49

IPPPSSOOT 185
 IRAF 184, 185

J

Jansky 5
 see also "flux"

L

leaks
 filters 47
 linearity 120
 detector 111
 lines
 atomic 266
 molecular 266
 LOW-SKY 72
 background option 72

M

magnitude
 CIT system 259
 flux conversion 258
 infrared system 256
 UKIRT system 259
 zero points 259
 map patterns
 SPIRAL-MAP 173
 mapping 165
 MLI (Multi-Layer Insulation)
 see also "cooling system"
 modes 31
 ACCUM 128, 130
 ACQ 31, 128
 BRIGHTOBJ 128, 129
 detector readout 28, 127
 INT-ACQ 31, 80
 mode-2 acquisition 78, 139
 MULITACCUM 128
 MULTIACCUM 127, 129, 133
 RAMP 128, 129
 molecular lines 266
 mosaic 164
 MULTIACCUM 14, 15, 29, 30, 65
 dark current calibration 138

- data format 193
- dynamic range 133
- function of 128
- mode, described 28, 133
- SAMP-TIME 133
- multi-object spectroscopy 94
- multiple accumulate mode, see "MULTI-ACCUM"
- multiple initial and final reads 131, 145, 148

N

- NCC (NICMOS CryoCooler)
 - see also "cooling system"
- NCS 21
- NCS (NICMOS Cooling System)
 - see also "cooling system" 3
- NEXP 168, 190
- NIC1 11, 13, 15, 55
 - encircled energy 55
 - optimal focus 55
- NIC1 through NIC3-FIX
 - see "aperture" 104
- NIC2 11, 13, 15, 55
 - encircled energy 55
- NIC3 11, 13, 15
 - best focus 60
 - campaigns 20
 - PSF 62
 - vignetting 62
- nicmos cooling system 25
- nicmos cryocooler
- NICMOS-ORIENT 105
- NIC-SPIRAL-DITH 169
- nitrogen
 - triple point 19
- Node 1 120
- Node 2 120
- non-destructive read 127
- non-destructive readout 130, 133
- NREAD 30, 130
- NSAMP 133
- nyquist sampling 63

O

- observation
 - attached parallel 31
 - coronagraphic, planning 84
 - grism, planning 100
 - planning 33
 - polarimetry, planning 91
- observing patterns
 - predesigned 169
 - NIC-MAP 169
 - NIC-ONE-CHOP 169
 - NIC-ONE-SKY-CHOP 169
 - NIC-SPIRAL-DITH 169
 - NIC-SPIRAL-DITH-CHOP 169
 - NIC-SPIRAL-DITH-SKY-CHOP 169
 - NIC-SPIRAL-MAP 169
 - NIC-SQUARE-WAVE-DITH 169
 - NIC-TWO-CHOP 169
 - NIC-TWO-SKY-CHOP 169
 - NIC-XSTRIP-DITH 169
 - NIC-XSTRIP-DITH-CHOP 169
 - NIC-XSTRIP-DITH-SKY-CHOP 169
 - NIC-YSTRIP-DITH 169
 - NIC-YSTRIP-DITH-CHOP 169
- OFFSET 178
- on-board acquisition 31
- operating mode
 - overheads 157
- operating temperature 4
- optical baffles 125
- optical elements
 - grisms 93
- optical telescope assembly
 - breathing 64
- optics
 - astigmatism 63
 - coma 63
 - dewar 22
 - elements 39
 - emissivity 70
 - filters 40
 - grisms 45
- OPUS
 - see "calibration" and "pipeline" 183
- orbits

- required, calculating 159
- time requests 155
- ORIENT 105
- orientation
 - described 105
- OTA
 - see "optical telescope assembly"
- out-of-band leaks 146
- overhead 155
 - coronagraphy 159
 - example, polarimetry 159
 - examples 159
 - in observations 155
 - instrument specific 156
 - NICMOS specific 156
 - observatory level 156

P

- paint flakes
 - see "grot"
- PAM 11, 20, 52
 - see "pupil alignment mechanism"
- parallels
 - attached 31
- PATTERN 178
- pattern parameter form 164
- PCE (Power Conversion Electronics)
 - see also "cooling system"
- persistence 30
 - cosmic ray 65, 66, 83, 145
 - cosmic-ray 14
 - photon 14, 65
- photodiode 108
- photometric stability 49
- photometry
 - expected accuracy 197
 - Johnson's system 256
 - photometric systems 73
 - red source 50
 - sources with extreme colors 49
 - stability 49
 - Vega 256
 - young stellar objects 50
- photon-limited 144
- pipeline 183, 187

- calibration process 183
- pointing
 - HST 15
- polarimetry 18
 - example 159
 - expected accuracy 197
 - filters 40
 - spectral coverage 40
- polarizers 24
- POS-TARG 103, 104, 168, 169, 172
- product 185
- proposal
 - instructions 9
 - overheads, exposure 156
 - Phase I 4
 - Phase II 4
 - Phase II Proposal Instructions 4
 - submission process 9
 - unsupported modes 16
- PSF 63, 149
 - centering 81
 - field dependence 64
 - field offset mirror 64
 - NIC3 15
 - nyquist sampling 63
 - subtraction 14
 - temporal dependence 64
 - temporal variations 81
 - TinyTIm 55
- pupil alignment mechanism 11, 19
 - focus 52
 - NIC3 focus position 13
 - optical path 22

Q

- quality
 - image 55
- quality flags 191

R

- RAMP 29
 - data format 191
 - function of 129
- RE-ACQ 179

- re-acquisitions 156
- read noise 144
- readnoise
 - described 119
 - detector 111
- readout
 - ACCUM 130
 - ACCUM mode 128
 - ACQ mode 128, 139
 - BRIGHTOBJ mode 128, 275
 - BRIGHTOBJ, exposure times 276
 - FAST mode 138
 - MULTIACCUM mode 128, 132
 - non-destructive 130
 - NSAMP 133
 - RAMP mode 129
 - SAMP-TIME 133
 - SLOW mode 138
- readout modes
 - detector 28
- reference files
 - calibration 184
- resetting 130
- resolution
 - cameras 23
- re-use target acquisition
 - described 31
- reuse target offset 31, 80, 82, 84
- RT ANALYSIS 80
- RTO
 - see "reuse target offset"

S

- SAA
 - see "south atlantic anomaly"
- SAM
 - see "small angle maneuvers" 103
- SAM-NO-GYRO 179
- SAM-NO-REACQ 179
- samples array
 - described 192
- SAMP-TIME 133
- saturation
 - detector 111
- science image 191

- described 192
- sensitivity
 - F164N, camera 3 244
 - F171M, camera 2 225
 - F175W, camera 3 246
 - F187N, camera 3 247
 - F190N, camera 3 248
 - F196N, camera 3 249
 - F200N, camera 3 250
 - F212N, camera 3 251
 - F215N, camera 3 252
 - F222M, camera 3 253
 - F237M, camera 2 237
 - F240M, camera 3 254
 - grisms 96
 - limits 18
 - polarizers 88
- servicing mission
 - SM2 19
 - SM3B 3, 27
- servicing mission observatory verification (see "SMOV") 197
- servicing missions
 - SM3B 21
- shading 30, 79, 111, 121
 - dark current removal 138
 - described 30, 121
- shutter
 - detector reset 129
- shutter mechanism 129
- signal to noise 143, 148
 - calculating 147
 - calculation 147
- sky brightness
 - zodiacal background 67
- SLOW
 - readout mode 138
- small angle maneuvers 103, 157, 178, 179
- SMOV 198
 - activities 198
 - testing 197
- software
 - spectroscopy reduction 100
- south atlantic anomaly 66
- Space Telescope European Coordinating Facil-

- ity (ST-ECF) 10
- spacecraft jitter 26
- spacecraft orientations 105
- spectroscopy 18
 - central wavelength 93
 - complex fields 100
 - dispersion 94, 99
 - G141 99
 - G206 99
 - grism, general 18
 - grism, multi-object 94
 - grisms, described 93
 - multi-object 94
 - sensitivity 96
 - spectral coverage 93
- StarView 183
- static calibrations 187
- STSDAS 184, 185
 - calibration 52, 184
- system level thermal vacuum test (see "SLTV")

T

- target acquisition 31
 - ACQ mode, described 31
 - aperture 103, 104
 - interactive 31
 - onboard 31, 139
 - re-use target offset 31
- target acquisition mode 28
- TECs
 - see "thermally electrically cooled shells 21
- telescope
 - motion 103
 - motion, overhead 156
 - small angle maneuvers 103
- thermal background 67, 97, 146, 164, 196
- thermal electrically cooled shells 21
- thermal emission 70, 117
- thermal regime 13, 14
- thermal short
 - see "dewar" 11
- thermal stress 63
- throughput 18
- time
 - overheads 155

- time-resolved images 29
- TinyTim 55, 60
- TWO-CHOP 159

U

- unit conversion tool 257
- units
 - in Handbook 5
 - microns 5
- user support
 - Help Desk 9

V

- vapor cooled shield 21
- vapor-cooled shield (VCS) 19
- VCS
 - see "vapor-cooled shield" 19
- Vega 256
- vignetting 58
 - cameras 1 and 2 58
 - cold 62
 - NIC3 62
 - warm 62

W

- wavefront error 62
- wavelength
 - units 5
- World Wide Web
 - advisories 10
 - documents 10
 - NICMOS web page 10

Y

- young stellar objects (YSOs) 50, 51

Z

- zodiacal background 67, 68, 146
- zodiacal light 67

